# DRAFT
# CBETA Conceptual Design Report

### Cornell-Brookhaven ERL Test Accelerator

*Editors:* G. Hoffstaetter and D. Trbojevic

*Contributors:* J. Barley, I. Bazarov, A. Bartnik, I. Ben-Zvi, J. S. Berg, S. Brooks, D. Douglas, J. Dobbins, B. Dunham, R. Eichhorn, R. Gallagher, C. Gulliford, G. Hoffstaetter, Y. Li, M. Liepe, W. Lou, G. Mahler, C. Mayes, F. Méot, M. Minty, R. Patterson, S. Peggs, V. Ptitsyn, T. Roser, D. Sabol, E. Smith, J. Tuozzolo, D. Trbojevic, N. Tsoupas, H. Witte

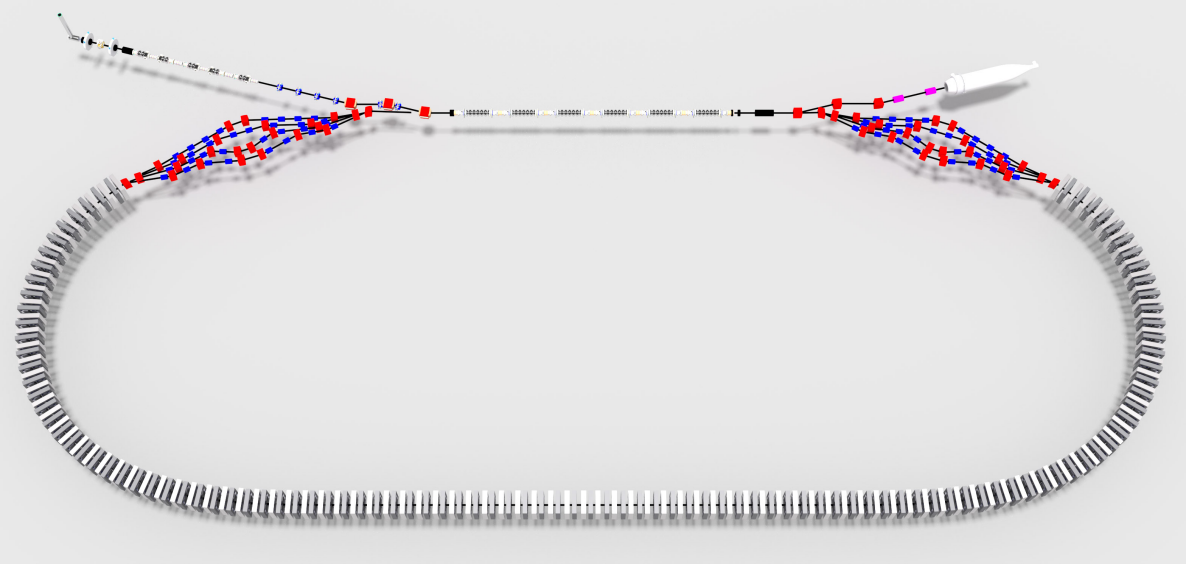

June 7, 2016

# Contents


**1 Introduction** **7**
- 1.1 Executive Summary . . . 7
- 1.2 The L0E experimental hall at Cornell . . . 8
- 1.3 Existing Components at Cornell . . . 10
- 1.4 Component to be development for CBETA . . . 12
- References . . . 13

**2 Accelerator Physics** **15**
- 2.1 Accelerator Layout . . . 15
- 2.2 Optics overview . . . 19
- 2.3 Injector (IN) . . . 23
- 2.4 Linac (LA) . . . 26
- 2.5 Splitters (S1-4, R1-4) . . . 27
- 2.6 FFAG arcs (FA, FB, TA, TB, ZA, ZB) . . . 29
  - 2.6.1 Hard Edge Design . . . 30
  - 2.6.2 Field Maps . . . 31
  - 2.6.3 FA, TA, ZA sections . . . 34
- 2.7 High-Energy Loop for Users . . . 37
- 2.8 Bunch patterns . . . 39
  - 2.8.1 Alternative Pattern for $h = 335$ Circumference . . . 41
- 2.9 CSR . . . 43
- 2.10 Space Charge . . . 44
- 2.11 Wakefields, . . . 47
- 2.12 Beam Loss due to Gas Scattering . . . 50
- 2.13 Orbit & Optics correction . . . 52
- 2.14 Tolerances . . . 54
  - 2.14.1 Analysis Process . . . 54
  - 2.14.2 Estimates . . . 54
  - 2.14.3 Alignment Sensitivity . . . 54
  - 2.14.4 Impact of Excitation Errors . . . 55
  - 2.14.5 RF Phase/Amplitude Response . . . 56
  - 2.14.6 Summary . . . 57
- 2.15 Start-to-End Simulation . . . 58
- 2.16 Beam instabilities: BBU . . . 67
  - 2.16.1 Introduction . . . 67
  - 2.16.2 Bmad Simulation Overview . . . 67
  - 2.16.3 Bmad Simulation Result . . . 67

2.16.4 Aim for higher $I_{\text{th}}$ . . . 70
2.17 Halo . . . 71
References . . . 72

**3 FFAG Magnets** **75**
3.1 Iron-based Permanent Magnet Design . . . 75
3.1.1 General Concept . . . 75
3.1.2 Finite Element Simulations . . . 76
3.1.3 Requirements and Basic Magnet Design . . . 76
3.1.4 Temperature Compensation . . . 78
3.1.5 Quadrupole Corrector . . . 80
3.1.6 Engineering . . . 80
3.1.7 Corrector Magnets for the Iron Dominated Magnets . . . 87
3.2 Backup magnets: Halbach-type Design . . . 98
3.2.1 Comparison of Features vs. Iron Poled Magnets . . . 98
3.2.2 Halbach Magnet Design . . . 98
3.2.3 Tracking and Compatibility with FFAG Lattice . . . 102
3.2.4 Window-Frame Correctors . . . 104
3.2.5 Halbach Magnet R&D and Shimming Results . . . 112
3.2.6 CBETA Halbach Prototypes Unshimmed Results . . . 119
3.2.7 Manufacturing Pipeline and Vendors . . . 124
3.3 Magnet Girder Support System . . . 125
3.4 Power supplies . . . 126
3.4.1 Dipole and Quad Power Supplies for the Spreaders . . . 126
3.4.2 Corrector Magnet Power Supplies . . . 128
References . . . 131

**4 Injector** **135**
4.1 Introduction . . . 135
4.2 The DC Photoemission Gun . . . 135
4.3 Photocathodes . . . 143
4.4 The Laser System . . . 144
4.5 Buncher System . . . 147
4.6 Injector Linac . . . 150
4.6.1 Introduction . . . 150
4.6.2 Injector cavities . . . 150
4.6.3 Injector input coupler . . . 153
4.6.4 Wakefield and HOM calculations . . . 155
4.6.5 Injector HOM dampers . . . 156
4.6.6 Injector RF stability requirements and LLRF . . . 158
4.6.7 RF Power System for the Injector Linac . . . 159
4.6.8 Injector cryomodule . . . 160
4.7 Beam Stop . . . 165
References . . . 168

**5 Linac and RF systems** **171**
5.1 Introduction . . . 171
5.2 MCL Overview . . . 172
5.3 Beam Line Components . . . 172
5.3.1 SRF Cavities . . . 172
5.3.2 Fundamental Power Couplers . . . 175
5.3.3 Cavity Frequency Tuners . . . 175
5.3.4 HOM Absorbers . . . 177
5.4 MLC Design . . . 180
5.4.1 Mechanical Design . . . 180
5.4.2 Cryogenic Cooling Scheme . . . 180
5.4.3 80 K Thermal Shield . . . 180
5.4.4 Magnetic Shielding . . . 182
5.4.5 Vacuum Vessel . . . 182
5.4.6 Alignment . . . 182
5.5 Assembly Process, Cool-down, and Performance Testing . . . 184
5.5.1 MLC Assembly . . . 184
5.5.2 Preparation for Testing . . . 184
5.5.3 Initial Cool-down . . . 184
5.5.4 Cool-down Cycles . . . 187
5.5.5 RF Test Results . . . 187
5.5.6 HOM Damping Studies . . . 188
5.5.7 Tuning and Microphonics . . . 188
References . . . 190

**6 Cryogenics for the CBETA project** **193**
6.1 Overview . . . 193
6.1.1 Thermal loads expected . . . 193
6.1.2 Use of existing Wilson Lab cryoplant . . . 195
6.1.3 Subsystem Components . . . 195
6.2 Heat Exchanger Cans in greater detail . . . 196
6.2.1 Construction and Interfacing . . . 196
6.2.2 Prior performance . . . 198
6.3 Cryomodules in greater detail . . . 199
6.3.1 Construction and Interfacing . . . 199
6.3.2 Prior performance . . . 200
6.4 Sensors and Controls for the cryogenics system . . . 202
6.5 Safety Issues (that have already been considered for our prior test operations) . . . 202
6.6 Aspects still under development . . . 203
References . . . 203

**7 Vacuum System** **205**
7.1 Vacuum system layout and sections . . . 205
7.2 Vacuum system requirements and design considerations . . . 205

7.3 Vacuum system construction, installation, and operation . . . 206
7.3.1 FFAG Arcs and Straight . . . 206
7.3.2 Splitter and Combiner . . . 207
7.3.3 RF-shielded bellows . . . 207
7.3.4 Ion clearing electrodes . . . 208
7.3.5 Vacuum system construction and installation . . . 208
7.3.6 Vacuum pumping . . . 209
7.3.7 Vacuum instrumentation and operation . . . 209
7.4 Vacuum pumping and performance simulations . . . 209
References . . . 210

**8 Diagnostics and Control 213**
8.1 Introduction . . . 213
8.1.1 Beam position measurement system . . . 213
8.1.2 Bunch Arrival Monitors . . . 216
8.1.3 Beam Size . . . 216
8.1.4 Beam Loss Monitors . . . 217
References . . . 217

**9 Personnel Safety 219**
9.1 General considerations . . . 219
9.2 More on Radiation Safety . . . 221
9.3 Accident Rate and Training Compliance . . . 221
9.4 CBETA-specific safety challenges . . . 222
9.4.1 New collaborators . . . 222
9.4.2 Radiation safety . . . 222
9.4.3 Cryogenic safety . . . 223
9.4.4 Electrical safety . . . 223
References . . . 223

**10 Commissioning 225**
10.1 Concepts and Philosophy . . . 225
10.2 Goals and Overview . . . 226
10.3 Commissioning Flow . . . 227
10.4 Outline of Process . . . 227
10.5 Injector and Merger . . . 229
10.5.1 Linac . . . 229
10.6 First Turn . . . 230
10.6.1 FFAG, First Turn . . . 230
10.6.2 Linac, Second Pass . . . 230
10.6.3 High Current, First Turn . . . 230
10.7 Multiple Turns . . . 231
References . . . 231

# 1 Introduction

## 1.1 Executive Summary

The Cornell-BNL ERL Test Accelerator (CBETA) will be a unique resource to carry out accelerator science and enable exciting research in nuclear physics, materials science and industrial applications. Initially it will prototype components and evaluate concepts that are essential for Department of Energy (DOE) plans for an Electron-Ion Collider (EIC).

CBETA is an Energy-Recovery Linac (ERL) that is being constructed at Cornell University. It will be the first ever multi-turn Energy Recovery Linac with superconducting RF (SRF) acceleration. And it will be the first ERL based on Fixed Field Alternating Gradient (FFAG) optics.

The Nuclear Physics (NP) division of DOE has been planning for an EIC for more than a decade. Research and development on this project is mostly performed at Brookhaven National Laboratory (BNL) and at the Thomas Jefferson National Accelerator Facility (TJNAF). BNL on Long Island, NY is planning to transform the Relativistic Heavy Ion Collider (RHIC) into eRHIC [1] while TJNAF is planning to collide an existing electron beam with a new, electron-cooled ion beam in the Medium-Energy Electron Ion Collider (MEIC).

Both EIC projects need an ERL as an electron cooler for low-emittance ion beams. For eRHIC, a new electron accelerator would be installed in the existing RHIC tunnel at BNL, colliding polarized electrons with polarized protons and $^3$He ions, or with unpolarized ions from deuterons to Uranium. The electron beam can either be stored in a ring for a ring-ring collider or it can be provided by an ERL for a linac-ring collider. Because experiments have to be performed for all combinations of helicity, bunches with alternating polarization have to be provided for the collisions. An electron ring can provide these conditions only when it is regularly filled by a linac. Both eRHIC designs therefore have a recirculating linac with return loops around the RHIC tunnel.

Significant simplification and cost reduction is possible by configuring eRHIC with non-scaling (NS-FFAG) optics in combination with an ERL. Two NS-FFAG beamline arcs placed on top of each other allow multiple passes through a single superconducting linac. For a large accelerator like eRHIC, where each separate return loop is many kilometers long, an FFAG-ERL produces a significantly more cost-optimized accelerator.

CBETA will establish the operation of a multi-turn ERL. The return arc, made of an FFAG lattice with large energy acceptance, will be commissioned, establishing this cost-reducing solution for eRHIC. Many effects that are critical for designing the EIC will be measured, including the Beam-Breakup (BBU) instability, halo-development and collimation, growth in energy spread from Coherent Synchrotron Radiation (CSR), and CSR micro bunching. In particular, CBETA will use an NS-FFAG lattice that is very compact, enabling multiple passes of the electron beam in a single recirculation beamline, using the SRF linac four times.

Because the prime accelerator-science motivations for CBETA are essential for an EIC, and

address items that are perceived as the main risks of eRHIC, its construction is an important milestone for the NP division of DOE and for BNL.

But the scientific merits of CBETA are even broader, because it produces significantly improved, cost-effective, compact continuous wave (CW) high-brightness electron beams that will enable exciting and important physics experiments, including dark matter and dark energy searches [2], Q-weak tests at lower energies [3], proton charge radius measurements, and an array of polarized-electron-enabled nuclear physics experiments. High brightness, narrow line-width gamma rays can be generated by Compton scattering [4] using the ERL beam, to be used for nuclear resonance fluorescence, the detection of special nuclear materials, and an array of astrophysical measurements. The energy and current range of CBETA will also be ideal for studying high power free electron laser (FEL) physics for materials research and for industrial applications.

CBETA brings together the resources and expertise of a large DOE National Laboratory, BNL, and a leading research university, Cornell. CBETA will be built in an existing building at Cornell, using many components that have been developed at Cornell under previous R&D programs that were supported by the National Science Foundation (NSF), New York State, and Cornell University. These components are a fully commissioned world-leading photoemission electron source, a high-power injector, and an ERL accelerator module, both based on SRF systems, and a high-power beam stop. The only elements that require design and construction from scratch are the FFAG magnet transport lattices of the return arc.

The collaborative effort between Brookhaven and Cornell University to build a particle accelerator will be a model for future projects between universities and national laboratories, taking advantage of the expertise and resources of both to investigate new topics in a timely and cost-effective manner.

## 1.2 The L0E experimental hall at Cornell

Cornell's Wilson laboratory has an experimental hall that has already largely been freed up for the installation of CBETA. It was originally constructed as the experimental hall for extracted-beam experiments with Cornell's 12 GeV Synchrotron. It is equipped with a high ceiling and an 80 ton crane, with easy access and a suitable environment, mostly below ground level. The dimensions of CBETA fit well into this hall, as shown in Fig. 1.2.1 with the parameters of Tab. 1.2.1.

The DC photo-emitter electron source, the injector linac, the ERL merger, the high-current ERL linac module, and the ERL beam stop are already installed in this hall and are connected to their cryogenic systems and to other necessary infrastructure.

CBETA is not only an excellent accelerator for prototyping components and for developing concepts for the EIC, and in particular for eRHIC, in its experimental hall at Cornell. It is also an important part of future plans at Cornell for accelerator research, nuclear physics research, materials studies, and for ongoing ERL studies.

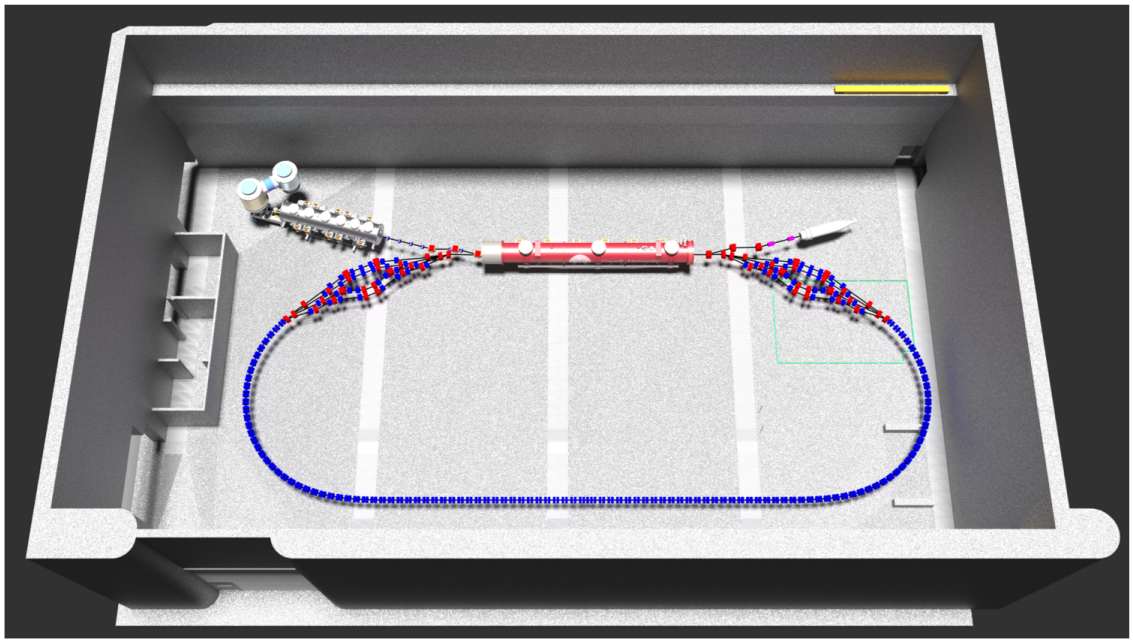

Figure 1.2.1: Floor plan of the Cornell-BNL ERL Test Accelerator in the L0E experimental hall at Cornell's Wilson laboratory.

Table 1.2.1: Primary parameters of the Cornell-BNL ERL Test Accelerator.

| Parameter | Value | Unit |
|---|---|---|
| Largest energy | 150 | MeV |
| Injection energy | 6 | MeV |
| Linac energy gain | 36 | MeV |
| Injector current (max) | 40 | mA |
| Linac passes | 8 | 4 accel. + 4 decel. |
| Energy sequence in the arc | 42,78,114,150,114,78,42 | MeV |
| RF frequency | 1300. | MHz |
| Bunch frequency (high-current mode) | 325. | MHz |
| Circumference harmonic | 333 | |
| Circumference length | 76.793 | m |
| Circumference time | 0.256154 | $\mu$s |
| Normalized transverse rms emittances | 2 | $\mu$m |
| Bunch length | 3 | ps |
| Typical arc beta functions | 0.4 | m |
| Typical splitter beta functions | 50. | m |
| Transverse rms bunch size (max) | 2806 | $\mu$m |
| Transverse rms bunch size (min) | 52 | $\mu$m |
| Bunch charge (min) | 1 | pC |
| Bunch charge (max) | 123 | pC |

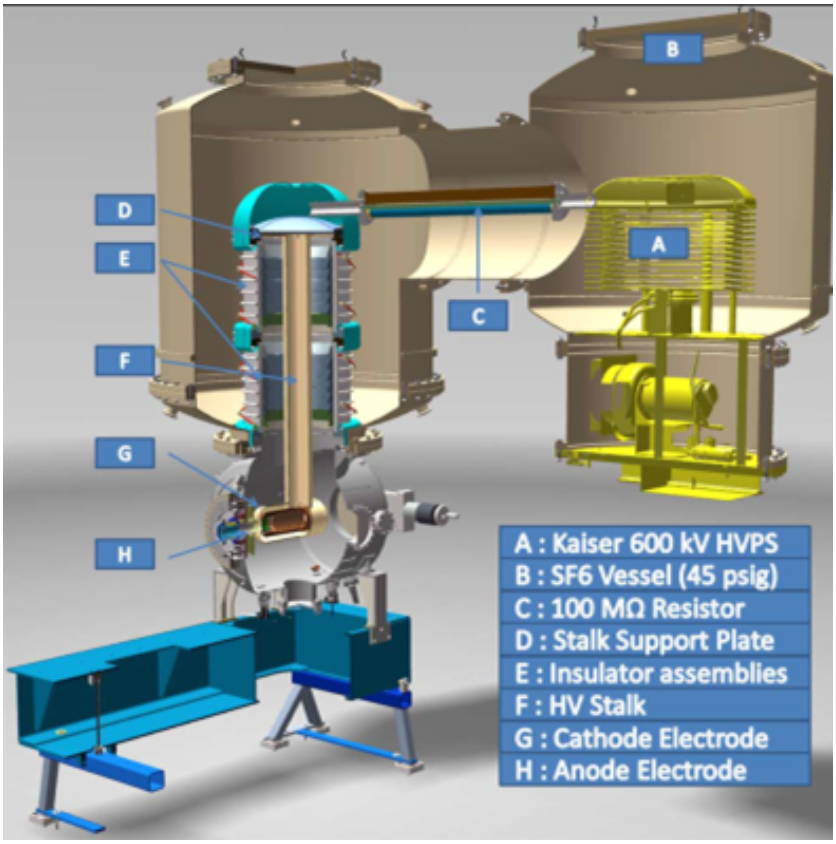


Figure 1.3.1: A cutaway view of the DC photoemission gun. Photocathodes are prepared in a load lock system mounted on the large flange at the left, and transported through the cathode cylinder to the operating position in the Pierce electrode shape on the right. The beam exits through the small flange to the right.

## 1.3 Existing Components at Cornell

**DC photo-emitter electron source:** High voltage DC photoemission electron guns offer a robust option for photoelectron sources, with applications such as ERLs. A DC gun for a high brightness, high intensity photoinjector requires a high voltage power supply (HVPS) supplying hundreds of kV to the high voltage (HV) surfaces of the gun. At Cornell, the gun HV power supply for 750 kV at 100 mA is based on proprietary insulating core transformer technology. This technology is schematically shown in Fig. 1.3.1 for Cornell's DC photoemitter gun. This gun holds the world record in sustained current of up to 75mA.

**High-Power CW SRF injector linac:** The photoemission electron injector shown in Fig. 1.3.2 is fully operational, and requires no further development. It has achieved the world-record current of 75 mA [5–7], and record low beam emittances for any CW photoinjector [8], with normalized brightness that outperforms other sources by a substantial factor. Cornell has established a world-leading effort in photoinjector source development, in the underlying beam

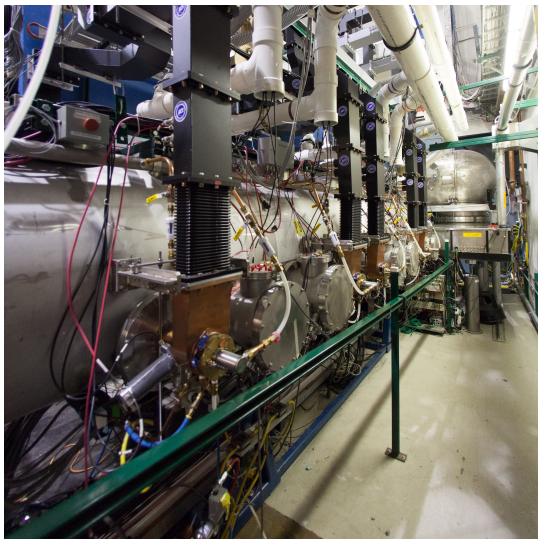

(a) Injector cryomodule

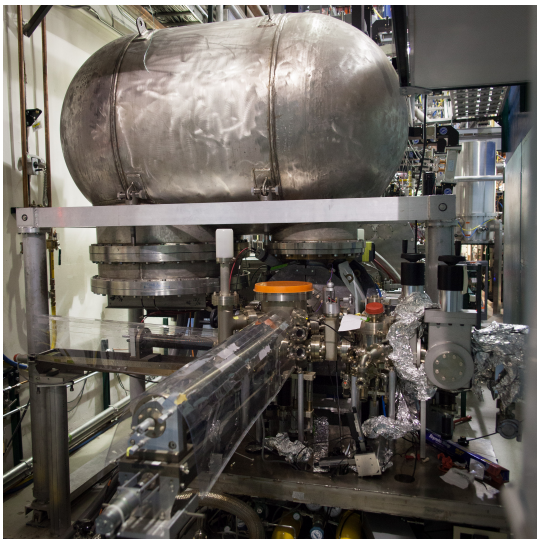

(b) DC gun

Figure 1.3.2: The photographs show (from right to left) the high voltage DC gun, an emittance compensation section, the RF buncher, and the cryomodule. Accelerated beam is then directed into a beamline or into the beam stop.

theory and simulations, with expertise in guns, photocathodes, and lasers. The injector delivers up to 500 kW of RF power to the beam at 1300 MHz. The buncher cavity uses a 16 kW IOT tube, which has adequate overhead for all modes of operation. The injector cryomodule is powered through ten 50 kW input couplers, using five 130 kW CW klystrons. The power from each klystron is split to feed two input couplers attached to one individual 2-cell SRF cavity. An additional klystron is available as a backup, or to power a deflection cavity for bunch length measurements.

**High-current ERL cryomodule:** For CBETA, the main accelerator module will be the Main Linac Cryomodule (MLC), which was built as a prototype for the NSF-funded Cornell hard-X-ray ERL project. This cryomodule houses six 1.3GHz SRF cavities, powered via individual CW RF solid state amplifiers. Higher order mode (HOM) beamline absorbers are placed in-between the SRF cavities to ensure strong suppression of HOMs, and thus enable high current ERL operation. The module, shown in Fig. 1.3.3 was finished by the Cornell group in November 2014 and successfully cooled-down and operated starting in September 2015. The MLC will be powered by 6 individual solid-state RF amplifiers with 5 kW average power per amplifier. Each cavity has one input coupler. One amplifier is currently available for testing purposes, so an additional 5 amplifiers are needed for this project.

**ERL merger and ERL beam stop:** In Fig. 1.2.1, three merger magnets are shown between the Injector Cryomodule (ICM) and the MLC. These merger magnets steer the injected beam with 6 MeV from the ICM into the MLC, bypassing the recirculated beams of higher energy. This merger has already been tested after the ICM, and it was shown that its influence on the

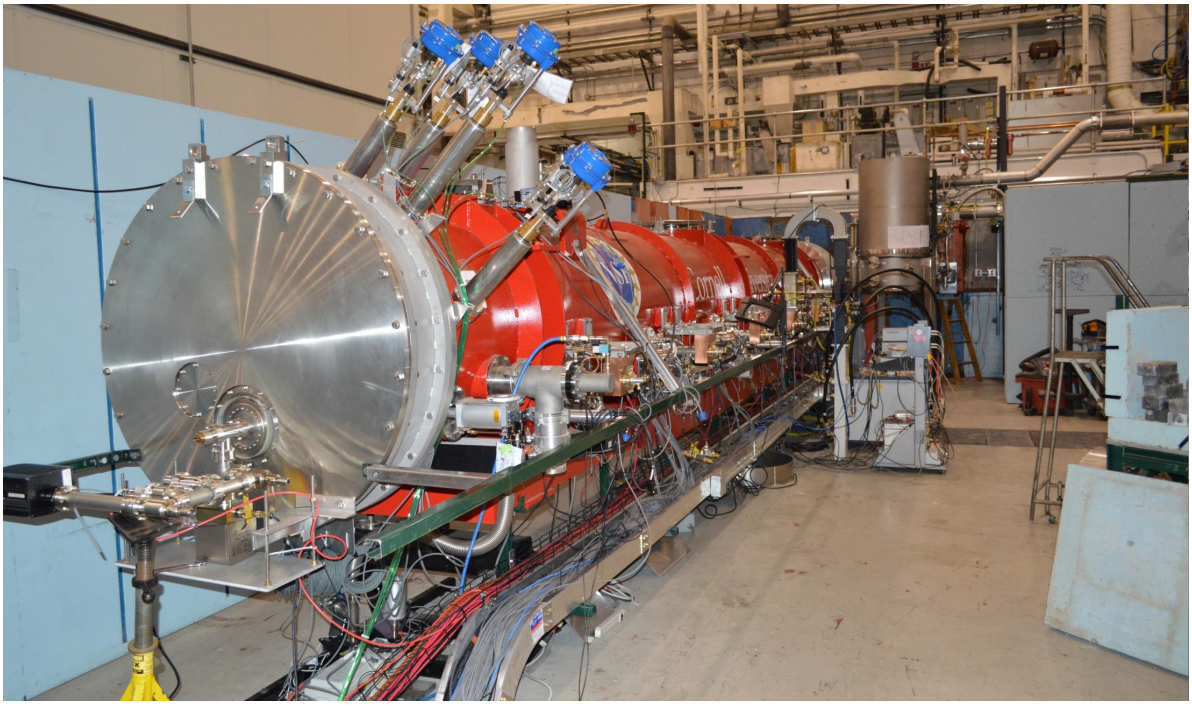

Figure 1.3.3: The Cornell Main Linac Cryomodule (MLC) installed for RF testing in the experimental hall L0E.

beam emittances can be minimized. The beam stop in the top left of that picture also already exits, and with a power limit 600kW it can absorb all beams that are specified for CBETA.

## 1.4 Component to be development for CBETA

While the splitter and recombiner sections to the right and the left of the MLC in Fig. 1.2.1 are equipped with conventional electro magnets, the magnets of the FFAG arc are made of permanent magnets. The field of these quadrupoles is shaped by iron poles, but the magnetic flux is produced by cubes of permanent magnet material. A prototype of this design is shown in Fig. 1.4.1 on a field-measuring bench at BNL.

This report describes the following other larger systems that will be developed for CBETA:

- The vacuum system
- Girders for magnets and beamlines
- Beam-Position Monitor (BPM) system
- The control system and other beam instrumentation

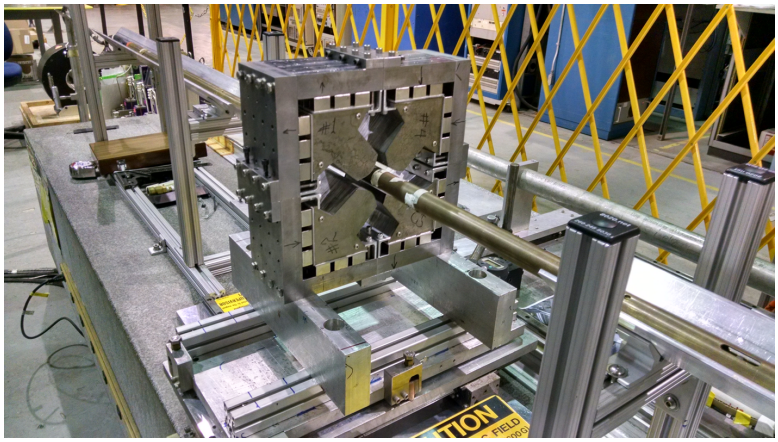

Figure 1.4.1: The FFAG magnet QD on a rotating coil test bench.

## References


[1] E.C. Aschenauer, e. a. *eRHIC Design Study: An Electron-Ion Collider at BNL*. Technical report (2014).

[2] (ed.) et al., R. M. *Proceedings of the Workshop to Explore Physics Opportunities with Intense, Polarized Electron Beams up to 300 MeV*. In *AIP Conf. Proc.*, 1563. Cambridge, MA (2013).

[3] D. Androi, e. a. *First Determination of the Weak Charge of the Proton*. Physical Review Letters, **141803** (111) (2013).

[4] F. Albert, e. a. *Design of narrow-band Compton scattering sources for nuclear resonance fluorescence*. Physical Review ST-AB, **050703** (14) (2011).

[5] L. Cultrera, e. a. *Growth and characterization of rugged sodium potassium antimonide photocathodes for high brilliance photoinjector*. Applied Physics Letters, **103504** (103) (2013).

[6] B.M. Dunham, e. a. *Record high-average current from a high-brightness photoinjector*. Applied Physics Letters, **034105** (102) (2013).

[7] L. Cultrera, e. a. *Photocathode Behavior during High Current Running in the Cornell ERL Photoinjector*. Physical Review ST-AB, **120101** (14) (2011).

[8] C. Gulliford, e. a. *Demonstration of low emittance in the Cornell energy recovery linac photoinjector prototype*. Physical Review ST-AB, **73401** (16) (2013).

# 2 Accelerator Physics

## 2.1 Accelerator Layout

CBETA is a four-pass energy recovery linac. It incorporates the existing Cornell ERL high-power injector, MLC, and beam stop, to demonstrate four passes up in energy and four passes down in energy through a single arc section consisting of FFAG magnets with a common vacuum chamber. In order to properly inject into and extract from this FFAG arc, splitter sections are inserted between the MLC and the FFAG arc.

The layout is broken into nine major sections:

**IN** Injector: DC gun, front-end, injector cryomodule, and merger.

**LA** Linac, containing the MLC.

**SX** Splitters S1, S2, S3, and S4.

**FA** FFAG arc

**TA** Transition from arc-to-straight

**ZA** Straight FFAG section.

**ZB** Straight FFAG section. This is a mirror of ZA.

**FB** FFAG straigth-to-arc, arc. This is a mirror of FA.

**TB** Transition from straight-to-arc

**RX** Splitters (recombiners) R1, R2, R3, R4. This is similar to a mirror of SX sections.

**BS** Beam stop, including demerging.

These are shown in Fig. 2.1.1. The geometry is roughly symmetric, with angles shown in Fig. 2.1.2. Tables 2.1.1 and 2.1.2 show the magnet counts for all sections.

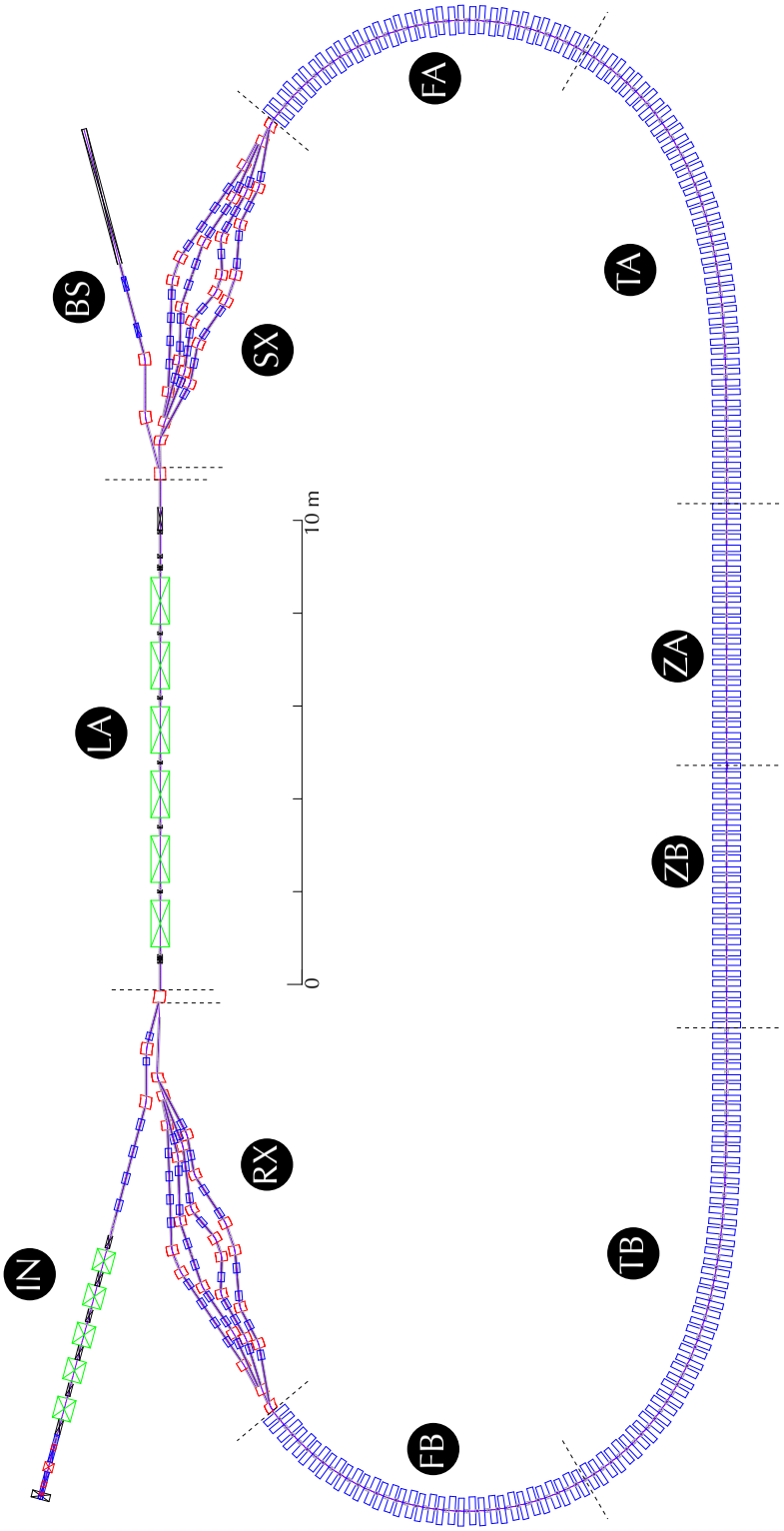


Figure 2.1.1: CBETA layout with all major sections.

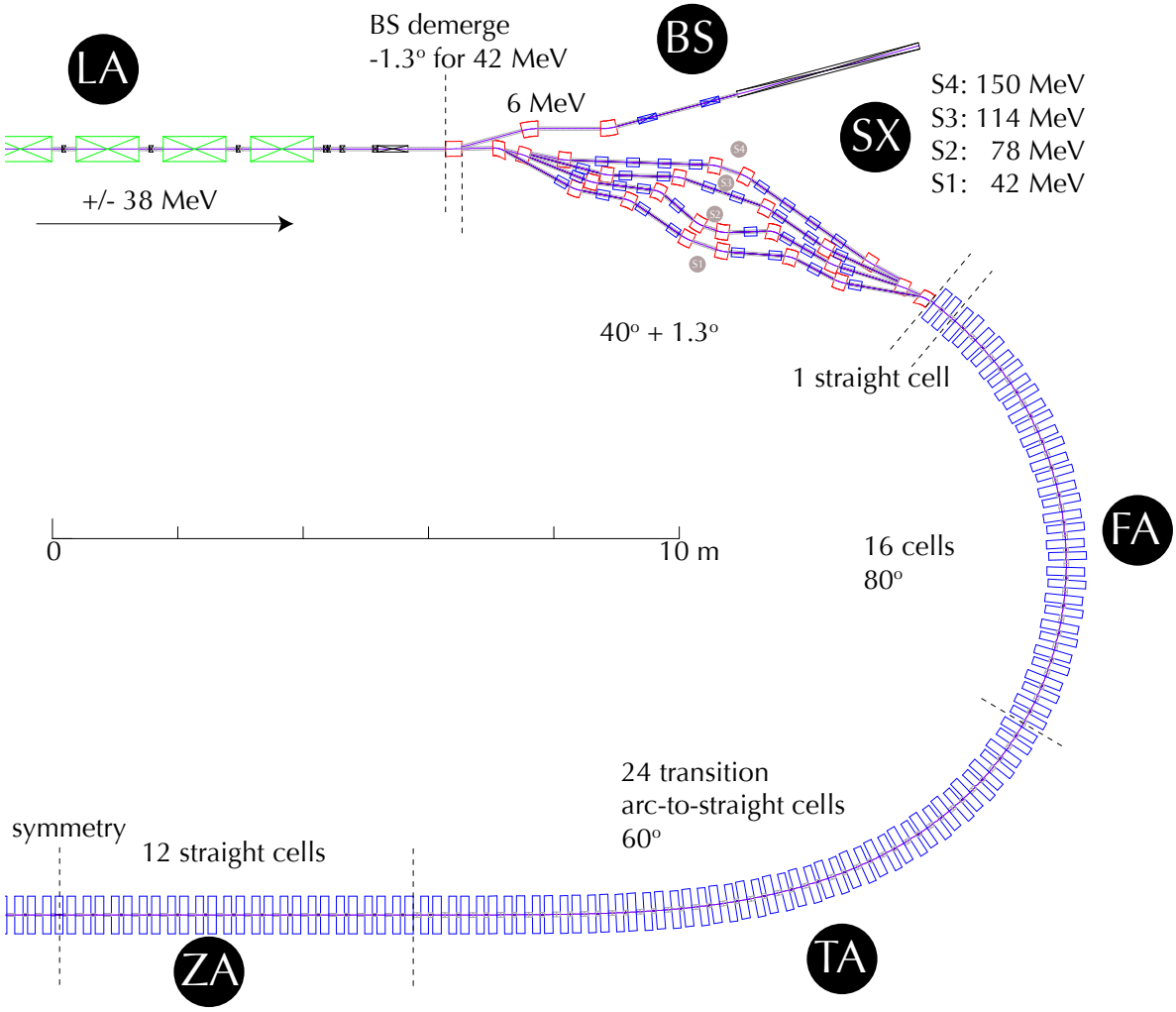


Figure 2.1.2: CBETA symmetric geometry.

Table 2.1.1: Component count for splitter and recombiner sections. Dipole and Quadrupole magnets are conventional electromagnets. Correctors counts are for combined horizontal and vertical correctors.

| Section | Dipole | Quad | BPM | Corrector |
|---|---|---|---|---|
| S1 | 8 | 8 | 8 | 8 |
| S2 | 8 | 8 | 8 | 8 |
| S3 | 4 | 8 | 8 | 8 |
| S4 | 4 | 8 | 8 | 8 |
| R1 | 8 | 8 | 8 | 8 |
| R2 | 8 | 8 | 8 | 8 |
| R3 | 4 | 8 | 8 | 8 |
| R4 | 4 | 8 | 8 | 8 |
| Total | 48 | 64 | 64 | 64 |

Table 2.1.2: Component count for FFAG sections. Corrector counts are for separated horizontal (H) and vertical (V) correctors.

| Section | Focusing (F) Quad | Defocusing (D) Quad | BPM | Corrector (H) | Corrector (V) |
|---|---|---|---|---|---|
| FA | 17 | 17 | 17 | 17 | 17 |
| TA | 24 | 24 | 24 | 24 | 24 |
| ZA | 12 | 13 | 13 | 12 | 13 |
| ZB | 12 | 12 | 12 | 12 | 12 |
| TB | 24 | 24 | 24 | 12 | 12 |
| FB | 17 | 17 | 17 | 17 | 17 |
| Total | 106 | 107 | 107 | 106 | 107 |

## 2.2 Optics overview

The last two decades have seen a remarkable revival of interest in Scaling Fixed Field Alternating Gradient (S-FFAG) accelerators. Originally developed in the 1950s [1–3], S-FFFAGs have very large momentum acceptances, with a constant magnetic field that varies across the aperture according to

$$B \sim B_o \left( \frac{r}{r_o} \right)^k \tag{2.2.1}$$

where the scaling exponent $k \sim 150$ is as large as possible. The revival began in Japan, with a proof-of-principle proton accelerator at KEK followed by a 150 MeV proton accelerator at Osaka University (now at Kyushu University) and many smaller electron S-FFAGs built for a variety of applications such as food irradiation.

Although S-FFAGs have the advantages of fixed magnetic fields, zero chromaticities, and fixed tunes, nonetheless synchrotrons mostly dominate, despite their need for magnet cycling, because synchrotrons have much smaller apertures – a few centimeters compared to of order one meter for S-FFAGs. The international muon collider collaboration proposed that S-FFAGs accelerate short lifetime muons, avoiding the need for very rapid cycling synchrotrons [4]. Similarly, Electron Recovery Linacs cannot use synchrotron-like arcs, because it is not possible to rapidly change the magnetic field during electron acceleration. Except for CBETA, all proposed and operational multipass ERLs (and RLAs) use multiple beamlines – one beamline for every electron energy.

Non-Scaling FFAG (NS-FFAG) optics [5, 6] reduce the number of beamlines required in a multipass ERL to one, while preserving centimeter-scale apertures. Aperture reduction is enabled by ensuring very small values of horizontal dispersion $D_x$, since

$$\Delta x = D_x \frac{\Delta p}{p} \tag{2.2.2}$$

where $\Delta x$ is the orbit offset, and $p$ is the electron momentum. For example, if the dispersion $D_x \approx 40$ mm, then the orbit offsets are only $\Delta x \approx \pm 20$ mm for a momentum range $\Delta p/p \approx \pm 50\%$ that corresponds to an energy range of 3 for relativistic particles. The magnetic field in NS-FFAG optics is purely linear, with

$$\begin{aligned} B_y &= B_0 + G(s)\, x \\ B_x &= \qquad G(s)\, y \end{aligned} \tag{2.2.3}$$

This in stark contrast to the nonlinear field variation in S-FFAG magnets. All NS-FFAG magnets are linear combined function magnets, often just transversely displaced quadrupoles. However, abandoning nonlinear scaling has a price – the tunes and the chromaticities now vary with energy, and the time-of-flight is a parabolic function of energy.

Tuning the NS-FFAG optics to minimize the orbit offsets is similar to minimizing the natural emittance of a synchrotron light source, because both refer to the dispersion action function

$$H = \left( \frac{D}{\sqrt{\beta}} \right)^2 + \left( D' \sqrt{\beta} + \frac{\alpha D}{\sqrt{\beta}} \right)^2 \tag{2.2.4}$$

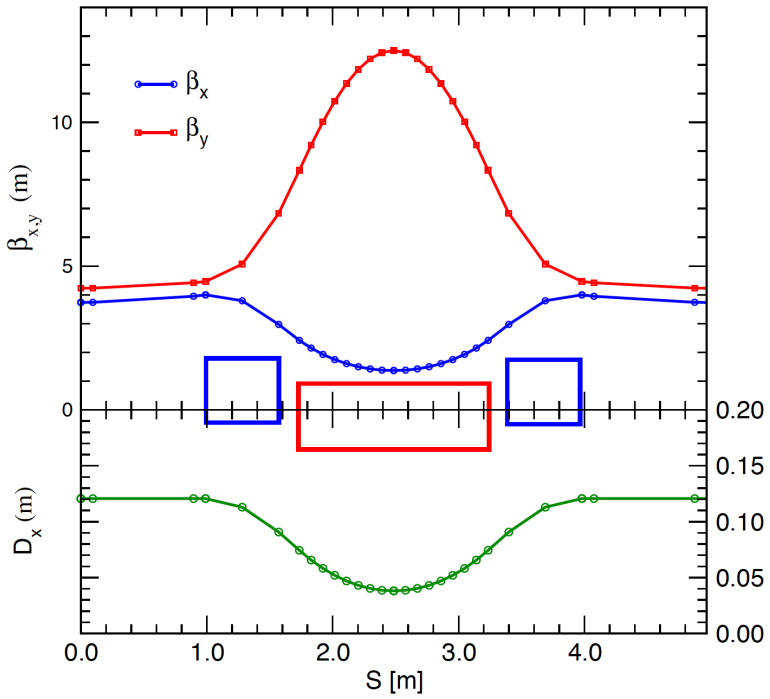


Figure 2.2.1: Betatron and dispersion functions at the central energy in a triplet cell with a central combined function dipole.

where $D'$ is the slope of the dispersion function, and $\beta$ and $\alpha$ are Twiss functions [7, 8]. The minimum emittance is achieved in a synchrotron light source by minimizing the average dispersion action

$$\langle H \rangle \;=\; \frac{1}{L}\int_0^L H(s)ds \tag{2.2.5}$$

For a given lattice cell geometry, such as the triplet configuration shown in Figure 2.2.1, this is accomplished by adjusting the parameters so that

$$\frac{\partial\langle H\rangle}{\partial D_0} \;=\; \frac{\partial\langle H\rangle}{\partial\beta_0} \;=\; 0 \tag{2.2.6}$$

where $D_0$ and $\beta_0$ are the periodic values at the cell ends [7]. The performance of three such configurations – triplet, FODO, and doublet – is shown in Figure 2.2.2, by following the evolution of the normalized dispersion vector $\sqrt{H}$ in $(\chi, \xi)$ space, where

$$\begin{aligned} \chi &= D'\sqrt{\beta} + \frac{\alpha D}{\sqrt{\beta}} \\ \xi &= \frac{D}{\sqrt{\beta}} \end{aligned} \tag{2.2.7}$$

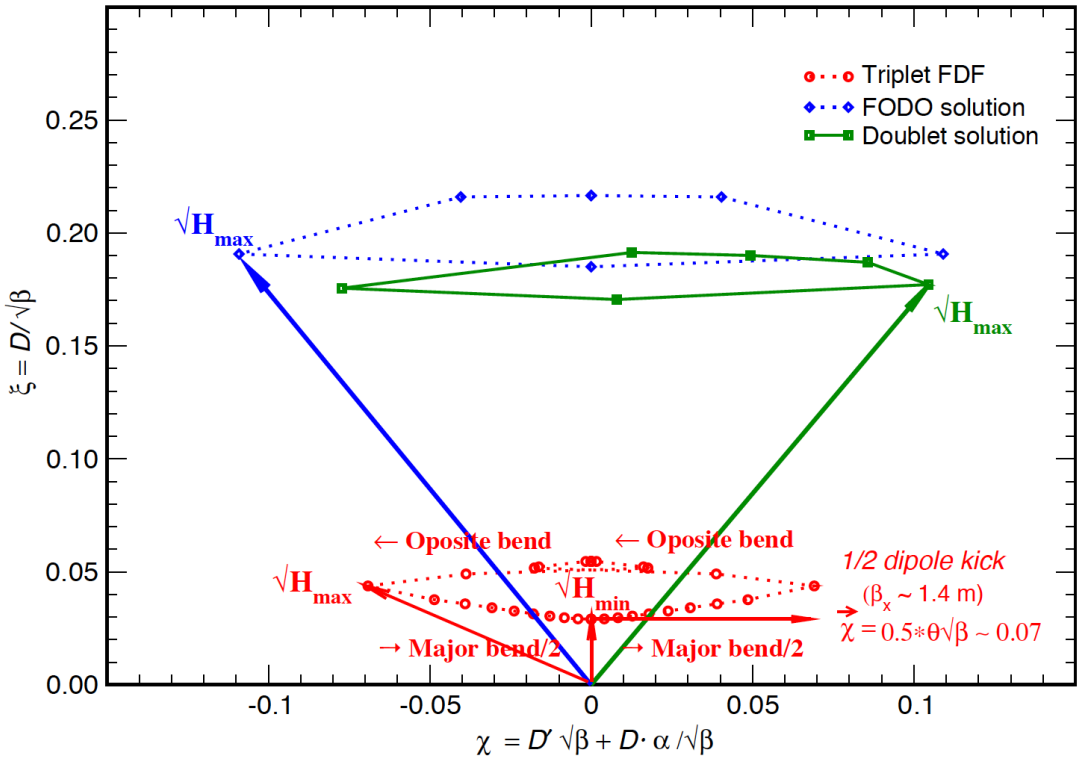


Figure 2.2.2: Normalized dispersion function for three basic cell configurations – triplet, FODO, and doublet – using the same magnets.

Superficially the triplet configuration is the most advantageous, with smaller maximum orbit offsets and smaller path length differences. However, it is difficult to implement a triplet configuration when space is limited, as it was for the first NS-FFAG accelerator, the Electron Model for Many Application-EMMA [9]. Space is also very constrained for CBETA, making it difficult to include the two small drifts between the two focusing magnets and the central defocusing combined function magnet.

The outer transverse size of the magnets depends directly on the maximum orbit offsets within the magnets – smaller orbit offsets allow a smaller pole tip radius. The optimum solution for the CBETA cell is to use two kinds of combined function magnet: one with a larger focusing gradient and a small dipole field, and the other with a smaller defocusing gradient providing most of the bending. These combined function fields are achieved by displacing two different kinds of quadrupole. The smallest possible gradient values are achieved by displacing focusing and defocusing quadrupoles in opposite directions, maximizing the good field region when the orbit displacement is at its maximum. The focusing quadrupole is displaced away from the center of the circular arc, and the defocusing quadrupole is displaced inwards.

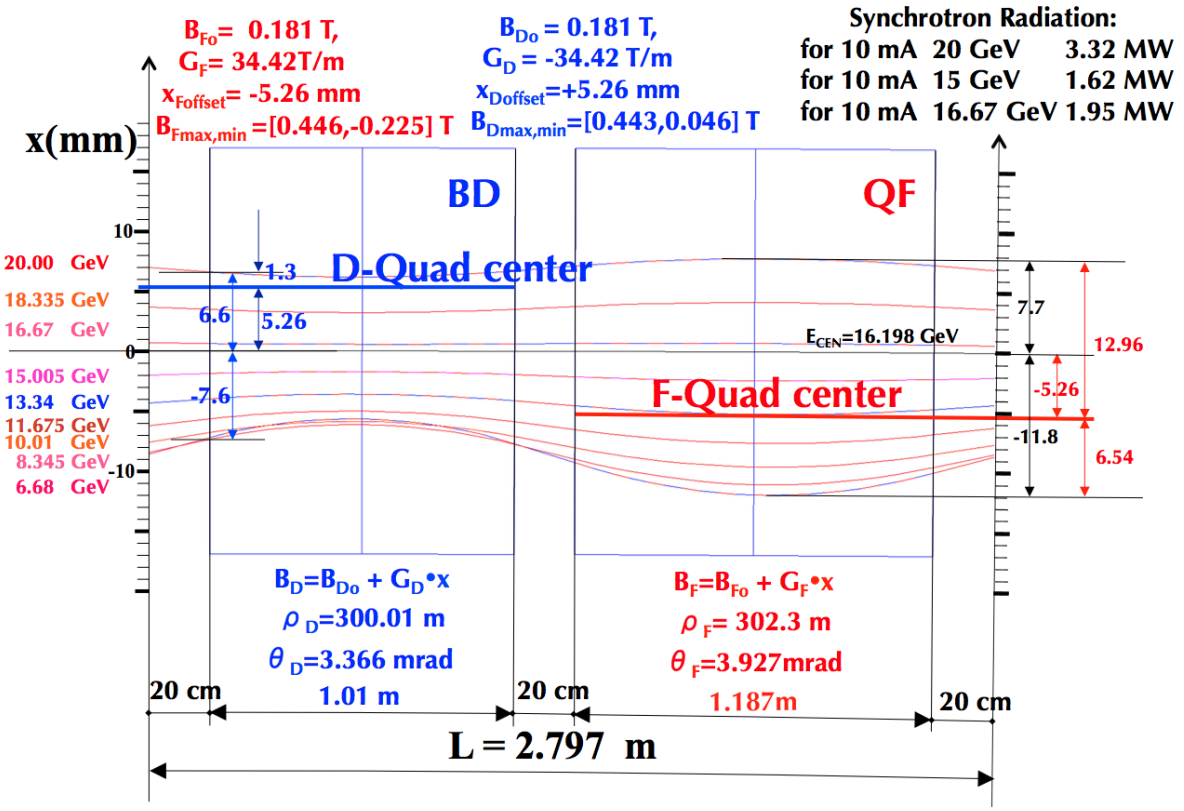


Figure 2.2.3: Orbits and dimensions of the eRHIC NS-FFAG basic arc cell.

The NS-FFAG lattice for the Electron-Ion Collider has far milder magnet size and bending radii requirements. Synchrotron radiation is a serious challenge at the highest energy (20 GeV) in eRHIC, even though the average radius of the RHIC tunnel is $\sim$ 330 meters. To simplify the eRHIC magnet design, the gradients and the bending fields of the focusing and defocusing combined function magnets are made equal. Combined function magnets are obtained by radially displacing the quadrupoles by only $\pm$ 5.26 mm in opposite directions, as shown in Figure 2.2.3 .

The most important difference between eRHIC magnets and CBETA magnets is in the orbit offsets. The maximum orbit offsets at the highest energy in eRHIC (with respect to the magnetic axis of the quadrupole) are $\sim$ 13 mm and $\sim$ 14, for focusing and defocusing magnets, respectively. The offsets in CBETA are significantly larger because the arc radius of the curvature is only $\sim$ 5 m. This is discussed in detail in the later chapters.

## 2.3 Injector (IN)

The design, layout, and performance of the Cornell high brightness, high current photoinjector has been well documented [10–12]. The injector dynamics are strongly space charge dominated. Consequently, the 3D space charge simulation code General Particle Tracer (GPT) is used as the base model of the injector dynamics. All of the beamline elements relevant for the space charge simulations in this work have been modeled using realistic field maps. Poisson Superfish [13] was used to generate 2D cylindrically symmetric fields specifying $E_r(r,z)$ and $E_z(r,z)$ as well as $B_r(r,z)$ and $B_z(r,z)$, for the high-voltage DC and emittance compensation solenoids, respectively. Detailed plots of these fields can be found in [10].

The dipole and quadrupole fields are described using the following off axis expansion for the fields [14]:

$$B_x^D \sim \mathcal{O}(4), \qquad B_y^D = B_0(y) - \frac{y^2}{2}\frac{d^2B_0}{dz^2} + \mathcal{O}(4), \qquad B_z^D = y\frac{dB_0}{dz} + \mathcal{O}(4) \tag{2.3.1}$$

$$\begin{aligned} B_x^Q &= y\left[G(z) - \frac{1}{2}\left(3x^2+y^2\right)\frac{d^2G}{dz^2}\right] + \mathcal{O}(5), \\ B_y^Q &= x\left[G(z) - \frac{1}{2}\left(3y^2+x^2\right)\frac{d^2G}{dz^2}\right] + \mathcal{O}(5), \\ B_z^Q &= xy\frac{dG(z)}{dz} + \mathcal{O}(4). \end{aligned} \tag{2.3.2}$$

In this expression $B_0 = B_y^D(r=0,z)$ is the on-axis field in the dipole and $G(z) = \partial B_y^Q(r=0,z)/\partial x$ is the on-axis quad field gradient. Both of these quantities are extracted from full 3D maps generated using Opera3D [15].

All RF cavity fields were generated using the eigenmode 3D field solver in CST MICROWAVE STUDIO (MWS) [16]. For the SRF cavities, two solutions for the fields are generated and then combined using the method described in [17] in order to correctly include the asymmetric quadrupole focusing of the input power couplers. Currently, these combined field maps have been constructed with powers in their fully retracted position, typically used for low current.

In order to facilitate using both GPT as well as ASTRA if desirable, a standalone input particle distribution generator was written in C++, and was used for all space charge simulations discussed in this section. This code uses standard sub-random sequences to generate particle phase space coordinates and allows for nearly arbitrary six-dimensional phase space distributions to specified either from a file or using the combination of several continuously variable basic distribution shapes. For example, this allows one to load the measured transverse laser profile on the cathode along with a simulated longitudinal laser profile using a model of the longitudinal shaping crystals. See [12] for examples of generating realistic particle distributions from measured laser profiles.

The determination of the appropriate optics in the injector is set by the requirements for the FFAG ring. In particular it is important to inject with a beam that is suitably matched into the first splitter section. Because the dynamics in the injector and largely through the first

pass through the linac are dominated by space charge forces, multi-objective genetic algorithm (MOGA) optimizations of the injector model have been performed (see [10, 12] for a detailed description of the optimization procedure) for beams traveling through the first pass of the linac.

MOGA optimizations for 100 pC/bunch, 6 MeV injector energy, and linac energy gain of roughly 48.5 MeV have been performed in order to investigate the trade-off between the transverse normalized emittances and how well the Twiss parameters after the linac can be matched. Initial results showed a strong trade-off between these parameters. To remove this, an additional quadrupole was placed right in front of the main linac. Figure 2.3.1 shows the resulting trade-off. From this front, the solution with the smallest maximum Twiss error

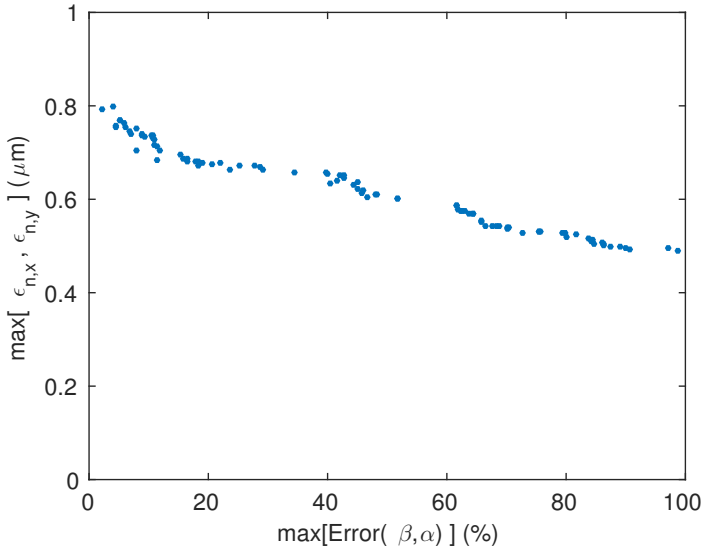


Figure 2.3.1: Trade off between emittance and matching into the lowest energy FFAG passes, extra quadrupole added in front of MLC.

was further refined by using a standard root finding algorithm to more closely match the desired Twiss parameters. Figure 2.3.2a, Fig. 2.3.2b, and Fig. 2.3.3 show the beta functions, alpha functions, and emittances along the injector and main linac beamlines. The particle distribution resulting from this simulation has been converted into a Bmad form and simulated through the machine.

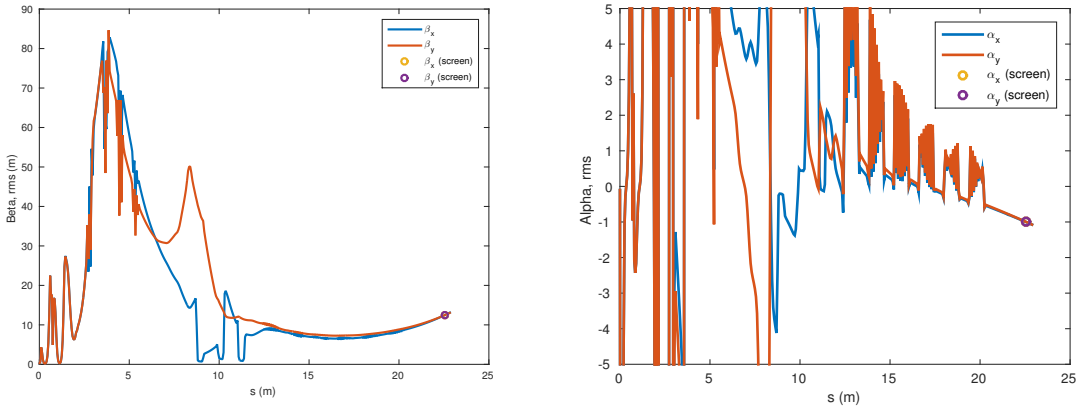


(a) beta functions

(b) alpha functions

Figure 2.3.2: Beta and alpha functions through injector and main linac for 100 pC bunches. $\beta_{x,y} = 12.5$ m and $\alpha_{x,y} = -1$ at the screen position marked by the circles.

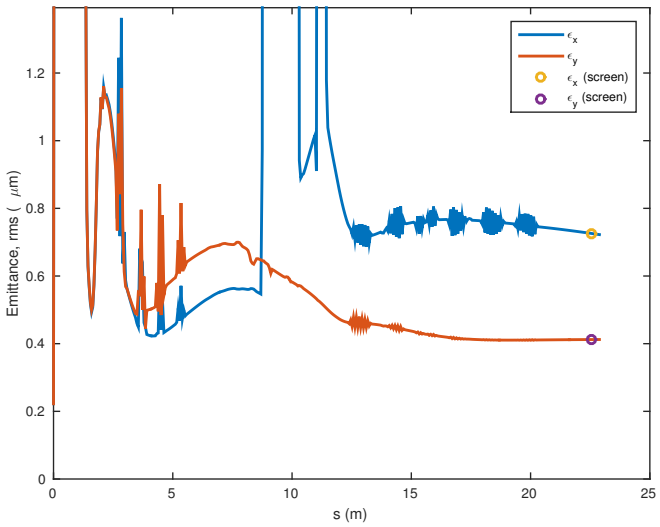


Figure 2.3.3: Transverse emittances through injector and main linac for 100 pC bunches.

## 2.4 Linac (LA)

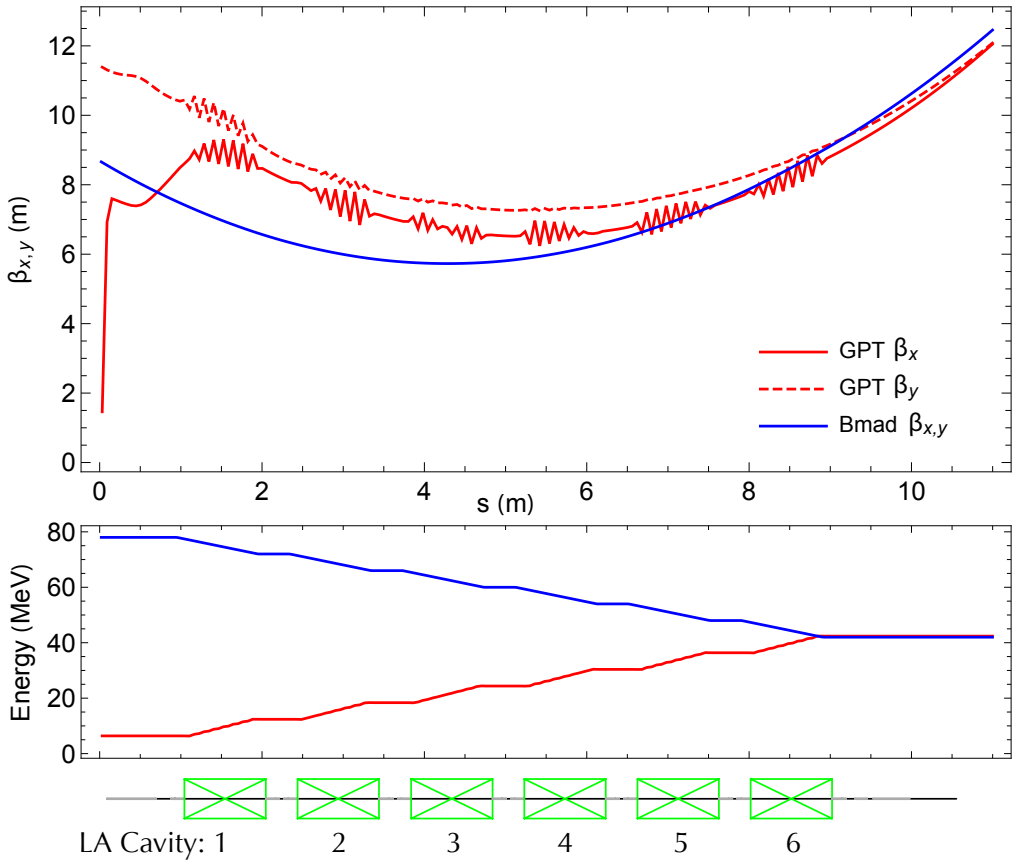


Figure 2.4.1: Beam optics for the first pass accelerating beam, calculated with space charge using GPT, and the second to last pass decelerating beam using Bmad without space charge. Both beams continue to go through the same S1 splitter section. Optics for subsequent passes are nearly identical to the Bmad curve.

The linac section (LA), consisting mainly of the MLC, has no independent adjustments for beam focusing. The beam's behavior is thus governed almost entirely by its incoming properties. Roughly speaking, all beams are focused through LA with minimum average horizontal and vertical beta functions. For simplicity we specify that $\beta_{x,y} = 12.5\,\mathrm{m}$ and $\alpha_{x,y} = -1$ at the end of this section for the first seven passes of the beam, with the eighth pass adjusted to match into the beam stop (BS). This imposes a matching criteria for all eight beams propagating through the linac.

The first and last passes start and end, respectively, at low energy. In this regime, cavity focusing and space charge can be significant, so space charge is used in the calculation. Figure 2.4.1 shows how the first pass beam, starting at 6 MeV and ending at 42 MeV, is matched to the same optics second-to-last pass beam starting at 78 MeV and decelerating to 42 MeV. Both beams then propagate through the splitter section S1.

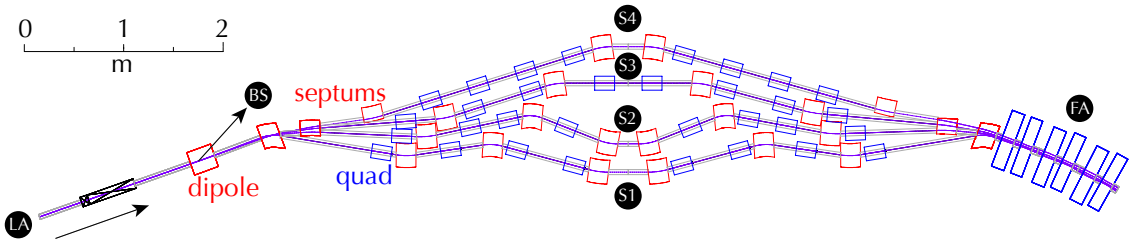


Figure 2.5.1: SX layout

## 2.5 Splitters (S1-4, R1-4)

The splitter design matches four different energy beams, on-axis, with relatively large beam sizes into the FFAG arc with off-axis orbits. The first three lines (S1, S2, S3) accommodate two beams each, one that had just been accelerated and one that had just been decelerated. These sections S1–S4 must:

- Have path path lengths so that passes 1–3 have the same harmonic.
- Match beam sizes and dispersion into FA arc (6 parameters).
- Match orbits into FA.
- Provide $r_{56}$ adjustment.

The last line (S4) only receives a beam that has been accelerated and is only traversed once. It has a path length that is an integer plus 1/2 of the linac RF wavelength, thus setting up the beam for deceleration for its fifth pass through the linac. The second splitter (recombiner) section RX, consisting of lines R1–R4, are nearly symmetric and identical to lines S1–S4.

Figure 2.5.1 shows the layout of these lines. For additional path length adjustment, the inner four dipole magnets and the pipes connecting them are designed to move. The details of this movement are under development.

In order to achieve the optics requirements, each line would need at least seven independent quadrupole magnets to satisfy the six optics parameters and single $r_{56}$ parameter. For additional flexibility and symmetry, we use eight quadrupole magnets per line. Figure 2.5.2 summarizes the optics for each splitter, and shows how each matches into the appropriate FFAG optics.

Unfortunately it is very difficult to make the $r_{56}$ of each pass zero. However, the $r_{56}$ of the four splitters can be adjusted so that the map after a symmetric four passes has $r_{56}$ close to zero, so that the machine as a whole is roughly isochronous. This fact is evident from start-to-end beam tracking as shown in Fig. 2.15.2, where the bunch length is nearly the same as injection in the center of the fourth pass.

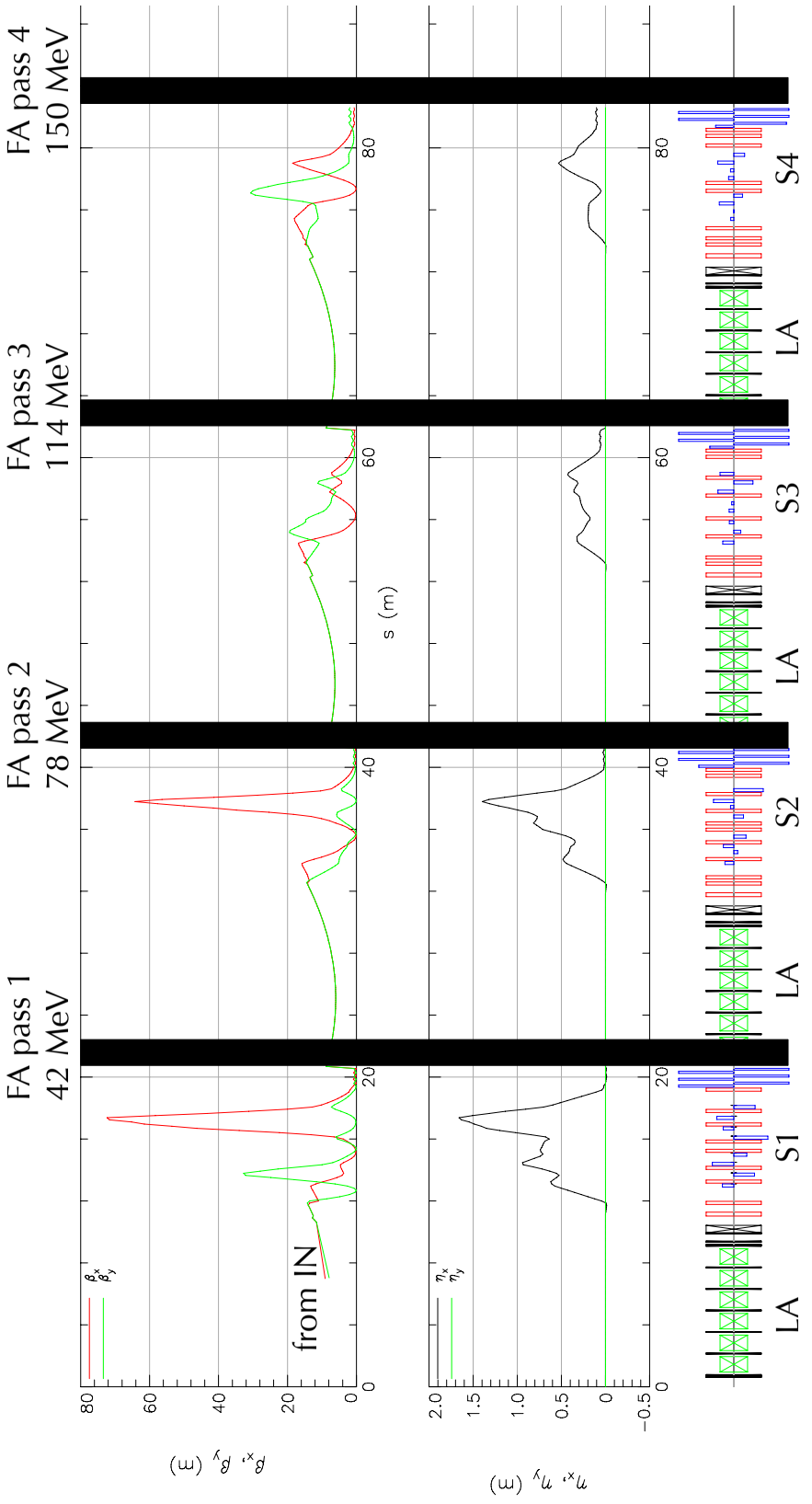


Figure 2.5.2: SX optics summary

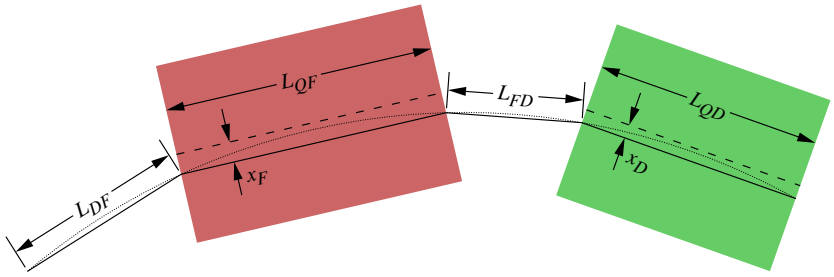


Figure 2.6.1: Arc cell geometry. The dotted line is an arc of a circle. The dashed lines are the centers of the quadrupoles.

The machine will be commissioned in a staged approach. The total path lengths of this section will be reconfigured for 1, 2, 3, and 4-pass operation by lengthening or shortening the final pass by 1/4 of an RF wavelength for both SX and RX lines to provide energy recovery. In the future, an eRHIC style 650 MHz cavity will be tested in this layout, which will require further lengthening of each line.

## 2.6 FFAG arcs (FA, FB, TA, TB, ZA, ZB)

Each arc cell contains a focusing (F) and defocusing (D) quadrupole in a doublet configuration. The magnets have fields formed by iron poles, and are driven by permanent magnets. The quadrupole axes are not centered on a reference orbit, but are offset from one another. The geometry we define for the arc cell is shown in Fig. 2.6.1. The magnets are laid out along a circle with a fixed radius. Each magnet or drift length is the length of a chord of that circle. The axis of each magnet is displaced from its chord by a given amount.

Engineering constraints create the basic constraints for the design:

- The long drift will be at least 11 cm of usable space to accommodate a variety of devices.
- The short drift will be at least 5 cm long to accommodate a BPM.
- The actual drifts will be slightly longer to allow for overhang of corrector coils and other magnet hardware.
- There will be at least 12 mm clearance from the closed orbits to the inside of the beam pipe, and the beam pipe could be up to 3 mm thick.
- The beam pipe will have an annular cross-section in the midplane.
- The size of the room dictates a maximum arc radius of around 5 m.

Because the orbits in the defocusing quadrupole are concentrated on the inside portion of the magnet, whereas in the F quadrupole they are distributed over a wider horizontal range and more toward the outside of the magnet, the requirement for the annular beam pipe cross-section brings the beam pipe very close to, if not under, the inside pole of the D quadrupole.

The beam pipe constraints therefore effectively require the D quadrupole to have a minimum size. As a result, there is no real gain in having the D quadrupole have a good field region below 34 mm.

The design proceeds in two stages. In the first stage, we create a hard-edge design that we will target. In the second stage, we lay out magnets according to the geometry of the hard edge design, and field maps will be created. These field maps are then adjusted to create lattice behavior very close to the hard-edge design.

### 2.6.1 Hard Edge Design

For a quadrupole with iron poles, driven by permanent magnets, the outer transverse size of the magnets is approximately proportional to $B_1 r_p^2$ where $B_1$ is the gradient and $r_p$ is the pole radius. In practice our quadrupoles are have large transverse sizes, so we will try to minimize that transverse size in our lattice design. This will mean in practice making the magnet sizes equal. This could be accomplished with the D and F magnets having different gradients and pole radii, but doing so only appears to result in a gain of 10% or so. Thus we choose the magnets to have identical gradients and beam excursions. Shorter drifts are also more favorable for magnet size, so we keep the drifts as short as tolerable from engineering constraints, namely 12 cm and 7 cm. Our studies showed that the magnets were smaller if excursions were smaller and the magnet aperture could reduce with that excursion. We thus constrain the beam excursions be at or below the minimum good field region of 34 mm defined by the beam pipe constraints discussed above.

We wished to have sufficient margin for the magnet design. We wanted to keep the fields in the pole to be below 1.5 T. We also wanted to have sufficient space in the region where the permanent magnets are installed for temperature compensation, assembly overhead, and other engineering margins. Given the size constraint of the hall, our studies indicated that a maximum energy of 150 MeV and a 5 degree bend angle per arc cell are a good choice.

Large horizontal tunes and low vertical tunes also reduce requirements on the magnets. However, the horizontal tune per cell will be constrained to be below 0.5 at low energy. Furthermore, we want to have some headroom at both the low and high energy end, but simultaneously giving the horizontal tune some margin above 1/3. Thus we constrain the horizontal tune at the lowest energy to be 0.365 and keep the high energy vertical tune above 0.036.

For fixed magnet lengths, we varied the radius of curvature, two horizontal magnet displacements, and the common gradient to center the beam, have the required horizontal tune at low energy, the required bending angle, and have the maximum beam radius be the same in both magnets. We scanned the magnet lengths in 1 mm steps to find the best compromise between arc radius (preferred lower) and magnet gradient (preferred lower), while keeping the beam radius in the magnets below the maximum and the vertical tune at high energy above the minimum. The resulting design is given in Tab. 2.6.1.

Note that the gradients in the hard edge design are different despite what we said above. This is because the D quadrupole is shorter than the F quadrupole, and when the magnets are realized, the D quadrupole would have a lower gradient than the F quadrupole if it had the same transverse size as the F quadrupole. The hard-edge design has the D gradient set to 0.9431 times the F gradient to compensate for this. The factor 0.9431 came from the iterative

Table 2.6.1: Hard edge arc cell design parameters.

| | | |
|---|---|---|
| Injection Total Energy (MeV) | 6 | |
| Maximum Total Energy (MeV) | 150 | |
| Linac Passes | 4 | |
| Reference Radius (m) | 5.099439 | |
| $L_{DF}$ (mm) | 120 | |
| $L_{FD}$ (mm) | 70 | |
| $\alpha$ | F | D |
| $L_{Q\alpha}$ (mm) | 133 | 122 |
| $x_\alpha$ (mm) | −7.182 | +20.132 |
| Gradient (T/m) | +10.621 | −10.017 |

Table 2.6.2: Horizontal displacements for the real magnets, determined using field maps.

| | |
|---|---|
| $x_F$ (mm) | −4.089 |
| $x_D$ (mm) | +17.313 |

design process with field maps described below that was performed on earlier iterations of the design with very similar parameters.

Figure 2.6.2 shows the periodic orbits and optics for the hard edge design. The BPM is centered in the short drift.

### 2.6.2 Field Maps

The geometric layout from Tab. 2.6.1 and Fig. 2.6.1 was used to lay out the magnets. The physical length of the quadrupole iron matches the hard-edge quadrupole length. Three field maps are then constructed, each of which contains the iron for the all of the magnets in the cell. The field maps differ in whether the permanent magnets are installed in the individual magnets or whether there is just air in their place. The field maps thus have F, D, or both F and D powered.

A common scaling factor is applied to the F and D field maps, and the field maps are translated thereby adjusting $x_F$ and $x_D$. These three parameters are varied and closed orbits are found for the field maps so as to meet three constraints: the cosines of the tunes, summed over the four energies and two planes, are the same as the design lattice; the beam is centered on the reference circle; and the maximum orbit radii in the magnets are identical. A new set of field maps is then created with different amounts of permanent magnet material and different values for $x_F$ and $x_D$ based on the corrections estimated from this calculation. The process is repeated until the the combined field map matches the behavior of the design lattice. The displacements of the magnets when the field maps are used are given in Tab. 2.6.2.

The gradients for the resulting field map are shown in Fig. 2.6.3. Figure 2.6.4 shows the

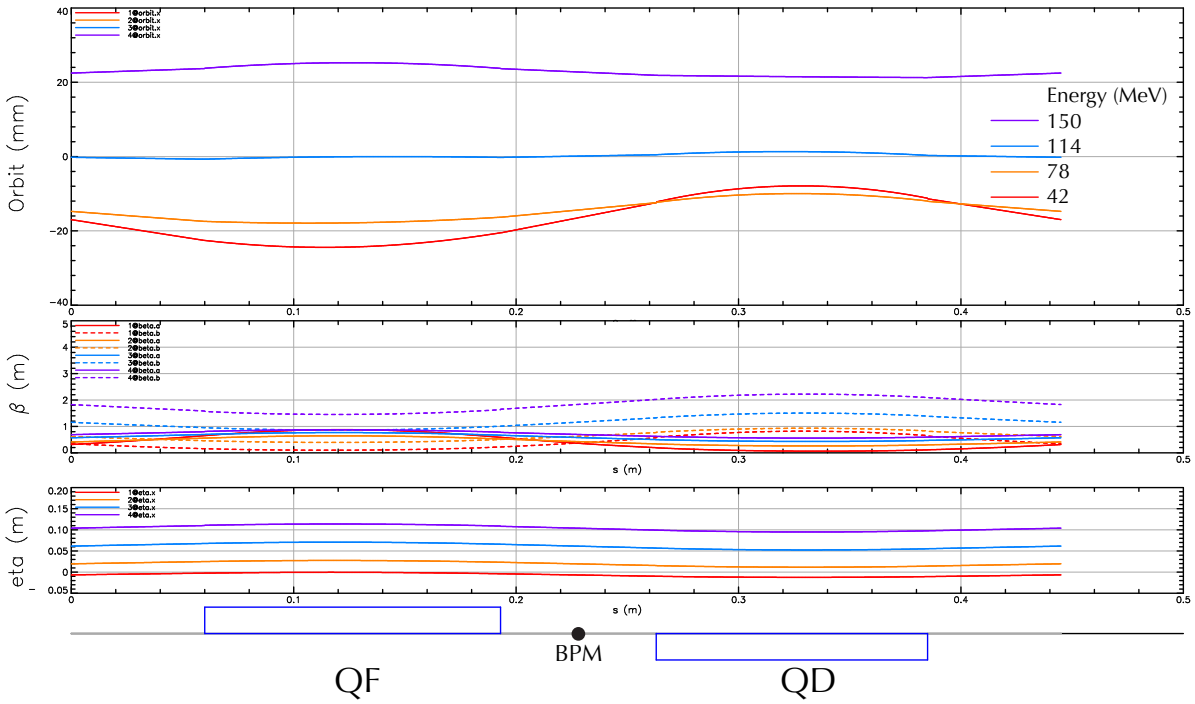


Figure 2.6.2: FA arc cell periodic orbits optics.

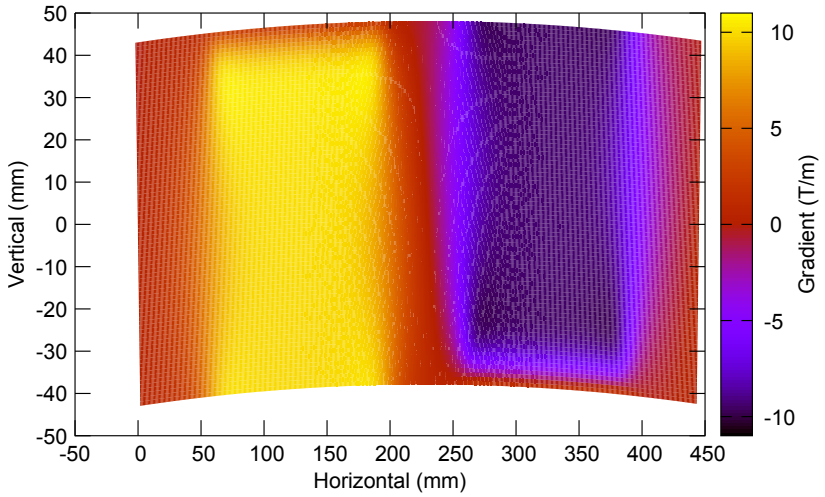


Figure 2.6.3: Gradients in the radial direction for the field map we used.

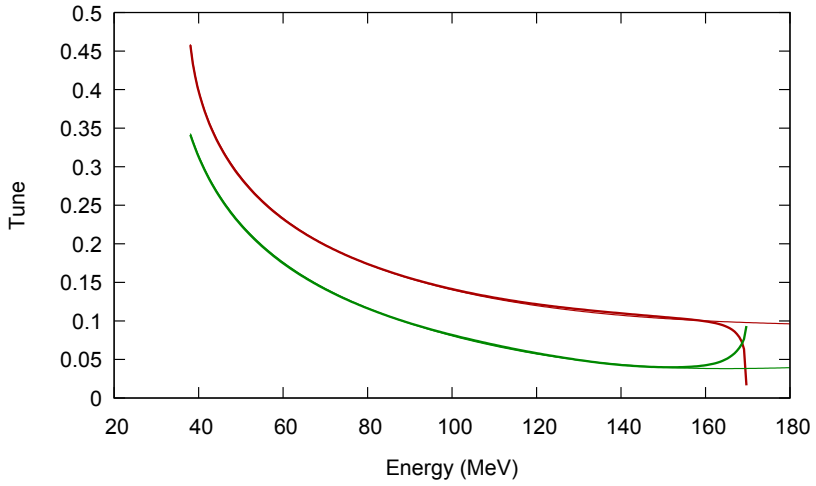


Figure 2.6.4: Horizontal (higher) and vertical (lower) tunes as a function of energy. Thick lines are for the field map, thin lines are the hard edge design.

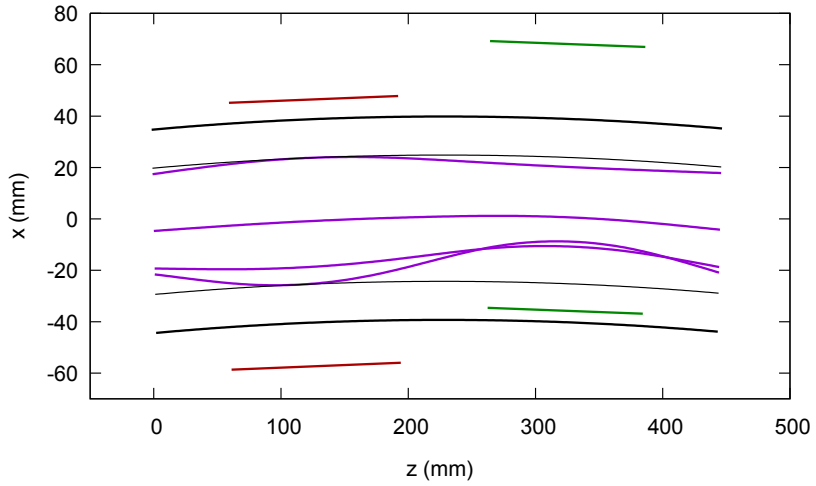


Figure 2.6.5: Closed orbits, stay-clear regions for a pipe, and magnet pole positions. Violet lines are closed orbits at the design energies. Thick lines are arcs which have a minimum horizontal distance of 15 mm from the beam; they outline the minimum enclosed region for a 3 mm thick beam pipe in the midplane. Thin lines are arcs at the extremes of the horizontal beam excursion. They bound a region where the inside height of the pipe must be at least 12 mm. Short straight lines are the position where the magnet pole is at its minimum height.

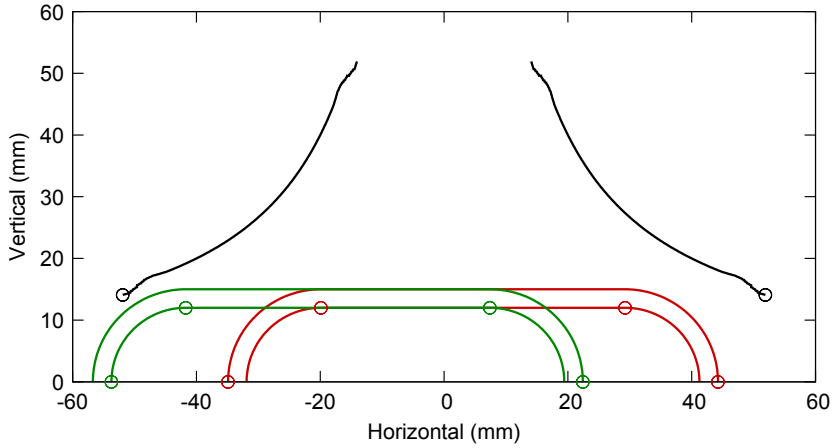


Figure 2.6.6: Inner edge of the pole face (black) and a minimum size for a 3 mm thick beam pipe that maintains a 12 mm distance from its inner edge to the closed orbits. Green is the beam pipe at its closed approach to the D quadrupole, red is the beam pipe at its closest approach to the F quadrupole. Circles correspond to lines that appear somewhere in Fig. 2.6.5.

tunes we obtained, and Fig. 2.6.5 shows the closed orbits.

Figure 2.6.5 in combination with Fig. 2.6.6 shows that the magnet poles can clear a beam pipe that meets the requirements. There is over 2 mm or horizontal distance between the pole and the stay-clear region for the pipe. That space should be maintained in the beam pipe design, and a mechanism to shift the magnets horizontally should be in place in case a systematic deviation in the production magnets from the design field maps occurs. There is space to increase the horizontal pipe size in the positive radial direction if desired.

### 2.6.3 FA, TA, ZA sections

The FFAG section consists of a pure arc section FA, a transition from arc-to-straight section TA, where the cell angles are gradually tapered, and a straight cell section ZA. The taper is accomplished by relaxing all angles and offsets by a transition factor

$$f(x) = 1 - 3x^2 + 2x^3 \tag{2.6.1}$$

where $x = \frac{i+1}{n_{\text{transition}}+1}$ for the $i^{\text{th}}$ transition cell out of $n_{\text{transition}}$. This is the only polynomial with $f(0) = 1$, $f(1) = 1$, $f'(0) = f'(1) = 0$. The total angle of such a transition is exactly $n_{\text{transition}}/2$ times the angle of a single arc cell. Figure 2.6.7 shows this transition.

We will use the same magnets in the straight cell that are used in the arc cell. We wish to minimize the beta function mismatch between the arc and the straight to minimize the mismatch when the taper is included. Since we cannot match at all the energies, the metric

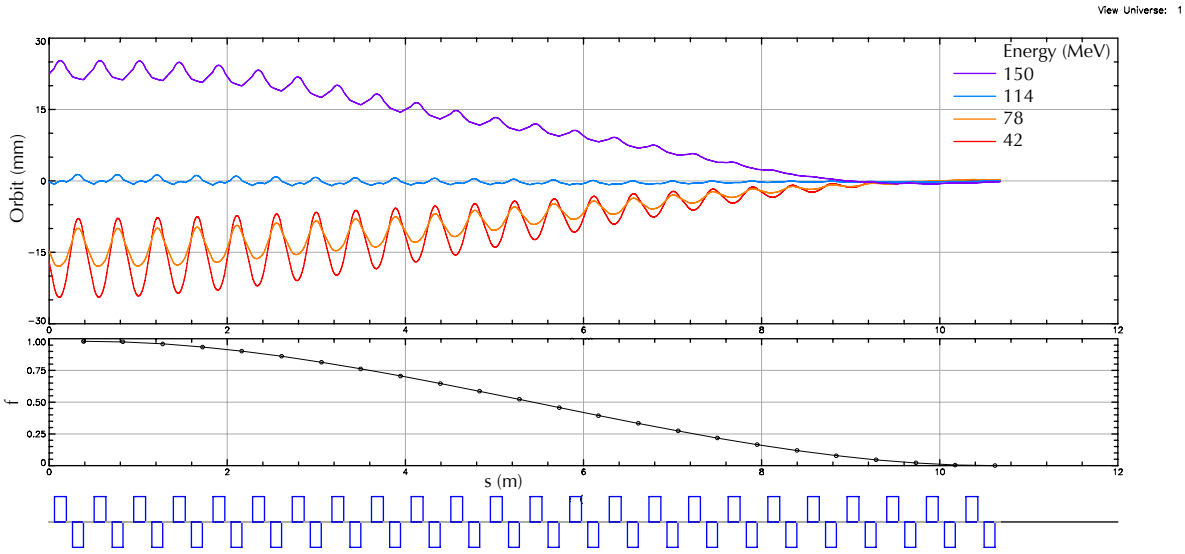


Figure 2.6.7: TA transition arc-to-straight section orbits and transition factor. When all cell angles and quad offsets relax according to this factor, described by Eq. (2.6.1), the orbits and dispersion naturally relax to the centerline. The longer the transition, the better the match to zero. We use $n_{\text{transition}} = 24$, for a total angle of 60°.

Table 2.6.3: Drifts for the magnets in the straight that have a good betatron match to the arcs.

| | |
|---|---|
| $L_{DF}$ (mm) | 123 |
| $L_{FD}$ (mm) | 73 |

that we use to define the mismatch is

$$\sum_{i\sigma} \frac{1}{\nu_{i\sigma}} \left[ \left( \sqrt{\frac{\beta_{\sigma i\text{s}}}{\beta_{\sigma i\text{a}}}} - \sqrt{\frac{\beta_{\sigma i\text{a}}}{\beta_{\sigma i\text{s}}}} \right)^2 + \left( \alpha_{\sigma i\text{a}} \sqrt{\frac{\beta_{\sigma i\text{s}}}{\beta_{\sigma i\text{a}}}} - \alpha_{\sigma i\text{s}} \sqrt{\frac{\beta_{\sigma i\text{a}}}{\beta_{\sigma i\text{s}}}} \right)^2 \right] \tag{2.6.2}$$

where $i$ refers to the energies, $\sigma$ to the plane, a is for the arc, and s is for the straight. This is just the usual expression for the emittance mismatch, weighted by the tunes. The logic for the weighting by the tunes is that the adiabatic taper will naturally give some matching, but that match will be better when the phase advance is larger.

Since the same magnets are being used, the only variables that can be used to achieve the match are the drift lengths in the straight. If a hard edge model is used, the best match occurs when the drifts increase to 82 mm and 137 mm from the arc values of 70 mm and 120 mm. However, when the magnets are modeled, the process of shifting the magnets to a common axis appears to effectively increase their strength. This is likely because when the center of one magnet is facing the poles of the other magnet, the poles of that second magnet effectively

short out some of the flux horizontally. The result is that the lowest mismatch occurs with drifts that are comparable to the drifts in the arcs. The precise value (requiring an integral length in mm) are given in Tab. 2.6.3.

Putting this all together results in the optics shown in Fig. 2.6.8.

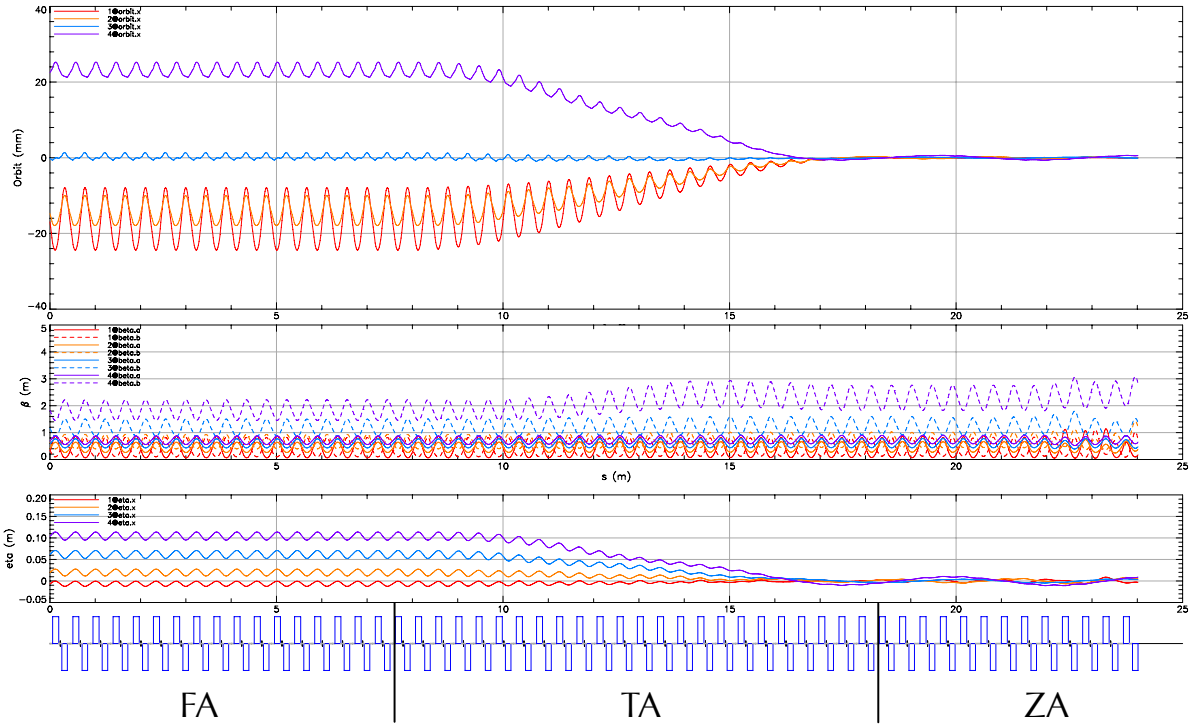


Figure 2.6.8: Complete optics for the FA, TA, and ZA sections.

## 2.7 High-Energy Loop for Users

In the early operational stages of CBETA energy recovery begins after four acceleration passes through the linac. A $\pi/2$ change in RF phase is achieved by adjusting the path length in both the spreader after the fourth acceleration pass, and in the combiner before the first deceleration pass.

In the final operational stage, a straight CBETA beamline will be made available for experimental users, delivering highest energy electrons. Extraction to the experimental line from the arc is made possible by including a couple of special open mid-plane magnets, as indicated in Fig. 2.7.1. These can be achieved by using Halbach-style magnets. Prototype Halbach quadrupoles intended for eRHIC have already been built and successfully tested at BNL, as shown in Figure 2.7.2.

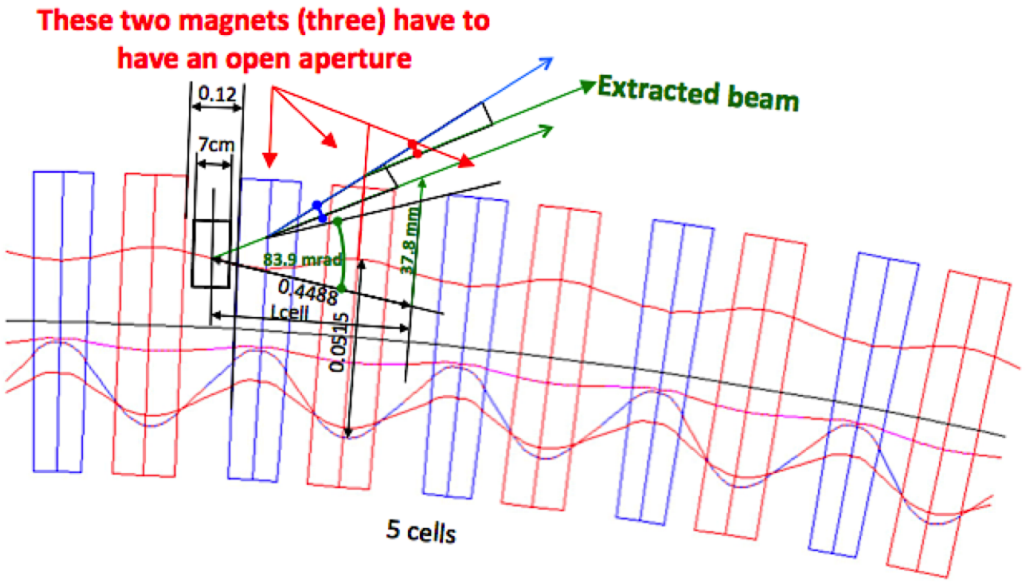


Figure 2.7.1: Orbit of the extracted beam through couple of FFAG arc magnets.

The highest energy beam is naturally radially displaced by more than 20 mm. It passes through the field of a 70 mm long Halbach dipole inside the beam pipe, placed in the 120 mm drift between two adjacent quadrupoles. Plated permanent magnet blocks within the pipe are ultra-high vacuum compatible. A preliminary design of the extraction dipole is shown in Fig. 2.7.3.

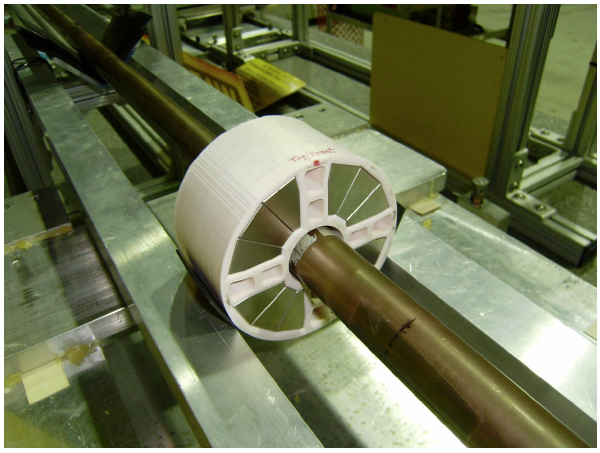

Figure 2.7.2: A prototype eRHIC Halbach style quadrupole, with an open mid-plane that allows synchrotron radiation to escape.

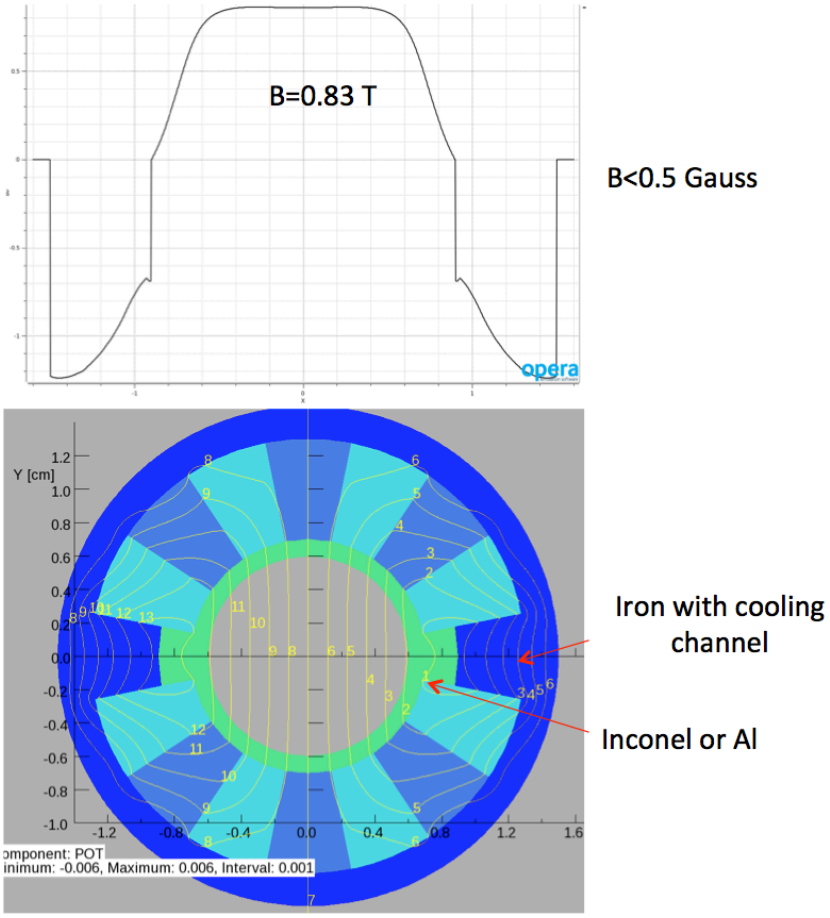


Figure 2.7.3: Preliminary design of the Halbach extraction dipole. (Courtesy of N. Tsoupas).

Table 2.8.1: Operational Modes

| | Commissioning | eRHIC | High-current | |
|---|---|---|---|---|
| Injection Rate | 0.97 | 19.4 | 325 | MHz |
| Max Bunch Charge | 125 | 125 | 125 | pC |
| Max Current | 0.12 | 2.4 | 40 | mA |
| Probe Bunch Rate | N/A | ≤0.97 | ≤0.43 | MHz |

## 2.8 Bunch patterns

CBETA will support multiple operating modes, single pass and multi-pass/multi-energy, pulsed and CW, with and without energy recovery. Many of these modes are only intended for commissioning and machine studies. These modes must cover a wide range of average current, suitable for the wide range of necessary diagnostics — nanoamp for viewscreens, microamp for BPMs, and milliamp for full current operation. But, within each of these ranges, the full range of bunch charge may need to be explored, in order to better isolate possible limiting effects. In general, the beam modes must be well matched the goals of the commissioning, the precise manner that they will be achieved, and the diagnostics that will be used.

The RF cavities in the CBETA linac operate at 1300 MHz. The injector must supply bunches at a sub-harmonic of this frequency. The multiple passes of these bunches through CBETA produce inter-bunch timing patterns which depend on the injection frequency and the revolution period. Additionally the decelerating bunches must have a timing which is an integer + one-half RF cycles offset from the accelerating bunches. Additional path length in the highest-energy splitter lines delays the highest energy turn by 1.5 RF periods.

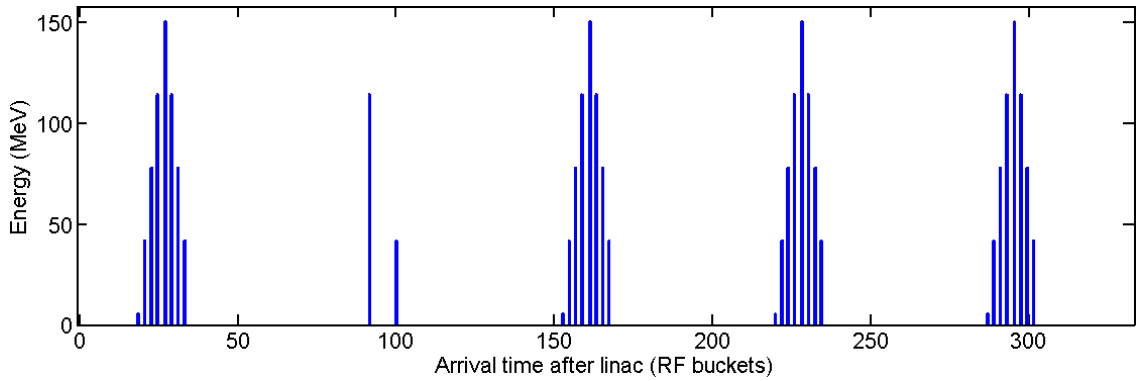


Figure 2.8.1: Bunch pattern produced in the eRHIC-like mode for a circumference of 333 RF periods.

The baseline scheme with three operational modes is shown below.

- 333 RF period circumference.
- **Commissioning mode**: Probe bunch injected every 335*4 periods (∼4 turns). There

would be two passing through the linac at any time, one accelerating, one decelerating, separated by 6.5 periods. This 6.5 period gap is sufficient for conventional diagnostics to resolve the two bunches. In this manner, complete knowledge of the bunches at all energies will be available from the BPM system. Full current from the gun in this mode, assuming a typical bunch charge of 125 pC, is around 100 $\mu$A.

- **eRHIC-like mode**: Bunches injected at a 1.3GHz/67 frequency (335/5 = 67). This produces 5 bunch trains simultaneously in the ring. Within each train the bunch-to-bunch separation is 2 wavelengths ("650MHz"), with 1.5 wavelengths removed at the top energy, giving 8 bunches spread over 12.5 wavelengths. One of the trains is replaced by the above pair of probe bunches by selectively suppressing laser pulses for it on 3 out of every 4 turns. This is shown in Fig. 2.8.1. This allows the BPM electronics to continue operating in an identical fashion to the commissioning mode, and complete knowledge of the probe bunches is still maintained in this operating mode. Full current from the gun in this mode, assuming a typical bunch charge of 125 pC, is around 2.0 mA.

- **High-current mode**: Inject at 1.3GHz/4=325MHz. The circumference 333 is equivalent to 1 (modulo 4), so each successive turn's CW bunch train would slip 1 RF wavelength and fill every RF peak. Then, during deceleration, after the 1.5 wavelength offset, all the decelerating troughs would also be filled. So in total all the available RF peaks and troughs would be used (at 2.6GHz total rate). This is shown in Fig. 2.8.2. Pilot bunches may still be injected, but would have to be injected at a lower rate than in the previous two modes. To do so, a gap in the bunches needs to be introduced once per turn, for at least 7 turns on either side of the pilot bunch, allowing it to be seen in isolation from the rest of the bunches. Full current from the gun in this mode, assuming a typical bunch charge of 125 pC, is around 40.0 mA.

Note that this initial 1.3GHz configuration of the machine has an odd harmonic number, because this is required for the high-current operating mode. When the 650MHz eRHIC prototype cavity is installed, the circumference will be lengthened to 334 1.3GHz wavelengths, or h=167 for the new 650MHz frequency, by shifting the splitter lines. Since 167=168-1, any small factor of 168 (F=1,2,3,4,6,7,8,12,14,21) may be chosen for the number of trains and injection would happen at 650*F/168 MHz. In both of these schemes, the circumference is smaller than the injection periodicity, so the bunches in the ring 'overtake' before newly injected ones arrive.

Both of the lower-current modes include the 'probe bunches', of which two would be in the ring at any one time (one accelerating and one decelerating), as they are injected every fourth turn. These would replace one of the five 8-bunch trains in the case of the eRHIC-like scheme (the second train in Fig. 2.8.1). The two probe bunches are separated by 8.5 RF periods, or 6.5 ns, which allows the BPMs to distinguish their signals. The probe bunches are also separated from the bunches of adjacent bunch trains by at least this time interval. To be explicit, the bunch trains are 12.5 RF periods long and recur every 67 periods, thus the gap between them is 54.5 RF periods. Each BPM measures the probe bunch as it passes with successively increasing then decreasing energy on each turn, giving orbits for all seven FFAG passes.

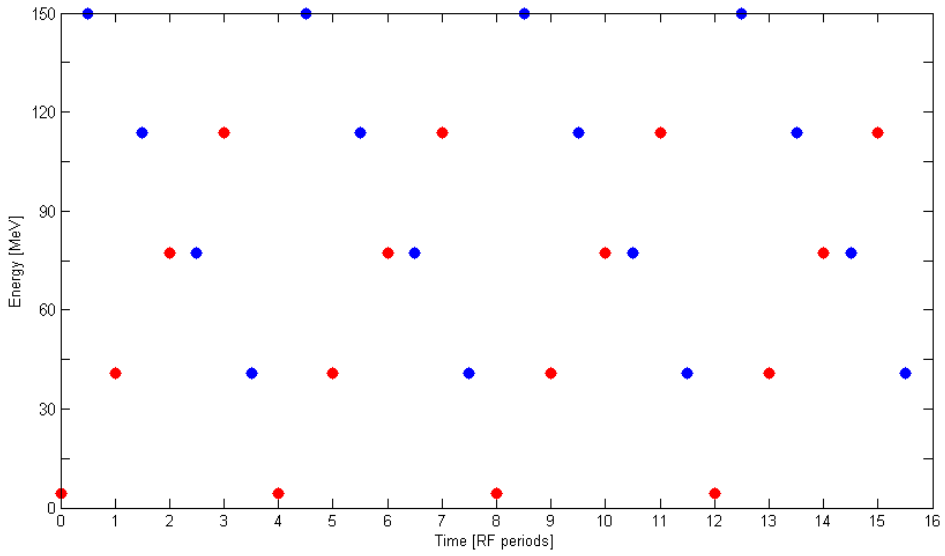


Figure 2.8.2: Bunches passing a reference point at the start of the linac in the high-current mode, with one accelerating bunch and one decelerating bunch in every RF period. Red and blue dots represent accelerating and decelerating bunches, respectively.

The same time domain BPM electronics that is used in the low frequency commissioning mode serves for the eRHIC-like mode also, with the denser bunch 'trains' remaining unmeasured (except perhaps on an average basis). The important principle to be demonstrated is that measurements on well-separated probe bunches can provide enough information to operate the machine with the high-average-current trains in it.

Injection using the eRHIC-like mode will allow for for a per energy beam current of 1 mA at around 60 pC bunch charge and therefore enables achievement of all the Key Performance Parameters. The Ultimate Performance Parameters can only be achieved using the high-current mode.

In the high-current mode, the pilot bunch pattern will need to be changed. In this case, seven gaps needs to be introduced before, during, and after a pilot bunch, separated in time by the circumference of the ring. In that manner, the gaps will overlap with each other as they pass around the ring. Thus, the maximum rate of the pilot bunches is once per every 9 round trips. In this mode, there is a single pilot bunch, which will gain energy 4 times before it gives the energy back, so the maximum rate of pilot bunches may be additionally limited by that transient load on the RF.

### 2.8.1 Alternative Pattern for $h = 335$ Circumference

An alternative scheme exists for a circumference of 335 wavelengths and injecting bunches at a factor of 333 periods, for instance every 333/9=37 RF periods. This will create 9 eRHIC-like bunch trains in the ring instead of 5, which increases the average current possible in this mode

with a given bunch charge by 80%. The trains are also filled the opposite way around, with each new bunch arriving 2 RF periods sooner rather than 2 RF periods later than the previous turn. This inverts the situation with the final turn: every ninth bunch is injected at 37*9=333 RF periods delay, whereas the final turn circumference is 335+1.5=336.5 wavelengths, giving a gap of 336.5-333=3.5 RF wavelengths at the top energy. This situation is shown in Fig. 2.8.3.

The final turn is elongated by 1.5 wavelengths (of 1.3GHz) compared to the others. This is a consequence of the required half-integer offset to go into a decelerating bucket and the outermost splitter line requiring a longer path length to avoid hitting the other lines. In the above scheme, this gives a total circumference of 333+1.5=334.5 wavelengths for the final turn. However, in the eRHIC mode, every fifth bunch is injected at 67*5=335 RF periods delay, meaning this final turn will only create a 335-334.5=0.5 RF wavelength gap, rather than the usual 2-wavelength ("650 MHz") gaps.

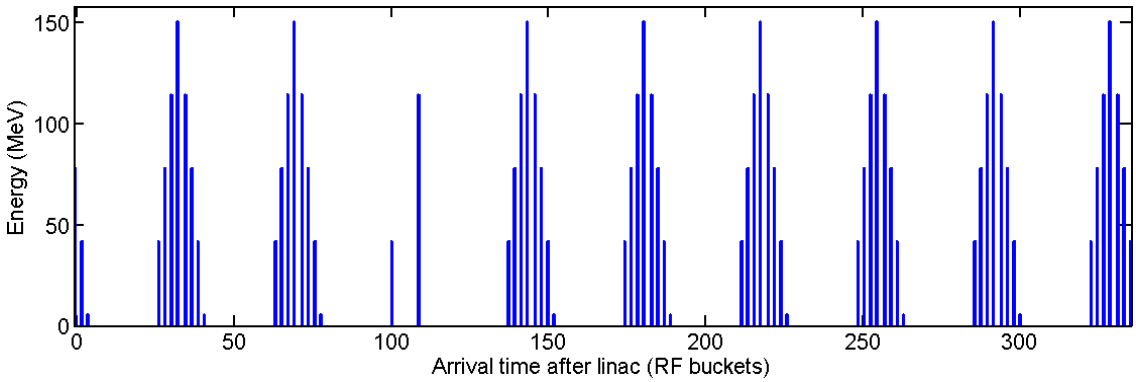


Figure 2.8.3: Bunch pattern produced in the eRHIC-like mode. This is in the $h = 335$ harmonic number case, where the top-energy bunches are well-separated (by 3.5 RF wavelengths).

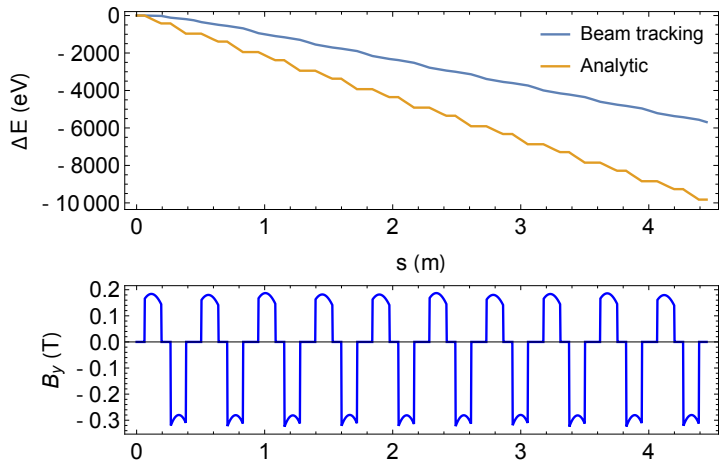


Figure 2.9.1: CSR average energy losses through 10 FFAG cells for a bunch at energy 42 MeV, 77 pC charge, and 3 ps duration by tracking in Bmad. The analytic calculation is simply accumulating $0.35 \times W_0$ with curvature based on the local magnetic field $B_y$, and represents a lower limit on the average loss.

## 2.9 CSR

When a charged particle is transversely accelerated in a bending magnet, it produces radiation according to the well-known synchrotron radiation spectrum. When $N$ such particles are bunched on a scale of length $\sigma$, the power spectrum per particle at frequencies smaller than $c/\sigma$ in this spectrum is enhanced by roughly a factor $N$. This results in increased radiation, and hence increased energy losses from the individual particles. This coherent synchrotron radiation was first calculated in a seminal paper by Schwinger [18].

The CSR wake $W_{\rm CSR}(z)$ is the energy change per unit length of a particle with longitudinal position $z$ in a bunch, and it can be shown that for ultra-relativistic particles this $W_{\rm CSR}(z)$ scales with the factor

$$W_0 = N r_c m c^2 \frac{\kappa^{2/3}}{\sigma^{4/3}} \tag{2.9.1}$$

where $m$ is the mass of a single particle, $r_c$ is its classical electromagnetic radius, and $\kappa$ is the trajectory curvature (e.g. see [19]). For a Gaussian bunch moving on a continuous circle, called 'steady-state CSR', the average energy loss per unit length is approximately $0.35 \times W_0$, and the maximum energy loss per unit length is approximately $0.6 \times W_0$, near the center of the bunch.

Bmad simulates the effect of CSR using the one-dimensional model described in [20]. The formalism accounts for arbitrary geometries, and also includes the effect of the beam chamber via an image charge method. The code has recently been modified to include well off-axis orbits, and uses the actual orbit history to compute the CSR force.

Figure 2.9.1 shows tracking results with CSR in Bmad. The difference in the curves implies that the bunch is in a partially steady state regime due to the finite lengths of the magnets and accounting for CSR propagation between magnets. The slope implies a loss of about 123 eV per cell. For 280° of FFAG arc in CBETA, this implies an average relative energy loss

of $0.17 \times 10^{-3}$, and a maximum induced energy spread of about twice that.

Detailed CSR studies are quite involved and require extensive testing. These will be performed over the coming months.

## 2.10 Space Charge

The relatively low energy of the first pass through CBETA (42 MeV) requires estimation of the effects of both transverse and longitudinal space charge. To compute space charge fields Bmad uses an approximate relativistic for the fields from longitudinal slices of the beam which is Gaussian transversely (see [20] for details). To test the validity of this model, simulations of a zero emittance Gaussian beam drifting for 80 meters at 42 MeV was simulated in Bmad as well as GPT, a standard 3D space charge code. The bunch charge/length for this comparison was 100 pC and 4 ps, respectively. Figure 2.10.1 and Fig. 2.10.2 show the horizontal rms beam size and normalized emittance, respectively. As the comparison shows, at this energy the beam size growth is well modeled in Bmad, however there is some discrepancy with the emittance growth. This can be seen in the final transverse phase space, shown in Fig. 2.10.3.

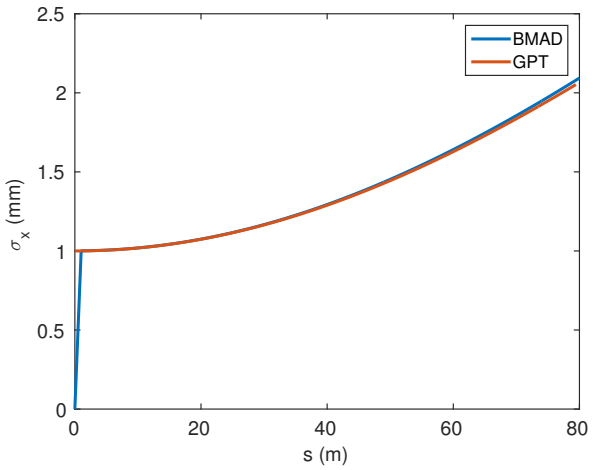


Figure 2.10.1: Comparison of Bmad and GPT space charge models for a drifting 42 MeV Gaussian beam.

Note that for this examples the Bmad model overestimates the emittance growth. The effects of longitudinal space charge at this energy, bunch charge, and bunch length were negligible. For a final comparison, the example bunch shown in the linac optics section was sent through one pass of the machine with space charge on and off. Figure 2.10.5 shows the relative error in the horizontal beta function through one pass computed with space charge on and off. The relative error through the FFAG section is roughly 10%. Figure 2.10.5 shows the corresponding resulting emittances through the same pass. From both these plots, it appears that space charge is not a major effect at this bunch charge (100 pC) and energy (42 MeV). Initial simulations with CSR show that CSR will have a larger effect on the dynamics than space charge.

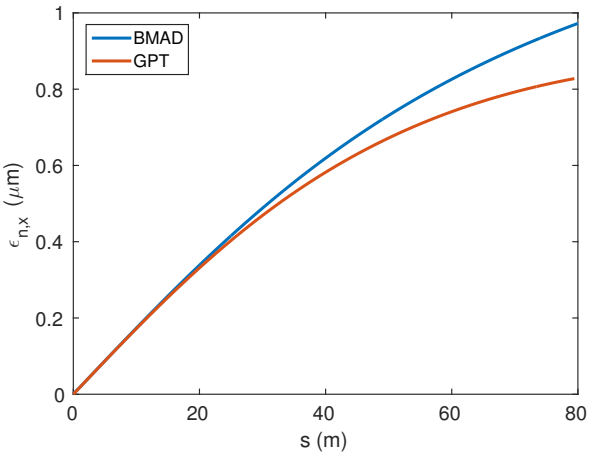


Figure 2.10.2: Comparison of Bmad and GPT space charge models for a drifting 42 MeV Gaussian beam.

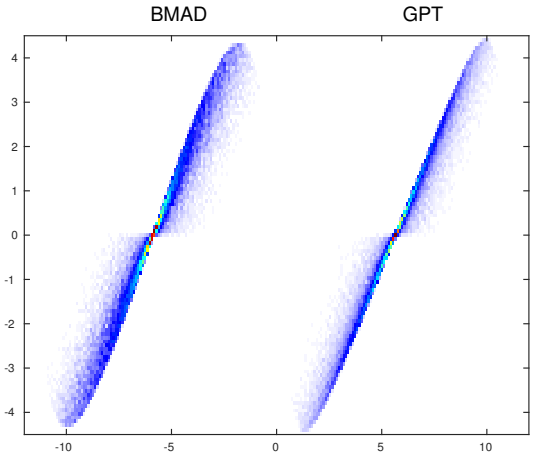


Figure 2.10.3: Comparison of Bmad and GPT space charge models for a drifting 42 MeV Gaussian beam.

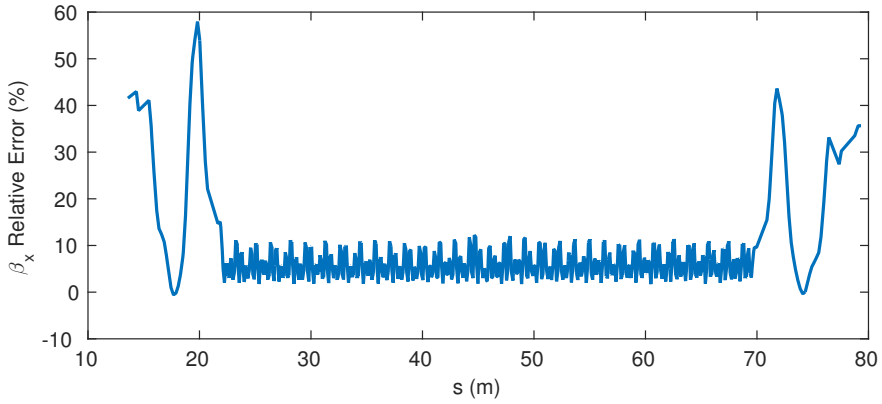


Figure 2.10.4: Relative error in the horizontal beta function computed with and without the Bmad space charge model.

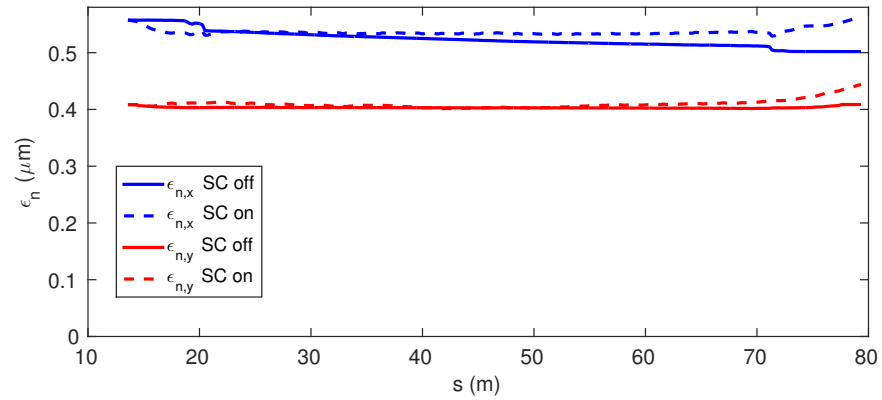


Figure 2.10.5: Comparison of horizontal emittances with (dashed lines) and without (solid lines) the Bmad space charge model.

## 2.11 Wakefields,

Assuming the beam remains stable, the primary difficulty due to wakefields will be increased energy spread. The resistive wall and surface roughness contributions are usually dominant but individual devices will need to be looked at to make sure there are no problems. For resistive wall we used the low frequency approximation for the longitudinal wake potential

$$W(s) = \frac{d}{ds}H(s)\frac{cL}{2\pi b}\sqrt{\frac{Z_0\rho_e}{\pi s}}, \tag{2.11.1}$$

where $Z_0 = 377\Omega$, $s \geq 0$ is the lag distance, $c$ is the speed of light, $L$ is the length of the resistive section, $b$ is the pipe radius, and $\rho_e$ is the electrical resistivity. When applying equation (2.11.1) and in formulas below we use integration by parts to obtain actual voltages. The numerics are very straightforward and will not be discussed.

For the wake potential due to surface roughness we used Stupakov's formula [21]. Define

$$W(s) = \frac{d}{ds}H(s)Re(\Phi(s)).$$

In MKS units

$$\Phi(s) = \int_0^\infty dk_z \int_{-\infty}^\infty dk_x |k_z|^{3/2} \frac{\langle|\hat{s}(k_x,k_z)|^2\rangle}{\epsilon_0 b^2\sqrt{\pi}} \frac{1-i}{\sqrt{s}} \exp\left(i\frac{k_x^2+k_z^2}{2k_z}\right) \tag{2.11.2}$$

where the angular brackets $\langle\rangle$ denote statistical averages and

$$\hat{s}(k_x,k_z) = \int_0^L dz \int_0^{2\pi b} dx \frac{h(z,x)}{(2\pi)^2} \exp(ik_z z + ik_x x), \tag{2.11.3}$$

with surface roughness $h(x,z)$ where $z$ is measured along the beam direction. For $h = h_0 \cos kz$ one has

$$\langle|\hat{s}(k_x,k_z)|^2\rangle = \frac{h_0^2 Lb}{8\pi}\delta(k_x)\delta(k_z - k).$$

and

$$W_0(s) = \frac{d}{ds}H(s)Lh_0^2 k^{3/2}\frac{\cos(ks/2)+\sin(ks/2)}{8\epsilon_0\pi^{3/2}b}. \tag{2.11.4}$$

Figure 2.11.1 and Fig. 2.11.2 show the input and results of an ABCI [22] simulation and equation (2.11.4). For these parameters the agreement is excellent. Other parameters have been checked and the amplitude of the wake is always good within a factor of 2.

To get the impedance due to wall roughness requires a statistical model. For simplicity we take a stationary random process and a correlation function given by

$$\langle h(x_1,z_1)h(x_2,z_2)\rangle = C(x_1-x_2, z_1-z_2) \tag{2.11.5}$$

$$= h_0^2 \exp\left(-\frac{(x_1-x_2)^2}{2\sigma_x^2} - \frac{(z_1-z_2)^2}{2\sigma_z^2}\right), \tag{2.11.6}$$

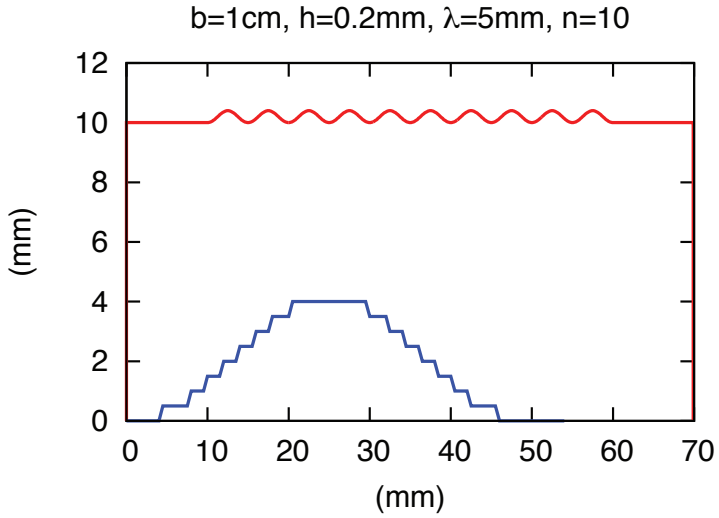


Figure 2.11.1: geometry to compare Stupakov's formula with ABCI. The red curve is the ideal geometry. The blue staircase is a 10 fold zoom of an actual convolution used in the simulation.

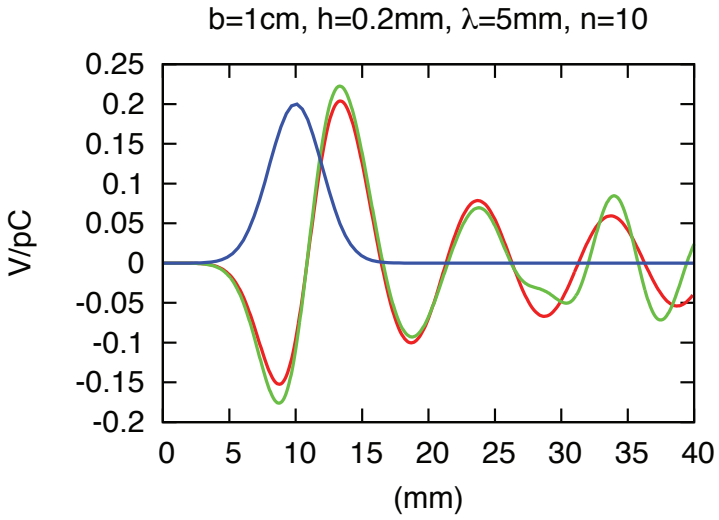


Figure 2.11.2: wakefields from Stupakov's formula and ABCI.

where $h_0$ is the rms distortion, $\sigma_z$ is the correlation length along the axis of the pipe and $\sigma_x$ is along the circumference. Using the Wiener-Khinchin theorem

$$\langle|\hat{s}(k_x,k_z)|^2\rangle = \frac{bL}{(2\pi)^3}\int_{-\infty}^{\infty} dxdz\; C(x,z)\exp(ik_z z + ik_x x) \tag{2.11.7}$$

$$= \frac{bLh_0^2\sigma_x\sigma_z}{(2\pi)^2}\exp(-k_x^2\sigma_x^2/2 - k_z^2\sigma_z^2/2). \tag{2.11.8}$$

Inserting (2.11.8) in (2.11.2) and doing the $k_x$ integration yields.

$$\Phi(s) = \frac{\sqrt{2}(1-i)h_0^2\sigma_x\sigma_z}{(2\pi)^2\epsilon_0 b\sqrt{s}}\int_0^{\infty} dk_z \frac{k_z^2\exp(-k_z^2\sigma_z^2/2 + ik_z s/2)}{\sqrt{\sigma_x^2 k_x - is}}. \tag{2.11.9}$$

In (2.11.9) the square root has a positive real part and a negative imaginary part for for $s > 0$. The integral is done numerically.

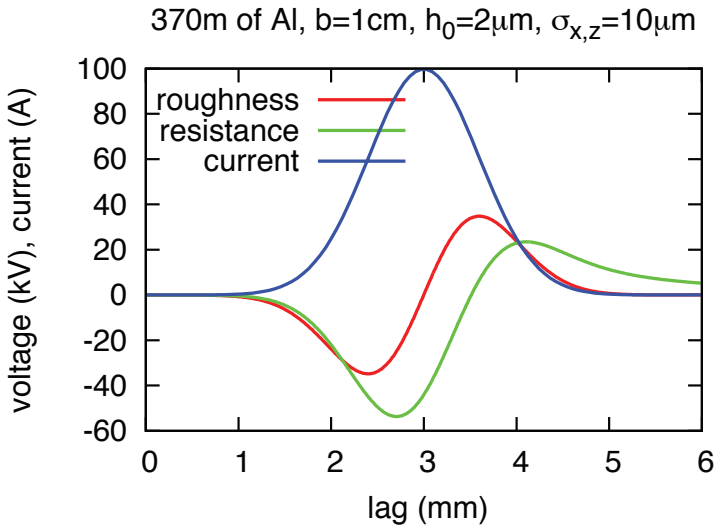


Figure 2.11.3: bunch current and induced voltage

Figure 2.11.3 shows the net voltage for a pipe of radius 1 cm and length equal to 4 passes up and 4 passes down. The roughness of $h_0 = 2\,\mu$m with $10\,\mu$m correlation length will require some care but is well within the state of the art. The extraction energy is 6 MeV so the $\pm 2\%$ energy spread should be easy to accommodate. The chamber profile is a flat oval chamber of 24 mm full height. Generalizing equation (2.11.2) to general apertures requires knowledge of all transverse electric and transverse magnetic microwave modes as well as a tractable approximation for their cutoff frequencies at high energy, a formidable task. On the other hand we note that the surface roughness acts much like a surface impedance. Figure 8 in [23] shows the low frequency, longitudinal resistive wall wake for elliptical pipes. For all values the impedance is within 10% of the wake for a round pipe with the smaller aperture. Because a

flat chamber can be taken as the limit of one semi-principle axis going to infinity, the flat oval chamber should be very close to the round chamber results.

These estimates therefore indicate that the energy spread from resistive wakes and from roughness wakes is acceptably small. It does not prohibit the clean transport of the decelerated beam to the beam stop.

## 2.12 Beam Loss due to Gas Scattering

Electrons in the beam can interact with residue gas molecules left in the vacuum chamber, leading to beam losses and formation of the beam halo. In addition, the lost high energy electrons may further induce desorption of the vacuum chamber and quenches the superconducting components.

Beam losses due to two types of beam-gas scattering have been analytically estimated for the CBETA ring: elastic scattering and Bremsstrahlung. The elastic scattering of the electrons in the beam off the residue gas molecules can change the trajectory of the electrons and excite betatron oscillations. If the scattering angle is larger than the deflection angle aperture set by the collimator, the electrons will get lost at the location of the collimator [24, 25]. In the process of Bremsstrahlung, an electron in the beam scatters off the gas nucleus and emits a photon, which results in an abrupt energy change of the electron. If the energy change is beyond the energy deviation aperture, the electron will also be lost [24]. Using the parameters listed in Tab. 2.12.1, the beam losses due to gas scattering in the CBETA ring are analytically estimated and shown in Fig. 2.12.1 for the both the initial and the stable operation modes. Assuming that the limiting transverse aperture locates at the last linac pass, the analytical estimate shows that in the initial operation stage, the beam loss due to elastic scattering ranges from 2.16 pA (2.5 cm aperture) to 13.4 pA (1 cm aperture) and the beam loss due to Bremsstrahlung ranges from 0.22 pA (0.1 MeV energy aperture) to 0.14 pA (1 MeV energy aperture). At the stable operation stage, the beam loss due to both processes reduces by a factor of 2.

More accurate estimates can be achieved through element-by-element simulation with the detailed lattice design and environment parameters.

Table 2.12.1: Parameters used in the estimates of beam losses due to beam-gas scattering.

| | Arcs | Linac |
|---|---|---|
| Electron bunch charge | 123 pC | |
| Repetition frequency | 325 MHz | |
| Number of FFAG passes | 7 | |
| Energy gain per pass | 36 MeV | |
| Avg. beta function | 0.5 m | 50 m |
| Temperature | 300 K | 2 K |
| Gas Pressure | 1 nTorr | 10-3 nTorr |
| Length | 54.34m | 10m |
| Initial operations | H2 (50%), CO (30%), H2O (20%) | |
| Stable operations | H2 (78%), CO (12%), H2O (10%) | |

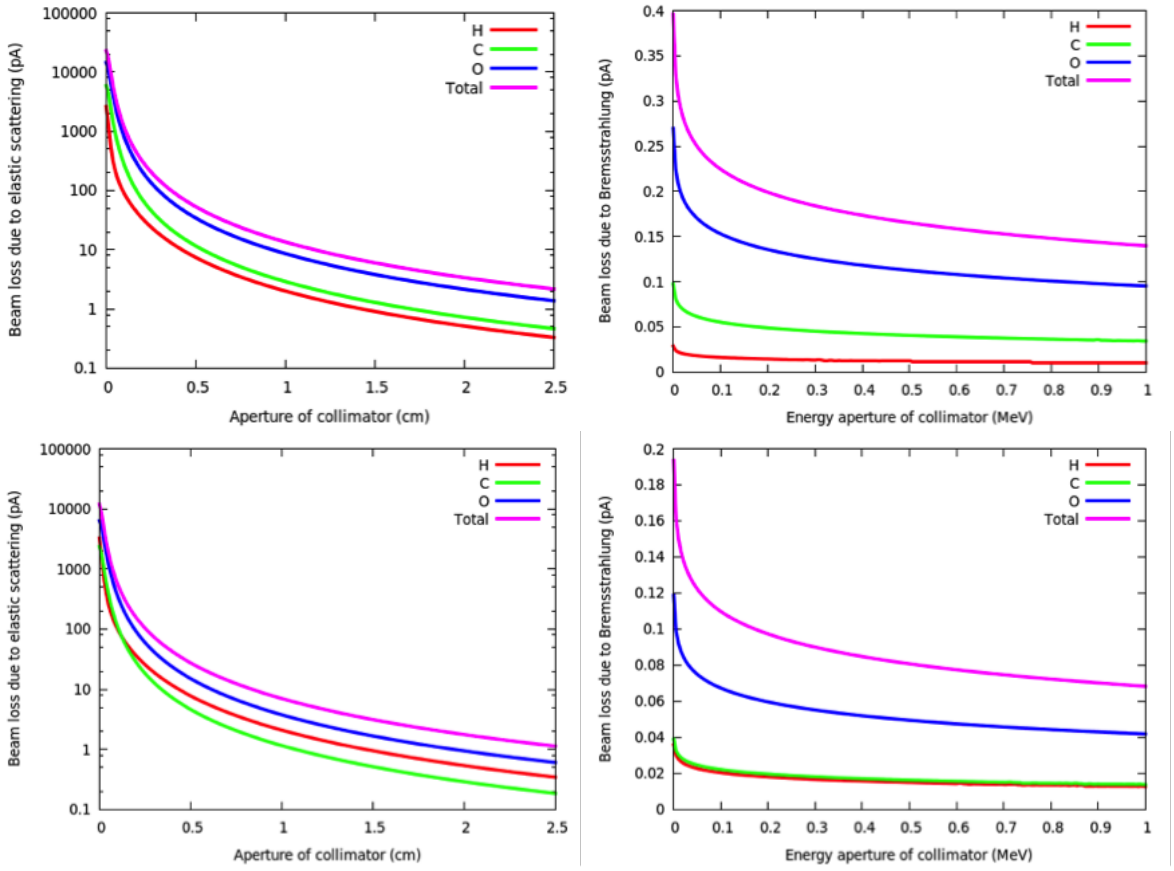


Figure 2.12.1: Analytical estimation of electron beam losses due to scattering off residue gases in CBETA. Electrons pass through the FFAG arc for 7 times and the linac for 8 times. (Left) beam losses due to elastic scattering as a function of the aperture of a collimator located at the last pass of the linac; (Right) beam losses due to the energy aperture of a collimator located at the last pass of linac. Parameters from Tab. 2.12.1 are used. The top graphs were computed for gas species of the initial operation. For the bottom two graphs, gas species of the later, stable operation are used.

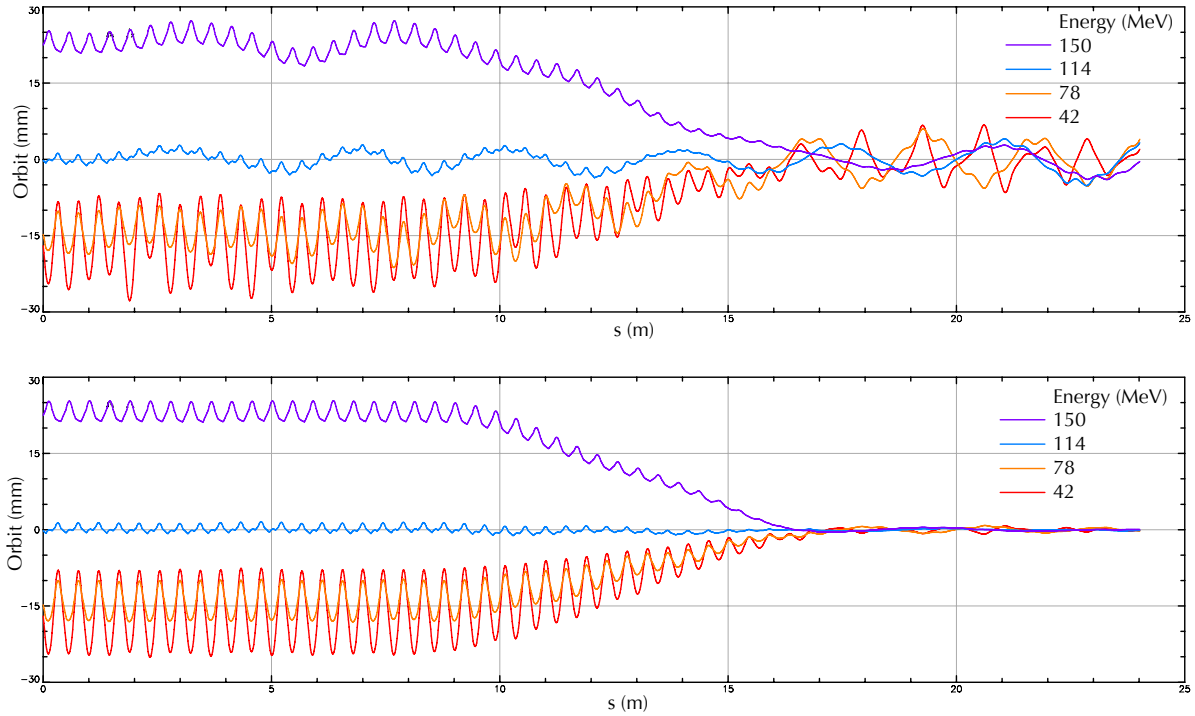


Figure 2.13.1: Example of simultaneous orbit correction for four beams with uniform horizontal and vertical offset errors in all FFAG magnets. Offsets are uniformly distributed within $\pm 200\,\mu$m. Every F quadrupole has a horizontal corrector, and every D quadrupole has a vertical corrector. BPMs are placed in the short drift between these magnets in each cell.

## 2.13 Orbit & Optics correction

This machine has the unique requirement that beams with four different energies must propagate through the same FFAG section, and any correction applied will affect all beams simultaneously. At first glance it may seem impossible to correct all beams perfectly at every BPM, and this is true. Fortunately this correction only needs to be approximate at every BPM, with some locations more important than others (e.g. the ends of the FFAG section, and the straight section), and correction with this understanding is possible.

Practically this correction is achieved by using the response matrix from all correctors to all BPMs, calculating its pseudoinverse by singular value decomposition (SVD), and applying this to measured offsets from ideal BPM readings. As long as the computer model of the machine is not wildly different from the actual machine, this response matrix can be calculated from the computer model and not the 'true' corrector-to-BPM response in the live machine.

Figure 2.13.1 shows how this correction works with offset errors in all FFAG magnets. It assumes that all beams enter the FFAG perfectly, and that the BPMs can read each beam position independently. Even though the computer could calculate an exact corrector-to-BPM response matrix in the perturbed system, we use the method described above where the design optics are used to calculate this matrix once and for all, in order to simulate how the actual

Table 2.13.1: Orbit correction analysis procedure. Typically this procedure is iterated for $N = 100$ times.

| Step | Procedure |
|---|---|
| 1 | Initialize design lattice |
| 2 | Calculate orbit and dispersion response matrices |
| 3 | Perturb the lattice with random set of errors |
| 4 | Apply the SVD orbit correction algorithm |
| 5 | Save this perturbed lattice |
| 6 | Track particles through, and save statistics |
| 7 | Reset the lattice |
| 8 | Repeat steps 3-7 $N$ times |

machine will be operated.

Orbit correction studies are important to estimate what errors can be corrected, and what corrector strengths are required for this correction. In order to get meaningful statistical information, simulations must be preformed repeatedly. Table 2.13.1 outlines the procedures for such studies.

Figure 2.13.2 summarizes some results from such a study.

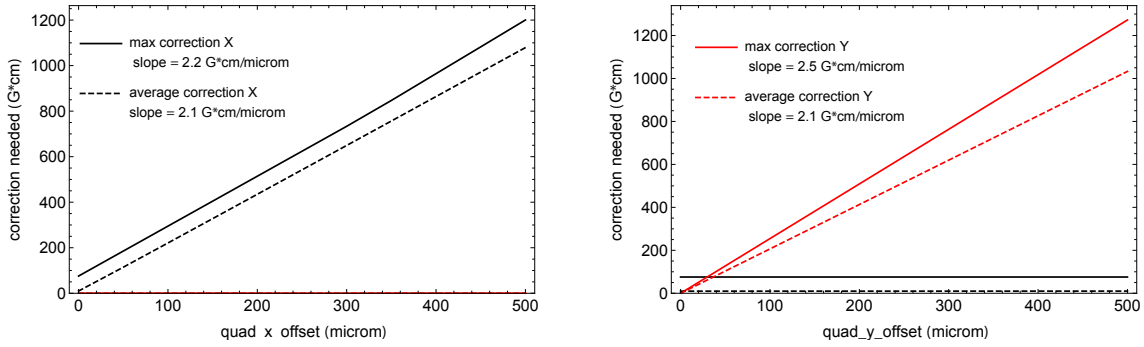


Figure 2.13.2: Summary of orbit correction of horizontal and vertical FFAG magnet offset errors. The layout, corrector layout, and definition of the errors are the same as in Fig. 2.13.1. For example, if one expects horizontal offset errors of all quadrupole magnets distributed uniformly in the range $\pm 200\,\mu$m, then the figure implies that the average horizontal corrector strength needed will be approximately 420 G-cm, and anticipates that the maximum strength will need to be approximately 500 G-cm.

## 2.14 Tolerances

### 2.14.1 Analysis Process

ERLs — as they are intended to generate and precisely control phase/energy correlations within the beam — are, architecturally, time-of-flight spectrometers. As such, they may require very stringent tolerances on timing, energy, and transport component excitation, location/alignment, and field quality. A preliminary validation of a design must therefore include estimates of magnet alignment and excitation tolerances, response to RF phase and amplitude errors, and validate the impact of magnetic field inhomogeneity. The latter effect can result in significant degradation of beam quality during energy recovery via a coupling of field-error-driven betatron oscillations to energy by way of RF phase errors [26, 27]. Estimates of performance response to errors then are used to inform simulation studies of machine behavior in the presence of realistic errors. When system sensitivity to individual errors is thus evaluated (and tolerances at which error response become nonlinear thereby known), an error budget can be developed by imposing multiple error classes in an ensemble of test cases. Potential interactions amongst errors can then be studied, and operationally realistic correction (local) and compensation (global) schemes tested. The impact of residual errors (after correction/compensation) is thus characterized, "large" individual error terms can be assessed to determine signatures associated with out-of-tolerance hardware (blunders), and the ability of control algorithms to deal with accumulated "subliminal" errors — those below the resolution of local sets of diagnostics, but large enough to degrade performance — assessed.

### 2.14.2 Estimates

Standard methods can be used to evaluate the impact of perturbations on accelerator performance [28–31]. These involve evaluating the linear response of a particular parameter (or parameters) to single perturbations, and superposing 'the effect of sequential random errors of the same class. For accelerators, typical perturbations include RF phase and amplitude errors, magnet misalignments, excitation errors, and field inhomogeneity. We now provide estimates for examples of each of these in the context of CBETA.

### 2.14.3 Alignment Sensitivity

Misalignment of a quadrupole by dx from its nominal location will result in a deflection $\delta x' \sim \delta x/f$ (where $1/f = B'L/(B\rho)$ is the quadrupole inverse focal length) of a beam entering the quad on its reference orbit, resulting in a betatron oscillation downstream. If independent offsets are encountered at $N$ quadrupoles along a monoenergetic beamline, an average of the mean square betatron displacement over an ensemble of misalignments and betatron phase along the line give the following result for the rms orbit offset at the end of the line [28, 29].

$$\langle x \rangle \sim \sqrt{\frac{N}{2}} \frac{\bar{\beta}}{\bar{f}} \langle \delta x \rangle \tag{2.14.1}$$

Here, $\bar{\beta}$ is the average lattice Twiss envelope in the line, $\bar{f}$ the average quad focal length, and $\langle \delta x \rangle$ the rms misalignment.

If — as in CBETA — multiple passes through a single line occur but the passes are separated by notionally arbitrary (or random) phase advance, betatron phase averaging simply replaces $N$ by $2N$. If the effects of the perturbation are to be observed at a different energy, a factor of $\sqrt{p_{\rm perturbation}/p_{\rm observation}}$ is applied to account for adiabatic damping or antidamping.

For CBETA, $1/f = B'L/(B\rho) \sim (100\,{\rm kg/m} \times 0.1\,{\rm m})/(33.3564\,{\rm kg-m/(GeV/c)}p_{\rm arc}$. The average $\beta$ is $\sim 0.5\,{\rm m}$, and $N \sim 200$ for each pass. For the first arc only, with $p \sim 0.04\,{\rm GeV/c}$, this yields $\langle x \rangle \sim 37.5\,{\rm m}\,\langle \delta x \rangle$. An rms alignment tolerance of $100\,\mu{\rm m}$ would thus yield $\sim 4\,{\rm mm}$ rms orbit error at the end of the first turn. This is notionally operationally manageable.

$$\langle x \rangle \sim \sqrt{N}\frac{\bar{\beta}}{f_0}\left[\frac{1}{\sqrt{p_1 p_{\rm dump}}} + \frac{1}{\sqrt{p_2 p_{\rm dump}}} + \frac{1}{\sqrt{p_3 p_{\rm dump}}} + \frac{1}{\sqrt{p_4 p_{\rm dump}}}\right]\langle \delta x \rangle \tag{2.14.2}$$

Over multiple turns, the uncorrected orbit will wander significantly further afield, especially when decelerated. Denoting by $1/f_0$ the "generic" focusing strength $B'L/(B\rho_0)$ of $100\,{\rm kg/m} \times 0.1\,{\rm m}/33.3564\,{\rm kg-m/(GeV/c)} \sim (0.3\,{\rm GeV/c})/{\rm m}$, a roll-up of the contributions described above gives the following result for the rms orbit excursion at the dump (where $p_n$ is (for $n$=1, 2, 3, and 4) the momentum for each of the four nominal beam energy levels). The $\sqrt{2}$ associated with the fourth energy accounts for the single passage through the FFAG system at the highest energy. For injection/extraction at 10 MeV/c and full energy of 150 MeV, $p_1 = 45\,{\rm MeV/c}$, $p_2 = 80\,{\rm MeV/c}$, $p_3 = 115\,{\rm MeV/c}$, and $p_4 = 150\,{\rm MeV/c}$, yielding $\langle x \rangle \sim 280\,{\rm m}\,\langle \delta x \rangle$. A $100\,\mu{\rm m}$ alignment tolerance thus — over the full system — results in a significant potential offset. Commissioning and operational practices must therefore make provision for local — or at least pass-to-pass — orbit correction. As the system transports multiple beams in a common structure, orbit optimization will thus likely be iterative and may involve degrading lower energy passes so as to bring higher-energy passes within operating tolerances [32].

### 2.14.4 Impact of Excitation Errors

Excitation errors in beamline components can arise due to fabrication or powering errors, or the variation in magnetic properties of materials used in magnets. An error in gradient will result in deviations from design focusing, with beam envelope and/or lattice function mismatch evolving as a consequence. The scale of various effects along a monoenergetic section of a beamline is set by the number of perturbed elements N, the average lattice functions at perturbations, and the deviation of focusing from nominal. In notation consistent with that used above, the envelope, divergence, phase, and dispersion errors at the end of the beamline segment under consideration are — in terms of the rms focal length deviation $\langle \delta(1/f) \rangle$, as follows [30].

$$\left\langle \frac{\Delta\beta}{\beta} \right\rangle = \langle \alpha \rangle = \sqrt{\frac{N}{2}}\bar{\beta}\left\langle \delta\left(\frac{1}{f}\right)\right\rangle \tag{2.14.3}$$

$$\langle \Delta\psi \rangle = \frac{1}{4\pi}\sqrt{\frac{3N}{2}}\bar{\beta}\left\langle \delta\left(\frac{1}{f}\right)\right\rangle \tag{2.14.4}$$

$$\langle \Delta\eta \rangle = \sqrt{\frac{N}{2}}\bar{\beta}\bar{\eta}\left\langle \delta\left(\frac{1}{f}\right)\right\rangle \tag{2.14.5}$$

The impact of the lattice and beam parameters to focusing errors may then be evaluated in much the same manner as in the case of misalignments. For the lowest energy (45 MeV) pass in CBETA, $N \sim 200$, $\bar{\beta} \sim 0.5\,\mathrm{m}$, $\bar{\eta} \sim 0.03\,\mathrm{m}$, and $\langle\delta(1/f)\rangle \sim T(1/\bar{f})$, with $T$ an error tolerance and $1/\bar{f}$) the average inverse focal length of $(100\mathrm{kg/m} \times 0.1\mathrm{m}/(33.3564\mathrm{kg-m}/(\mathrm{GeV/c}) \times 0.045\mathrm{GeV/c}) \sim 6.7/\mathrm{m}$. The scaling then gives

$$\left\langle \frac{\Delta\beta}{\beta} \right\rangle = \langle\Delta\alpha\rangle \sim 33.5\,\mathrm{T} \tag{2.14.6}$$

$$\langle\Delta\psi\rangle \sim 4.6\,\mathrm{T} \tag{2.14.7}$$

$$\langle\Delta\eta\rangle \sim 1.0\,\mathrm{T} \tag{2.14.8}$$

For absolute excitation errors at the 1% level (either due to deviations in excitation, errors in energy, or to being offset — as the low and high energy beams will be — in an inhomogeneous region of the quad field), dispersion and envelope errors are at the 33% level, with phase advance errors of a few degrees of betatron phase. The envelope and dispersion effects are significant, and may be expected to accumulate through the machine, with associated deviation of the transport system response to errors — and the beam envelopes/sizes — from design. Operational algorithms — such as those employed in CEBAF [33] — may be required to negotiate corrections amongst the various passes of beams through the system so as to avoid lattice error hypersensitivity, beam size blowup, or problems with halo and beam transmission.

### 2.14.5 RF Phase/Amplitude Response

As noted, ERLs are time of flight spectrometers; consequently, lattice perturbations that couple to path length may have an effect on time of flight (RF phase), resulting in variations in parameters that influence RF performance. Details of RF power/beam transient effects are described in Reference [31], which characterizes the RF power required to control cavity fields under various scenarios for pass-to-pass phasing (including the impact of phase transients) and energy recovery.

Here, we estimate the impact of two path-length-related effects: the impact of alignment errors on path length, and the magnitude of pass-to-pass phase errors resulting from field inhomogeneities. In the first case, misalignment of quadrupoles from design position will — in addition to the positional errors evaluated in §2.14.3 — lead to path length errors via the coupling of path length to angular deflection via $R_{52}$: $\delta l = R_{52}\delta x'$. If the deflection occurs at a non-dispersed location, the $R_{52}$ from the deflection to the next pass through the linac will be zero (the evolved path length is second order in the deflection); when the deflection is at a dispersed location, $R_{52} = \eta$, yielding the following scaling of path length with misalignment. In this case, $\delta l = R_{52}\delta x' = \eta\,\langle\delta x\rangle\,/f$. Summing the rms path length over $N$ quadrupoles at dispersed locations with average focal length with average focal length gives the following expression.

$$\delta l = \sqrt{N}\bar{\eta}\left(\frac{1}{f}\right)\langle\delta x\rangle \tag{2.14.9}$$

Inserting first arc values as outlined above (with $N \sim 100$ rather than 200, as the backleg — about half the quads — is nondispersed) gives $\langle\delta l\rangle \sim 10 \times 0.03 \times [100 \times 0.1/(33.3564 \times 0.045)]\,\langle\delta x\rangle \sim 2\,\mathrm{m}\,\langle\delta x\rangle$. An alignment tolerance of $100\,\mu\mathrm{m} \sim 0.2\,\mathrm{mm}$ path length error —

about 0.3 RF degrees. This estimate can be used to guide the design of path length correction algorithms, and to set the scale for turn-to-turn path length discrepancies.

Magnetic field inhomogeneities are a significant challenge for ERL performance. To date, successful microtrons, recirculating linacs, and ERLs have had field homogeneity at the 0.01% level. Variations in field quality couple to path length, thence RF phase, and from there downstream beam behavior. Local discrepancies in field will generate angular deflections of portions of the beam phase spaces (or, in an FFAG, of one beam relative to another) leading to phase — and eventually energy — errors [26, 27]. In the first/last pass of CBETA, a relative field error $\Delta B/B$ in a magnet of length $L$ would lead to an angular deflection $\Delta BL/(B\rho)$, which, integrated over the entire beamline (360° of bending) would lead to a path length error as follows:

$$\delta l = R_{52}\delta x' = \frac{\eta \Delta B L}{B\rho} = \eta \left(\frac{\Delta B}{B}\right)\theta \tag{2.14.10}$$

For $\eta \sim 0.03\,\mathrm{m}$, $\theta \sim 2\pi$ radians (full arc), this suggests that there will be a sensitivity of order $\delta l \sim 0.2(\Delta B/B)\,\mathrm{m}$. Thus, a 1% field error would result in 2 mm path length error of one pass relative to another — or an order of 3° RF at 1.3 GHz.

An accurate assessment of these effects will require simulation of an ensemble of machines based on the final lattice design while modeling errors at levels similar to those observed in prototype hardware. Results of such simulations can be used to set specifications on RF power requirements and/or define phase/path length stabilization methods and requirements.

### 2.14.6 Summary

The strong focusing inherent in FFAG transport reduces sensitivity to typical beamline errors and accelerator component imperfections. Estimates of typical errors suggest that appropriately conservative operational algorithms can compensate and/or correct the effect of imperfections expected in CBETA; of particular ongoing interest will be errors that can lead to irreproducible and/or time-transient path length errors, inasmuch as these will constrain the RF drive power required for stable operation.

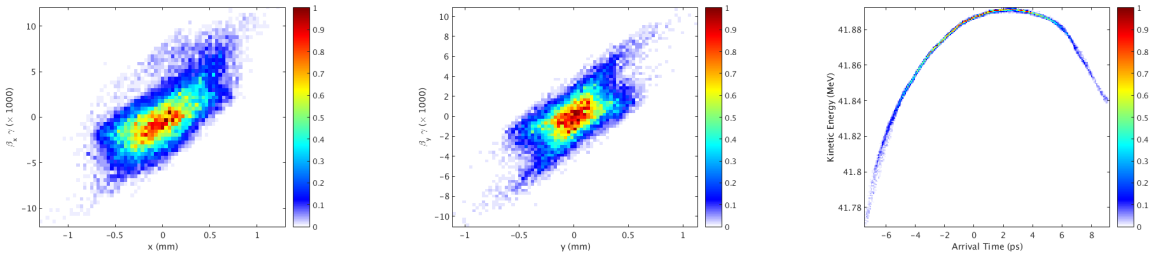


Figure 2.15.1: Bunch phase space sections at the end of the first pass through LA using GPT with space charge. The bunch charge is 100 pC. This bunch is used for start-to-end tracking using Bmad.

## 2.15 Start-to-End Simulation

Our initial start-to-end simulations start by optimizing and tracking a bunch from creation through the LA section using GPT with space charge. Figure 2.15.1 shows such a bunch. This bunch is then tracked through all passes of the machine using Bmad. Figure 2.15.2 shows optics and beam sizes for this tracking. Figure 2.15.3 to Fig. 2.15.9 show the details of each pass.

In the future, these simulations will include space charge, micro-bunching, CSR, resistive wall wakefields, and other wakefields into the calculation. Furthermore, with the orbit correction scheme in place, we will track bunches though lattices with corrected errors. We can also study emittance growth by tracking bunches with large energy spread, as well as the dynamic aperture.

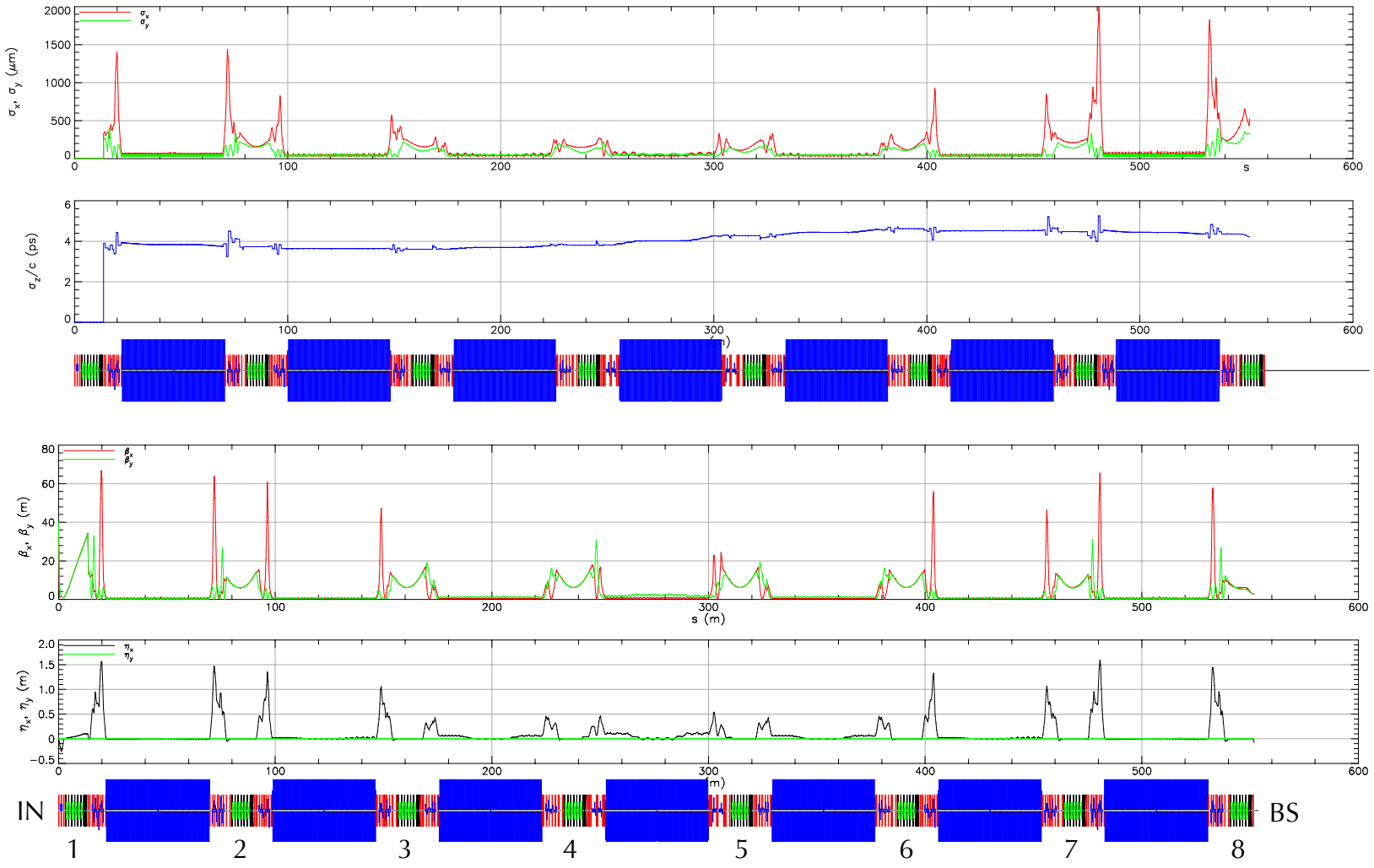


Figure 2.15.2: Optics and beam sizes summary for all passes from injection to dump. Numbers below the linac indicate the pass number through the linac.

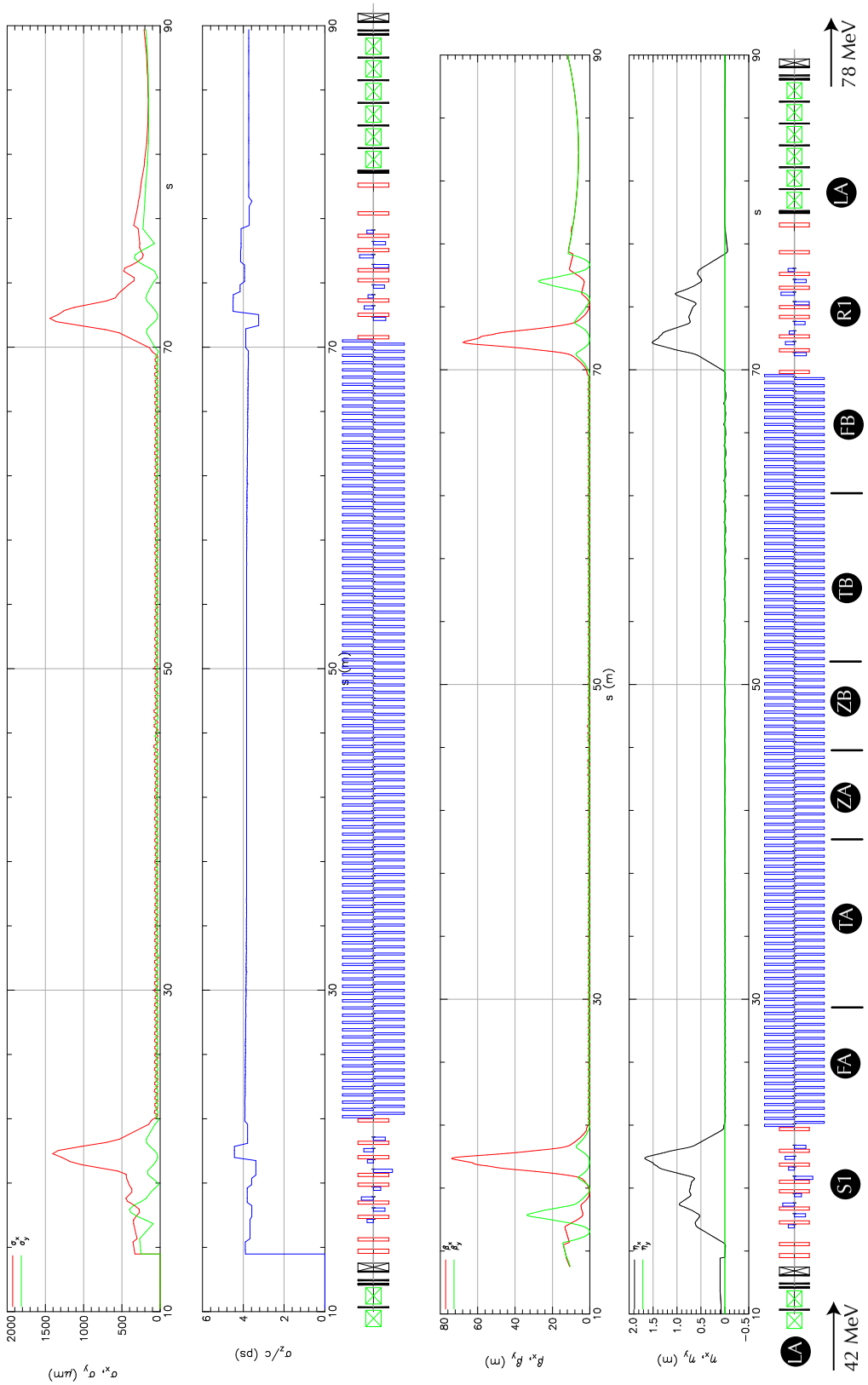


Figure 2.15.3: Optics and beam sizes for pass 1, 42 MeV

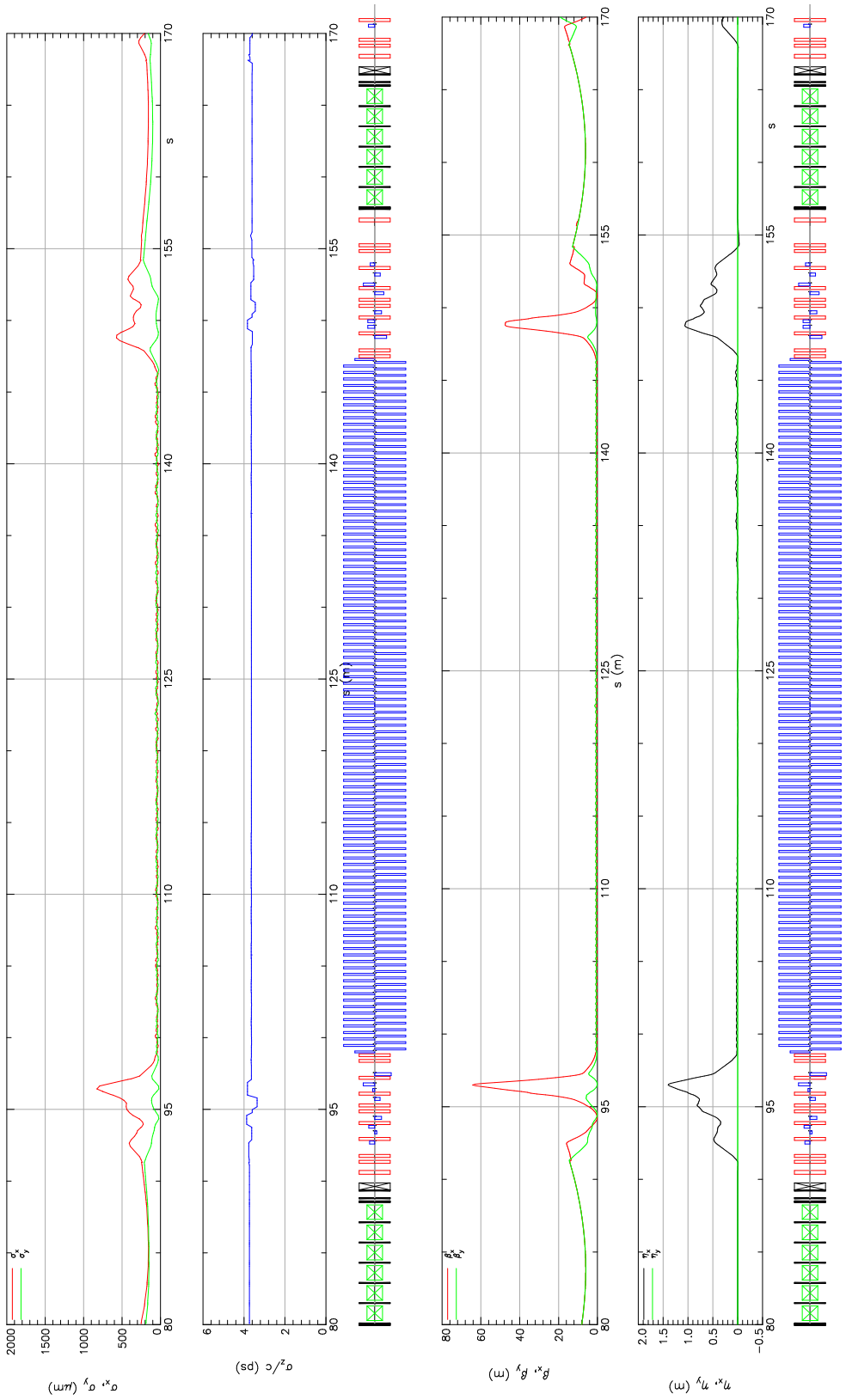


Figure 2.15.4: Optics and beam sizes for pass 2, 78 MeV

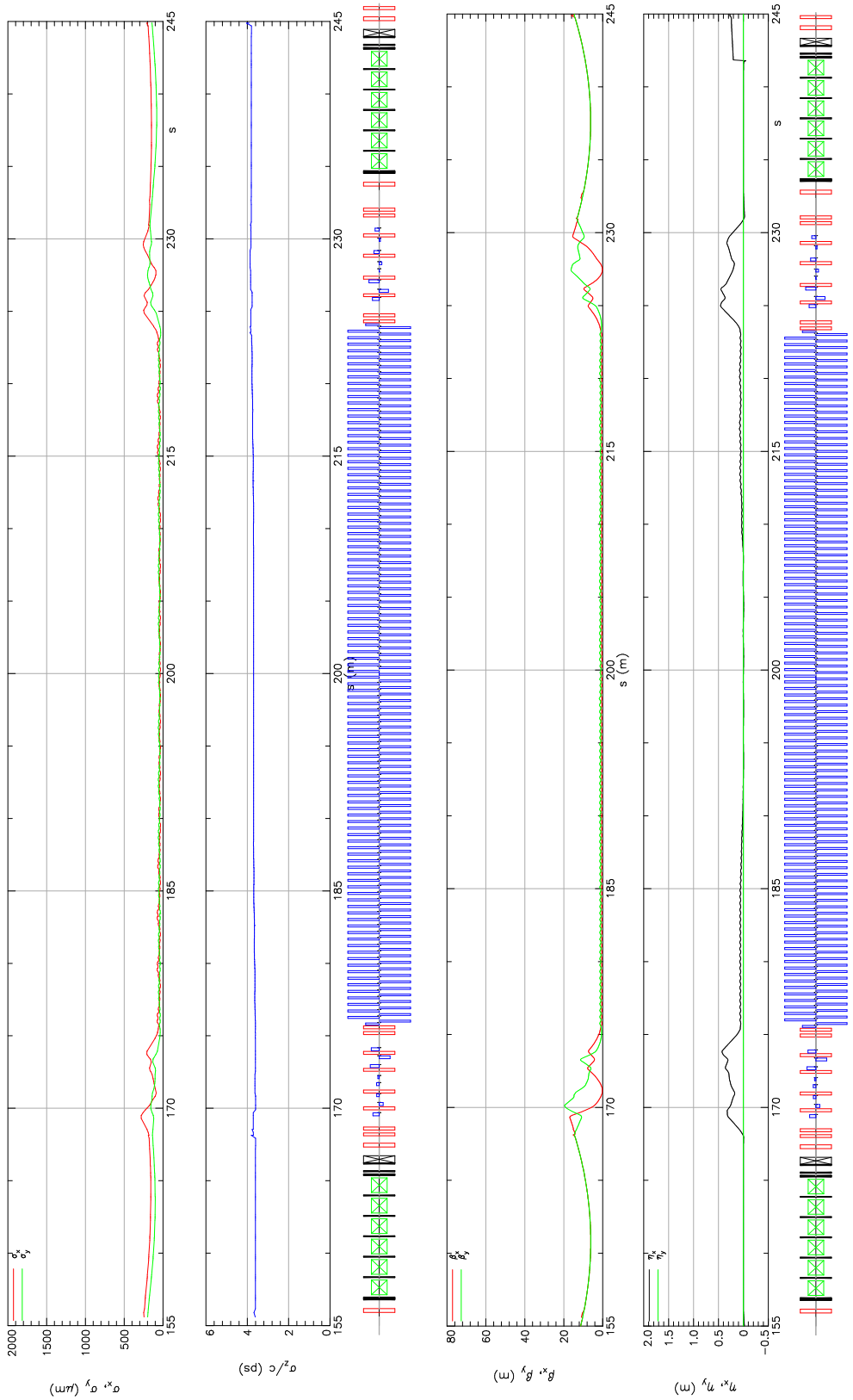


Figure 2.15.5: Optics and beam sizes for pass 3, 114 MeV

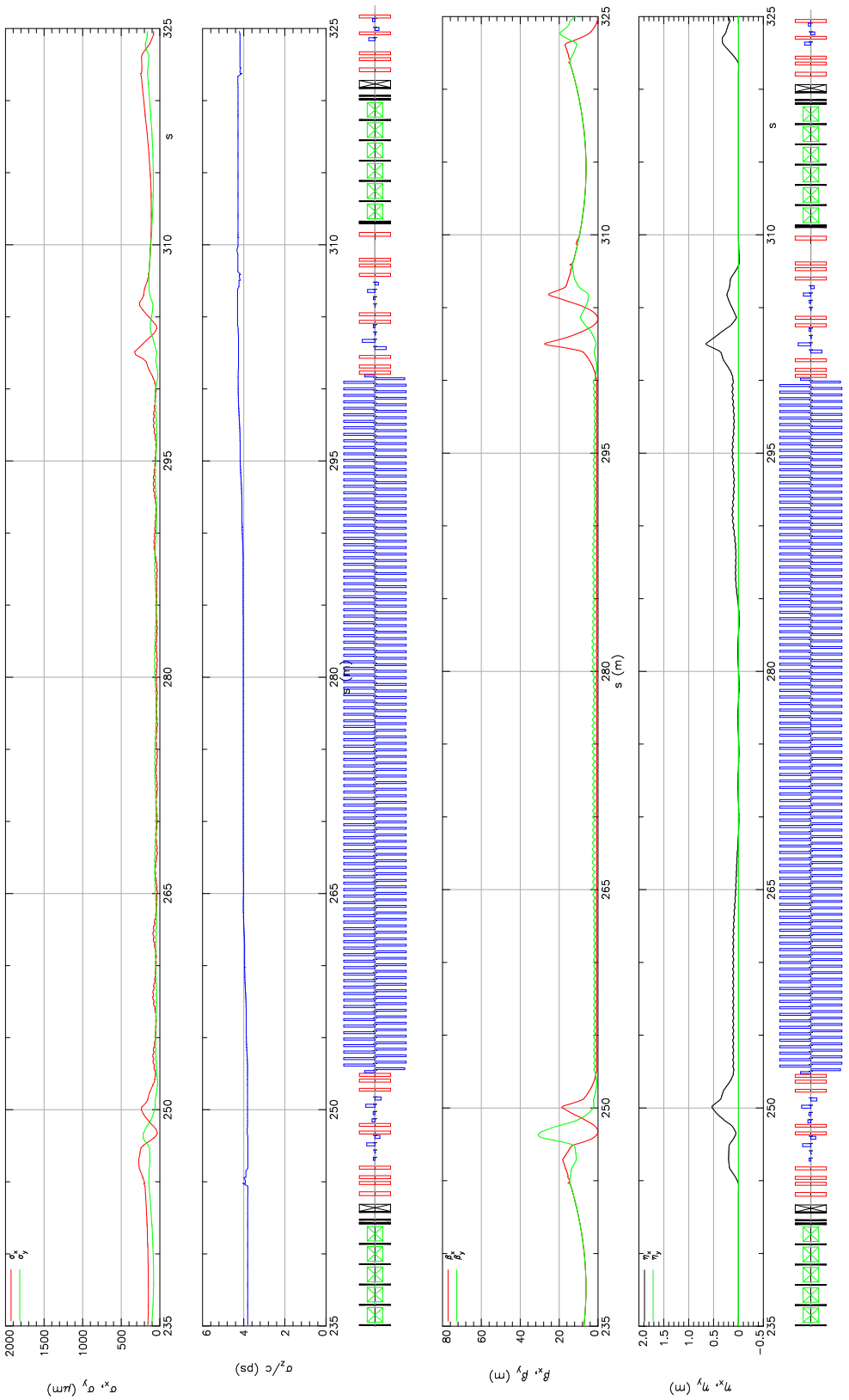


Figure 2.15.6: Optics and beam sizes for pass 4, 150 MeV

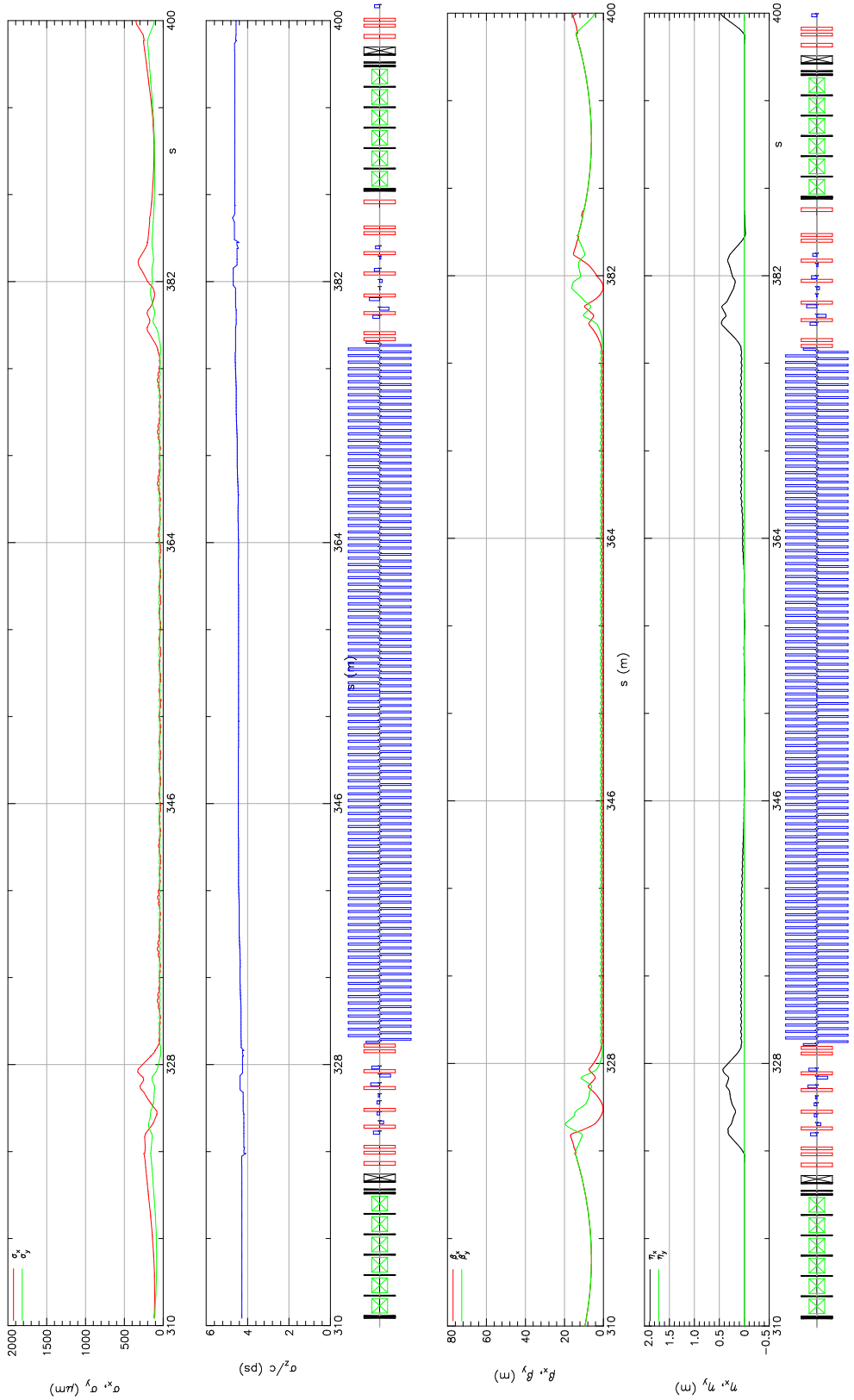


Figure 2.15.7: Optics and beam sizes for pass 5, 114 MeV

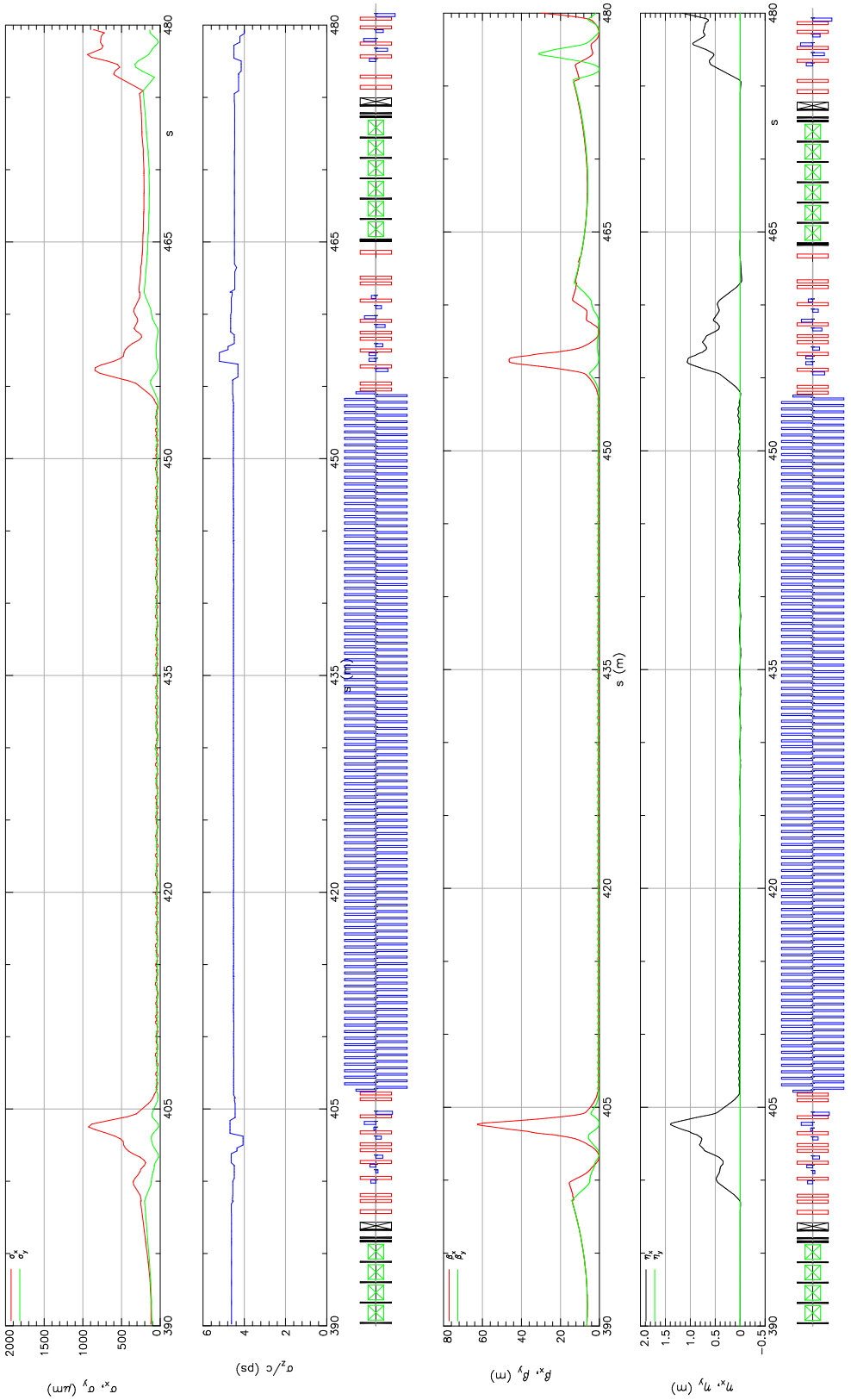


Figure 2.15.8: Optics and beam sizes for pass 6, 78 MeV

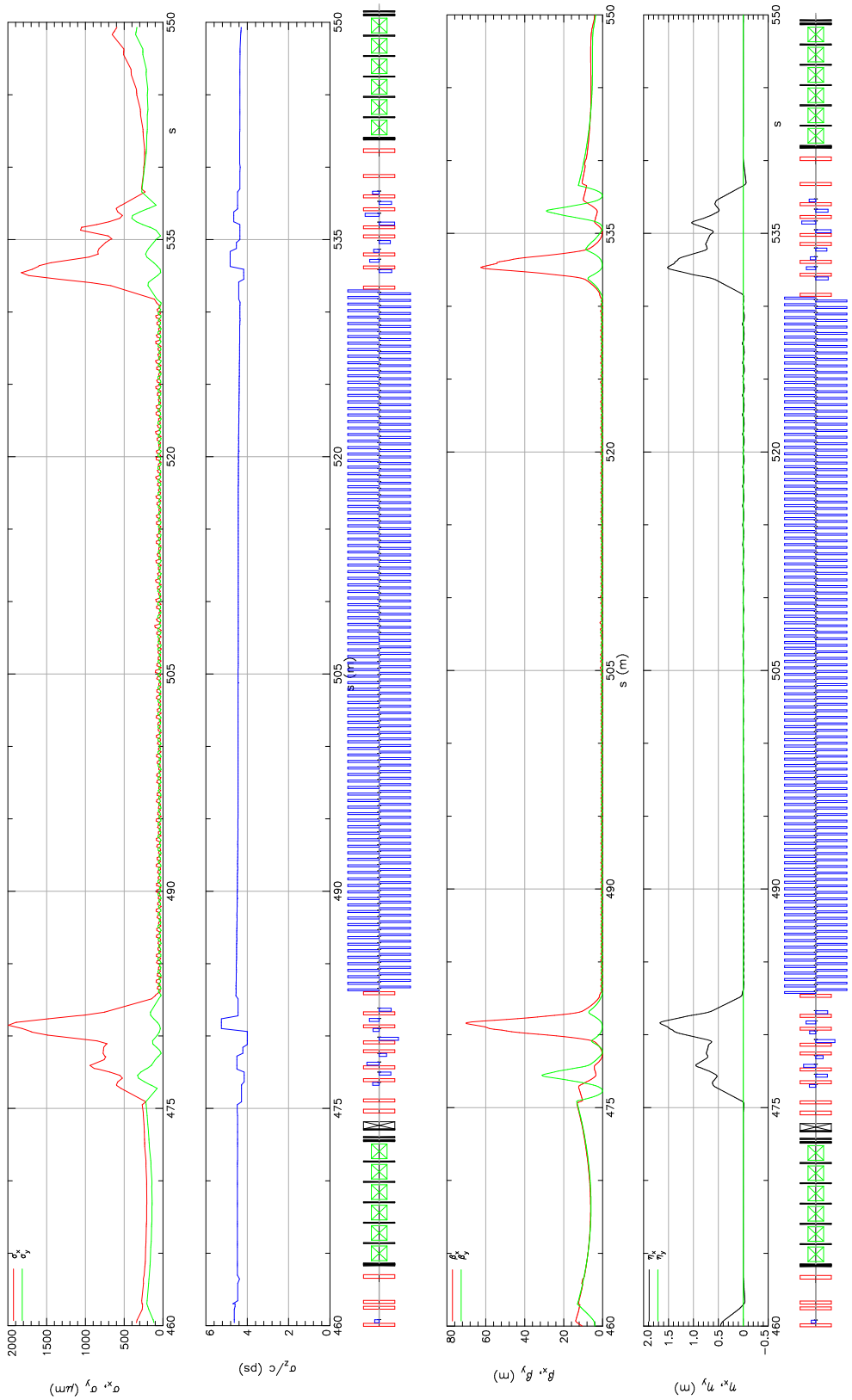


Figure 2.15.9: Optics and beam sizes for pass 7, 42 MeV

## 2.16 Beam instabilities: BBU

### 2.16.1 Introduction

BBU occurs in recirculating accelerators when a recirculated beam interacts with HOMs of the accelerating cavities. The most dominant HOMs are the dipole HOMs which give transverse kick to the beam bunches. The off-orbit bunches return to the same cavity and excite more dipole HOMs which, if in phase with the existing dipole HOMs, can kick the bunches more in the same direction. The effect can build up and eventually result in beam loss. Therefore, BBU is a primary limiting factor of the beam current, and the maximum achievable current is called the threshold current $I_{\text{th}}$. With more recirculation passes, bunches interact with cavities for more times, and $I_{\text{th}}$ can significantly decrease [34]. The target current of CBETA is 100mA for the 1-pass machine, and 40mA for the 4-pass machine. Simulations are required to check whether $I_{\text{th}}$ is above this limit.

### 2.16.2 Bmad Simulation Overview

Cornell University has developed a simulation software called Bmad to model relativistic beam dynamics in customized accelerator lattices. Subroutines have been written to simulate BBU effect and find $I_{\text{th}}$ for a specific design. A complete lattice provided to the program must include at least one multi-pass cavity with HOM(s) assigned to it. It is possible to assign HOMs of different orders to a single cavity, and also a different set of HOMs to other cavities. Parameters such as bunch frequency and numerical tolerances can also be specified to the program.

For each simulation, the program starts with a test current and records the voltage of all assigned HOMs over time. As the beam pass by the cavities, the momentum exchange between the bunches and wake fields are calculated, as well as the new HOM voltages. If all HOM voltages are stable over time, the test current is considered stable, and a new greater current will be tested. In contrast, if at least one HOM voltage is unstable, the test current is regarded unstable, and a smaller current will be tested. Usually $I_{\text{th}}$ can be pinned down within 50 test currents.

In BBU simulation, only cavities with HOM(s) assigned are essential, so other lattice structures can be hybridized. Hybridization is a process of merging certain lattice components into an equivalent Taylor map (up to linear order). A single BBU simulation on a CBETA 1-pass hybridized lattice takes up to 20 minutes, better than hours without hybridization. To efficiently find $I_{\text{th}}$ for various HOM assignments or design change, hybridization is necessary.

### 2.16.3 Bmad Simulation Result

Dipole HOMs of a single CBETA SRF cavity have been simulated by Nick Valles [35]. Random errors were introduced to each ellipse parameter of the cavity shape, resulting in a spectrum of dipole HOMs, and their characteristics ( shunt impedance $(R/Q)$, quality factor $Q$, and frequency $f$) were recorded. Each random error comes from a uniform distribution, with 4 different error cases: $\pm$ 125, 250, 500, and 1000 $\mu$m. For simplicity, we use $\epsilon$ to denote the error case: "$\epsilon = 125\,\mu$m" means the errors introduced come from a $\pm$ 125 $\mu$m uniform distribution. A cavity with smaller $\epsilon$ has better manufacture precision. For each error case, 400 unique

cavities were provided, and the top 10 "worst" dipole HOMs (ones with greater HOM figure of merit $\xi = (R/Q)\sqrt{Q}/f$) were recorded for each cavity.

Practically the 6 CBETA cavities are not identical, but manufactured with similar precision. Thus, for simulation each cavity is assigned with a different (randomly chosen) set of 10 dipole HOMs, and all 6 sets have the same $\epsilon$. Hundreds of simulations with different HOM assignments were run, and to statistical distributions of $I_{\rm th}$ were obtained for each specific design and choice of $\epsilon$. Three distributions will be presented as histograms in this section:

1) CBETA 1-pass with $\epsilon = 125\,\mu$m
2) CBETA 4-pass with $\epsilon = 125\,\mu$m
3) CBETA 4-pass with $\epsilon = 250\,\mu$m

### (1) CBETA 1-pass with $\epsilon = 125\,\mu$m

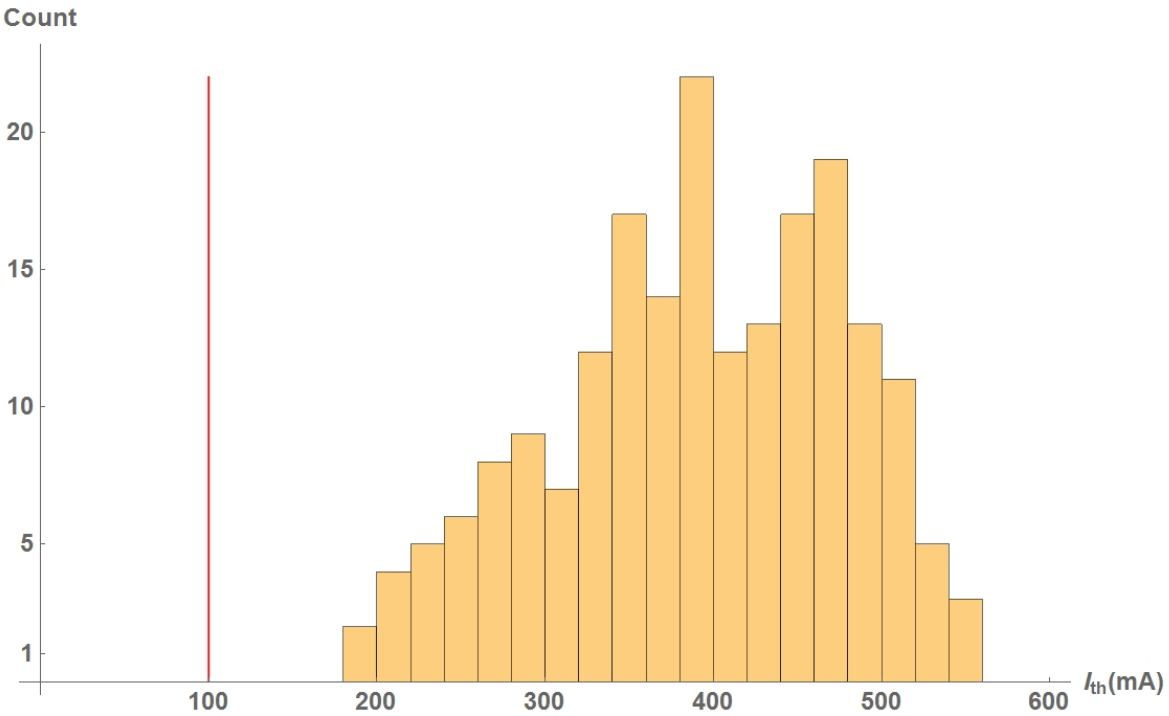


Figure 2.16.1: 200 BBU simulation results of $I_{\rm th}$ for the CBETA 1-pass lattice. Each cavity is assigned with a random set of 10 dipole HOMs ($\epsilon = 125\,\mu$m). The red line indicates the design goal of 100mA.

Figure 2.16.1 shows that all 200 simulations results exceed the 100mA goal for CBETA 1-pass machine. Moreover, 198 of them have $I_{\rm th}$ above 200mA, and the average $I_{\rm th}$ is 391mA. The result is quite promising.

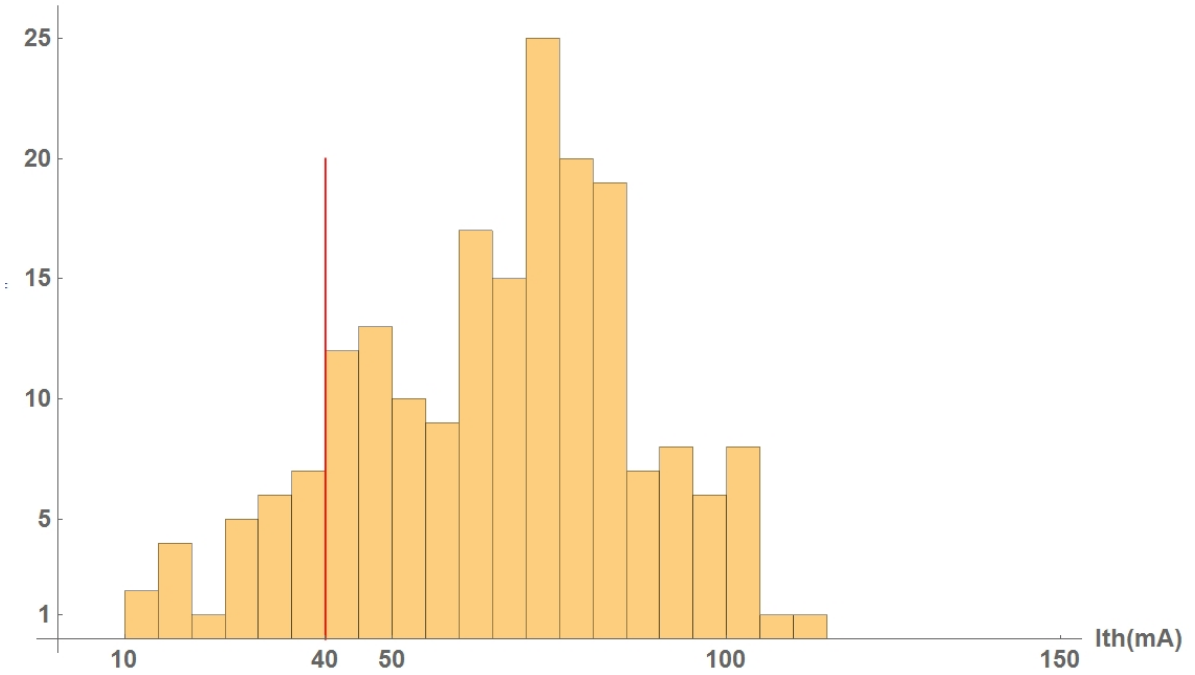


Figure 2.16.2: 200 BBU simulation results of $I_{\text{th}}$ for the CBETA 4-pass lattice. Each cavity is assigned with a random set of 10 dipole HOMs ($\epsilon = 125\,\mu$m). The red line indicates the ultimate performance parameters (UPPs) of 40mA, limited by HOM heating.

#### (2) CBETA 4-pass with $\epsilon = 125\,\mu$m

Figure 2.16.2 shows that out of 200 simulations, 172 of them exceed the 40mA goal for CBETA 4-pass machine, and the remaining 28 are above 10mA. This implies that with certain combinations of HOMs present in the cavities, $I_{\text{th}}$ can be limited, but still within the key performance parameters (KPPs) of 1mA.

#### (3) CBETA 4-pass with $\epsilon = 250\,\mu$m

It is interesting to see how $I_{\text{th}}$ behaves differently with a different $\epsilon$ for the 4-pass lattice. For $\epsilon = 250\,\mu$m, 167 out of 200 simulations are above the UPPs of 40mA and all are well above the KPPs of 1mA (See Fig. 2.16.3). This is not significantly different from the $\epsilon = 125\,\mu$m case, with similar implications. The $\epsilon = 500\,\mu$m and $\epsilon = 1000\,\mu$m cases are not investigated because modern cavities are built with better manufacture precision.

There are several ways to improve the accuracy of the results. Perhaps the most important one is to assign the actual HOM spectra measured directly from the built SRF cavities. However, measurement takes time, and complication may arise in identifying the HOM mode orders and choosing which ones to be included in simulation. Besides improving the simulation accuracy, a more important issue is to achieve a greater $I_{\text{th}}$, as discussed in the following section.

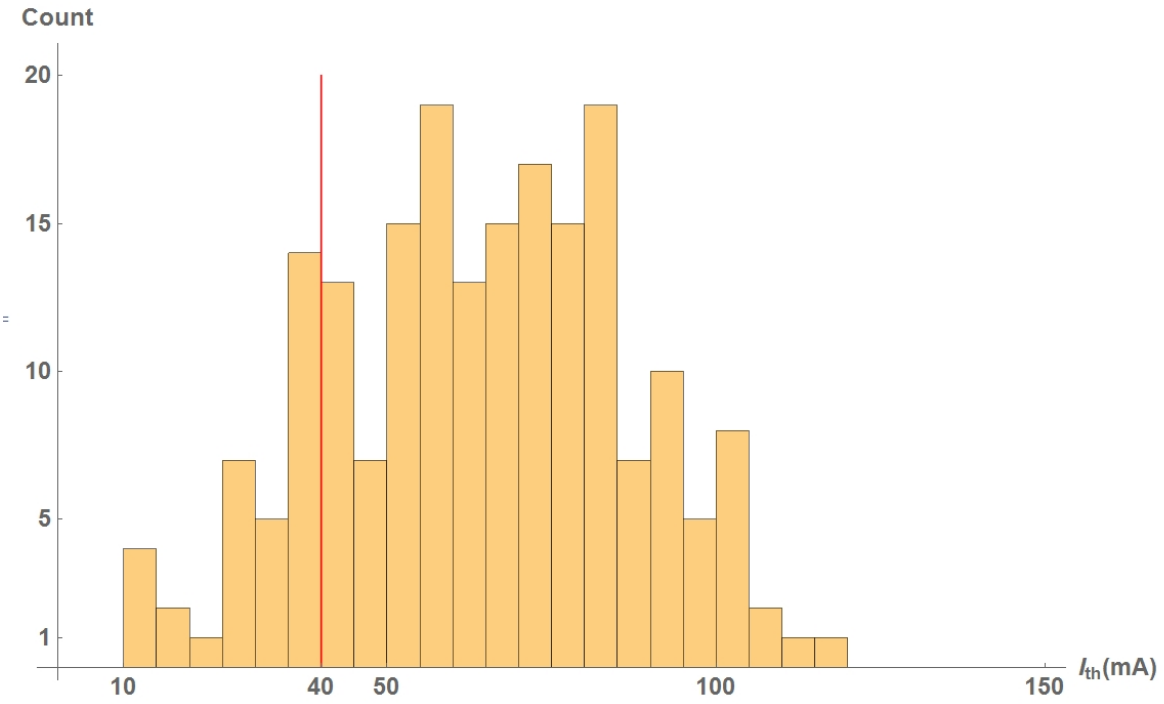


Figure 2.16.3: 200 BBU simulation results of $I_{\rm th}$ for the CBETA 4-pass lattice. Each cavity is assigned with a random set of 10 dipole HOMs ($\epsilon = 250\,\mu$m). The red line indicates the UPPs of 40mA.

### 2.16.4 Aim for higher $I_{\rm th}$

To achieve a higher $I_{\rm th}$, three ways have been proposed, and their effects can be simulated. The first way is to change the bunch frequency $f_b$ (repetition rate) by an integer multiple. Simulations on a CBETA 1-pass lattice show a change of $I_{\rm th}$ fewer than 5% over various choices of $f_b$. Such result may imply that $I_{\rm th}$ could not be systematically improved by changing $f_b$. On the other hand, rigorous calculation [34] has shown that $I_{\rm th}$ depends on $f_b$ in a non-linear way for a multi-pass ERL, and it will be interesting to experiment this effect on the realistic CBETA.

The second way is to change the phase advance between the multi-pass cavities. This method equivalently changes the $T_{12}$ element of the transfer matrices, and smaller $T_{12}$ values physically correspond to a greater $I_{\rm th}$ [34]. The effect is being investigated by simulations.

The third way involves x/y coupling in the transverse optics, so that horizontal HOMs excite vertical oscillations. This has been shown to be very effective for one-turn ERLs. Whether it increases $I_{th}$ significantly for a 4-turn ERL has yet to be studied.

## 2.17 Halo

"Halo" comprises the notionally diffuse components of the beam that can potentially sample large amplitudes. It is typically multicomponent, non-Gaussian, and mismatched to the beam core. As a result, it often is at very low density and may not be observable without use of extremely large dynamic range (LDR) diagnostics [36]. Halo emittance can readily exceed ERL transport system acceptance, leading to beam loss at aperture restrictions and/or locations with large lattice beam envelope function. During high-power CW operation, halo possesses significant levels of beam power, and thus is a serious machine protection concern - it has, in fact, posed one of the most severe operational challenges for all "true" CW SRF ERLs (those with full beam power exceeding installed linac RF drive).

There are many sources of halo. In the electron source, scattered light generated in the drive laser transport can illuminate active areas of the cathode outside the nominal source spot. Reflections off the cathode and gun structure can generate photoelectrons at essentially arbitrary phase and location. Masking of the cathode mitigates, but does not eliminate, the resulting large amplitude beam components. Depending on the choice of cathode material, cathode relaxation may lead to temporal tails at bunch formation. When operating with subharmonic bunch repetition rates, finite extinction ratio in drive laser pulse train gating can lead to so-called "ghost pulses", which will (due to their very low charge) be mismatched to the injector focusing (which is optimized for high charge) and will evolve as halo. The beam dynamics of of bunch formation and capture also generate halo [37]. Finally, field emission in the gun structure or in early cells of the first injector SRF cavities can be captured and accelerated, forming well defined beam components [38].

Various beam dynamical processes contribute to halo formation at higher energy. Intrabeam scattering, especially Touschek scattering, can potentially lead to significant intensity at large amplitude. Beam/gas scattering similarly contributes. Very bright and/or intense beams can, in principle, evolve halo in the form of long beam tails generated via nonlinear collective effects, CSR, LSC, microbunching, wakefields, and beam interactions with environmental impedances.

Halo management is critical to successful ERL operation. As noted, this has been a primary operational challenge in all high power SRF ERLs operated to date (see, e.g. [39]); beam loss must be avoided so as to avoid hardware damage and/or activation. This will be particularly critical in CBETA because of the widespread use of permanent magnet materials. At high full energy beam powers (MW levels), typical losses - which must be restricted to $\sim$ W/m levels - thus call for halo control and confinement at the few part per million. Machine design and operations must allow for beam components with emittances significantly exceeding that of the beam core, and which are not characterized by the same Twiss parameters. In particular, apertures cannot be established by use of "rms beam sizes" as these are not directly connected to the halo (inasmuch as it has different emittance, phase space distributions, and envelopes - which themselves may be mismatched to the transport lattice focusing structure that has been optimized for the core [27].

ERL designs thus generally provide a "working aperture allowance" to accommodate largely unknown and machine-dependent effects. LDR (with as much as six orders of magnitude range) instrumentation is needed, and control algorithms that optimize halo transmission as well as core behavior are required to achieve very high powers. Collimation can prove palliative - but as in ring injection systems, it is not in general curative - and has not yet been successfully

demonstrated in a high-power ERL environment, despite testing on the JLab IR Demo [40]. Sensitivity of system designs to halo can be evaluated by evaluating halo "maps" [41, 42] - which are basically the envelope of all possible orbits in the machine. This can be generated by displacing the beam in position and/or angle at regular, closely spaced locations along the beamline and tracking its motion throughout the rest of the system. Transverse halo maps determine potential aperture restrictions and possible points of significant beam loss (and thus serve to guide the location of beam loss monitors for machine protection and/or collimators [41]; longitudinal maps define a momentum aperture that can be compared to the deviations anticipated from Touschek scattering. Similar interpretation of intrabeam scattering and beam-gas scattering results will provide guidance on potential aperture requirements and restrictions.

## References

[1] Symon, K. R. *Fixed-Field Alternating-Gradient Particle Accelerators.* Physical Review, **103** (6), pages 1837–1859 (September 1956).

[2] Ohkawa, T. *FFAG Accelerator.* Symposium on Nuclear Physics of the Physical Society of Japan (1953).

[3] Kolomenski, A. *Electron Ring Phasotron.* Zhurnal Eksp. Teor. Fiz., **33** (298) (1957).

[4] Ankenbrandt, C. M., *et al. Status of muon collider research and development and future plans.* Phys. Rev. ST Accel. Beams, **2**, page 081001 (Aug 1999).

[5] Trbojevic, D., E. D. Courant, and A. Garren. *FFAG lattice without opposite bends.* AIP Conf. Proc., **530**, pages 333–338 (2000).

[6] Johnstone, C., W. Wan, and A. Garren. *Fixed Field Circular Accelerator Design.* In *Proceedings of the 1999 Particle Accelerator Conference, New York*, pages 3068–3070 (May 1999).

[7] Trbojevic, D., E. D. Courant, and M. Blaskiewicz. *Design of a nonscaling fixed field alternating gradient accelerator.* Phys. Rev. ST Accel. Beams, **8**, page 050101 (May 2005).

[8] Machida, S. *Fixed field alternating gradient.* arXiv preprint arXiv:1302.2026 (2013).

[9] Machida, S., *et al. Acceleration in the linear non-scaling fixed-field alternating-gradient accelerator EMMA.* Nature Physics, **8** (3), pages 243–247 (January 2012).

[10] Gulliford, C., *et al. Demonstration of low emittance in the Cornell energy recovery linac injector prototype.* Phys. Rev. ST Accel. Beams, **16**, page 073401 (Jul 2013).

[11] Dunham, B., *et al. Record high-average current from a high-brightness photoinjector.* Applied Physics Letters, **102** (3), page 034105 (2013).

[12] Gulliford, C., *et al. Demonstration of cathode emittance dominated high bunch charge beams in a DC gun-based photoinjector.* Applied Physics Letters, **106** (9), 094101 (2015).

[13] http://laacg.lanl.gov/laacg/services/download_sf.phtml (2012).

[14] Wei, J., Y. Papaphilippou, and R. Talman. *Scaling law for the impact of magnet fringe fields.* In *Particle accelerator. Proceedings, 7th European Conference, EPAC 2000, Vienna, Austria, June 26-30, 2000. Vol. 1-3*, pages 1092–1094 (2000).

[15] http://www.cobham.com/about-cobham/aerospace-and-security/about-us/antenna-systems/kidlington/products/opera-3d.aspx (2008).

[16] http://www.cst.com/Content/Products/MWS/Overview.aspx (2013).

[17] Gulliford, C., *et al. Asymmetric focusing study from twin input power couplers using realistic rf cavity field maps.* Phys. Rev. ST Accel. Beams, **14**, page 032002 (Mar 2011).

[18] Schwinger, J. *On Radiation by Electrons in a Betatron.* In K. A. Milton, editor, *A Quantum Legacy: Seminal Papers of Julian Schwinger*, pages 307–331. World Scientific, Singapore (1945). Also in Report LBNL-39088.

[19] Mayes, C. and G. Hoffstaetter. *Exact 1D model for coherent synchrotron radiation with shielding and bunch compression.* Phys. Rev. ST Accel. Beams, **12** (2), page 024401 (Feb 2009).

[20] Sagan, D., *et al. Extended one-dimensional method for coherent synchrotron radiation including shielding.* Phys. Rev. ST Accel. Beams, **12** (4), page 040703 (Apr 2009).

[21] Stupakov, G. *Surface Roughness Impedance.* Technical Report SLAC-PUB-8743, SLAC (2000).

[22] Chin, Y. H. *User's guide for ABCI Version 9.4 (Azimuthal Beam Cavity Interaction).* KEK Report 2005-06 (2005).

[23] Yokoya, K. *Resistive Wall Impedance Of Beam Pipes Of General Cross Section.* Particle Accelerators, **41**, pages 221–248 (1992).

[24] Tenenbaum, P. *Beam-Gas and Thermal Photon Scattering in the NLC Main Linac as a Source of Beam Halo.* Technical Report LCC-NOTE-0051, SLAC (2001).

[25] Temnykh, A. B., M. P. Ehrlichman, and G. Hoffstaetter. *Beam losses due to intra-beam and residual gas scattering for Cornell's energy recovery linacs.* In *eleventh European Particle Accelerator Conference, EPAC'08*, pages 214–216. Genoa,Italy (2008).

[26] Douglas, D. *A Magnet Field Quality Limitation on ERL Performance.* Technical Report JLAB-TN-02-002, JLAB (2002).

[27] Douglas, D. *et al. An instrumentation wish list for high power/high brightness ERLs.* In *Proceedings of Beam Instrumentation Workshop BIW10, Santa Fe, New Mexico*, volume 506 (2010).

[28] Douglas, D. R., J. Y. Tang, and R. C. York. *Error analyses and modeling for CEBAF beam optical systems: Beamline element specifications and alignment error tolerances.* Conf. Proc., **C910506**, pages 443–445 (1991).

[29] Douglas, D. R. *Chromatic correction in the CEBAF beam transport system.* Conf. Proc., **C910506**, pages 449–451 (1991).

[30] Douglas, D. *Error Estimates for the IR FEL Transport System.* Technical Report CEBAF-TN-96-036, CEBAF (July 1996).

[31] Powers, T. and C. Tennant. *Implications of Incomplete Energy Recovery in SRF-Based Energy Recovery Linacs.* In *Proceedings, ERL 07* (2007).

[32] Bodenstein, R. M. and M. G. Tiefenback. *Multipass Steering Protocols at Jefferson Lab.* Conf. Proc., **C070625**, page 3648 (2007).

[33] Lebedev, V. A., *et al. Linear Optics Correction in the CEBAF Accelerator.* Conf. Proc., **C970512**, page 2128 (1997).

[34] Hoffstaetter, G. H. and I. V. Bazarov. *Beam-breakup instability theory for energy recovery linacs.* Physical Review Special Topics - Accelerators and Beams, **7** (2004).

[35] Valles, N., D. S. Klein, and M. Liepe. *Beam break-up studies for Cornell's energy recovery linac.* In *Proceedings of SRF2011, Chicago, IL USA* (2011).

[36] Evtushenko, P. and D. Douglas. *High Dynamic Range Beam Imaging With Two Simultaneously Sampling CCDs.* In *Proc. FEL 2012, Nara, Japan* (2012).

[37] Evtushenko, P. *Electron Beam Diagnostics for High Current FEL Drivers.* In *Proc. FEL 2011, Shanghai, China* (2011).

[38] Evtushenko, P. Private Communication.

[39] Alarcon, R., *et al. Transmission of Megawatt Relativistic Electron Beams through Millimeter Apertures.* Phys. Rev. Lett., **111**, page 164801 (Oct 2013).

[40] Neil, G. Private Communication.

[41] Johnson, D., D. Douglas, and J. Coleman. *Determination of Beam Loss Sensitivity for 10 kW FEL Upgrade.* Technical Report JLAB-TN-02-031, Jefferson Lab (2002).

[42] Evtushenko, P. and C. Tennant. *Halo Effects in High-Power FEL Driver ERLs.* Technical Report JLAB-TN-12-017, Jefferson Lab (2011).

# 3 FFAG Magnets

## 3.1 Iron-based Permanent Magnet Design

### 3.1.1 General Concept

Iron-dominated magnets for CBETA were developed as a low-risk option. The magnets rely on established accelerator magnet design and manufacturing techniques as far as possible. The design idea of the quadrupoles is a copy of the permanent magnet quadrupoles used for the Fermilab Recycler, which have been in use for a number of years [1]. Relying on the experience of the Fermilab personnel in deciding for this approach was also an important factor. The light source in Brazil follows a very similar approach, which could also be a valuable resource for information [2].

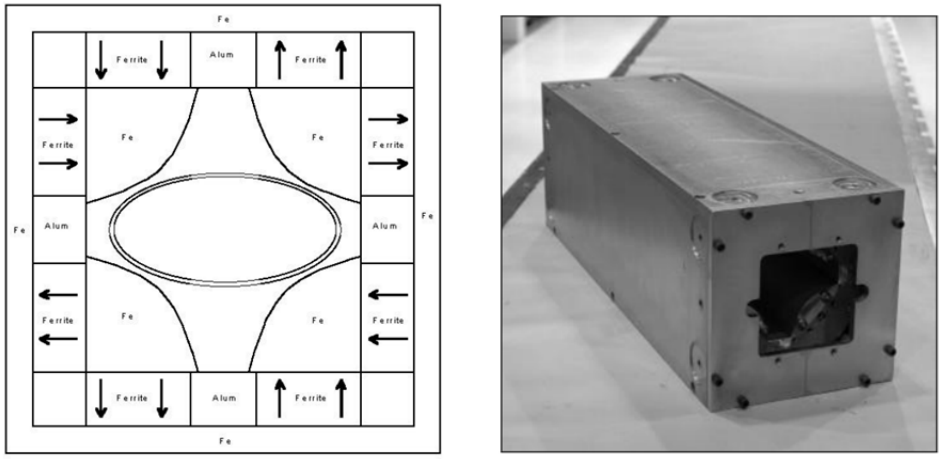


(a) (b)

Figure 3.1.1: (Left) Schematic of the Fermilab Recycler magnet. The magnet is 8.25" wide and tall. (Right) Picture of a Fermilab recycler quadrupole.

Figure 3.1.1 (a) and (b) illustrate the concept. In general the magnet is a standard quadrupole, but the necessary flux is generated by several permanent magnets which are placed around the pole. The advantage of this design is that this is largely a conventional approach, that means the field quality in principle will only be determined by the pole shape (for which ample experience exists). As the permanent magnets are only providing magnetic flux, the mechanical and magnetic tolerances of the permanent magnets are easy to handle. This is important as the permanent magnets will be the component in the design with the largest tolerances (magnetically and mechanically).

The permanent magnets themselves have a very simple shape (block shape), which multiple suppliers can provide. Industry is well accustomed to this shape of permanent magnet, which means short lead-times and reduced cost. A further advantage of this design is that the quadrupole strength can be adjusted easily with a pole winding, this will be discussed later on in this report. A further significant advantage is the fact that these magnets can be temperature compensated. NdFeB possesses a negative temperature coefficient, which otherwise would lead to a change in gradient of 0.1%/K. Temperature compensation will be discussed in a separate section of this report.

Magnet to magnet reproducibility can be expected to be high due to the use of laminations (shuffling), the matching of a large number of small permanent magnets to provide the same amount of flux and the aforementioned temperature compensation. These concepts will be addressed in more detail in the following sections.

This design approach also has a number of disadvantages. The first is that due to the lattice the magnets need to be placed closely together. This leads to unwanted flux leakage and crosstalk, as the distance between magnets becomes comparable to the distance between the poles. Due to a horizontal offset of the magnets with respect to each other each side of one quadrupole sees a different cross-section of the neighboring quadrupole, which means for each half of the quadrupole this effect is slightly different. This leads to an imbalanced quadrupole, where one side is stronger than the other side. In recent lattices this effect has been small (∼percent level) and does not cause a problem.

As mentioned earlier, unwanted temperature effects of NdFeB can be compensated for, but the downside of this is that the performance of the quadrupole will be lower by 20% in comparison to an uncompensated magnet. Correction coils are difficult to accommodate due to space restraints. The magnets tend to be large to obtain an optimum working point for the permanent magnets.

### 3.1.2 Finite Element Simulations

The magnets described in this report have been simulated with the commercial finite element software package COMSOL Multiphysics, which is a combined 2D and 3D code. For the mesh a second order (quadratic) element is used for accuracy reasons. 3D models usually employ a Tetrahedral mesh; regions of specific interest (for field maps) use an extruded quadrilateral mesh (Hexahedron). Periodic boundary conditions are used at the end of the cell to mimic an infinitely long series of magnets. For permanent magnets we assume NdFeB grade N49M with a $B_r$ of $1.37 - -1.42$T. For iron we use a non-linear BH-curve which is equivalent to ultra low-carbon steel (better than AISI 1006, see section 3.1.6). An iterative solver is used for 3D problems (Conjugate Gradients, Multigrid); 2D problems are solved with a direct solver (MUMPS).

### 3.1.3 Requirements and Basic Magnet Design

The CBETA lattice used as a basis for the magnet design is shown in Fig. 3.1.2a. The lattice was specifically optimized to be compatible with iron dominated magnets. The lattice requires relatively low gradient quadrupole magnets (10.24 T/m, hard-edge model). A special feature of this lattice is that the focusing and defocusing magnets differ only in length; required gradient

and beam excursion are identical.

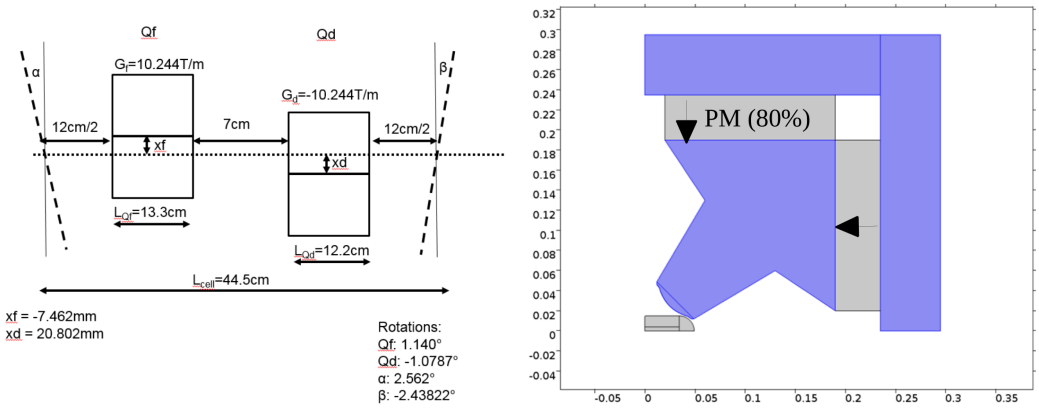


(a) (b)

Figure 3.1.2: (Left) Lattice 11/9. (right) Quadrupole Magnet. The direction of the magnetization is indicated by the arrows.

Figure 3.1.2b shows a possible magnet design for this lattice. Shown in blue is the iron part of the magnet; the permanent magnets are located above and next to the pole in grey. It is assumed that 80% of the available volume will be filled with permanent magnetic material. The remaining 20% are required for temperature compensation.

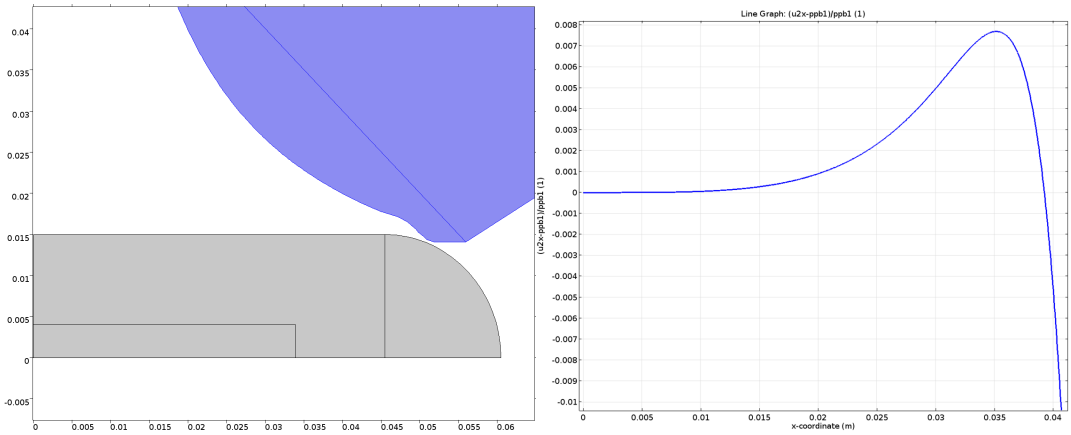


(a) (b)

Figure 3.1.3: (Left) Pole region including stay clear region for beam pipe with margin. (right) Gradient quality $\Delta G/G_0$.

Figure 3.1.3a shows the region around the pole of the magnet. Shown in gray is the stay-clear area around the beam, which is sufficient to accommodate a suitable beam pipe. The maximum possible clearance for this design is 16.5 mm from each point of the beam aperture.

Figure 3.1.3b shows the simulated gradient quality on the center plane of the magnet. In

a 2D simulation the magnet delivers a gradient of 18.335 T/m with a good gradient quality up to 40 mm. A gradient quality of 1% was requested and should be tolerable; the primary effects of a departure from linearity of the field profile are a change in the tune range and orbit excursion. Nonlinear effects from this nonlinearity are significantly smaller than those that arise from the magnet ends.

### 3.1.4 Temperature Compensation

NdFeB permanent magnets are envisaged to be used for this project. One disadvantage of NdFeB is the temperature coefficient, which means the residual induction $B_r$ changes with small changes in temperature. The temperature coefficient $\alpha$, defined as $(\Delta B/B)/\Delta T$, is about $-1.1 \times 10^{-3}$/K.

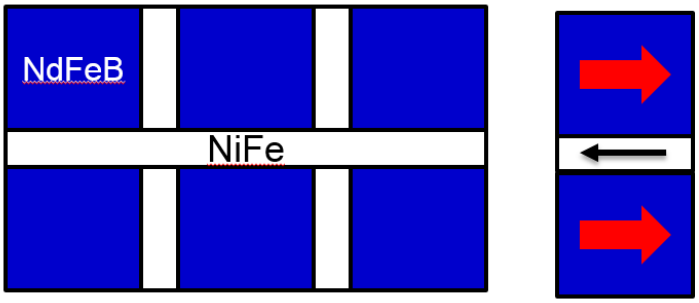


(a) (b)

Figure 3.1.4: (Left) Permanent Magnets interleaved with NiFe, top view. (right) Permanent Magnets interleaved with NiFe, side view.

The temperature dependence of this magnet can be compensated for by a method pioneered by Fermilab [3] (CERN tested this for a very similar design). The principle idea is that strips of NiFe are placed next to the permanent magnets, parallel to the magnetization direction of the NdFeB as shown in Fig. 3.1.4a and Fig. 3.1.4b. 30-32% Ni-Fe possesses a relatively low Curie temperature around 60°C. The NiFe strips act as temperature dependent magnetic shunts, shunting away a certain amount of magnetic flux. If the temperature increases the permanent magnets will be less powerful, but at the same time the NiFe shunts will be less effective. If the volume ratios are correct (about 20% NiFe) temperature effects over a range of 10-20K can be excluded.

This was simulated in 2D and 3D finite element simulations for the magnet design under consideration. The magnetic saturation data was taken from the data sheet of the manufacturer shown in Fig. 3.1.5a. In a 2D linear simulation a Nelder-Mead algorithm was used to minimize the field difference at the outermost beam position at two different temperatures (20 and 30°C). As shown in the figure, the process converges rapidly. It is worth noting that in practice it is sufficient to measure the temperature effects for two different volume fractions of NiFe, as the temperature effects will change linearly with the cross-section (and volume) of the NiFe. It was also verified that the interleaving of permanent magnets with NiFe strips does not influence the gradient quality.

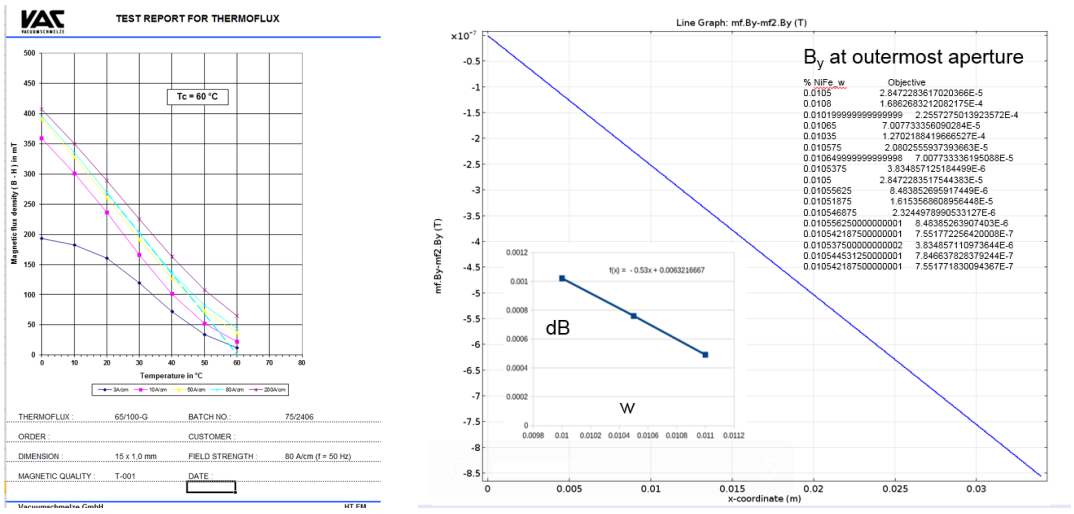


(a) (b)

Figure 3.1.5: (Left) Saturation magnetization of NiFe. (Right) 2D optimization of the thickness of NiFe strips; shown is the difference of the vertical magnetic field on the center plane for two different temperatures (20 and 30°C) at the outermost beam position.

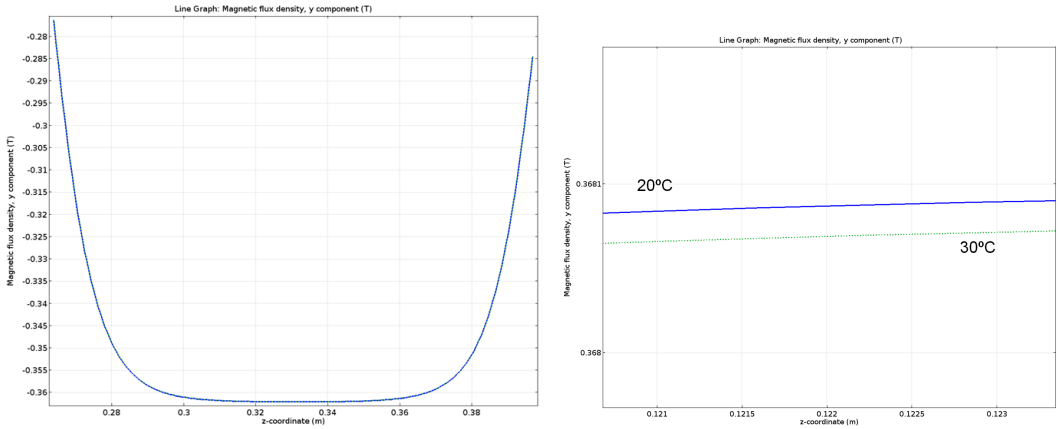


(a) (b)

Figure 3.1.6: (Left) Vertical magnetic field (20 and 30°) on center plane for Qd magnet. (right) Vertical magnetic field on center plane for Qf magnet.

Figure 3.1.6a and Fig. 3.1.6b show the simulation results for the temperature compensated Qf and Qd magnet, which show an almost perfect compensation between 20°C and 30°C. The volume fraction of NiFe was not adjusted going from a 2D to the 3D simulation; crosstalk did have no effect on the temperature compensation. In earlier simulations it was verified that the exact location of the NiFe strips is not crucial, that means that NiFe strips of a fixed thickness can be used to accomplish the required volume fraction.

In the simulation with the correct $B_r$ for the permanent magnets including the temperature compensation both magnets exceeded the required performance by about 9%. This is identical to a volume reduction of 9% of the permanent magnetic material, which is important to allow for space between the magnets during assembly .

### 3.1.5 Quadrupole Corrector

The quadrupole component of each magnet can be changed with a simple pole winding. It is anticipated that this will be implemented for every magnet. An example of this is shown in Fig. 3.1.7a.

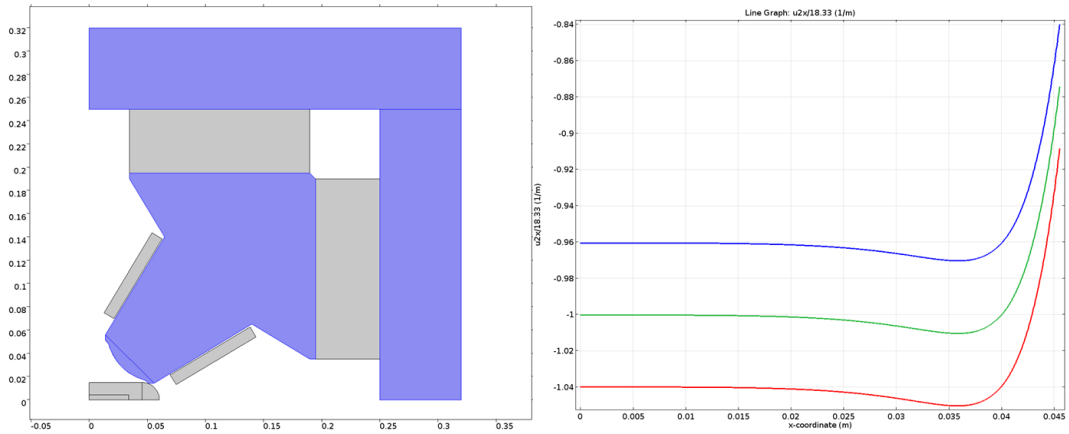


(a) (b)

Figure 3.1.7: (Left) Pole winding for quadrupole adjustment. (right) Change in gradient for a current density of $\pm 1 A/mm^2$ in the pole winding.

A current density of $1 A/mm^2$ is sufficient to change the quadrupole level by about 4% as shown in Fig. 3.1.7b. No significant change in gradient quality is observed as shown in Fig. 3.1.8.

### 3.1.6 Engineering

The yoke of the quadrupole magnets for CBETA will be made from laminations, each up to 2 mm thick. Stamping will ensure good mechanical tolerances for the pole; at the same time this process is very cost efficient.

One of the requirements for the CBETA magnets is small magnet to magnet variability. Laminations are ideally suited for this, as the individual laminations can be shuffled. This

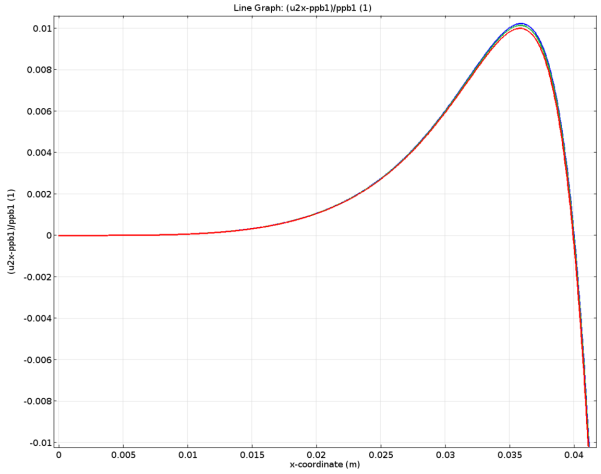


Figure 3.1.8: Simulated gradient quality for the maximum, minimum and nominal gradient.

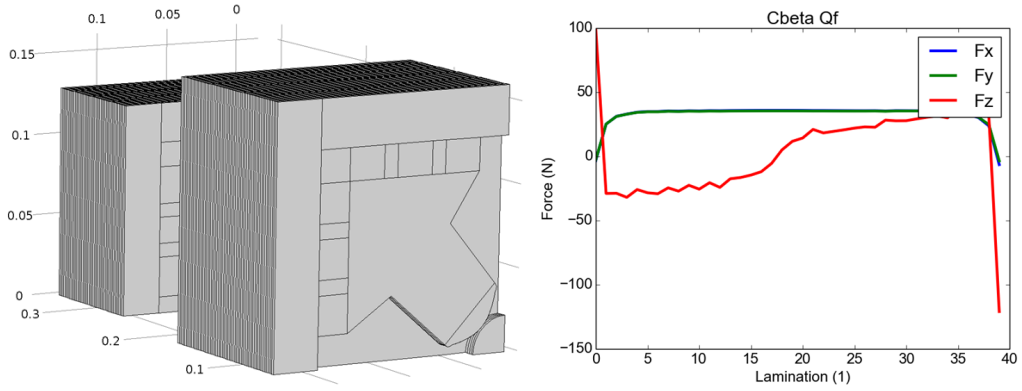


(a) (b)

Figure 3.1.9: (Left) Laminated quadrupoles for CBETA. (right) Force on the laminations of the Qf magnet.

process is well established and has been used for example for the Fermilab Main Injector magnets [4] and the ALBA light source [5]. By shuffling the geometric and magnetic property variations are averaged over different magnets. The force on the individual laminations for the test magnet have been evaluated using the Maxwell stress tensor. The results are shown in Fig. 3.1.9b.

### Required Pole Tolerance

Stamping accuracies of 20-30 $\mu$m have been reported, but less stringent tolerance requirements are preferable in terms of cost and the number of potential suppliers. A study was carried out to determine the required pole accuracy for CBETA.

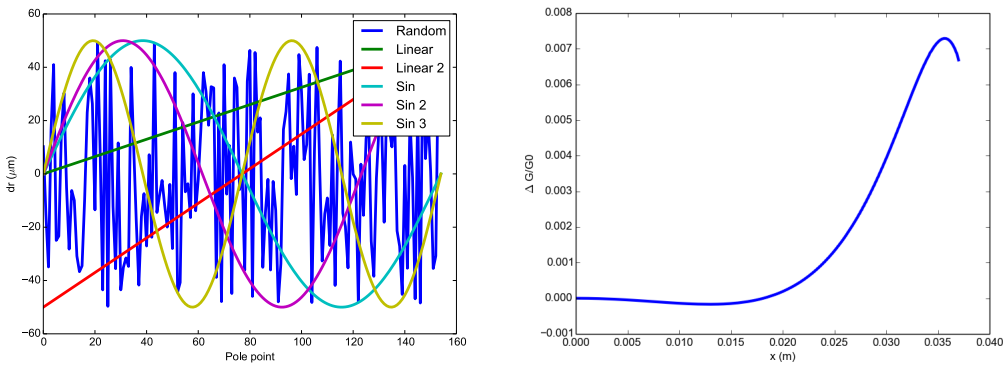


(a) (b)

Figure 3.1.10: Error functions applied to the pole shape of the CBETA magnets (right). Simulated gradient quality with a linear pole error of 50 $\mu$m (right).

Various error functions were applied to the pole shape of the CBETA magnets, mimicking a systematic error in the punch accuracy. The considered error functions are shown in Fig. 3.1.10a. For the initial study the amplitude of the error functions was assumed to be 50 $\mu$m.

The pole shapes were evaluated in 3D tracking studies; the error function with the largest effect on the orbit distortion was chosen ('linear2') and the amplitude of the error function was increased up to 150 $\mu$m. It was found that even in this scenario the orbit distortion was less than 0.5 mm, which is not a concern.

### Permanent Magnet Tolerances

Permanent magnets are subject to mechanical as well as magnetic tolerances. Typically, the total magnetization varies by up to 3%. The standard variation of the magnetization angle according to manufacturers is 3° (guaranteed 5°). Tighter tolerances of the angle are possible (1°), but drive the cost [6].

For the iron dominated quadrupoles most of the variations of the magnetic properties are not crucial. It is essential that each pole receives the same amount of magnetic flux from its

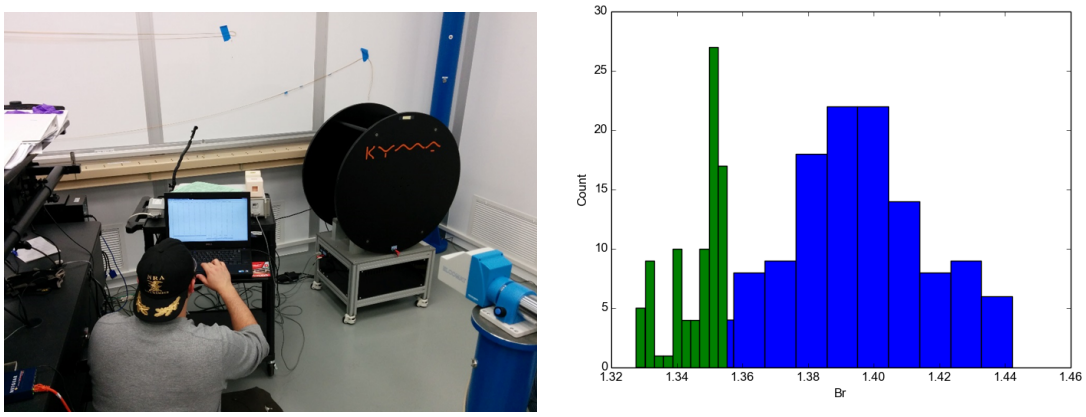


(a) (b)

Figure 3.1.11: (Left) Helmholtz coil for measuring the magnetic flux of the permanent magnets. (Right) Results of the block measurements for the prototype Qf (blue) and Qd magnet (green).

permanent magnets. This can be ensured in two different ways: either by matching permanent magnets or by using shunts.

The permanent magnet blocks were measured using a Helmholtz-coil at Brookhaven National Lab. The setup is located in a temperature controlled environment ($\Delta T < 0.2K$). The permanent magnets were left in the temperature controlled environment for more than 12h before the measurement to ensure little or no temperature difference.

The Helmholtz-coil measures subsequently the flux through all six surfaces of each permanent magnet, which can then be used to calculate the remanent magnetic field and its orientation. Figure 3.1.11b shows the distribution of $B_r$ for the permanent magnets of Qf and Qd. The figure shows that the variation in $B_r$ is much smaller than anticipated (about $\pm 0.5\%$ for Qd and about $\pm 1.0\%$ for Qf). All permanent magnets in general have a smaller $B_r$ than anticipated ($-3.6$ and $-4.4\%$). Figure 3.1.12a and Fig. 3.1.12b show the angle of the magnetization of the blocks with respect to the intended magnetization direction (z-axis).

Using a simple algorithm it was possible to match different permanent magnets so that the same amount of flux is delivered to each pole. The deviation between the poles from the measured data is expected to be smaller than $< 1 \times 10^{-5}$.

It is also possible to compensate different strengths of the individual poles of the quadrupole by using shunts, similar to the concept for compensating crosstalk and temperature variation. Geometric variations of the permanent magnets are less crucial. Thickness variations (which are not likely) can be compensated for with shims of soft iron. Length and height variations do not play a role.

### Iron Specification

For the iron yoke of the CBETA magnets initially high purity iron was specified due to its superior performance. Two products are considered, which are Extra Ferrite Electric (EFE)

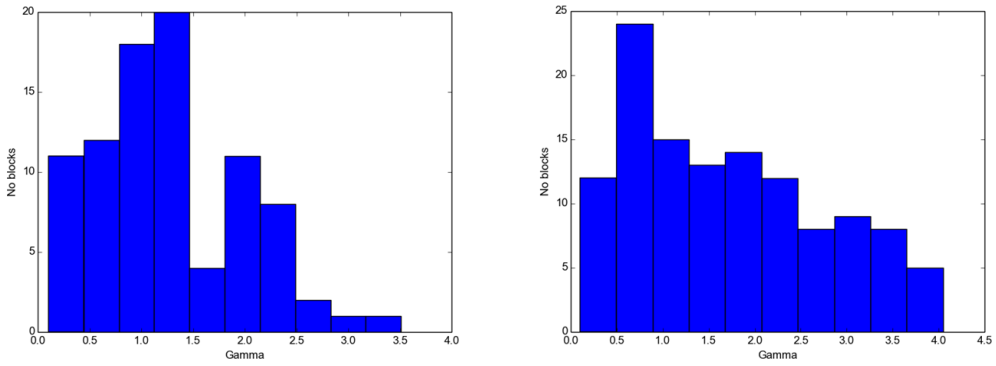


(a) (b)

Figure 3.1.12: Angle between the magnetization direction and intended magnetization direction for Qf (Left) and Qd (right) permanent magnets.

from JFE and ARMCO Pure Iron. The magnetization curves are shown in Fig. 3.1.13a.

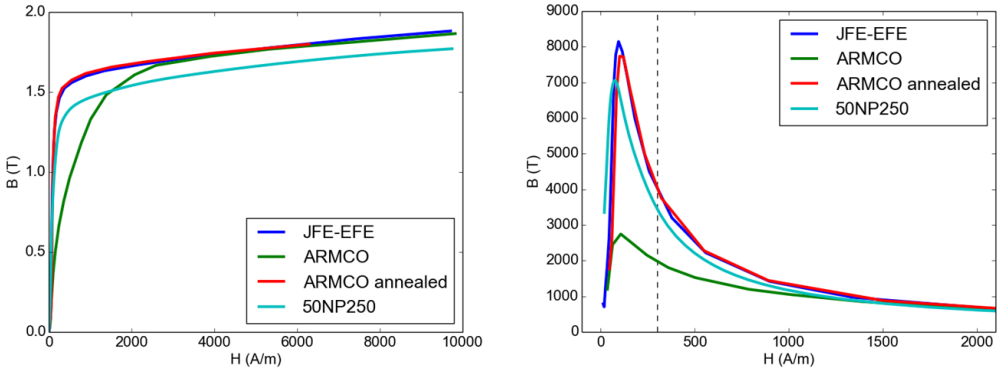


(a) (b)

Figure 3.1.13: Magnetization curves of soft irons (left) and relative permeabilities (right).

Recently a large quantity of JFE-EFE was purchased for a magnetic shielding application; in several magnetic tests it was confirmed that the material performs according to spec. Magnetic measurements are available for the material as delivered, machined and machined plus subsequent annealing. ARMCO iron as shown in the figure performs equally well and material data is available from the manufacturer.

For comparison reasons 3% SiFe was considered as well for the yoke, which is labeled in the figure as 50NP250. In 3D simulations it was found that the magnets delivered a slightly smaller gradient by 0.2%, which is likely caused by partial saturation in the back yoke. If the material is chosen, it is expected that the back yoke thickness can be increased by a small amount to bring both quadrupoles back to nominal strength.

### Status of Prototype

The yoke parts were manufactured from ARMCO iron; the pole consists of 2 mm thick laminations, whereas the back yoke consists of solid material. For cost reasons the laminations were cut to the desired shape using a wire eroder. Permanent magnets have been ordered from two different manufacturers. The first manufacturer is a company very well acquainted with the requirements of particle accelerators and light sources. The delivered permanent magnets will be measured by the company using a Helmholtz coil setup.

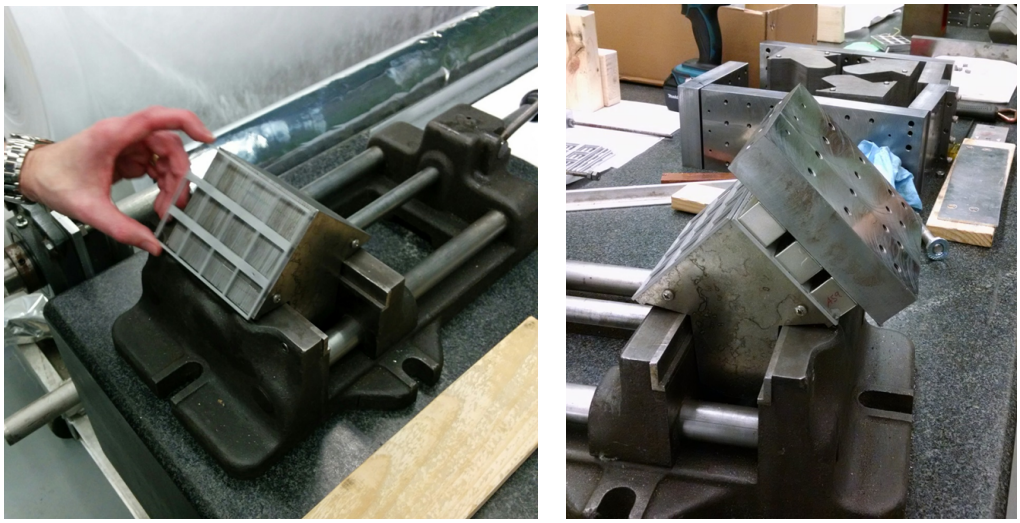

(a) (b)

Figure 3.1.14: (Left) Grid which is used to assemble the permanent magnets on the iron pole. Assembly of a single section of the Qd magnet (right).

The second manufacturer is a Chinese based company, which is substantially cheaper. These permanent magnets were measured using a Helmholtz coil at BNL. The permanent magnets were matched to deliver the same amount of flux to each pole (within the accuracy of the Helmholtz coil). These permanent magnets were used for the demonstrator magnets.

The magnets were assembled using a grid concept, which was developed and tested at BNL. Figure 3.1.14a shows a 2 mm thick plastic spacer, which is attached to the pole. The grid facilitates the positioning of the permanent magnets; the support from the grid and the holding force to the yoke (approximately equivalent to 20 kg) is sufficient to hold the permanent magnets in place. A fully assembled quarter section of the Qd magnet is shown in Fig. 3.1.14b, the fully assembled magnets in Fig. 3.1.15a and Fig. 3.1.15b.

The space in between the permanent magnets can be used for magnetic shunts for temperature and crosstalk compensation. As a suitable temperature controlled environment was not available initially, in first instance the magnets were assembled without the NiFe temperature compensation.

At the time of writing only the Qd magnet was measured using the BNL rotating coil setup

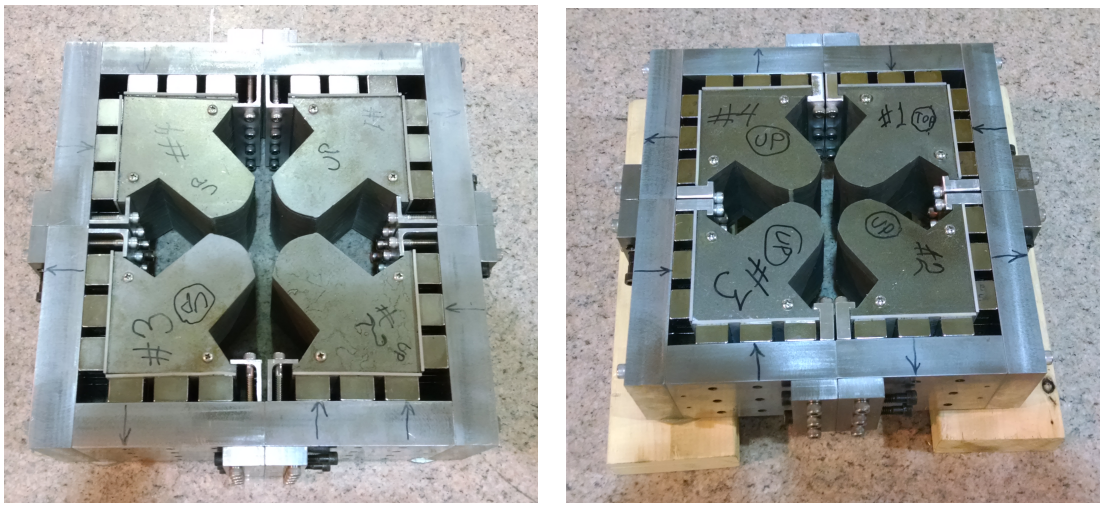

(a) (b)

Figure 3.1.15: Fully assembled Qd (left) and Qf magnet (right).

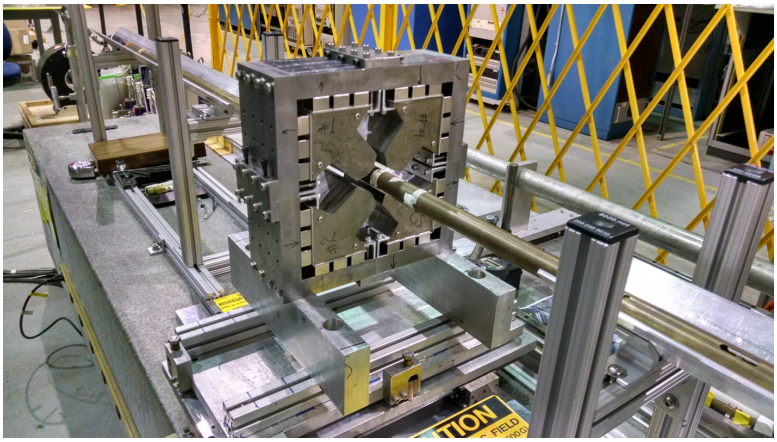

Figure 3.1.16: Qd magnet on the rotating coil test bench.

as shown in Fig. 3.1.16. The normal $B_{\mathrm{n}}$ and skew harmonics $A_{\mathrm{n}}$ as defined by

$$B = B_y + iB_x = \sum_{n=1}^{\infty} [B_n + iA_n] \left( \frac{z}{R_{\mathrm{ref}}} \right)^{n-1} \tag{3.1.1}$$

are shown in Tab. 3.1.1. The values in the tables are normalized to 10000 units of the quadrupole component. The measured gradient strength is 27.6 T/m (clear bore 23 mm), which is about 0.5% less than predicted by computer simulations.

Table 3.1.1: Normalized harmonics (normal and skew) of Qd, $\mathrm{R_{ref}} = 10$ mm

| | | | |
|---|---|---|---|
| b'1 | 0 | a'1 | 0 |
| b'2 | 10000 | a'2 | 0 |
| b'3 | 3.92 | a'3 | 13.65 |
| b'4 | 7.962 | a'4 | -0.699 |
| b'5 | 0.214 | a'5 | -1.288 |
| b'6 | -2.551 | a'6 | -0.145 |
| b'7 | -0.002 | a'7 | -0.029 |
| b'8 | -0.042 | a'8 | 0.007 |
| b'9 | -0.005 | a'9 | 0.008 |
| b'10 | 0.012 | a'10 | 0.001 |
| b'11 | 0 | a'11 | 0 |
| b'12 | 0 | a'12 | 0 |
| b'13 | -0.001 | a'13 | 0 |
| b'14 | 0 | a'14 | 0 |
| b'15 | 0 | a'15 | 0 |

As shown in the tables, a small sextupole and octupole component is present (four and eight units respectively). These harmonics are not expected from the simulation; after investigation it was found that the poles are not perfectly aligned. The horizontal spacing of the upper two poles is about 0.4 mm larger than the spacing of the lower two poles. Simulations confirmed that this can qualitatively and quantitatively explain the sextupole and octupole component. It was also found that this discrepancy changes from the front to the back of the magnet, which could explain the skew sextupole component. After re-alignment the magnet will be remeasured.

The Qf magnet is expected to be measured shortly; further tests include the temperature compensation and a Hall probe measurement of the completely assembled cell to study the crosstalk effect. All measurements will be compared with the expected results from finite element simulations.

### 3.1.7 Corrector Magnets for the Iron Dominated Magnets

#### Conclusions on the Electromagnetic Design of the Correctors of the Iron Dominated Magnets

The electromagnetic study on the design of the corrector magnets for the iron dominated magnets provides information to assist in the fabrication of normal, and skew dipole correctors

and the normal quadrupole correctors. The goal of the study is to design correctors with the required integrated field strength and with field uniformity of $10^{-3}$ in the transverse direction and in the range $\pm 3$ cm. The conductors of the corrector coil will be air cooled and should have a cross sectional area of 15 mm$^2$ to allow a maximum current density of 100 A/cm$^2$ which will be provided by inexpensive 15 A power supplies. This study is a guide to choose the number of conductors at a given location of the corrector coil which will satisfy the field requirements of the correctors. An additional electromagnetic study on the correctors is also required to obtain information on the cross talk of each corrector with the upstream and downstream magnets.

### Introduction

In this subsection we present results on the correctors of the iron dominated permanent magnets. The correctors for the Halbach type permanent magnets are discussed in the following section under the title "Halbach-type Design". The function of the correctors is threefold, first to correct the dipole or quadrupole field of the main magnet to agree with the design values, second to compensate for magnetic field variations which are caused by temperature variation at the location of the magnet, and third to be used as a beam orbit and betatron tune corrector. In the following subsections we present results from 2D and 3D calculations for the following correctors: a) Normal dipole corrector, b) Skew dipole corrector and c) Normal quadrupole corrector. Each subsection will provide results of the field homogeneity of each corrector from the 2D design. The 3D design will provide information on the integrated strength of the main corrector and its multipoles. Beam optics calculations dictate that a maximum field strength of $\pm 50$ Gauss is required for the normal and skew dipole correctors and $\pm 0.5$ T/m for the quadrupole correctors. Although water cooled conductors provide larger range of correction strength at a reduced copper cross section this design is based on air cooled conductors therefore the current density in the copper conductors should not exceed 100 A/cm$^2$.

### The Skew Dipole Corrector

The skew dipole corrector will provide vertical beam deflection for vertical orbit correction. Figure 3.1.17 is a cross section of the magnet showing the iron material in blue and the coil in red. The permanent magnet material is excluded from the calculations since the purpose of this study is to evaluate and optimize the correctors. The inclusion of the permanent magnets in the calculations will generate a field which will linearly superimpose to that of the corrector's field. This superposition has been proven experimentally [7]. The left picture in Fig. 3.1.17 is the cross section of the whole magnet, and in the right is an expanded view of the center of the magnet to make the details of the coil more visible. The green traces in the pictures are the vector equipotential lines. The 2D design provides a fast way to calculate the current densities in each conductor which will generate a rather uniform field distribution. The 3D design provides the integrated strength of the corrector and that of the multipoles generated by the correctors.

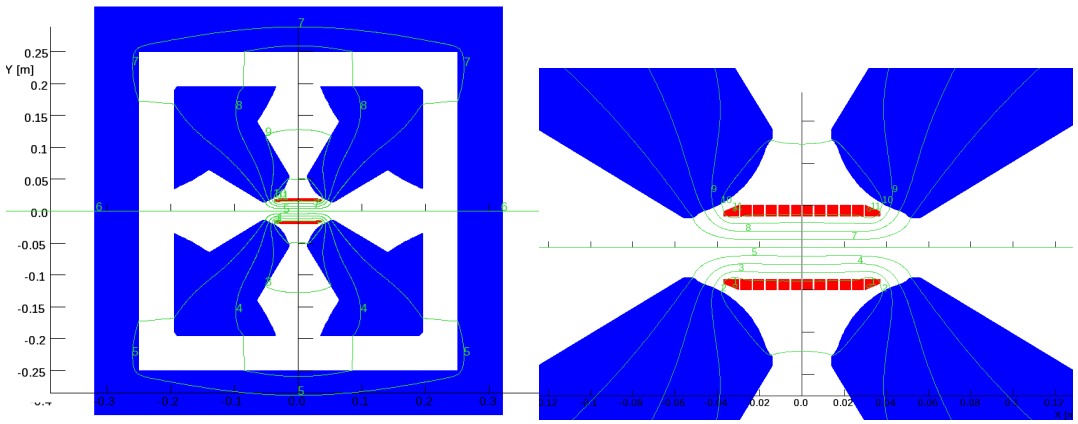


(a) (b)

Figure 3.1.17: (Left) Cross section of the iron dominated magnet with the Skew-Dipole-coils shown in red. (Right) Same cross section on a different scale to make the conductors (red rectangles) more visible. The green lines are the vector equipotential lines.

### The 2D Design of the Skew Dipole Corrector

The current carrying conductors above the median plane in Fig. 3.1.17 carry a current density of 100 A/cm$^2$ in the same direction, and all the conductors below the median plane carry the same current density but in the opposite direction. The left graph in Fig. 3.1.18 plots the $B_x$ component vs x at y=0 for two different cases the non-optimized case (black trace) where the conductors carry a current of 100 A/cm$^2$, and the optimized one where the four outermost conductors carry a current density of 350 A/cm$^2$. The right picture in Fig. 3.1.18 plots the homogeneity of the $B_x$ component vs x at y=0. Although the homogeneity can further be improved, what is clear from the plots in Fig. 3.1.18 is that improvement of homogeneity requires a larger number of conductors at specified locations of the coil to maintain the current density below the value of 100 A/cm$^2$. Note that the optimized corrector provides of skew dipole field of 50 Gauss.

### The 3D Design of the Skew Dipole Corrector

The 3D design provides information on the integrated multipoles including the fringe fields. It also provides a rather realistic position of the conductors of the coil as shown by the isometric view of the corrector in Fig. 3.1.19. Table 3.1.2 provides the integrated multipoles for non-optimized and optimized coil correctors. The numerical values of the current density in the conductors of the non-optimized coil corrector is 100 A/cm$^2$, and for the optimized correctors is also 100 A/cm$^2$ except for the four outmost conductors of the coil which is 450 A/cm$^2$ and the four adjacent conductors whose current density is set to 0 A/cm$^2$. Figure 3.1.20 shows the homogeneity if the $B_x$ component of the field as a function of x. On Fig. 3.1.20 we superimpose the x-y plane cross-section of the magnet to show the current densities of the conductors. Further optimization is possible by modifying the number of conductors

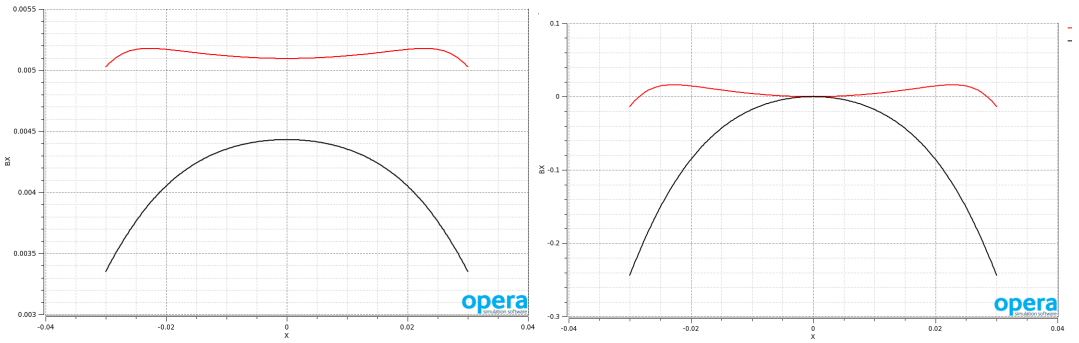


(a) (b)

Figure 3.1.18: (Left) The $B_x$ component of the field at y=0 for non optimized (black trace) and optimized coil (red trace). (Right) Same as the left picture but plotted is the homogeneity of $B_x$ vs x. The Vertical scales are in Tesla and the horizontal in meters.

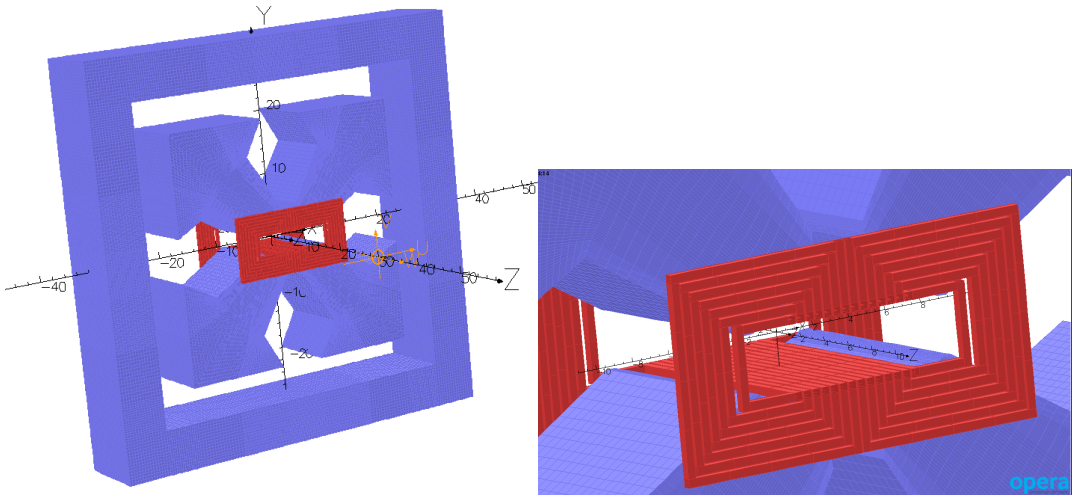


(a) (b)

Figure 3.1.19: (Left) Isometric view of the magnet with the coil of the skew dipole corrector. (Right) Same as the left picture but expanded view at the center of the magnet.

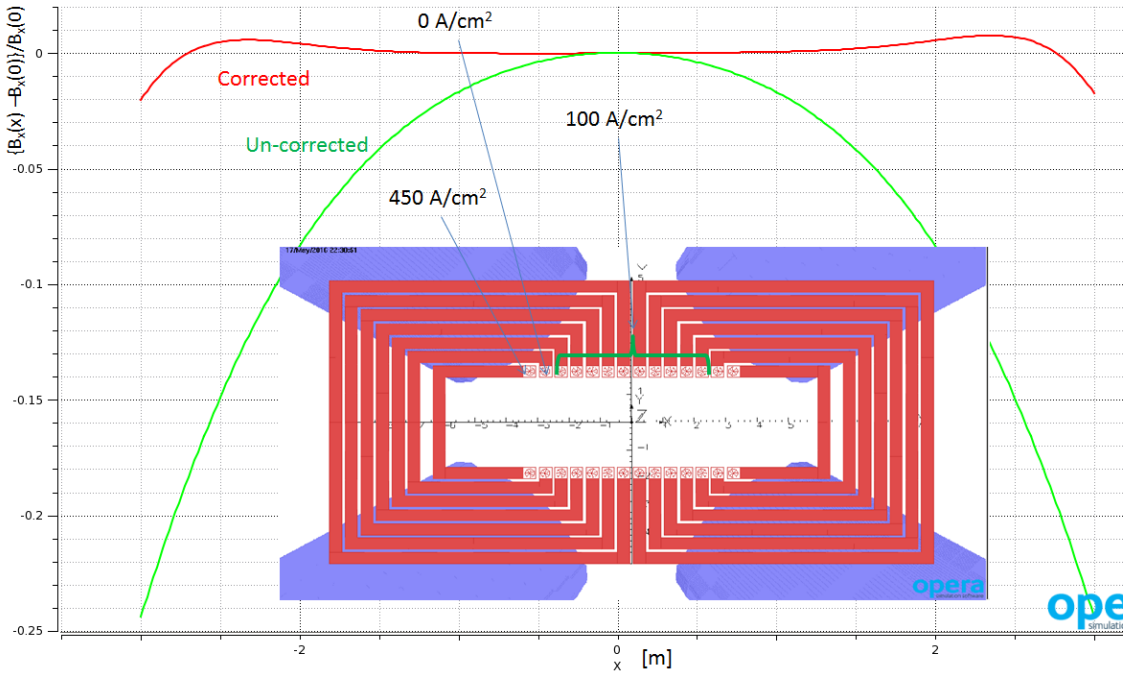


Figure 3.1.20: The green curve is the homogeneity of the $B_x$ component as function of x for the non-optimized coil, and the red curve for the optimized coil. Note that for the optimized coil, the current densities of the four outermost conductors is 450 A/cm$^2$, and the four adjacent conductors whose current density is set to 0 A/cm$^2$.

Table 3.1.2: The integrated multipoles at R=1 cm generated by the skew dipole corrector for the non-optimized ($2^{nd}$ column) and the optimized coil ($3^{rd}$ column). The iron of the magnet is 12 cm long.

| integr. multipole | Non-Optim-coil | Optimized-coil |
|---|---|---|
| Dipole [Gauss.cm] | 536.36 | 589.91 |
| Quadrupole [Gauss] | -0.04 | 0.12 |
| Sextupole [Gauss.cm$^{-1}$] | -7.52 | -0.71 |
| Octupole [Gauss.cm$^{-2}$] | -0.00 | 0.01 |
| Decapole [Gauss.cm$^{-3}$] | -0.63 | -0.07 |
| Duodecapole [Gauss.cm$^{-4}$] | -0.00 | -0.00 |

at specific coil locations. An additional study on the field generated by the corrector is also planned to include the magnets upstream and downstream of the magnet with the corrector.

### The Normal Dipole Corrector

The normal dipole corrector will provide horizontal beam deflection for horizontal orbit correction. Figure 3.1.21 is a cross section of the magnet showing the iron material in blue and the coil in red. The current in each of the conductors varies as the cos($\theta$), where $\theta$ is the azimuthal angle of the conductor's center. The permanent magnet material is excluded from the calculations since the purpose of this study is to evaluate and optimize the correctors. The inclusion of the permanent magnets in the calculations will generate a field which will be superimposed to that of the corrector's field. This has been proven experimentally by [7]. The left picture in Fig. 3.1.21 is the cross section of the whole magnet, and in the right picture is an expanded view of the center of the magnet to make the details of the coil more visible. The green traces in the left picture are the vector equipotential lines.

### The 2D Design of the Normal Dipole Corrector

The current density of the conductors in the first and fourth quadrant in Fig. 3.1.21 has the same direction and the conductors in the second and third quadrant have opposite direction. The left graph in Fig. 3.1.22 plots the homogeneity of the $B_y$ component vs x at y=0 for two different cases the non-optimized case (black trace) where the conductors carry a current proportional to the cos($\theta$), and the optimized case where the four outermost conductors carry a current of 71 [A]. The right picture in Fig. 3.1.22 plots the value of the $B_y$ component vs x at y=0 for the optimized coil. Although the homogeneity can further be improved, what is clear from the plots in Fig. 3.1.22 is that improvement of homogeneity requires a larger number of conductors at specified locations of the coil to maintain the current density below the value of 100 A/cm$^2$. Note that the optimized corrector provides a normal dipole field of 38 Gauss.

### The 3D Design of the Normal Dipole Corrector

The 3D design provides information on the integrated multipoles including the fringe fields. It also provides a rather realistic position of the conductors of the coil as shown by the isometric

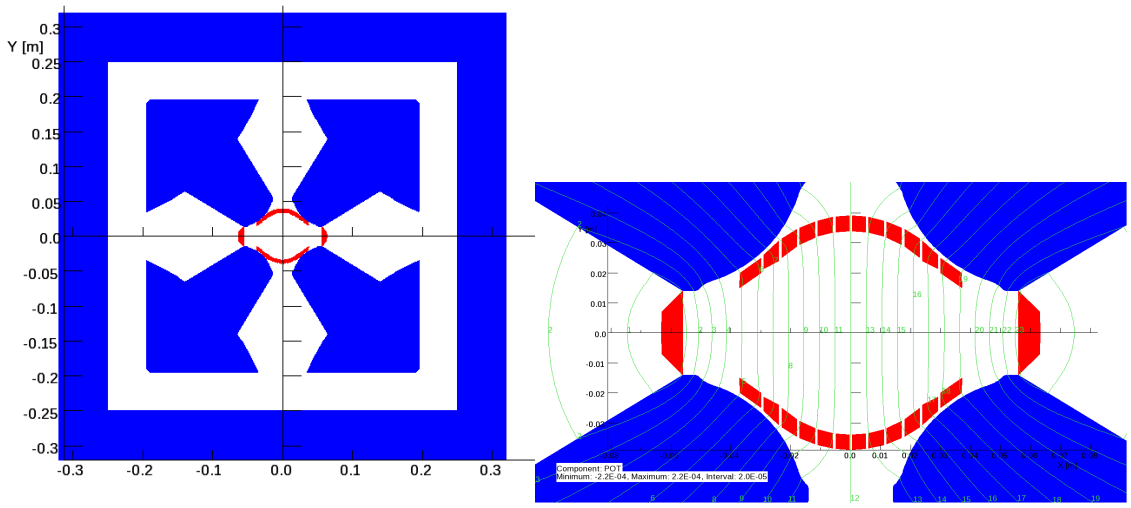


(a) (b)

Figure 3.1.21: (Left) Cross section of the iron dominated magnet with the Normal-Dipole-coils shown in red. (Right) Same cross section on a different scale to make the conductors (red rectangles) more visible. The green lines are the vector equipotential lines.

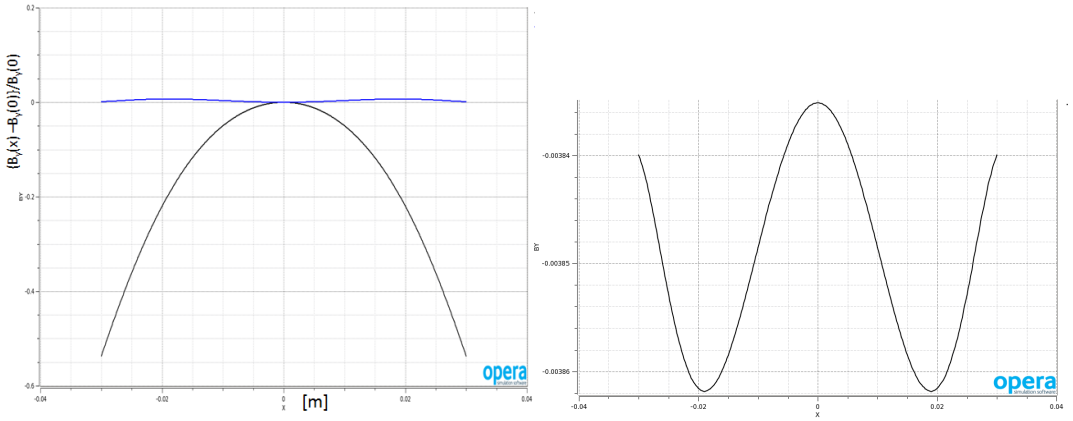


(a) (b)

Figure 3.1.22: (Left) The homogeneity of $B_y$ component of the field vs. x in m at y=0 for non optimized (black trace) and optimized coil (blue trace). (Right) The $B_y$ component of the field in Tesla vs. x for the optimized coil.

view in Fig. 3.1.23 Figure 3.1.24 plots the $B_y$ component of the field in Gauss at z=0 and y=0

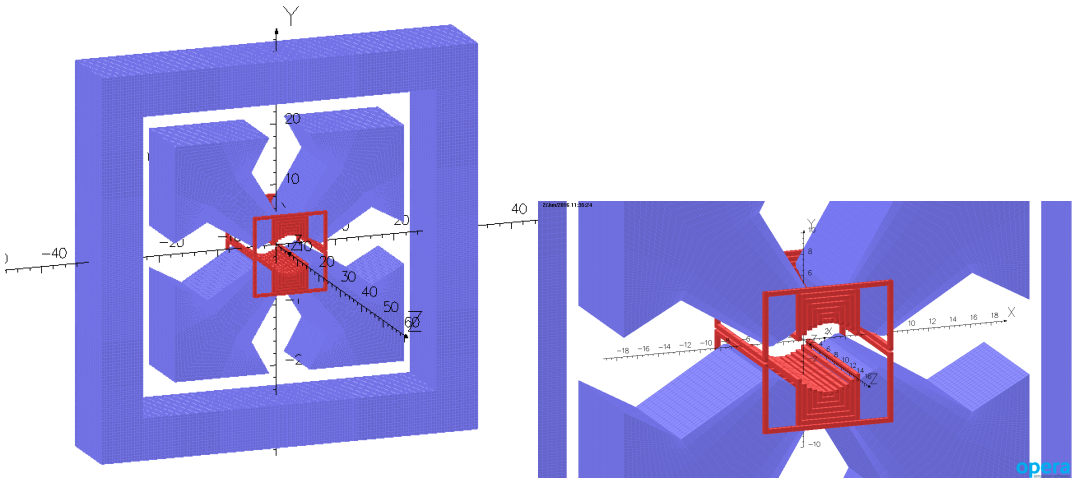

(a) (b)

Figure 3.1.23: (Left) Isometric view of the magnet with the coil of the normal dipole corrector. (Right) Same as the left picture but expanded view at the center of the magnet.

as a function of x in cm. The 22.5 Gauss strength of the corrector was generated by powering the outermost conductor with 270 A/cm$^2$ with the rest of the conductors to vary as cos($\theta$) but they are all below the value of 100 A/cm$^2$. To achieve the required strength of 50 Gauss more turns should be added in the coil. Table 3.1.3 provides the integrated multipoles for non-optimized and optimized coil correctors. The numerical values of the current density in the conductors of the non-optimized coil corrector is 100 A/cm$^2$, and for the optimized correctors is also 100 A/cm$^2$ except for the outermost conductor of the coil which is 270 A/cm$^2$. Further

Table 3.1.3: The integrated multipoles at R=1 cm generated by the normal dipole corrector for the optimized coil. The iron of the magnet is 12 cm long.

| integr. multipole | Optimized-coil |
|---|---|
| Dipole [Gauss.cm] | 347.26 |
| Quadrupole [Gauss] | 0.09 |
| Sextupole [Gauss.cm$^{-1}$] | 1.71 |
| Octupole [Gauss.cm$^{-2}$] | -0.00 |
| Decapole [Gauss.cm$^{-3}$] | -0.19 |
| Duodecapole [Gauss.cm$^{-4}$] | -0.00 |

optimization is possible by adding conductors at specified locations of the coil. An additional study on the field generated by the corrector is also planned to include the magnets upstream and downstream of the magnet with the corrector.

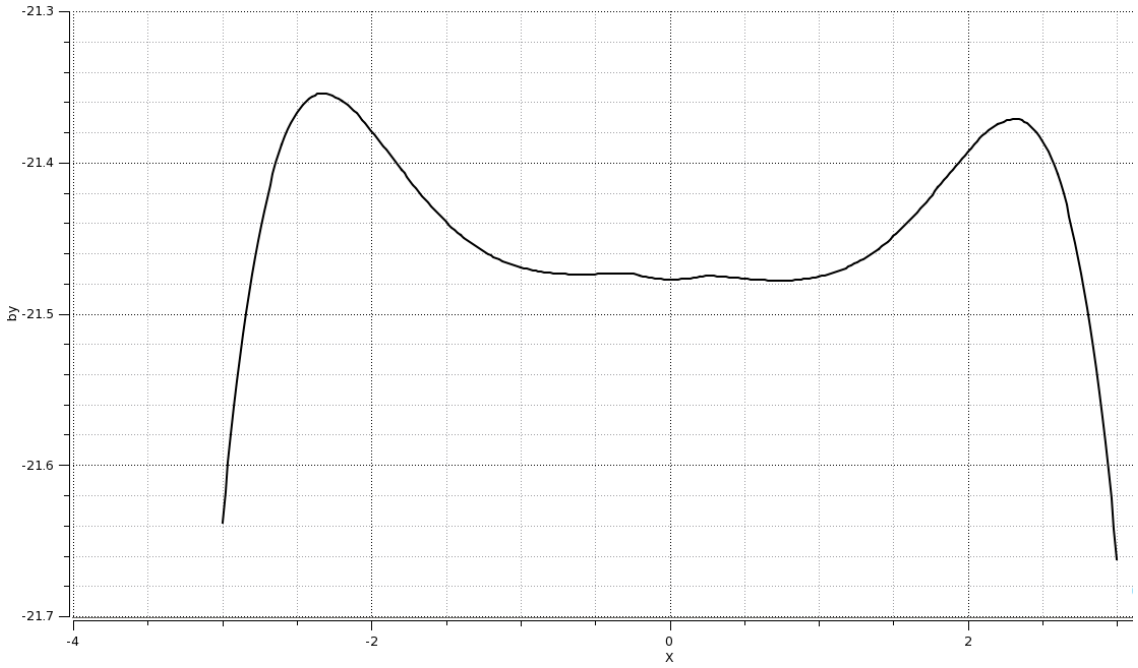


Figure 3.1.24: The $B_y$ component in Gauss at z=0 and y=0 as function of x in cm for the optimized coil. Note that for the optimized coil, the current densities of the outer most conductors is 270 A/cm$^2$, and the current density of the rest of the conductors vary as $\cos(\theta)$ but they are below the value of 100 A/cm$^2$. To achieve the required strength of 50 Gauss more turns should be added in the coil.

### The Normal Quadrupole Corrector

The normal quadrupole corrector will provide strength if needed to the focussing and/or defocusing quadrupole to attain the design strength. It will also provide additional strength for any betatron tune correction. There are two equivalent coil arrangements for the quadrupole corrector. Figure 3.1.25 shows the cross section of the magnet with the two possible coil arrangements of the normal quadrupole correctors. The left picture in Fig. 3.1.25 shows one possible coil (red areas) arrangement to generate the normal quadrupole corrector. The right picture shows an alternative coil arrangement, with the coils mounted on the return yoke, for the normal quadrupole corrector. The alternative coil arrangement removes the coil from the center of the magnet where the coils of the skew and dipole correctors should be placed. In addition by notching the return yoke the coil extend along the z-axis can be minimized and allow easier access in the drift space between the magnets. An isometric view of the two

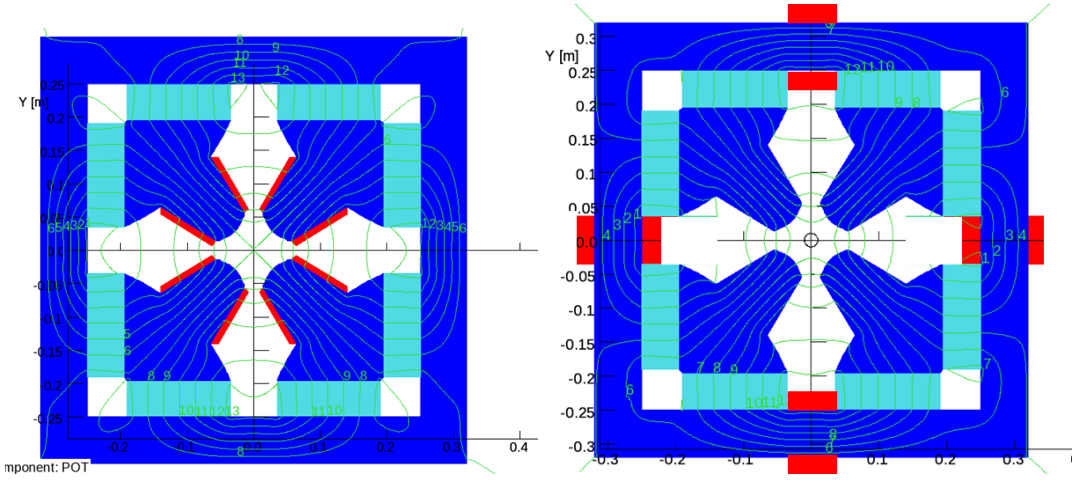


(a) (b)

Figure 3.1.25: (Left) Cross section of the magnet with the corrector coils on the poles . (Right) Cross section of the magnet with the corrector coils on the return yoke.

equivalent normal quadrupole correctors is shown in Fig. 3.1.26. The integrated multipoles for the two types of normal quadrupole correctors appears in Tab. 3.1.4. The integrated quadrupole strength of the corrector with the coils in the poles corresponds to a strength of $\pm 0.50$ T/m and that of coil in the yoke to $\pm 0.30$ T/m. In the later case more turns are needed to achieve the required strength of $\pm 0.50$ T/m.

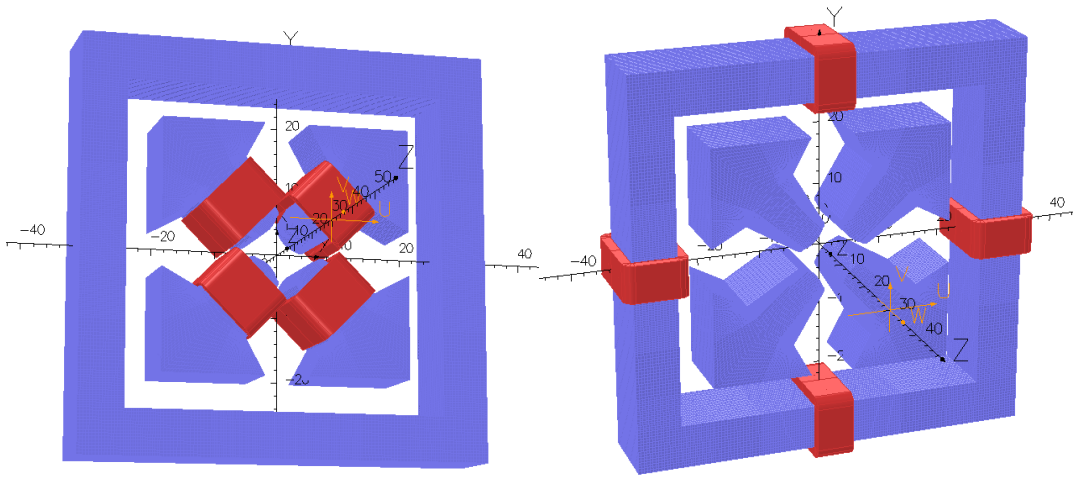

(a) (b)

Figure 3.1.26: (Left) Isometric view of the magnet with the corrector coils on the poles . (Right) Isometric view of the magnet with the corrector coils on the return yoke.

Table 3.1.4: The integrated multipoles at R=1 cm generated by the normal quadrupole corrector for the two different coil arrangements of the normal quadrupole corrector. The iron of the magnet is 12 cm long.

| integr. multipole | Coil in poles | Coil in ret. yoke |
|---|---|---|
| Dipole [Gauss.cm] | 0.00 | 0.00 |
| Quadrupole [Gauss] | 611.07 | 347.37 |
| Sextupole [Gauss.cm$^{-1}$] | 0.00 | 0.00 |
| Octupole [Gauss.cm$^{-2}$] | -0.00 | 0.00 |
| Decapole [Gauss.cm$^{-3}$] | 0.00 | 0.00 |
| Duodecapole [Gauss.cm$^{-4}$] | -0.03 | -0.01 |

## 3.2 Backup magnets: Halbach-type Design

An iron-free Halbach permanent magnet design was investigated for CBETA, which attains higher field strengths, allowing 250MeV top energy (61MeV linac energy gain). Halbach magnets are smaller in size than iron-yoked magnets and exhibit less cross-talk. This alternative design is described in the subsections below.

### 3.2.1 Comparison of Features vs. Iron Poled Magnets

A summary is provided in Tab. 3.2.1 to illustrate the technology differences between choosing a Halbach magnet design and an iron-dominated permanent magnet design in an accelerator. Permanent magnet materials all have a temperature dependence and this can be compensated in the magnet in various ways. The iron quadrupole uses a technique from the Fermilab recycler where the permanent magnet blocks sandwiched in the iron yoke are mixed with NiFe alloy whose magnetization contribution varies in the opposite way as magnetization of the blocks, to provide a temperature range of 20°C or more with virtually no field strength variation. In the Halbach magnets, the field and magnetization directions are not parallel, so this method does not work because the NiFe alloy would not provide compensating magnetization in the correct direction. Instead, the dipole and quadrupole correctors, which would be present in the design anyway, are used to compensate the field variation, which manifests as an overall reduction factor in field strength and is therefore linear as a function of position like the magnets themselves.

To compensate temperature changes, the correctors could be set either using data from the orbit position feedback, or a local field monitor. If the corrector coils themselves are water-cooled (as they are in the most recent design), it is possible to circulate a layer of water just outside the Halbach magnet blocks first, to stabilize their temperature to the extent that temperature compensation of any sort is no longer needed.

### 3.2.2 Halbach Magnet Design

The optimized FFAG cell required the QF magnet to be very close to a symmetrical quadrupole, i.e. with zero field at the center. To simplify matters, the bore location was adjusted slightly so that QF really was exactly symmetrical, so that its design is that of a conventional Halbach quadrupole. Cross-sections of the two magnets are shown in Fig. 3.2.1 below.

The BD magnet on the other hand contains a significant dipole component: in fact, all the beams go through the negative $B_y$ field region, which bends electrons clockwise in the L0E hall. The design of the BD magnet is also not a conventional Halbach arrangement: it requires a combination of dipole and quad, whereas conventional annular arrangements can only do one pure multipole at a time. It was considered to nest conventional dipole and quadrupole Halbach magnets but the outer magnet has to be quite large in that case. It was noticed that on one side of the nested magnet, the magnetizations were mostly cancelling anyway, so optimization was run on a design with only a single layer of permanent magnet wedges, but with variable thickness and different magnetization directions. This achieved a very accurate ($< 10^{-5}$ in the linear model) combined function integrated field as required, a result that

Table 3.2.1: Comparison of iron and Halbach-type magnets.

| | Iron Poles | Halbach |
|---|---|---|
| Field quality + tuning | Determined by iron pole shape. Adjustment would be via conventional pole shimming. | Determined by block magnetization vectors. Adjustment via floating shims/iron wires just inside aperture. |
| Field strength + tuning | Iron shunts to partially short-circuit flux applied to outside. Also block pre-measurement and sorting. EM quad corrector coils around poles. | Determined by block magnetization vectors. Tune with EM normal quad and dipole online correctors (see correctors' below). |
| Temperature sensitivity + compensation | 0.1%/K for NdFeB but can (at ∼20% strength penalty) incorporate NiFe material to passively compensate. | 0.1%/K for NdFeB, cancelled by using EM normal quad and dipole online correctors. |
| Cross-talk in doublet + compensation | Few percent cross-talk, can be corrected with shunts. | Negligible cross talk, mu∼1 linear field superposition. |
| Correctors (online/EM) | Normal quadrupole can be coils would around each pole. Others require special coils put within the bore. | Window-frame outside Halbach magnet using field superposition, because Halbach is magnetically transparent. |

was replicated to high accuracy ($\sim 10^{-4}$) by OPERA-3D simulations. It also uses much less material than a nested design.

### Magnet Simulation and Codes

Two codes were used in the design and simulation of these Halbach magnets, which have shown good agreement as shown in this section. The simpler of the two is PM2D written by Stephen Brooks, which is a current sheet approximation of the fields from permanent magnet polygons in 2D. This provides an accurate model of the "average" field (integrated field divided by permanent magnet piece length) through the magnet, provided two conditions hold:

- The materials stay in the linear part of their B-H curve. In fact, if this is violated, the magnets will experience permanent demagnetization, so any valid design ought to satisfy this condition. PM2D can also evaluate the demagnetizing flux from the other blocks at any point to ensure it does not go beyond the coercive force ($H_{cj}$) of the material.

- $\mu_r = 1$ for all materials. This is almost true of NdFeB, which has a $\mu_r$ of about 1.025.


(a) (b)

Figure 3.2.1: (Left) BD magnet. (Right) QF magnet. Orange graph is vertical field component $B_y$ on the y=0 axis, with varying x position. The green segment is the field within the region required by the beams, which is supposed to be linear. Magnetization axis is shown by blue arrows in each block.

PM2D was used for the initial optimization of the wedge sizes in the BD magnet, which tried to reduce the error multipoles to zero by changing their thickness and magnetization direction independently keeping the required symmetry in the y=0 midplane. This requires many iterations of the design to be simulated, so a faster code is preferred during this design stage, before coordinates of the wedge corners are generated as input for the 3D magnet simulation.

The second code used, by Nick Tsoupas for 3D simulations, is OPERA-3D, which is industry standard. Very good agreement was attained between the two codes (on integrated field multipoles) when the materials were not in the demagnetizing regime. Once the design was set, OPERA-3D was always used to do the final simulation and 3D field map generation.

Running in OPERA-3D required that a specific material grade and B-H curve was chosen for the permanent magnet blocks. These grades and curves vary by manufacturer, so a grade from AllStar Magnetics was selected, which is the manufacturer for blocks for the CBETA prototype magnets currently under order and shipping at the end of March 2016. The grade N35SH was selected, which combines a medium strength of 35 MGauss.Oe (the maximum available being ~52 MGauss.Oe) with a good resistance to external demagnetizing fields. This is what the "SH" suffix means: a strong resistance to heat, which stems from its high $H_{cj}$ demagnetizing field value (2.24 T) at room temperature. The strength translates into a residual field $B_r$ of 1.207 T.

After OPERA-3D models were run, a best fit with the magnetization "$B_r$" value used in PM2D, which assumes $\mu_r = 1$, was found (1.1939 T), which represents the average magnetization from the material including the small reduction from regions of reverse flux with $\mu_r$ being

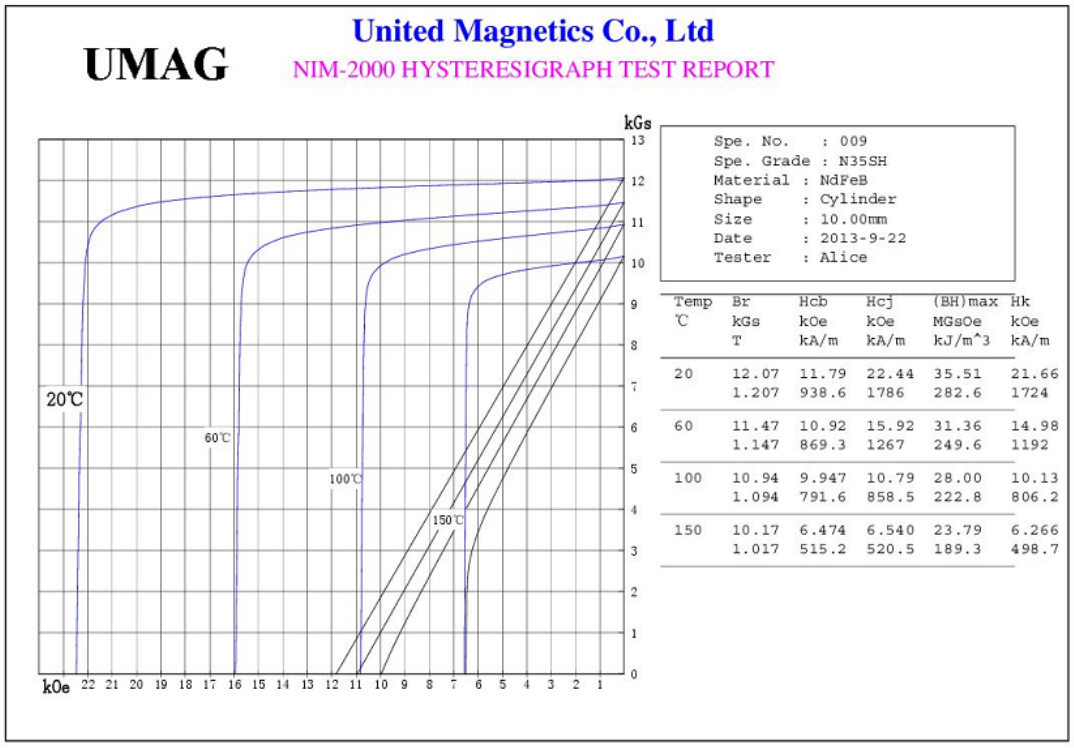


Figure 3.2.2: B-H curve of the AllStar Magnetics N35SH NdFeB permanent material, at various temperatures.

slightly larger than 1. This lies between $B_r$ and $H_{cb}$ of the material as expected. With this value, the PM2D designs could be loaded directly into OPERA-3D (with the N35SH material) and the strength would be correct, with no further design modifications required.

### 3.2.3 Tracking and Compatibility with FFAG Lattice

Once OPERA-3D field maps have been generated, they can be loaded back in to the Muon1 [8] tracking code, which is the same code used for the original lattice optimization done with field models rather than field maps.

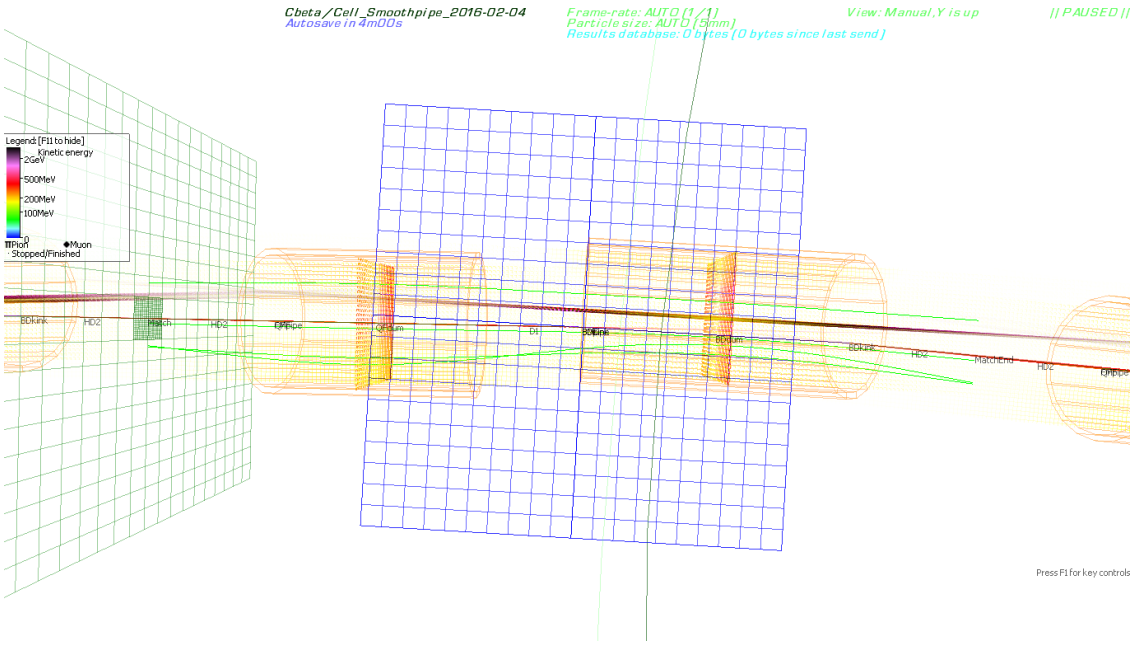


Figure 3.2.3: Matched orbits (green) for the four CBETA energies through an FFAG arc cell made with OPERA-3D field maps generated from Halbach magnets. The orange cylinders represent the approximate apertures of the vacuum pipe and the grids are 1cm per square.

Figure 3.2.3 above shows such a simulation, where Muon1 has found "closed orbits" for each energy, which exit the cell at the same position and angle that they enter. The closed orbits found through field maps will be slightly different than those found for the original field model in the lattice-design optimization, but as shown in the Fig. 3.2.4 and Tab. 3.2.2 below, the discrepancy is not very large (<1mm).

This good agreement is partly due to a fortunate choice of fringe field length in Muon1's soft-edged Maxwellian field model. Muon1 models the fall-off of multipole components near the entrance of exit of a magnet as proportional to $\frac{1}{2} + \frac{1}{2}\tanh(z/f)$ where $z$ is the longitudinal position relative to the magnet end and f is a "fringe length" parameter ($f$). It was chosen to be 2.5cm here, roughly the same order of size as the magnet apertures. Detailed studies suggested the best agreement with these field maps is obtained with $f = 2.7$cm. For these short magnets in CBETA, the fringe field makes up a large part of the field so it is important to

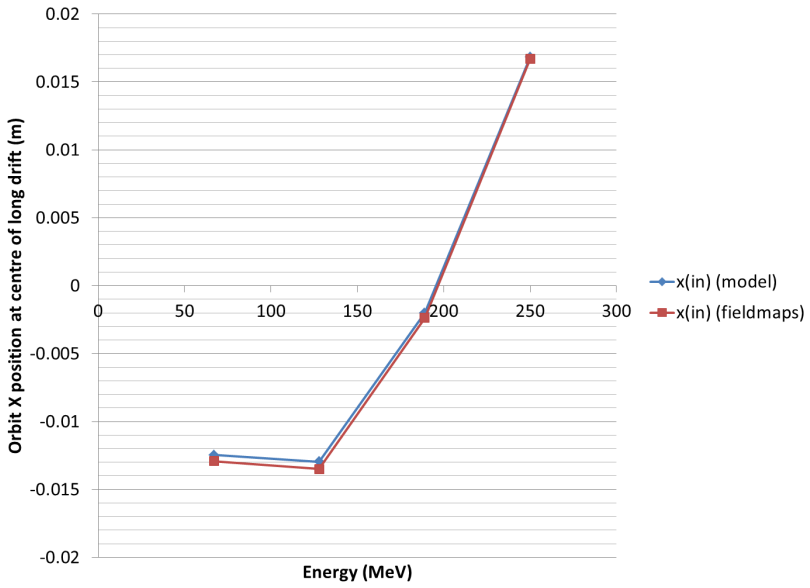


Figure 3.2.4: Transverse position (X, in meters) of the four closed orbits, as a function of energy, at the midpoint of the long drift in the CBETA FFAG arc cell. Blue dots are from a Muon1 simulation using field models and red dots from a Muon1 simulation using OPERA-3D field maps.

include it consistently (some hard-edged models do not have good agreement with the optics).

The closed orbit matching process also determines the shape of the beam (optical alpha and beta functions) that will be preserved on traversing once through the cell. This also allows the single-cell tunes in the X and Y planes to be calculated. A similar comparison of tunes from the field map versus the original optimizer's field model is shown in Fig. 3.2.5 and Tab. 3.2.3 below.

The cell tunes are important because they determine the limits on the stability of the beam (0 and 0.5 being the unstable limits) and its response to errors, the tune determining the frequency of error oscillations. The largest discrepancy between field map and model field is found in the low-energy (67MeV) beam, where the model predicts 0.3833 and the field maps

Table 3.2.2: Transverse position (X, in meters) of the four closed orbits, calculated with Muon1 soft-edged field models or OPERA-3D field maps, at the midpoint of the long drift in the CBETA FFAG arc cell.

| Energy (MeV) | $x$ (m) (model) | $x$ (m) (field maps) |
|---|---|---|
| 250 | 0.016825 | 0.01668 |
| 189 | -0.00201 | -0.00237 |
| 128 | -0.01296 | -0.01349 |
| 67 | -0.01246 | -0.01292 |

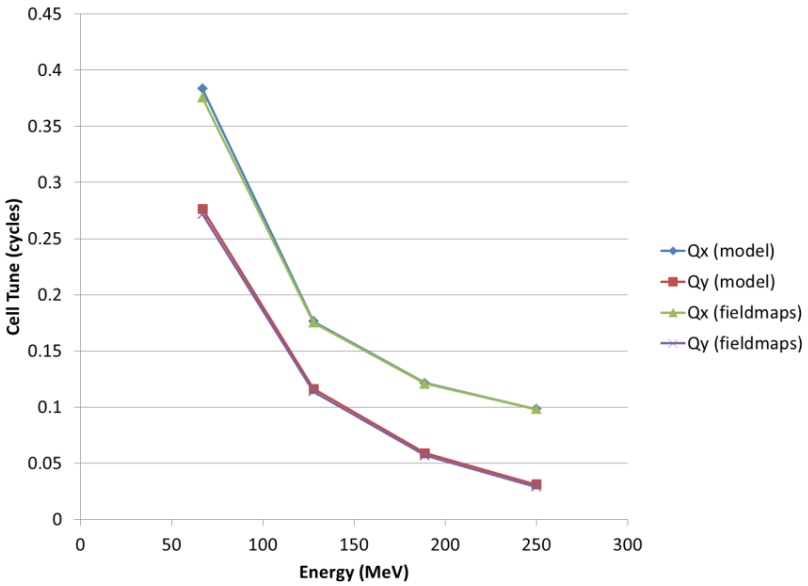


Figure 3.2.5: Comparison of the calculated X and Y tunes of the FFAG cell using Muon1's model field and OPERA-3D field maps as a function of energy.

Table 3.2.3: Comparison of the calculated X and Y tunes of the FFAG cell using Muon1's model field and OPERA-3D field maps.

| Energy (MeV) | $Q_x$ (model) | $Q_y$ (model) | $Q_x$ (field maps) | $Q_y$ (field maps) |
|---|---|---|---|---|
| 250 | 0.098132 | 0.031006 | 0.098272 | 0.029062 |
| 189 | 0.121474 | 0.058797 | 0.120911 | 0.056874 |
| 128 | 0.176315 | 0.11615 | 0.175274 | 0.113949 |
| 67 | 0.383309 | 0.276579 | 0.375643 | 0.271753 |

predict 0.3756, a difference of 0.0077 cycles per cell. This is not a large enough difference to put the beam into a resonance or drastically affect the optical behavior of the machine.

### 3.2.4 Window-Frame Correctors

The property of the permanent magnets to be magnetically saturated allows superposition of the magnetic fields and therefore permanent magnets can accept electromagnets as corrector magnets with no distortion of the their magnetic field. Figure 3.2.6 is an isometric view of an OPERA model of a Halbach-type magnet surrounded by a window frame electromagnet acting as a corrector.

In this section we will present results from the 3D OPERA calculations which prove the following statements:

1. The window frame magnets in spite their large aperture and short length, do not excite significant transverse magnetic multipoles except the ones are designed to produce.

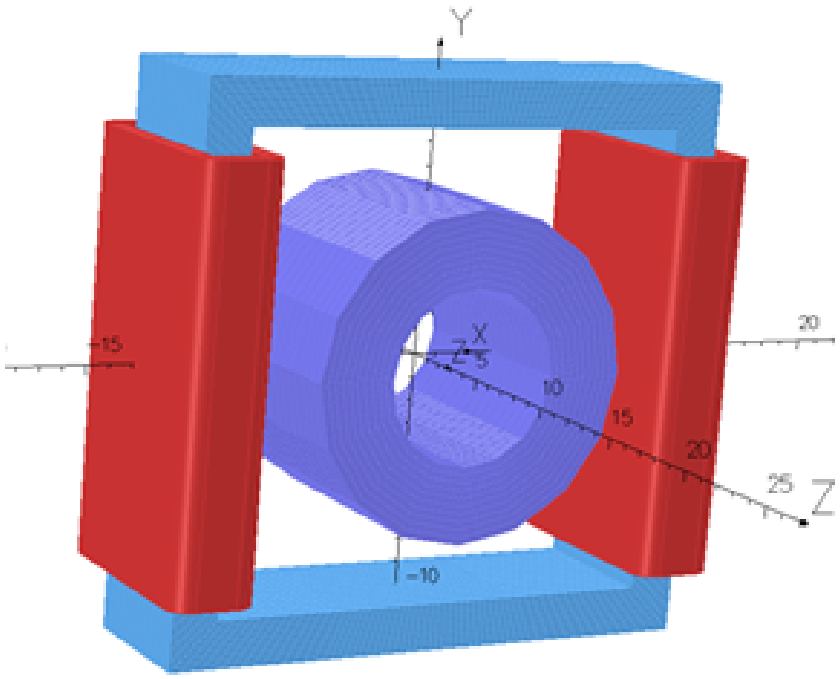


Figure 3.2.6: A window frame magnet with two coils generates a normal dipole field which is superimposed on the field of the permanent magnet.

2. An excited window frame magnet placed around a Halbach-type permanent magnet as in Fig. 3.2.6 does not alter significantly the multipoles of the Halbach-type magnet (measurements are under way) and there is an almost perfect superposition of the fields of the two magnets.

3. The Halbach-type magnets lend themselves easily to window-frame corrector magnets and do not interfere with possible access to the beam instrumentation which is placed in the short drift spaces between the magnets.

4. Four Halbach-type magnets were placed next to each other along their symmetry axis with the magnets touching each other and the integrated multipoles of all four magnets was measured to be equal to the sum of the of the integrated multipoles of each magnet measured separately. This measurement provides an almost perfect proof of field superposition. (Measurements have been made thus no results from calculations will be presented).

### The B_field of a Window-Frame Electromagnet

Figure 3.2.7 is a picture of 3D OPERA model window frame magnet to be used as corrector around a Halbach-magnet.

Figure 3.2.8 below is a projection on the x-y plane of the window frame magnet which shows that the maximum transverse directions of the corrector magnet surrounding a Halbach magnet is less than 30 cm.

Table 3.2.4 shows the integrated magnetic multipoles at R=1 cm of three different configurations of a quadrupole Halbach magnet and dipole window frame magnet. The 2nd row shows the integrated multipoles a dipole window frame magnet with no permanent magnet inside. Row 3 shows the integrated multipoles of a quadrupole Halbach-type magnet with no excitation of the dipole corrector and row 4 the multipoles of the dipoles window frame magnet excited, surrounding the quadrupole Halbach-type magnet. The permanent magnet material of the quadrupole magnet is NdFeB-N35 and the BH-curve for this material is shown in Fig. 3.2.9. The results from Tab. 3.2.4 show that the field of the window frame magnet is simply superimposed on the field of the quadrupole magnet.

Table 3.2.4: The integrated magnetic multipoles of the window frame magnet by itself (2nd row) of a quadrupole Halbach type magnet (3rd row), and of the window frame magnet surrounding the quadrupole Halbach-type magnet.

| Setup | Dipole [Gauss.cm] | Quad [Gauss] | Sext. [Gauss.cm$^{-1}$] | Oct. [Gauss.cm$^{-2}$] | Dec. [Gauss.cm$^{-3}$] | 12pole [Gauss.cm$^{-4}$] |
|---|---|---|---|---|---|---|
| WF only | 1931.14 | -0.0013 | 1.02 | 0.00003 | 0.014 | -0.000015 |
| PM only | 0.000003 | 27798.5 | 0.000003 | 0.00000002 | 0.000003 | 0.037 |
| WF+PM | 1933.7 | 27798.5 | 1.02 | 0.0123 | 0.017 | 0.016 |

The results of Tab. 3.2.4 corroborate the ideal superposition of the fields generated by a Halbach-type permanent magnet with the fields of the window-frame magnet. Experimental measurements to prove these results are under way.

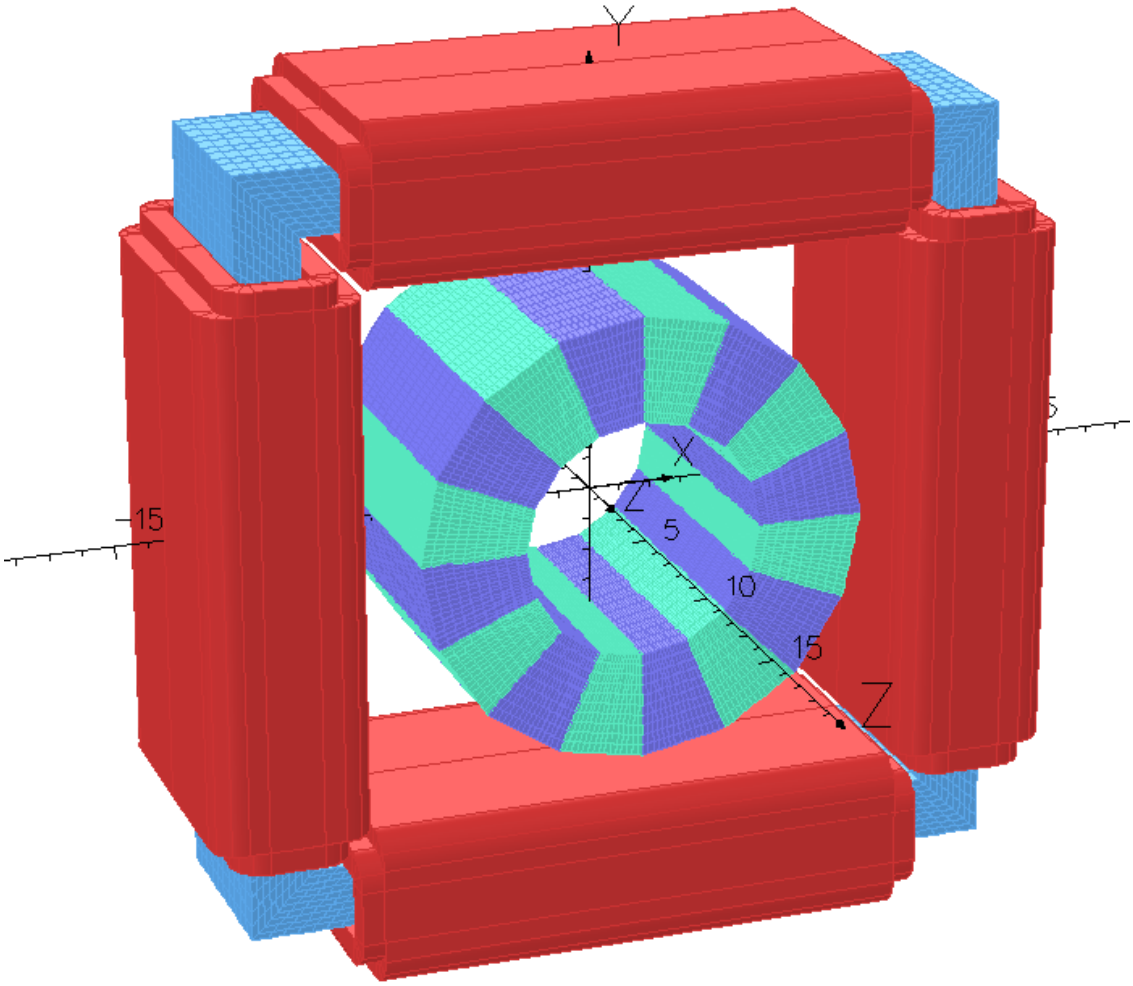


Figure 3.2.7: A window frame magnet with eight coils acting as normal and skew dipoles, and a normal quadrupole. By rotating the window frame by 45° we can generate a skew quadrupole instead of normal one.

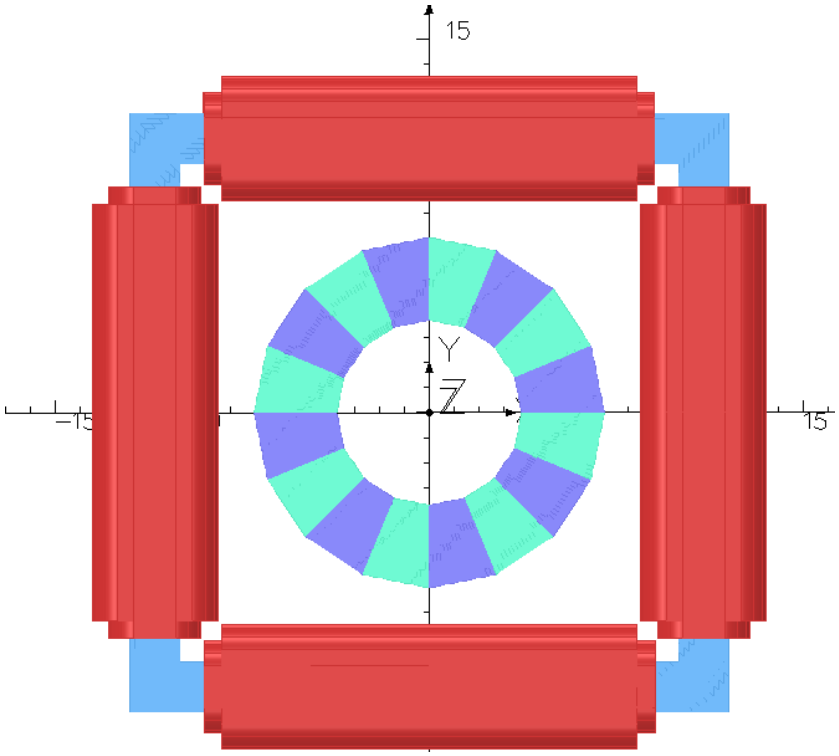


Figure 3.2.8: The projection of the window frame magnet on the x-y plane. The maximum transverse extend of the magnet is less than 30 cm.

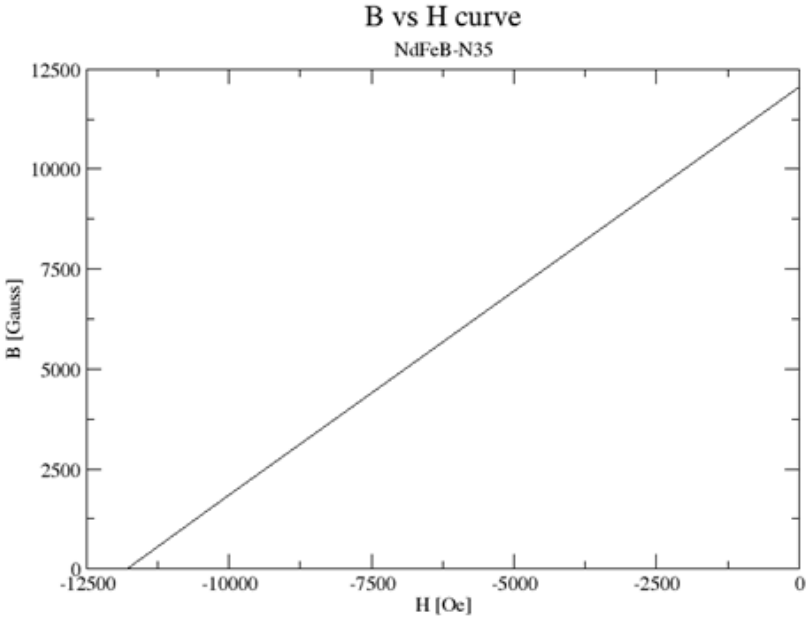


Figure 3.2.9: The BH curve of the NdFeB-N35 material.

Figure 3.2.10 is an isometric view of a few permanent magnets of the CBETA arc with correctors. This view shows that the window frame magnets do not extend into the drift space between the magnets. Figure 3.2.11 is the projection on the y-z plane of the six magnets showing in Fig. 3.2.10. The current through the coils of the window frame magnet can generate the required correction field for the permanent magnets.

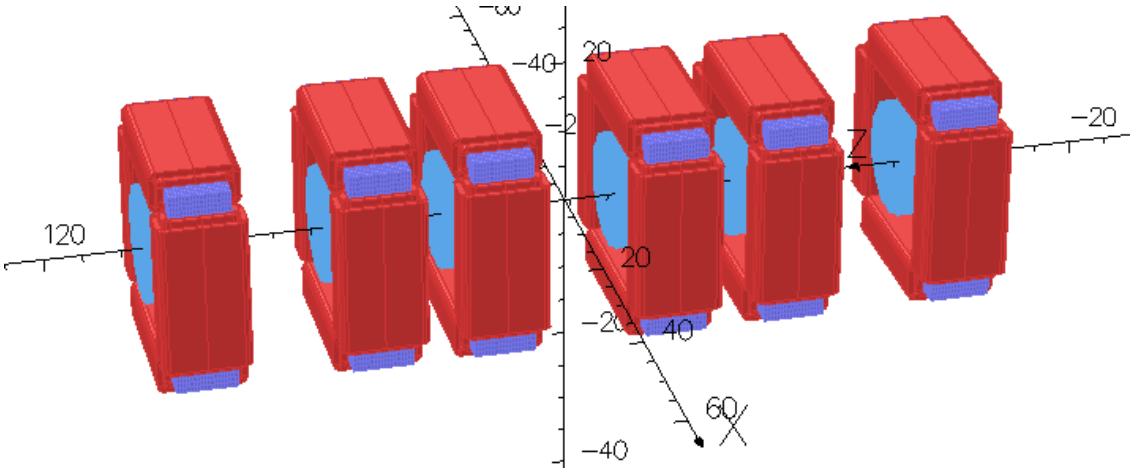


Figure 3.2.10: Isometric view of six of the permanent magnets of the CBETA arc.

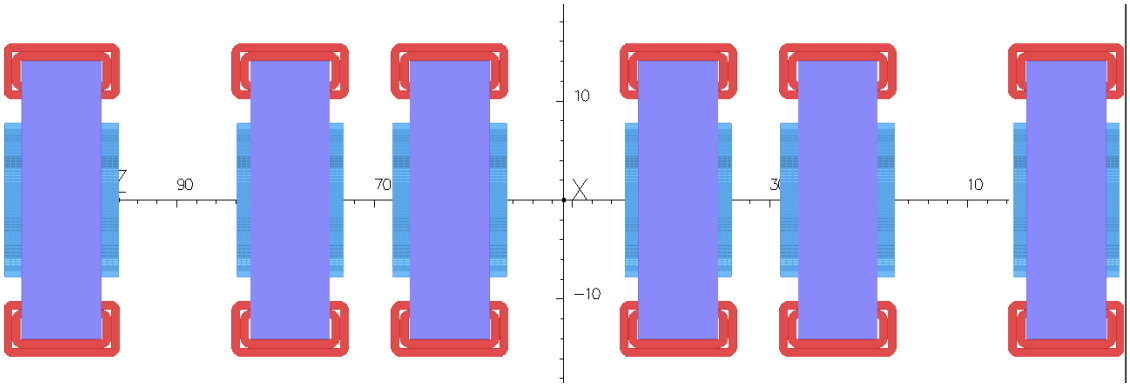


Figure 3.2.11: Projection on y-z plane of the six permanent magnets of the CBETA arc shown in Fig. 5a.

#### Power dissipation on the coils of the window frame magnets

The dipole corrector field of a window frame magnet is generated by two coils wound around two opposite sides of the window frame as shown in Fig. 3.2.6. The required dipole corrector field is ±50 Gauss over the ∼11 cm length of a permanent magnet. Calculations show that such a dipole field can be generated with two racetrack coils 8 mm thick as in Fig. 3.2.6, when a current density of 50 A/cm$^2$ flows through each of the racetrack coil.

The quadrupole corrector field is generated by four racetrack coils (Panofsky Quadrupole) wound each around each side of the window-frame, as shown in Fig. 3.2.7. The required quadrupole field is ±0.45 T/m over the ∼11 cm length of a permanent magnet. Calculations show that such a quadrupole field can be generated with four racetrack coils 8 mm thick as in Fig. 3.2.7, when a current density of 375 A/cm$^2$ flows through each of the racetrack coil.

The coils of either dipole or quadrupole correctors will be made of a hollow copper conductor of an approximate cross-section of 6mm×6mm with a hole to carry cooling water to abduct the heat generated by the relative large current density of 375 A/cm$^2$ required to excite the quadrupole multipole. It it turns out that the power supply which will provide this large current density is expensive we may think of placing "additional copper" or increase the ampere turns of the quadrupole coils to reduce the current provided by the power supply.

The column 5 and 6 of Tab. 3.2.5 provides the power dissipation per unit length of each racetrack coil shown in Fig. 3.2.6, Fig. 3.2.7, Fig. 3.2.8, Fig. 3.2.10, to generate dipole or quadrupole field. To find the actual power dissipated per corrector, the values of column 6 in Tab. 3.2.5 must be multiplied by the length of the racetrack coil.

Table 3.2.5: Dissipated power in the racetrack coils to generate the required dipole or quadrupole field.

| Type | Strength | # Racetrack coils | J [A/m$^2$] | Power/coil [W/m] | Power/corrector [W/m] |
|---|---|---|---|---|---|
| Dipole | ±50 Gauss | 2 | 50 | 6 | 12 |
| Quadrupole | ±0.45 T/m | 4 | 375 | 150 | 600 |

#### Temperature Stabilisation

As water cooling will be used for the window-frame corrector coils, it is inexpensive to add an additional layer of water in the magnet holder to stabilize the temperature of the permanent magnet blocks. This ideally will be the first place the cool water flows, before it gets heated up in the hollow copper conductors. A schematic of this scheme is shown in Fig. 3.2.12 below.

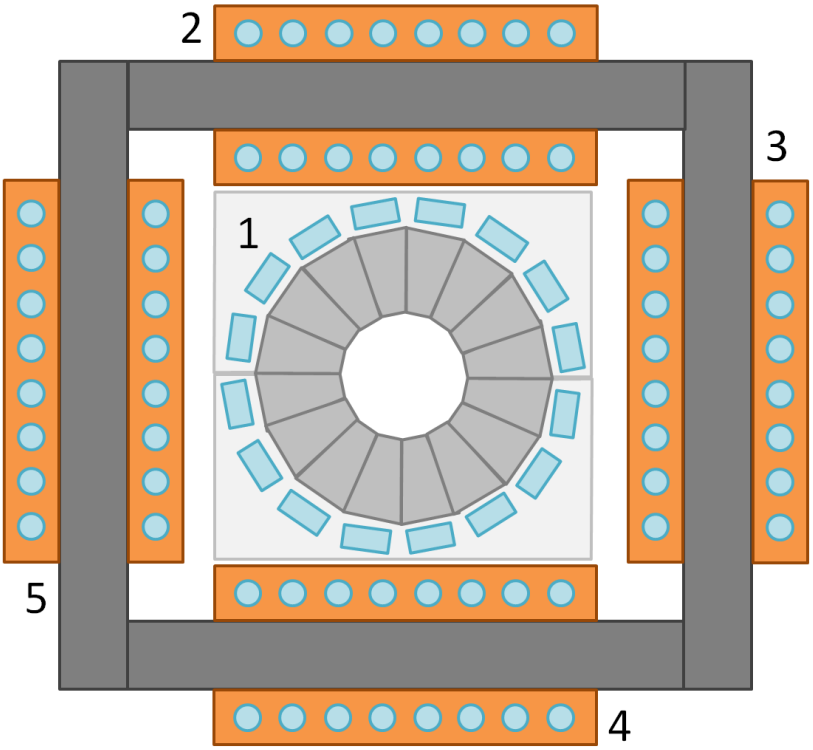


Figure 3.2.12: Schematic cross-section of the Halbach magnet and window-frame corrector assembly. Cooling water flows through channels in the magnet holder (1) before cooling the window frame corrector coils (2 through 5).

### 3.2.5 Halbach Magnet R&D and Shimming Results

BNL lab-directed R&D (LDRD) provided some money for constructing prototype permanent magnet quadrupoles for eRHIC, which is also an FFAG. Blocks were ordered from Shin-Etsu Corporation in August 2014 for three different designs, one of which was a Halbach quadrupole. The main differences between eRHIC and CBETA magnets are that eRHIC requires an open midplane to allow synchrotron radiation to be dumped and eRHIC's magnets are ∼1m long, an order of magnitude longer than CBETA's. However, to reduce cost, the eRHIC prototype magnets were built in 6cm sections, roughly the longest piece of permanent magnet the company could magnetize at once.

Table 3.2.6 below shows that the eRHIC prototype Halbach quadrupole is a good model for the CBETA magnets too, at least until the parts for purpose-built CBETA prototypes are delivered.

Table 3.2.6: Comparison of the Halbach shimming test magnet "5A" with requirements of CBETA magnets.

| Parameter | eRHIC prototype quad "5A" | CBETA QF requirement | CBETA BD requirement |
|---|---|---|---|
| Length | 60.0mm | 96.3mm | 126.4mm |
| Gradient | 27.5 T/m (measured) | -28.8 T/m | 19.2 T/m |
| Central dipole | 0 (by realignment) | 0 | -0.268 T |
| Material | SmCo R26HS (Shin-Etsu) | NdFeB N35SH (AllStar Magnetics) | NdFeB N35SH (AllStar Magnetics) |
| Min $R$ of physical magnet pieces | 22.5mm (design) 23.5mm (measured) | 36.5mm | 36.5mm |
| Max $R$ of beam centroid | 10mm (rotating coil) 15mm (extrapolated) | 19.5mm | 19.5mm |
| $R_{max,beam}/R_{min,magnet}$ | 43% (coil) 64% (extrapolated) | 53% | 53% |

The eRHIC magnet was constructed out of SmCo instead of NdFeB for historical reasons: concerns about radiation resistance, with SmCo being more resistant. Since then, a radiation test has shown NdFeB of an appropriate grade survives >100 Gy of radiation on the RHIC beam dump during a run. SmCo also contains much more cobalt, which can lead to long-term Co-60 activation.

#### Repeatability of Unshimmed Halbach Magnets

Five 6cm-long permanent magnet quadrupoles were made for eRHIC prototyping, of the kind shown in Fig. 3.2.13 below. Note that the holder was made on a 3D printer and the design for eRHIC incorporates midplane gaps for synchrotron radiation to exit.

These were all measured on the BNL magnet division rotating coil to test the field quality of Halbach quadrupoles without shimming. Blocks from this factory, typically have 1-2% magnetization strength error (the full width of magnetization bins in the Shin-Etsu materials

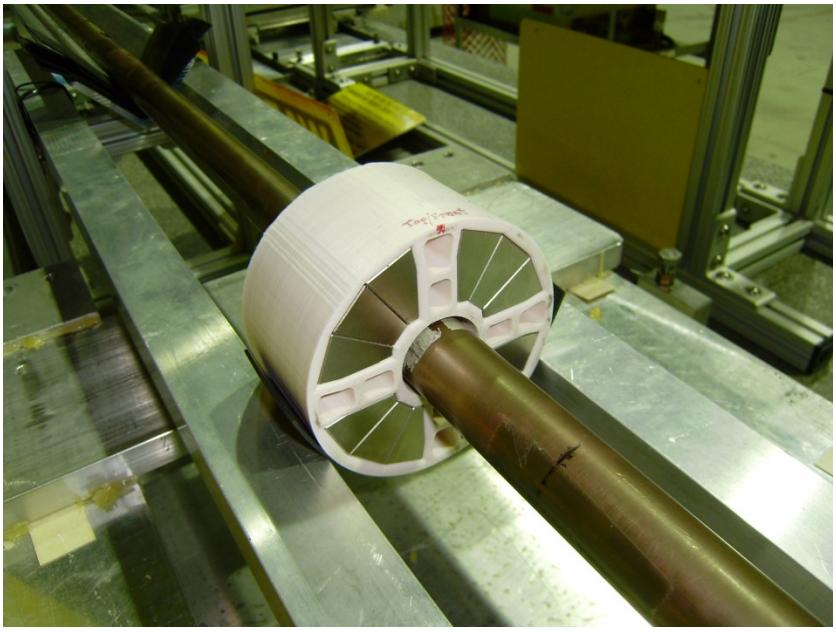

Figure 3.2.13: The 6cm-long eRHIC LDRD Halbach magnet being measured on the rotating coil at BNL's magnet division.

catalogue is ∼5%) and ±1° magnetization direction error, according to the supplier's quote. The five assemblies were measured on the rotating coil (not all the individual blocks), with results shown in Tab. 3.2.14 below.

The Normal Dodecapole error of ∼-190 units present in all magnets should be ignored for this comparison, since it was a systematic error made by the manufacturer using the wrong information for magnetizing some of the blocks. This was compensated for in later designs by moving the blocks.

The raw magnets have sextupole error magnitudes (normal and skew added in quadrature) of 13-57 units; octupole errors of 3-35 units; decapole errors of 6-13 units, with poles above dodecapole being less than 3 units. A unit is $10^{-4}$ relative to the main field, so these magnets are slightly better than 1% relative field error, which is roughly to be expected from the intrinsic magnetization errors of the blocks they are made from. This on its own is not yet good enough for the $10^{-3}$ level accuracy required by the accelerator, so shimming is required as described in the next section.

The coil is calibrated to measure at 1cm radius, which is smaller than the CBETA orbit excursion but as shown in the previous Tab. 3.2.6, the eRHIC prototype magnet had a smaller aperture overall.

#### Unshimmed Magnet Theoretical Error Study

Although the above experiment has shown what the field errors are in reality, it is also possible to put random magnetization errors into the simulation code in order to find out how specifications on the magnetization error range translate into average errors in the Halbach

**Summary of field measurements in eRHIC Permanent Magnet Quadrupoles (27-Apr-2015)**

Field harmonics are in "units" of $10^{-4}$ of the quadrupole field at a reference radius of 10 mm.

| Quantity | PMQ_0001 Run 2 | PMQ_0002 Run 3 | PMQ_0003 Run 2 | PMQ_0004 Run 3 | PMQ_0005 Run 2 |
|---|---|---|---|---|---|
| Integrated Gradient (T) | 1.8647 | 1.9097 | 1.9053 | 1.8958 | 1.9024 |
| Normal Dipole | -- | -- | -- | -- | -- |
| Normal Quadrupole | 10000.00 | 10000.00 | 10000.00 | 10000.00 | 10000.00 |
| Normal Sextupole | 27.83 | -29.83 | 35.83 | -4.53 | -11.95 |
| Normal Octupole | 5.39 | -3.12 | 32.81 | 16.50 | 3.61 |
| Normal Decapole | -4.92 | -2.44 | 2.90 | 7.09 | 3.86 |
| Normal Dodecapole | -188.14 | -194.57 | -188.00 | -192.96 | -190.26 |
| Normal 14-pole | -1.59 | 0.36 | -0.67 | 0.43 | 1.03 |
| Normal 16-pole | -0.44 | -0.22 | -1.10 | -0.58 | -1.31 |
| Normal 18-pole | -0.24 | 0.19 | -0.38 | -0.25 | 0.07 |
| Normal 20-pole | -2.37 | -2.88 | -3.13 | -2.93 | -2.91 |
| Normal 22-pole | 0.04 | 0.03 | 0.01 | 0.03 | -0.01 |
| Normal 24-pole | 0.02 | 0.00 | -0.02 | 0.01 | 0.04 |
| Normal 26-pole | 0.02 | -0.01 | 0.02 | -0.01 | -0.02 |
| Normal 28-pole | 0.11 | 0.12 | 0.12 | 0.13 | 0.12 |
| Normal 30-pole | 0.00 | 0.00 | 0.00 | 0.00 | 0.00 |

| Quantity | PMQ_0001 Run 2 | PMQ_0002 Run 3 | PMQ_0003 Run 2 | PMQ_0004 Run 3 | PMQ_0005 Run 2 |
|---|---|---|---|---|---|
| Field Angle (mr) | -- | -- | -- | -- | -- |
| Skew Dipole | -- | -- | -- | -- | -- |
| Skew Quadrupole | -- | -- | -- | -- | -- |
| Skew Sextupole | -16.41 | 1.90 | -43.69 | 28.96 | -5.28 |
| Skew Octupole | -12.32 | 0.25 | -12.55 | 4.03 | -18.51 |
| Skew Decapole | -11.98 | -6.08 | -5.68 | -1.00 | -8.52 |
| Skew Dodecapole | -2.27 | -0.99 | -3.12 | 0.87 | -4.96 |
| Skew 14-pole | 1.93 | 0.13 | 0.47 | 0.01 | 0.85 |
| Skew 16-pole | -0.22 | -0.09 | -0.02 | 0.27 | -0.13 |
| Skew 18-pole | 0.03 | 0.17 | -0.06 | 0.05 | 0.10 |
| Skew 20-pole | 0.08 | 0.00 | 0.07 | -0.20 | 0.01 |
| Skew 22-pole | 0.02 | 0.03 | 0.07 | -0.05 | 0.00 |
| Skew 24-pole | 0.01 | 0.00 | 0.02 | -0.02 | 0.01 |
| Skew 26-pole | 0.00 | 0.00 | 0.00 | -0.01 | 0.01 |
| Skew 28-pole | 0.00 | -0.01 | 0.00 | 0.01 | 0.00 |
| Skew 30-pole | 0.00 | 0.00 | 0.00 | 0.00 | 0.00 |

Figure 3.2.14: Table. Rotating coil measurements of 5 unshimmed Halbach permanent magnet quadrupoles.

magnets.

Each block's magnetization vector receives an independent random error. Since manufacturers give tolerances as total ranges (e.g. $\pm 2.5\%$ in strength), uniform distributions were used for these errors, with a parallel and perpendicular component being added for the magnetization strength and angle errors respectively. In the study shown in Tab. 3.2.7 and Fig. 3.2.15 below, two cases were considered: a fairly good case where the strength error is 1% and magnetization direction is also accurate to $1\% = 0.01$ radians $= 0.57$ degrees; and the worst case where the strength error is the full range of a material grade of 2.5% and the angle error is the worst quoted spec from a manufacturer of 5 degrees.

Table 3.2.7: Average over many runs of the total error in units ($10^{-4}$ of the quadrupole amplitude), where the total error is the quadrature sum of all the normal and skew error poles, measured at the largest beam radius.

| Magnet | Max. magnetization strength error | Max. magnetization direction error (radians) | (degrees) | Average total error ("units" = $10^{-4}$ of quad) |
|---|---|---|---|---|
| QF | 1.00% | 0.01 | 0.572958 | 31 |
| QF | 2.50% | 0.0873 | 5 | 212 |
| BD | 1.00% | 0.01 | 0.572958 | 29 |
| BD | 2.50% | 0.0873 | 5 | 201 |

The two magnets QF and BD behave very similarly in terms of average field error size. The field errors also ought to scale linearly with the magnetization error size. The real magnets

Amplitudes in units: (norm=24.8715)

| | |
|---|---|
| 2-pole: -13.70 | 2-skew: 0.94 |
| 4-pole: 10000.00 | 4-skew: 5.05 |
| 6-pole: 13.10 | 6-skew: 14.75 |
| 8-pole: -1.21 | 8-skew: -2.76 |
| 10-pole: -0.58 | 10-skew: -0.20 |
| 12-pole: -0.70 | 12-skew: 1.49 |
| 14-pole: 1.66 | 14-skew: -0.28 |
| 16-pole: 0.20 | 16-skew: 0.07 |
| 18-pole: -0.03 | 18-skew: 0.01 |
| 20-pole: -0.04 | 20-skew: 0.00 |
| 22-pole: -0.05 | 22-skew: -0.01 |
| 24-pole: -0.01 | 24-skew: 0.01 |
| 26-pole: 0.01 | 26-skew: -0.00 |
| 28-pole: 0.00 | 28-skew: 0.00 |
| 30-pole: -0.00 | 30-skew: -0.00 |
| 32-pole: 0.00 | 32-skew: -0.00 |
| 34-pole: -0.00 | 34-skew: 0.00 |

Amplitudes in units: (norm=270.095)

| | |
|---|---|
| 2-pole: -115.86 | 2-skew: -74.80 |
| 4-pole: 10000.00 | 4-skew: 220.91 |
| 6-pole: 40.11 | 6-skew: -56.84 |
| 8-pole: -6.03 | 8-skew: -8.19 |
| 10-pole: -5.38 | 10-skew: -6.89 |
| 12-pole: 3.98 | 12-skew: 5.87 |
| 14-pole: -1.87 | 14-skew: 7.00 |
| 16-pole: -0.32 | 16-skew: 2.79 |
| 18-pole: -0.53 | 18-skew: 0.48 |
| 20-pole: 0.34 | 20-skew: -0.04 |
| 22-pole: -0.05 | 22-skew: -0.03 |
| 24-pole: -0.01 | 24-skew: -0.04 |
| 26-pole: -0.02 | 26-skew: -0.04 |
| 28-pole: 0.00 | 28-skew: -0.00 |
| 30-pole: -0.00 | 30-skew: 0.00 |
| 32-pole: 0.00 | 32-skew: -0.00 |
| 34-pole: -0.00 | 34-skew: -0.00 |

Figure 3.2.15: Multipole errors in two randomly-chosen instances of the QF magnet. (Left) a magnet with 1% magnetization maximum amplitude error and 0.01rad maximum angle error. (Right) a magnet with 2.5% amplitude error and 5 degrees angle error.

ordered from Shin-Etsu Corporation in the previous section had total errors ranging from 26-67 units, with an average of 39, suggesting slightly (∼33%) worse tolerances than the 1%/0.57° case.

#### Field Quality Improvement after Iron Wire Shimming

The pieces from eRHIC magnet #5 were re-used to make a magnet that lacked the dodecapole error and served as a test-bed for shimming, as shown in Fig. 3.2.16 below.

The shimming method is that of "floating" iron shims, operating on the principle that a narrow iron cylinder placed in an ambient magnetic field will be magnetized in the same direction as the field. Provided the field is not so high that the iron saturates (assuming $\mu = \infty$ for the iron), the magnetization will be proportional to the ambient field magnitude. The shim field contribution from the uniformly transversely magnetized iron cylinder is the same as that of a $\cos(\theta)$ superconducting dipole of the same dimensions: that is, an ideal external dipole field. The dipole moment is proportional to both the ambient field and the cross-sectional area of the shim.

An analytic field model of these iron wires was added to PM2D and 36 of the wires were placed at 10 degree intervals around the inner bore of the magnet. The code was asked to vary the radii (areas) of the wires in order to cancel the error multipoles observed in an initial measurement of the magnet with the rotating coil. The results of this process are shown in Tab. 3.2.17 below.

An initial shimming designed to cancel only the sextupole was highly successful, reducing the sextupole amplitude from 20.5 units to 0.86 units, while the rest of the multipoles stayed

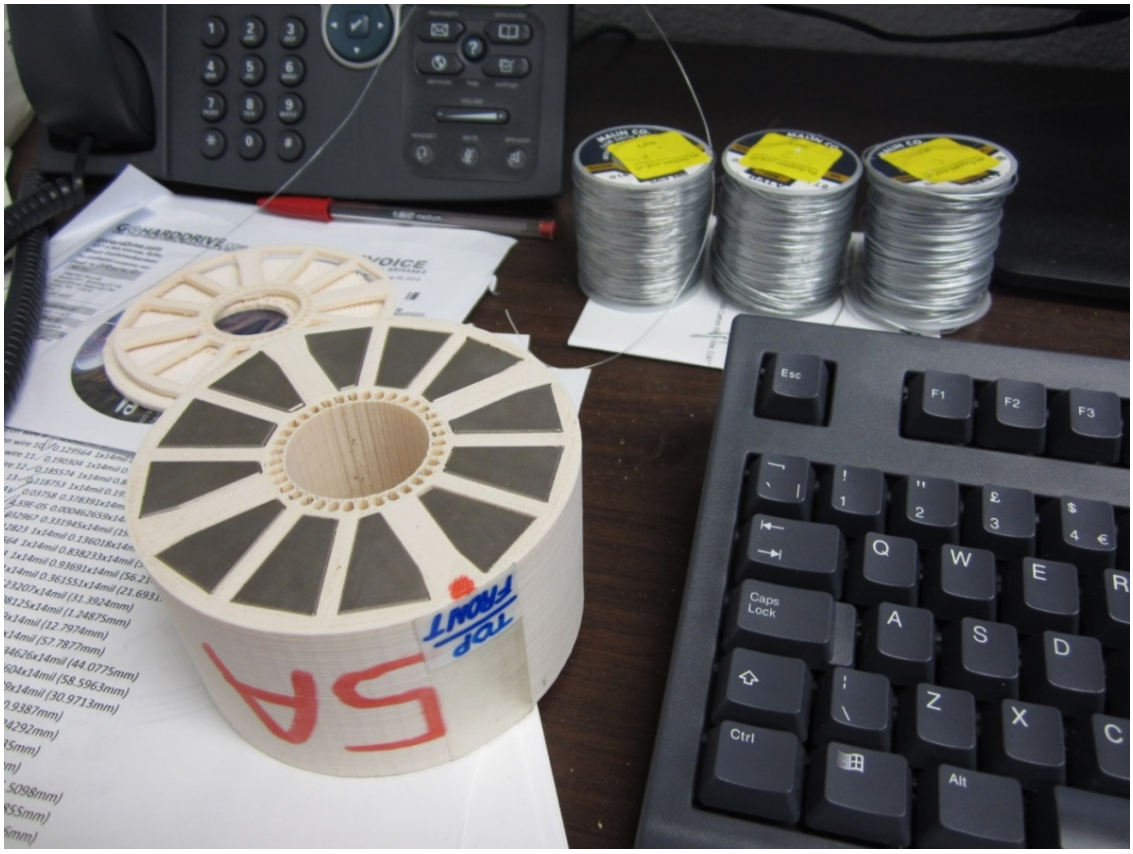


Figure 3.2.16: The pieces of the eRHIC LDRD Halbach magnet placed in a new 3D-printed holder to form magnet "5A". This is a corrected Halbach quadrupole whose holder incorporates holes for iron shims to be placed around the inside of the bore (iron wire grades shown in background).

**eRHIC Permanent Magnet Quadrupole PMQ_005A (26-Apr-2016)**

Field harmonics are in "units" of $10^{-4}$ of the quadrupole field at a reference radius of 10 mm.

| Quantity | 15-Dec-2015 PMQ_005A* Run 6(†) | 18-Apr-2016 PMQ_005A* Run 10(††) | 26-Apr-2016 PMQ_005A* Run 11(†††) |
|---|---|---|---|
| Integrated Gradient (T) | 1.6483 | 1.6513 | 1.6509 |
| Normal Dipole | -- | -- | -- |
| Normal Quadrupole | 10000.00 | 10000.00 | 10000.00 |
| Normal Sextupole | -18.67 | -4.37 | 0.26 |
| Normal Octupole | 5.34 | -1.19 | -1.53 |
| Normal Decapole | -0.88 | 0.35 | -0.72 |
| Normal Dodecapole | -1.04 | -0.80 | 0.09 |
| Normal 14-pole | 1.16 | 0.18 | 0.03 |
| Normal 16-pole | -1.46 | -0.25 | 0.03 |
| Normal 18-pole | 0.12 | 0.04 | 0.00 |
| Normal 20-pole | 0.45 | 0.20 | 0.03 |
| Normal 22-pole | -0.01 | 0.02 | 0.06 |
| Normal 24-pole | 0.03 | 0.01 | 0.01 |
| Normal 26-pole | 0.00 | -0.01 | -0.03 |
| Normal 28-pole | -0.12 | -0.10 | -0.10 |
| Normal 30-pole | 0.00 | 0.00 | 0.01 |
| Field quality figure of merit | 29.62 | 6.69 | 1.94 |

| Quantity | 15-Dec-2015 PMQ_005A* Run 6(†) | 18-Apr-2016 PMQ_005A* Run 10(††) | 26-Apr-2016 PMQ_005A* Run 11(†††) |
|---|---|---|---|
| Field Angle (mr) | -- | -- | -- |
| Skew Dipole | -- | -- | -- |
| Skew Quadrupole | -- | -- | -- |
| Skew Sextupole | -5.69 | -0.50 | 0.51 |
| Skew Octupole | -21.09 | -4.69 | 0.47 |
| Skew Decapole | -4.11 | -1.01 | -0.38 |
| Skew Dodecapole | 0.29 | 0.03 | 0.41 |
| Skew 14-pole | -0.09 | 0.05 | -0.12 |
| Skew 16-pole | -0.31 | 0.04 | 0.03 |
| Skew 18-pole | -0.03 | -0.07 | 0.05 |
| Skew 20-pole | 0.23 | 0.04 | 0.04 |
| Skew 22-pole | 0.00 | 0.03 | 0.01 |
| Skew 24-pole | -0.01 | -0.02 | 0.02 |
| Skew 26-pole | 0.00 | 0.00 | 0.00 |
| Skew 28-pole | 0.00 | -0.01 | -0.02 |
| Skew 30-pole | 0.00 | 0.00 | 0.01 |

* PMQ_005A is magnet built from magnets taken from PMQ_0005 and installed in a modified holder to reduce 12-pole

(†) Run 6 is measurement repeated with no iron shims, after several iterations of measurements with iron shims.

(††) Run 10 is iteration #1 with all wires pushed radially outward using thin wedges.

(†††) Run 11 is iteration #2 with all wires pushed radially outward using thin wedges.

Figure 3.2.17: Rotating coil measurements of the shimming test magnet before shimming (Run 6), after the first iteration of all-multipole correction using iron wire shims (Run 10) and after the second iteration (Run 11).

roughly the same. It should be noted there is some logic to the shim arrangement: for the sextupole shim ($n = 3$) in a pure quadrupole background field ($m = 2$), the shim pattern has pentagonal symmetry ($n + m = 5$) and areas proportional to $1 + \cos(5\theta + \phi)$ were used.

The optimizer was used to derive a shim distribution that would cancel all observed multipoles at once. Initially, the reduction was not as dramatic as with the sextupole alone, but reduced the quadrature sum of all error multipoles from 30.4 units to 4.34 units, with further iterations yielding no improvement. Careful investigation showed this was because cancelling all of the multipoles requires a greater mass of iron and the field becomes proportionately more sensitive to wire positioning as the mass increases. Re-measuring the original magnet and clamping the wires more securely yielded a reduction in quadrature sum from 29.6 to 6.69 to 1.94 units in two iterations, or three coil measurements: the original baseline, first iteration and measurement of second (final) iteration.

The rotating coil harmonics can be translated into polynomial fields with varying x across the y=0 midplane of the magnet, which is where the FFAG beam trajectories will be. These values are used in Fig. 3.2.18 to calculate the relative error at any point across the aperture.

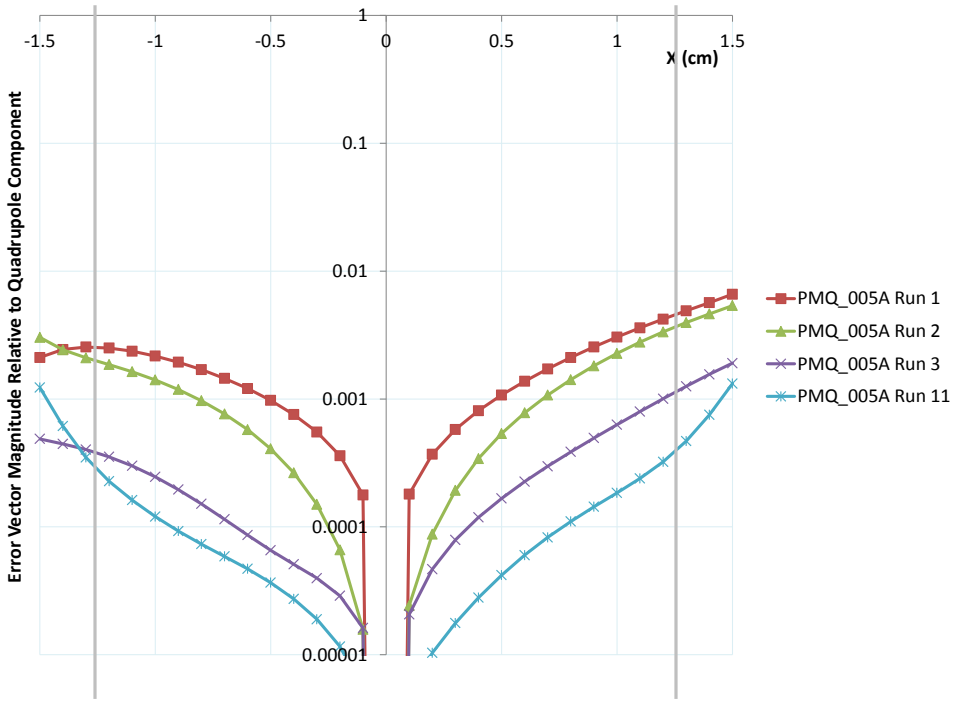


Figure 3.2.18: Relative field errors as a function of x on the y=0 midplane for the shimming test magnet: before shimming (Run 1, red); after sextupole cancellation (Run 2, green); after initial attempt at all-multipole shimming (Run 3, purple) and after all-multipole shimming with better clamped wires (Run 11, blue).

Reading off the worst values at the "53% of magnet aperture" value relevant to CBETA, this magnet had a 4.6e-3 relative field error on the midplane before shimming and a 4.0e-4 relative field error after shimming. These values are found by isolating the harmonics from sextupole and up: an alternative analysis is to allow the quadrupole to be varied (because there is a quadrupole trim coil) and find the setting that minimizes the maximum $|\Delta B/B|$ across the aperture. This gives a similar relative error of 4.9e-3 before shimming and 2.6e-4 after, with the latter using a -0.008 T/m trim.

### 3.2.6 CBETA Halbach Prototypes Unshimmed Results

Purpose-built prototype magnets for CBETA have also been built, including the "lopsided Halbach" magnet BD (Fig. 3.2.19 and Fig. 3.2.20). Due to the 2-3 month magnet lead times, these are from an old lattice design Cell_Brooks_2015-12-11 rather than the most recent Cell_Smoothpipe_2016-02-04 presented in this report, but they are similar. A comparison of the magnets in the two versions is given in Tab. 3.2.8 below.

Table 3.2.8: Comparison of current lattice Halbach magnets to those of the CBETA prototypes ordered.

| Parameter | QF current | QF prototype | BD current | BD prototype |
|---|---|---|---|---|
| Length | 96.3mm | 114.9mm | 126.4mm | 123.7mm |
| Gradient | -28.80 T/m | -23.62 T/m | 19.19 T/m | 19.12 T/m |
| Dipole at center | 0 | 0 | -0.2680 T | -0.3768 T |
| Max good field radius | 19.5mm | 20.2mm | 19.5mm | 13.7mm |
| Min inner radius | 36.5mm | 37.2mm | 36.5mm | 30.7mm |
| Max outer radius | 70.2mm | 62.4mm | 69.3mm | 59.4mm |
| Max field in good field region | 0.56 T | 0.48 T | 0.64 T | 0.64 T |
| Max field at "pole tip" | 1.05 T | 0.88 T | 0.97 T | 0.96 T |

These were ordered from AllStar Magnetics rather than Shin-Etsu (due to cost reasons), which means a larger magnetization angle error in the blocks of ±5 degrees as specified by their factory. Shimming methods will be tested to see if they can compensate for this larger error, possibly including shimming magnets instead of the iron wires.

At present the unshimmed measurements are available and shown in Fig. 3.2.21 for two BD magnets and Fig. 3.2.22 for the QF magnet. The BD results are quoted at R=10mm since its aperture is slightly smaller and only the 12mm radius coil would fit. Note that they are normalized to the quadrupole even though the dipole is larger. For BD, the desired dipole/quad ratio is -19707.305 units and this is enforced by choice of magnetic center and orientation adjustment. The QF from this lattice had a larger aperture and so could be measured on a larger coil with results quoted at R=25mm.

A reference radius of R=20mm would be most appropriate for this lattice, since the maximum beam excursion is 19.5mm. As results taken from coils of different radii are hard to compare, the quadrature sum of higher harmonics is shown in Tab. 3.2.9. Despite the looser tolerance on the magnetization angle, the size of the sextupole and higher harmonics look good, no term being above 17.5 units at R=10mm in the BD magnets. This is slightly better


Figure 3.2.19: The CBETA prototype BD magnet awaiting measurement at BNL.


Figure 3.2.20: The CBETA prototype QF (pure quadrupole) Halbach magnet.

than the results for the previous eRHIC-derived permanent magnet quadrupoles. For comparison, the largest harmonic term in the the initial assembly of the iron-based quadrupole was 13.65 units (also at R=10mm and without shimming). As the harmonics are comparable to those of the shimming test magnet, it is anticipated that there will be no problem using iron wire shimming to obtain similarly accurate results.

Table 3.2.9: The quadrature sum of higher harmonic units $\sqrt{\sum_{n=3}^{15} a_n^2 + b_n^2}$ in the Halbach prototypes, at the initial reference radius of the measurement and a conversion to R=20mm, which is approximately the full beam excursion.

| Reference Radius: | 10mm | 20mm | 25mm |
|---|---|---|---|
| BD2 | 22.29 | 78.56 | |
| BD3 | 22.60 | 65.14 | |
| QF1 | | 22.82 | 40.04 |
| Iron prototype Qd | 16.55 | 60.27 | |

**C-beta Halbach type BD magnet #2 PMQ_0302 (1-Jun-2016)**

Field harmonics are in "units" of $10^{-4}$ of the *quadrupole field* at a reference radius of 10 mm.

| | 1-Jun-2016 | 1-Jun-2016 |
|---|---|---|
| **Quantity** | **PMQ_0302 Run 2** | **PMQ_0303 Run 1** |
| **Integrated Gradient (T)** | -1.1825 | -1.1806 |
| **Normal Dipole** | 19704.4 | 19704.3 |
| **Normal Quadrupole** | -10000.0 | -10000.0 |
| **Normal Sextupole** | 14.8 | 17.5 |
| **Normal Octupole** | 11.2 | 5.6 |
| **Normal Decapole** | 0.5 | -0.6 |
| **Normal Dodecapole** | -1.6 | 0.0 |
| **Normal 14-pole** | 0.1 | -0.1 |
| **Normal 16-pole** | 0.0 | 0.0 |
| **Normal 18-pole** | 0.0 | 0.0 |
| **Normal 20-pole** | 0.0 | 0.0 |
| **Normal 22-pole** | 0.0 | 0.0 |
| **Normal 24-pole** | 0.0 | 0.0 |
| **Normal 26-pole** | 0.0 | 0.0 |
| **Normal 28-pole** | 0.0 | 0.0 |
| **Normal 30-pole** | 0.0 | 0.0 |

| | 1-Jun-2016 | 1-Jun-2016 |
|---|---|---|
| **Quantity** | **PMQ_0302 Run 2** | **PMQ_0303 Run 1** |
| **Integ. Dipole (T.m)** | 0.023299 | 0.023264 |
| **Skew Dipole** | 0.00 | -0.04 |
| **Skew Quadrupole** | 0.00 | 0.04 |
| **Skew Sextupole** | 6.32 | 6.60 |
| **Skew Octupole** | -9.95 | -11.26 |
| **Skew Decapole** | 3.43 | 1.38 |
| **Skew Dodecapole** | -0.02 | 0.00 |
| **Skew 14-pole** | 0.16 | -0.23 |
| **Skew 16-pole** | 0.03 | 0.03 |
| **Skew 18-pole** | -0.02 | 0.02 |
| **Skew 20-pole** | 0.01 | 0.00 |
| **Skew 22-pole** | 0.00 | 0.00 |
| **Skew 24-pole** | 0.00 | 0.00 |
| **Skew 26-pole** | 0.00 | 0.00 |
| **Skew 28-pole** | 0.00 | 0.00 |
| **Skew 30-pole** | 0.00 | 0.00 |

Figure 3.2.21: Unshimmed field harmonics from BD prototypes #2 and #3 at R=10mm. The nominal magnet length is 61.8597mm and the average dipole fields correspond to 0.37665 T and 0.37607 T, respectively. The average gradients are -19.115 T and -19.086 T.

**C-beta Halbach type QF magnet #1 PMQ_0501 (2-Jun-2016)**

Field harmonics are in "units" of $10^{-4}$ of the quadrupole field

***Reference radius used is 25 mm***

| | 2-Jun-2016 | | 2-Jun-2016 |
|---|---|---|---|
| **Quantity** | **PMQ_0501 Run 2** | **Quantity** | **PMQ_0501 Run 2** |
| **Integrated Gradient (T)** | 1.3579 | **Field anlge (mr)** | -- |
| **Normal Dipole** | -- | **Skew Dipole** | -- |
| **Normal Quadrupole** | 10000.0 | **Skew Quadrupole** | -- |
| **Normal Sextupole** | -6.9 | **Skew Sextupole** | 12.66 |
| **Normal Octupole** | 12.5 | **Skew Octupole** | 21.22 |
| **Normal Decapole** | -1.7 | **Skew Decapole** | -15.00 |
| **Normal Dodecapole** | -2.6 | **Skew Dodecapole** | 19.33 |
| **Normal 14-pole** | 2.1 | **Skew 14-pole** | 10.01 |
| **Normal 16-pole** | -5.6 | **Skew 16-pole** | -2.51 |
| **Normal 18-pole** | -3.5 | **Skew 18-pole** | 4.07 |
| **Normal 20-pole** | 0.5 | **Skew 20-pole** | 1.12 |
| **Normal 22-pole** | 1.0 | **Skew 22-pole** | 2.05 |
| **Normal 24-pole** | 0.3 | **Skew 24-pole** | -0.95 |
| **Normal 26-pole** | 0.2 | **Skew 26-pole** | 0.43 |
| **Normal 28-pole** | 0.0 | **Skew 28-pole** | 0.29 |
| **Normal 30-pole** | -0.1 | **Skew 30-pole** | -0.10 |

Figure 3.2.22: Unshimmed field harmonics from QF prototype #1 at R=25mm. The nominal magnet length is 57.4412mm and the average gradient corresponds to 23.640 T/m.

### 3.2.7 Manufacturing Pipeline and Vendors

Discussions are starting with magnet manufacturing companies about what they can build for CBETA. The pipeline of magnet manufacture and assembly onto the machine breaks down into the four stages below.

#### Permanent Magnet Wedges

These will be purchased, directly or indirectly, from a company. As mentioned previously, Shin-Etsu Corporation is a large manufacturer of the permanent magnet blocks with reasonably high quality. AllStar Magnetics has also provided BNL permanent magnets block in the past (for instance the radiation damage experiment), although they specify larger tolerances on their magnetization angles. Electron Energy Corporation (EEC) has recently succeeded in an SBIR proposal for CBETA and eRHIC magnet development. EEC manufactures both the blocks and magnet assemblies on-site in their machine shop. Finally, VacuumSchmelze GmbH has been contacted by Holger Witte for magnet blocks for the iron-poled quadrupole. Other companies not contacted yet include the undulator manufacturer KYMA.

Of these companies, AllStar generally provides the lowest cost but the least accurate magnetization vector guarantee ($\pm 5$ degrees). Shin-Etsu provides $\pm 1$ degree tolerance with some additional cost for tooling. EEC say even $\pm 0.5$ degrees is possible but there is an associated cost since additional steps of demagnetizing the block, re-grinding it to an accurate shape and re-magnetizing it have to occur.

#### Magnet Assembly

Although in theory this could be done on the BNL or Cornell sites, it seems that several companies are willing to bid for this work and are capable of doing it. EEC could be used as an end-to-end vendor for these first two steps. RadiaBeam LLC will make assemblies and girders but have to get the PM blocks from another company. They previously gave a cost estimate for assembling the CBETA magnets and girders and are the only ones to have significant accelerator field experience (in fact they also make Halbach magnets for electron microscopes). Their absolute tolerances on positioning magnets on the girders were 0.1mm.

#### Shimming and Rotating Coil Measurements

Discussions so far with magnet manufacturers are indicating that the rotating coil is a specialized piece of measurement equipment for accelerator applications. None of the companies contacted so far have functioning rotating coils, although Radiabeam and EEC have Hall probes for field mapping. The shimming method works best using a rotating coil, so this stage is likely to be done in the BNL magnet division, where they have done it before.

#### Alignment and Girder

Since the magnets will need to be removed to do separate rotating coil and shimming steps, a fully integrated manufacture (measurement while on girder) does not look possible. Instead, survey fittings will be included in the non-magnetic body during the magnet assembly step

and these will be used in the hall at Cornell to fit in with their on-site survey system. The survey references may also be used in the rotating coil stage to ensure alignment between the magnetic field and the magnet holder.

## 3.3 Magnet Girder Support System

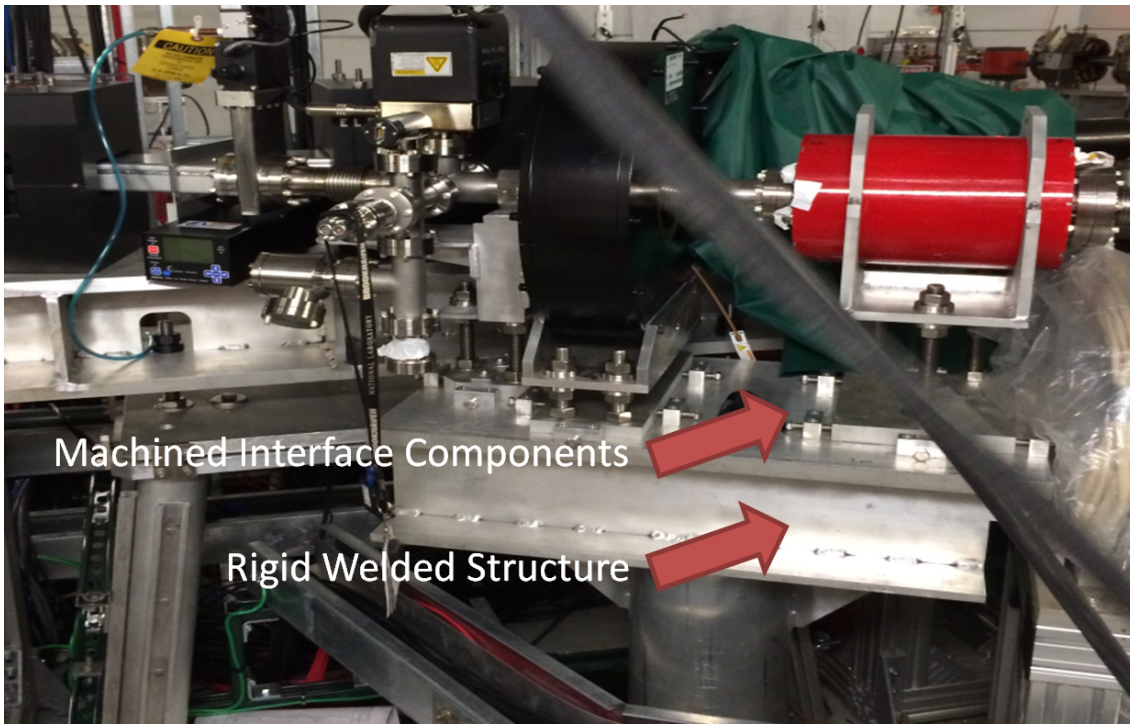


Figure 3.3.1: Welded structure.

A conceptual design has been proposed based upon the designs of existing girder support systems in a variety of other machines. Three particular designs had been proposed, those being:

1. A rigid welded structure with post process stress relief and subsequent machining combined with machined components that interface and adjust position of accelerator constituents. (Figure 3.3.1);

2. Modular structure using standardized aluminum extrusions and machined components that interface and adjust position of accelerator constituents. (Figure 3.3.2);

3. Concrete infill and machined components that interface and adjust position of accelerator constituents. (Figure 3.3.3).

Typically the favored design is the rigid welded structure (Figure 3.3.1) but the cost of such must also be considered, as it is the most expensive to produce. We will pursue the favored

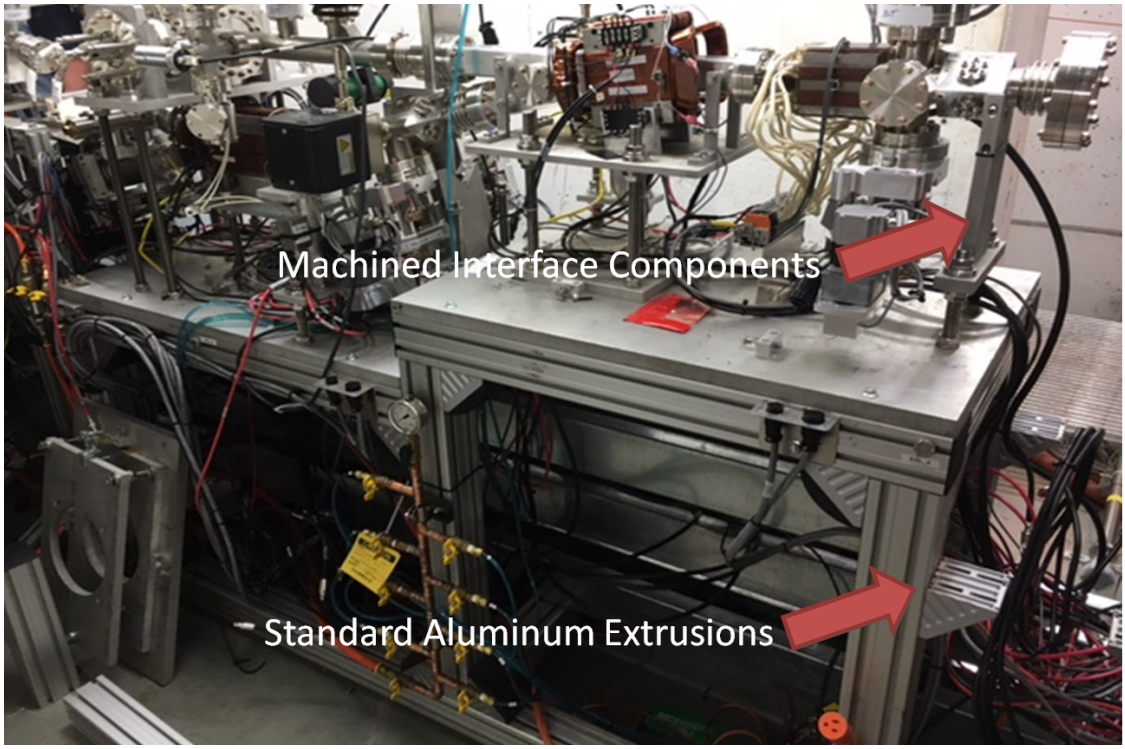


Figure 3.3.2: Modular structure.

design until budget constraints dictate otherwise. In general, the magnet girder support system must provide a stable platform for the accelerator constituents during assembly and after installation to tolerances defined by the required magnet stability. It must provide adjustment for the initial component alignment as well as subsequent alignment due to long term facility movement. We will also determine the resonant frequencies of the girder system and adjust structure to avoid building and machine frequencies.

## 3.4 Power supplies

The following sections describe possible magnet power supplies for the dipoles and quadrupoles in the spreaders and recombiners, and correction magnet power supplies for the spreaders, recombiners and arcs.

### 3.4.1 Dipole and Quad Power Supplies for the Spreaders

The present plan is to use off-the-shelf TDK/Lambda power supplies, which we have used successfully for many years. As soon as the current/voltage requirements are provided, we will add the appropriate model numbers and specifications.

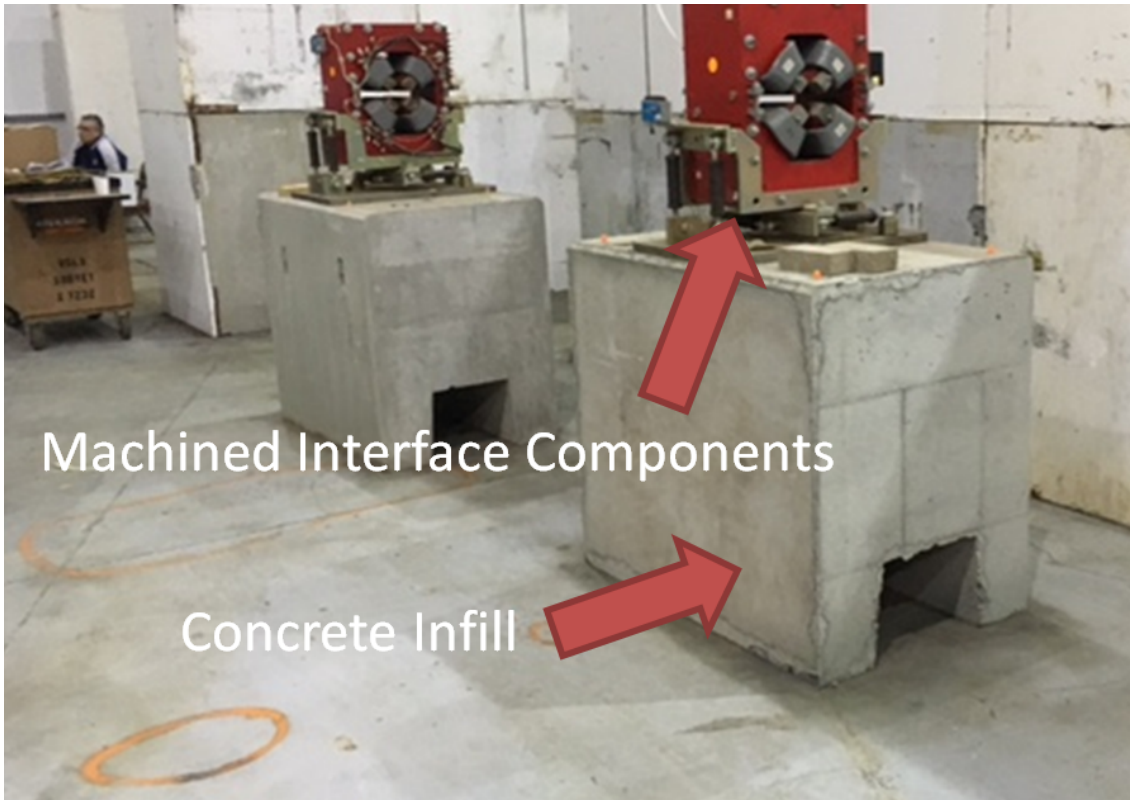


Figure 3.3.3: Concrete infill.

### 3.4.2 Corrector Magnet Power Supplies

The machine will have correction coils for steering in the spreader and recombiner regions, as well as the FFAG arcs and straight section. The FFAG magnets will additionally have correction coils to adjust the quadrupole strengths. At the current time we do not have current/voltage requirements, nor a count of the number of magnets. The following three sections describe possible bipolar power supplies that may be appropriate. The quadrupole correction power supplies may or may not need to be bipolar.

#### Kepco BOP 20-10M

We were able to obtain a number of used Kepco power supplies from BNL, approximately 120 units. They provide ±20 V and ±10 A with a smooth transition through zero. The supplies are 3U size with 1U of cooling space between units, and ventilation on on the top and rear. Each unit does not fill a rack width, thus wasting space on the sides. With an 8 foot rack, 13 supplies can be installed. See Fig. 3.4.1 and Fig. 3.4.1.

Figure 3.4.1: The front panels of the Kepco Supplies.

Kepco sells an upgrade card that allows for ethernet control on the supply. The upgrade includes a transformer replacement, rear panel modifications, and required about 2 man-days to complete the modifications and testing. We have contacted Kepco about having them install the cards, test each unit, and fix any problems. See Fig. 3.4.3 and Fig. 3.4.4 for details.

#### BiRa MCOR 12/30

BiRa produces blade power supplies in a 6U crate, with 2U for cooling fans and 1U for the bulk power supply (see Fig. 3.4.7). Each crate has 1 ethernet control card, 16 ±12 A modules (or 8 ±30 A modules). The 12 A modules can be configured to 2 A, 6 A, 9 A or 12 A maximum current.

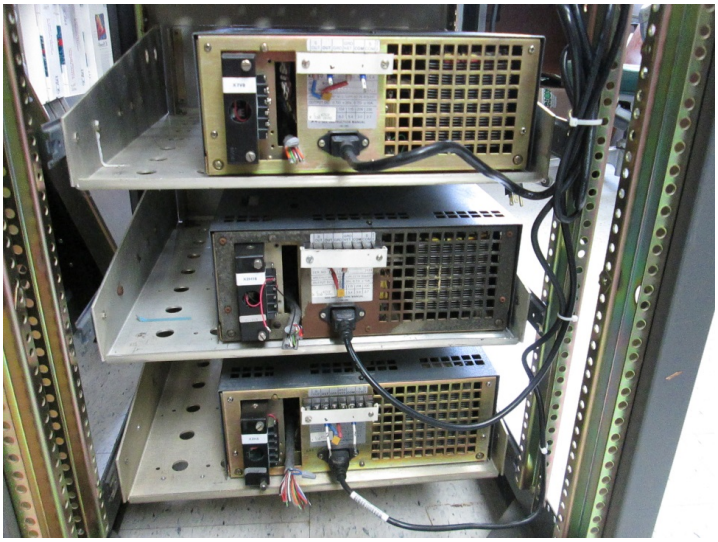

Figure 3.4.2: The back side of the Kepco supplies

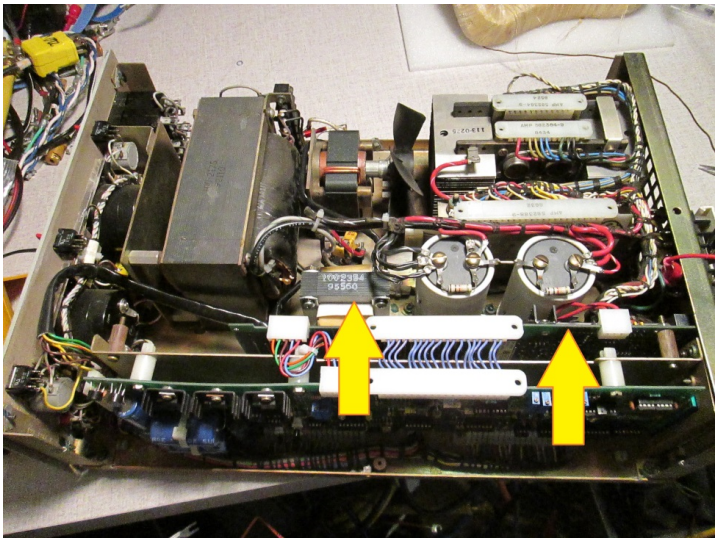

Figure 3.4.3: Modifications to install the ethernet card upgrade.

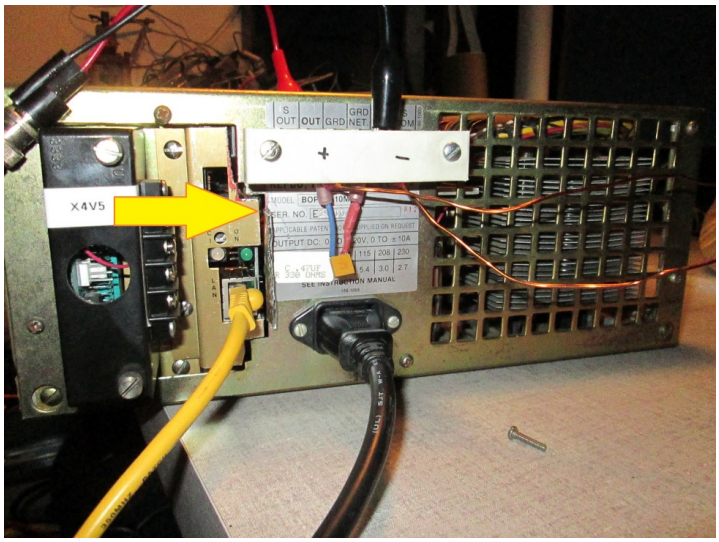


Figure 3.4.4: Back panel modifications to install the ethernet card upgrade

| MODEL | BANDWIDTH (d-c to $f_{-3dB}$) KHz (minimum) Mode | | RISE & FALL TIME 10% to 90% µsec (minimum) Mode | | LARGE SIGNAL FREQUENCY RESPONSE KHz (minimum) Mode | | SLEWING RATE (mimumum) Mode | | RECOVERY STEP LOAD µsec (minimum) Mode | |
|---|---|---|---|---|---|---|---|---|---|---|
| | V | I | V | I | V | I | V | I | V | I |
| 200 WATT | | | | | | | | | | |
| BOP 20-10M | 18 | 6 | 20 | 60 | 17 | 7 | 2V/µsec | 0.4A/µsec | 80 | 20 |

Figure 3.4.5: Dynamic specifications for the Kepco supply

| INFLUENCE QUANTITY | | OUTPUT EFFECTS (1) | | | | PREAMPLIFIER OFFSETS (4) | | REFERENCE ±10V |
|---|---|---|---|---|---|---|---|---|
| | | VOLTAGE MODE | | CURRENT MODE | | | | |
| | | TYPICAL | MAXIMUM | TYPICAL | MAXIMUM | $\Delta E_{io}$ | $\Delta I_{io}$ | |
| Source (min.-max.) | | <0.0005% | 0.001% | <0.002% | 0.005% | <5µV | <1nA | <0.0005% |
| Load (NL-FL) | | <0.001% | 0.002% | <0.5mA | 1mA | — | — | <0.0005% |
| Time (8-hour drift) | | <0.005% | 0.01% | <0.01% | 0.02% | <2.0µV | <1nA | <0.005% |
| Temperature, per °C | | <0.005% | 0.01% | <0.01% | 0.02% | <2.0µV | <1nA | <0.005% |
| Ripple and Noise (2) | rms | <1mV | 3mV | <0.01% | 0.02% | --- | — | — |
| | p-p | <10mV | 30mV | <0.01% | 0.02% | --- | — | — |

Figure 3.4.6: Static specifications for the Kepco supply

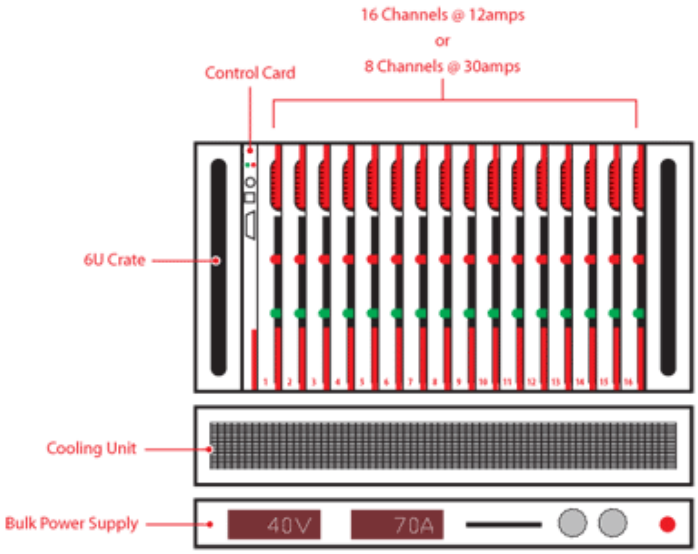


Figure 3.4.7: A schematic of the BiRa crate

### CAEN 20-10 Easy Driver

Caen has 1U standalone units with ±5 A and ±10 A version, with an ethernet interface (see Fig. 3.4.8. They have low-noise output with digital regulation loops, internal protections and auxiliary readbacks. An 8 foot rack can hold 54 channels.

The specifications are

- ±20 V, ±10 A
- 160 $\mu$A current setting resolution
- 20 bit output resolution for voltage and current
- output current ripple 50 ppm/FS
- output current stability 50 ppm/FS
- switching frequency 100 kHz
- closed loop bandwidth 1 kHz

## References

[1] Pruss, S., *et al. Hybrid permanent quadrupoles for the 8 GeV transfer line at Fermilab.* In *Proceedings of the 1997 Particle Accelerator Conference*, volume 3.


Figure 3.4.8: The Caen magnet power supply unit.

| | Easy - Driver | FAST-PS |
|---|---|---|
| ***Output Current*** | up to ±10 A | up to ±30 A |
| ***Output Voltage*** | up to ±20 V | up to ±80 V |
| ***Ouput Power*** | up to 200 W | up to 600 W |
| ***Local Display*** | ✔ | ✔ |
| ***Local Control*** | ✗ | ✔ |
| ***Control Loop Type*** | Digital | Digital |
| ***Control Loops*** | Current | Current<br>Voltage |
| ***External Interlocks*** | 1 | 2 |
| ***Status Signals*** | 1 solid state relay | 1 solid state relay<br>1 magnetic relay |
| ***Remote Sensing*** | No | Yes |
| ***Remote Interface*** | 10/100 Ethernet | 10/100/1000 Ethernet<br>SFP Fast Interface |
| ***Remote Update Rate*** | 250 Hz | 1 kHz - Ethernet<br>10 kHz - SFP Fast Interface |
| ***Other Features*** | Firmware Remote Update<br>Configurable Thresholds/Limits<br>Internal Protections | Firmware Remote Update<br>Waveform loading and execution<br>Configurable Thresholds/Limits<br>Internal Protections<br>Embedded Linux OS<br>USB host<br>External Trigger - *option*<br>Analog Control Input - *option* |

Figure 3.4.9: A comparison between the two Caen models.

[2] Tosin, G., *et al.* *Design of Magnet Prototypes for the new Brazilian Synchrotron Light Source - SIRIUS*. Conf. Proc., **C100523**, page WEPD003 (2010).

[3] Bertsche, K., J.-F. Ostiguy, and W. Foster. *Temperature considerations in the design of a permanent magnet storage ring*. In *Proceedings of the 1995 Particle Accelerator Conference, Dallas, TX, USA*, volume 2, pages 1381–1383.

[4] Russell, A., *et al.* *Selecting magnet laminations recipes using the method of simulated annealing*. In *Proceedings of the 1997 Particle Accelerator Conference*, volume 3, pages 3288–3290.

[5] Einfeld, D. *Specifications, quality control, manufacturing, and testing of accelerator magnets*. In *Proceedings, 2009 CAS-CERN Accelerator School: Specialised course on Magnets* (2011).

[6] Bell, B. *Private communication* (2015).

[7] Animesh, J. *Private communication*.

[8] Brooks, S. *Muon Capture Schemes for the Neutrino Factory*. http://ora.ox.ac.uk/objects/ora:4360, University of Oxford (2010).

# 4 Injector

## 4.1 Introduction

The Cornell accelerator group now operates the world's highest average current, high brightness photoinjector, a prerequisite for emerging machines in nuclear physics, high energy physics, FEL facilities, and industrial applications (see Fig. 4.1.1). The beam is produced in a laser-driven photoemission gun (A1), accelerated to as much as 10 MeV in superconducting RF cavities (A2), after which beam parameters are measured (A3, A4, C1, C2), and finally absorbed in a beam dump (A5). Among the achievements are the world-record average current of 75 mA from a photocathode injector with many-day cathode lifetimes at currents above 60 mA [12,13], and beam emittances approaching the thermal (intrinsic) photocathode emittance at a bunch charge of 80 pC in the space-charge dominated regime [14]. This frontier R&D facility has in many ways cleared the path towards ambitious future projects by demonstrating the world's highest brightness and average current photoemission-based source of relativistic electrons.

Photoinjectors are used at the majority of the electron linac-based accelerators today due to their efficiency, timing structure flexibility, and ability to produce high power, high brightness beams. These properties make the Cornell injector an ideal electron source for the FFAG-based ERL described in this document. The details of the injector and all of the subsystems are described in the following sections.

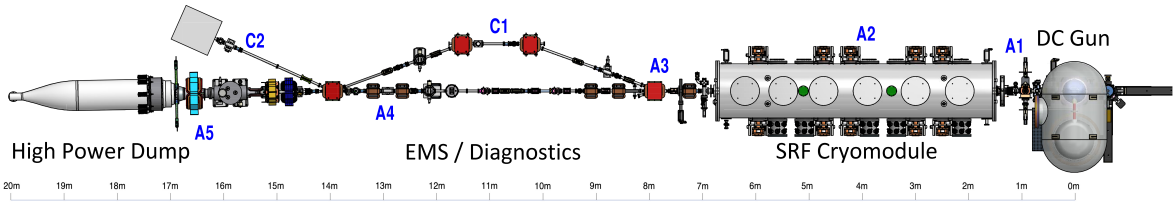


Figure 4.1.1: A schematic of the Cornell photoinjector, capable of providing beams up to 500 kW (5 MeV, 100 mA or equivalent).

## 4.2 The DC Photoemission Gun

High voltage DC photoemission electron guns offer a robust option for photoelectron sources, with applications such as ERLs, free electron lasers, ultrafast electron diffraction, and ultrafast electron microscopy. The technology for such guns was developed in the 1970's [1] and the simple conceptual design has remained relatively unchanged since that time.

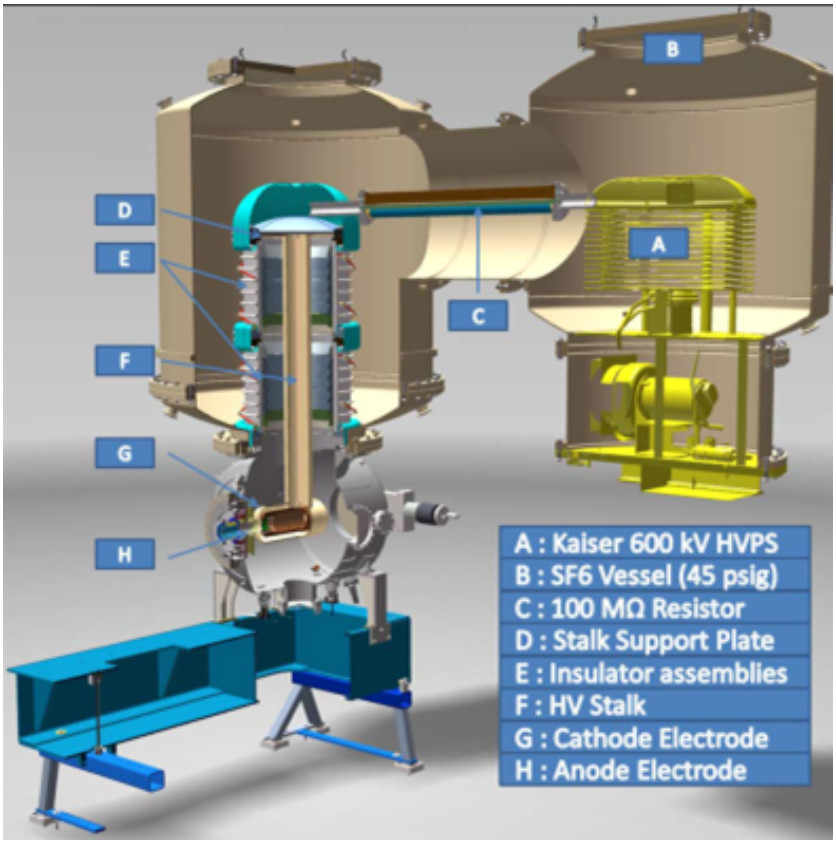


Figure 4.2.1: A cutaway view of the DC photoemission gun. Photocathodes are prepared in a load lock system mounted on the large flange at the left, and transported through the cathode cylinder to the operating position in the Pierce electrode shape on the right. The beam exits through the small flange to the right.

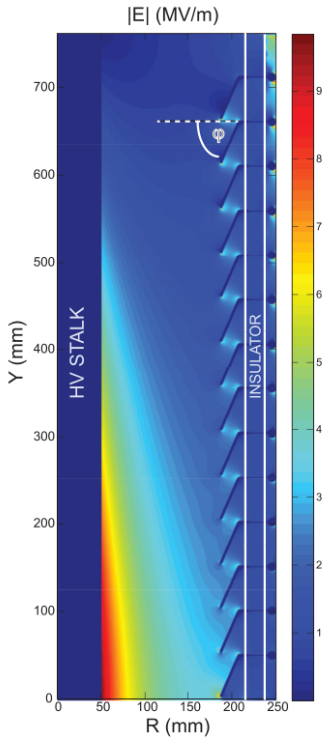


Figure 4.2.2: Simplified HV model made in the software Opera 2D. Shown is the HV stalk, insulator, and guard rings for the gun operating at 750 kV. Color corresponds to the magnitude of the electric field in MV/m. For simplicity, this HV model is monolithic, rather than made of two insulator assemblies (as built), and similarly does not show the triple point protection rings.

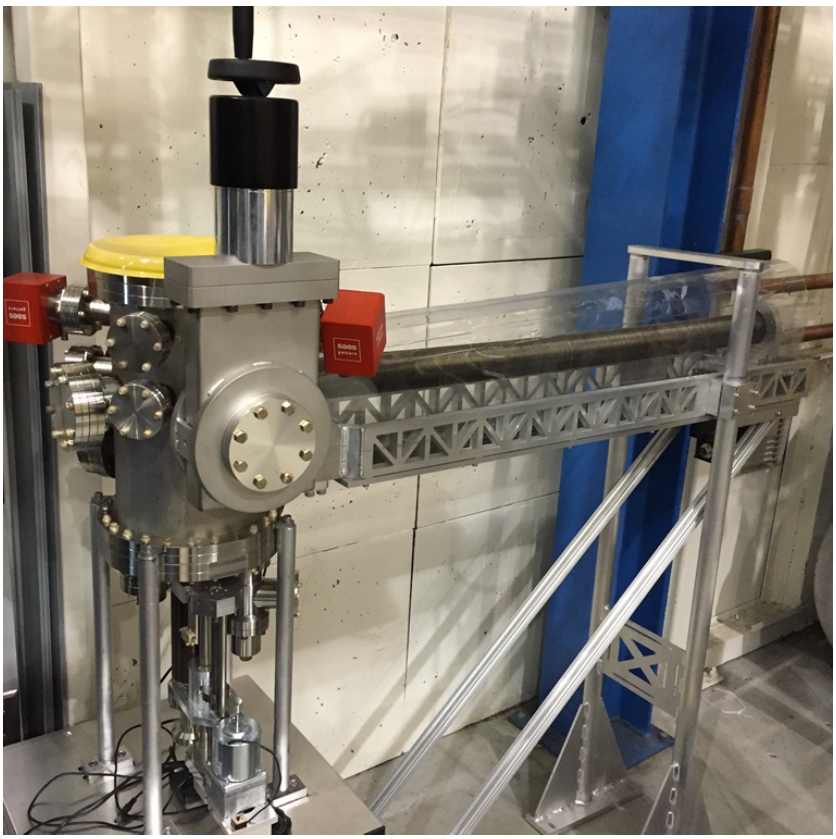

Figure 4.2.3: Cathodes are transported in a vacuum suitcase (not shown) and attached to the manual gate valve. Cathodes are moved from the suitcase into the central vacuum chamber, which can hold three cathode pucks. The bellows translation mechanism moves the pucks from the chamber into the gun.

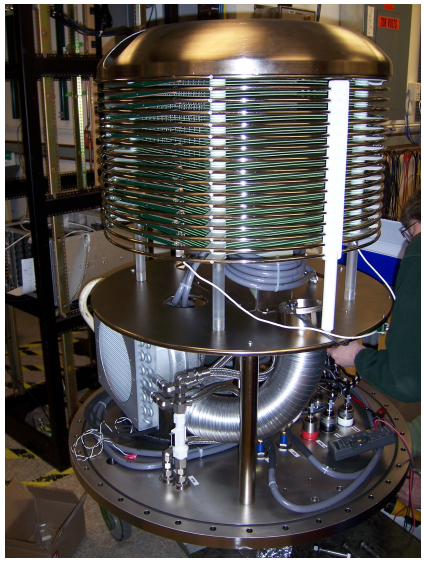

Figure 4.2.4: The HV section of the 750kV power supply. Individual circuit boards are visible inside the potential grading rings. The primary winding of the insulating core transformer is the large diameter gray-insulated wire below the circuit boards. The HV section is mounted in the pressurized $SF_6$ tank with its axis parallel to the axis of the gun ceramic.

A DC gun for a high brightness, high intensity photoinjector requires a high voltage power supply, usually some variant of the Cockcroft-Walton multiplier, supplying hundreds of kV to the high voltage surfaces of the gun. The power supply and outer gun structures at HV are often enclosed by a chamber pressurized with sulfur hexafluoride ($SF_6$) as a dielectric buffer gas to suppress arcing in the HVPS. The HV surfaces of the gun chamber are held off from the grounded chamber surfaces via an insulator structure. Inside the chamber, the cathode electrode is suspended in the chamber center via a support stalk, which also connects the HV to the cathode electrode.

The anode electrode is constructed from titanium, and is isolated from ground using small alumina washers. This allows the anode to be biased in order to reject ions that backstream into the anode-cathode gap region from further down the beamline. The anode can hold off up to 5 kV. At the rear of the gun a vacuum load-lock system allows cathodes to be inserted and removed without disturbing the gun vacuum. The cathode is illuminated from the front side of the gun using mirrors that are mounted in a light box between the first solenoid and the buncher.

An overview of the gun and its major components is shown in Fig. 4.2.1. One of the most important design differences between this gun and the original Cornell DC gun (17) is the use of a segmented insulator structure (Fig. 4.2.1(E)). The entire insulating structure is composed of two smaller insulator assemblies. Both insulator assemblies were manufactured by Friatec AG. Each insulator assembly has 7 segments, or 14 in total installed on the gun. Each segment is a ring of $Al_2O_3$ with an inner diameter of 435 mm, 50 mm tall, and 20 mm thick. The dielectric strength of the $Al_2O_3$ is quoted by Friatec to be beyond 30 kV/mm, with a resistivity

of $10^{15}$ $\Omega \cdot cm$ at room temperature. The top segment and bottom segment of each assembly is brazed into a 22.125 inch 316LN wire seal flange.

A kovar ring is brazed between each of the insulator segments. In vacuum, the kovar ring allows the attachment of the insulator guard rings (described below). These rings also extend outside the insulator body into the $SF_6$ environment. In the $SF_6$, a resistor chain from HV (at the top) to ground (at the bottom) connecting to each kovar ring directly defines the voltage on all segment interfaces and inner guard rings. Kovar was chosen as the interface ring material for its similar coefficient of thermal expansion to that of the $Al_2O_3$, so that the braze joint would be minimally stressed during thermal cycling. The kovar rings at the top and bottom of the insulator are shaped to fit into 22.125 inch 316LN wire seal flanges and welded.

The insulator guard rings between each segment block field emitted electrons from landing on the insulator surface, reducing the possibility of insulator damage. The rings were made of copper due to its ease of machining and high thermal conductivity, thereby minimizing the heating of the ring and nearby braze joints from any stray field emission. A simplified high voltage model of the guard rings, insulator, and HV stalk are shown in Fig. 4.2.2. The angle of each ring with respect to the horizontal, 67.5° , was chosen such that no field emitted electrons could reach the surface of an insulator segment, based on particle tracking. The angle of the lowermost ring was increased to 72.0° as the electric field lines changed near the ground plane, and some electrons could have reached the insulator with the 67.5° angle.

One of the most vulnerable locations with respect to field emission on any vacuum insulator is the so-called triple point junction, which is the interface between the stainless steel, ceramic, and vacuum. These junctions are shielded by additional triple point protection (TPP) rings which attach directly to the interior of the flanges, and are also made of stainless steel. The HV stalk (Fig. 4.2.1(F)) is a 1.25 m long hollow cylinder with 125 mm outer diameter. The stalk center axis is co-linear with the insulator's center axis (in Fig. 4.2.2, the line at R=0), and is attached to a support plate (Fig. 4.2.1(D)) which rests on top of the uppermost TPP ring. As the stalk supports the cathode electrode, its height, angle with respect to the y-axis, and rotation angle about the y-axis are of direct importance for the symmetry of fields in the photoemission region. Thus, adjustment screws on the stalk plate permit the adjustment of height, both angular offsets from the y-axis, and the rotation of the stalk.

The insulators and stalk sit on the gun vacuum chamber, which is held at ground potential, along with the $SF_6$ chamber walls. The gun chamber is a 600 mm diameter cylinder shell, 5 mm thick, with its symmetry axis along the direction of the beam. Pumping is provided by a three non-evaporable getter modules (SAES Capacitorr D-2000) and two 40 l/s ion pumps. Each ion pump is placed behind a NEG module in a single assembly, so that any gas load produced by the ion pumps would first be pumped by the NEG modules before entering the gun chamber. Each of these combined pumping assemblies is attached to a 8 inch ConFlat® flange on either side of gun chamber. A leak valve manifold with both a turbomolecular pump and a source of ultra-pure noble gas is attached to a UHV right-angle valve on the gun chamber for noble gas processing. The cathode electrode (Fig. 4.2.1(G)) design is identical to that of the original Cornell gun (17), as this design was shown to be an effective balance between providing optimal focusing and high photocathode field strength while having minimal electric fields outside of the photoemission region (18). Furthermore, this cathode design was shown to give excellent emittance for bunch charges up to 80 pC (16) for a gun operating at 350

kV. The cathode design is Pierce-type, with a focusing angle of 25°. The focusing introduced by this electrode angle serves to counteract the initial space charge expansion of an intense photoemitted beam.

The cathode electrode is made of vacuum remelt 316LN stainless steel. It features a leaf spring assembly inside the cathode interior to hold and register a removable photocathode puck (Fig. 4.2.1(1)) in the center of the Pierce electrode. The back of the cathode electrode is terminated with a half-torus to keep electric fields low, with the torus hole permitting the transfer of photocathodes in and out of the interior holder.

In general, we follow the procedures developed for cleaning SRF cavities whenever possible for surfaces supporting high electric fields. Although field emission is a poorly understood process, it is well known that the condition of the HV surface in terms of both roughness and contaminants strongly affect the fields at which field emission or pre-breakdown activity begins. Both particulate contaminants and scratches or roughness can cause field enhancements which precipitate field emission or vacuum breakdown [2, 3]. Furthermore, both surface contaminants and dielectric inclusions in the metal can alter the work function of the material.

First, all metallic HV surfaces of the gun, including stalk, cathode electrode, copper rings, TPP rings, and anode, were mechanically hand-polished using silicon carbide. For the stainless steel electrodes, an additional polishing with diamond paste is performed. Then, a chemical polishing step was applied to all mechanically polished parts. For stainless steel parts (stalk, cathode electrode TPP rings), standard electropolishing was performed, removing 10 $\mu$m of material. For the copper rings, a weak citric acid etch was performed, as this was shown via interferometric microscopy to produce a surface with smaller root-mean-square (RMS) roughness than a more powerful copper etchant (such as nitric and sulfuric acid). After electropolishing, all stainless steel vacuum components (including chamber, stalk, and electrodes) are baked in air at 400 C for 100 hours to reduce hydrogen outgassing.

After surface treatment, all vacuum surfaces (including the chamber itself, but excluding the vacuum pumps) in the gun were high pressure rinsed with DI water in clean room conditions equivalent to ISO 5 or better, to remove particulate contamination. The insulator itself was rinsed with 300 psi water, whereas all metallic surfaces were rinsed with pressures 600 psi (minimum), for approximately 3 h per part. Both copper and TPP rings were rinsed on a separate rinse stand, apart from the insulator.

After a full air dry of all parts in the clean room, the insulators were populated with rings manually. The cathode electrode was assembled on a test stand, and then suspended in the chamber via a temporary support from the back of the gun. The insulators were installed on to the chamber and cathode assembly via a clean room crane. The stalk without top plate was similarly lowered through the insulators via the crane, and was attached to the cathode and temporary cathode support. Finally, the top plate was installed and attached to the stalk, allowing the cathode electrode support to be removed. Using surveying mounts installed in the photocathode holding structure, the height and angle of the electrodes were adjusted to be concentric with the axis defined by the anode and load-lock chamber flanges. The gun was then sealed, evacuated and checked for leaks, then transported to its final location. A vacuum bake was performed at 150 C for approximately two days, followed by NEG activation at 500 C for 1 h. The final vacuum prior to processing was $2 \times 10^{-11}$ torr.

The gun HV power supply, 750 kV at 100 mA, is based on proprietary insulating core transformer technology and was manufactured by Excelitas Technologies (formerly Kaiser

Systems). It is comprised of a stack of circuit boards insulated from each other. Each board contains two ferrite cores which couple a high frequency magnetic field from one board to the next. Each board can deliver up to 12.5 kV at 100 mA, and is only 5 mm thick, leading to a very compact supply. 62 boards are used in the full stack, which is shown in Fig. 4.2.4. The primary of the ferrite insulating core transformer is powered by an external high frequency driver.

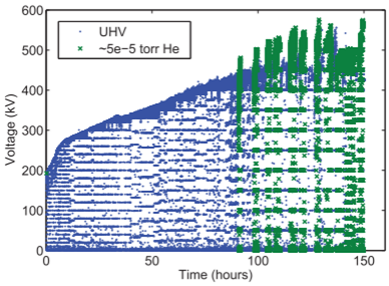


Figure 4.2.5: The voltage applied to the gun during conditioning, corrected for the voltage drop across the processing resistor. Data points are colored for UHV (blue dot) and gas (green x) conditioning.

HV conditioning to date has taken over 150 h. The gun was installed with a 600 kV DC power supply from Excelitas Technologies (we have a 750 kV and a 600 kV supply), in an $SF_6$ environment at 3 bar. The gun is connected to the power supply via three 300 MΩ film resistors (Nichrome Electronics, model 1000.300), each 1 m long, connected in parallel for redundancy. This processing resistor limits the current applied to the gun in case of a short circuit through an arc in the gun. Each segment of the insulator has two parallel sets of 1 GΩ resistors (Caddock resistor model MG815), giving the insulator a total resistance of 7 GΩ, as verified by an electrometer. Thus, a given voltage V applied by the power supply corresponds to a voltage across the gun of $(10.014) \times V$, as 1.4% of the supply voltage is dropped across the processing resistor.

A principle figure of merit during HV conditioning is the current drawn by field emitters or by fast emission events often called pre-breakdown events [3]. This current is read by a floating ammeter attached to the HVPS at high voltage. The floating ammeter is powered by infrared diode laser and photocell, via a fiber optic feedthrough in the $SF_6$ tank. Data from the ammeter is transmitted via a fiber optic transmitter/receiver. In principle, the total current could be read from the power supply itself, however the power supply has an associated leakage current which makes this value difficult to interpret, and does not have adequate resolution. However, this value is used to trip off the gun during a pre-breakdown event. The value was chosen such that the vacuum and emitted currents were within acceptable levels.

The floating ammeter has a maximum readable current of 150 $\mu$A. Furthermore, the insulator resistor chain has an expected current draw for a given voltage of 10-100 $\mu$A. Thus, there is limited headroom for the measurement of any excess current, defined as the difference of the expected current to the actual current, which decreases with increasing voltage. As such, many pre-breakdown events saturated the floating current monitor. This saturation does not affect the reading of the resistor chain excess current monitor.

The conditioning was performed with an anode-cathode gap of 50 mm. The voltage across the gun was slowly increased to a state of pre-breakdown, most often to the point of tripping off due to exceeding the current limit setting, with subsequent attempts permitting higher and higher voltages before tripping. The first voltage at which vacuum disturbance was detected was approximately 185 kV. Fig. 4.2.5 shows that the majority of our voltage progress was linear with time. Spikes of the resistor chain excess current correspond to emission from the HV stalk surface to the copper insulator guard rings, and was treated with extra caution, as such emission had previously caused punch-through in unprotected insulators. Large emission to the rings in the first 10 h of conditioning were found to abruptly cease, and the overall emission to the rings from them was usually less than 50 $\mu$A. After approximately 30 h of conditioning, we found that the integrated gas load on the NEG pumps was nearing saturation. At this time we also observed a downturn in the slope of progress. We believed this to be due to the increased gas load in chamber, as residual gas that is not pumped can be ionized to initiate pre-breakdown events. However, after NEG reactivation, the conditioning resumed without issue, and the slope of voltage progress increased back to its original value.

At voltages above 400 kV, field emitters began to be created that could not be pacified by normal UHV conditioning. We found that helium or krypton gas processing to be effective in suppressing these emitters (shown in green in Fig. 4.2.5). For gas processing, $5 \times 10^{-5}$ torr of gas was introduced into the gun via leak valve, with all ion pumps off and an external turbo pump connected. Noble gases are not well pumped by the NEG's, so do not saturate them. The use of gas routinely allowed a voltage setting above 500 kV, at which fields the more stable field emitters would show a gradual decrease in current drawn, and ultimately each one is eliminated. Conditioning then continued with alternating rounds of UHV and gas conditions, allowed us to apply conditioning voltages above 500 kV in UHV. At this time, the gun is stable enough for operations at 450 kV, but further processing is needed to be stable at 500 kV.

## 4.3 Photocathodes

During the original work on the ERL injector, GaAs photocathodes were used, as they are known to have the lowest intrinsic emittance of any photocathode, and our group had extensive experience with GaAs from polarized electron sources. It quickly became clear that GaAs photocathodes should not be used, due to their extreme sensitivity to vacuum conditions and poor lifetime at high average currents.

We switched to alkali photocathodes, which are known to be more robust from previous RF gun use [4] and as detectors in photomultiplier tubes. Following on the work of others, we developed recipes to grow various alkali cathode (a,b,c) and measured their properties. Numerous papers by our team give details on thermal emittance measurements and high current operation. Overall, alkali-type cathodes have roughly the same thermal emittance as GaAs cathode (at 520 nm), but are much less sensitive to vacuum disturbances and thus have reasonable lifetime.

The properties of various alkali cathodes have been measured by our group (see references). For operations, we typically use NaKSb type photocathodes, which are known to survive even at elevated temperatures. We performed high average current lifetime measurements using

a cathode of this type. Fig. 4.3.1 shows a plot of average current and quantum efficiency as a function of time, demonstrating that, with adequate laser power, one can operate for approximately 1 week using a single cathode.

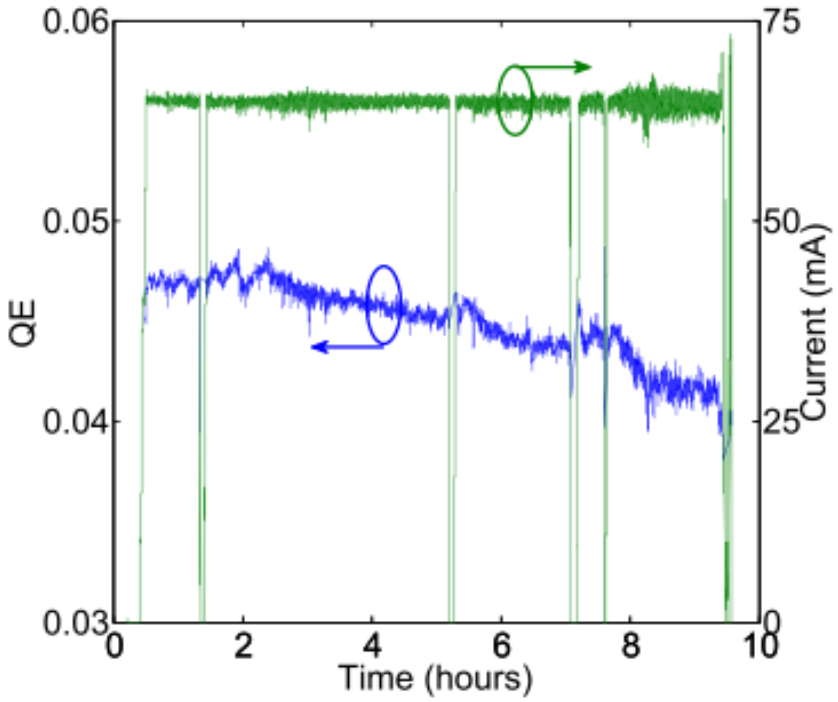


Figure 4.3.1: Photocurrent and QE of a NaKSb photocathode operated in a high average current run of the ERL injector. 65 mA of average current was been delivered for about 9 h. QE degradation with a 1/e time constant of 66 h was observed

## 4.4 The Laser System

The key design parameters of the ERL photoinjector laser system are given in Tab. 4.4.1. A brief justification for these parameter choices follows. The wavelength chosen for the laser is 515–530 nm – corresponding to the frequency of doubled Ytterbium fiber laser. This wavelength is a reasonable match to the desirable properties of alkali cathodes, and it is relatively easy to generate significant average optical powers. Yb lasers allow the generation of a high frequency comb of pulses with a range of optical pulse widths. It is also relatively easy to shape these visible optical pulses transversely and longitudinally, and to control the light reaching the photocathode with fast electro-optic devices.

As noted earlier, it is realistic to deliver 100 mA average beam current for >50 hours from a small illuminated spot on an alkali photocathode provided that 20 W of optical power can be delivered to the photocathode. Between the exit of the laser and the photocathode, a large number of optical and electro-optical devices are necessary, to transversely and longitudinally shape the optical pulses, transport them from the laser exit to the photocathode, focus them

Table 4.4.1: Key design parameters for the ERL photoinjector laser system

| | |
|---|---|
| Wavelength | 515–530 nm |
| Average power at the cathode | 20 Watts |
| Repetition rate | 325 MHz |
| Synchronization to external an RF signal | Better than 1 ps rms |
| Pulse duration (rms) | 10-30 ps |
| Pulse temporal shape | flat top, $< 2$ ps rise and fall |
| Transverse shape | Elliptical |
| Power stability | Better than 2% |
| Position stability | 10 microns rms |

on the photocathode, provide a suitable means to start up beam delivery for both tuning and full power operation, and finally to rapidly terminate beam delivery in the case of a fault. The large number of optical elements means that even with antireflection coatings on all surfaces, there will be a very significant optical power loss, from both reflection and absorption, between the laser and the photocathode. A factor of two loss is not exceptional, and indeed, requires care to achieve. Accordingly, we require that the laser system provide at least 50 W of average optical power at its exit, which has already been achieved. An even larger value may be required to provide additional headroom for optical losses, laser beam shaping, and feedback overhead.

The synchronization of the laser output pulses with the RF signal from the Master Oscillator affects the timing jitter of the beam bunches with the accelerator RF. This timing jitter is compressed during the bunching that takes place in the injector by a factor of 10–20. The present laser system has already achieved $< 1$ ps rms jitter.

The 10–30 ps optical pulse duration requirement is based on simulations showing that this pulse width range gives the smallest final beam emittance from the injector (the actual value is not very critical due to the presence of RF buncher). It is unlikely this pulse width range will be generated directly in the laser – rather it will be obtained by external optical pulse shaping. These simulations also show that the rise and fall times of the individual optical pulses must be no more than a few percent of the total pulse width, and that the smallest emittance is obtained with a transverse beam profile approaching elliptical shape (which can be well approximated with a truncated Gaussian beam).

A power stability of 1% is typically the best such a high power laser can produce without feedback. The sources of instability are thermal drift in mechanical components, vibrations in gain fibers or crystals, and noise in the pump lasers. For Yb-fiber lasers, the inversion time is on the order of milliseconds, producing noise at kHz rates, but the pulse-to-pulse stability at 325 MHz will be very good as the time between pulses is much shorter than this. Pump lasers can generate noise at many frequencies, from typical line frequencies to 100+ kHz for those using switching supplies. The electron beam current stability will need to be better than 1%, thus requiring a series of slow and fast feedback systems between the beam and the laser.

Poor pointing stability leads to a smearing out of the electron beam size (and shape), leading to emittance growth. Beam simulations show that a 10 $\mu$m rms position jitter is acceptable from the point of beam centroid jitter, which generally responds differently to the accelerator

optics than the beam envelope in the space charge dominated regime of the photoinjector. Based on our experience, the laser can achieve 10 $\mu$m rms jitter directly after second harmonic generation (SHG) crystal, at the position of a beam waist. Using a series of 1:1 imaging telescopes to transport the beam to the photocathode, the low jitter after the laser can be maintained. For cases when the position jitter specification cannot be met, position feedback systems exist which promise positional stability at these levels (www.Thorlabs.com)

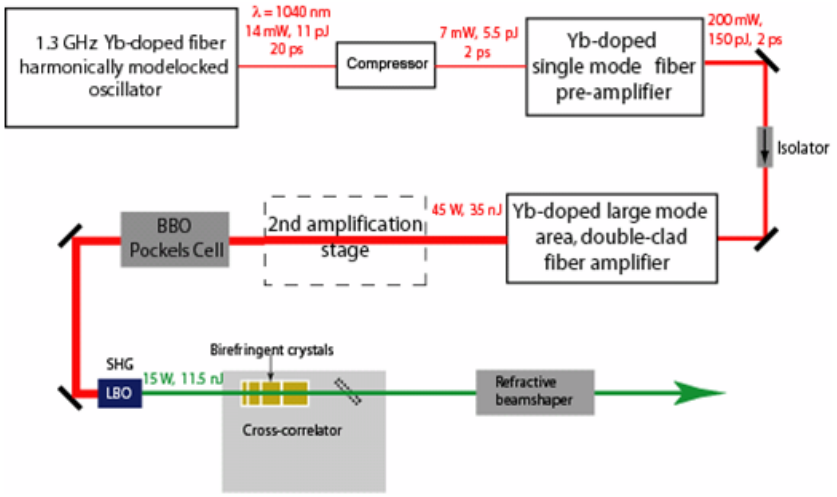


Figure 4.4.1: Drive laser system schematic.

The laser system is shown schematically in Fig. 4.4.1. The oscillator is a commercially built- harmonically mode-locked fiber laser [5]. It provides a 1.3 GHz train of 20 ps-long pulses synchronized to an external clock. For this project, a new oscillator operating at 325 MHz will be needed. The pulses are fed to a single mode fiber pre-amplifier where the pulse energy is boosted to 150 pJ (200 mW average power). This pulse energy is small enough to avoid nonlinear effects in the fiber. The required pulse energy of 100 nJ is achieved through amplification in a double-clad large-mode-area fiber amplifier built to work in a nearly single mode regime. The pulses are compressed to 2 ps after the amplifier using a pair of gratings. The amplified IR pulses are frequency doubled in a LBO crystal to produce pulses centered at 520 nm. Currently, with one high power amplification stage we have achieved 110 W average IR power and 60W average green power with good stability. This is the highest average power achieved with a fiber laser at this frequency.

As is well known, generating low emittance beams from a photocathode gun depends strongly on the laser shape incident on the cathode. We have developed a technique to shape the pulses longitudinally by stacking $2^n$ short pulses in $n$ birefringent crystals [6]. This technique produces a nearly flat-top laser pulse, has low optical losses, is easy to implement.

In the transverse plane, either a top-hat or an elliptical distribution is desirable for generating low emittance. We have tried a number of commercial devices with only moderate success. The old-fashioned method of expanding the laser before it passes through a pin-hole, then imaging the pinhole to the cathode is still the most reliable method. However, it wastes considerable beam power, leading to a rather high requirement for power at the laser exit. In our experience, the commercial devices are similarly inefficient in practical use.

Table 4.5.1: Buncher RF system specifications

| | |
|---|---|
| Operating frequency | 1.3 GHz |
| Cavity shunt impedance, Rsh = $V_{acc}^2/2P$ | 1.7 MΩ |
| Cavity quality factor | 20,000 |
| Nominal accelerating voltage | 120 kV |
| Cavity detuning by beam current at nominal voltage | 46.0 kHz |
| Cavity wall dissipation power at nominal voltage | 4.24 kW |
| Maximum accelerating voltage | 200 kV |
| Cavity detuning by beam current at maximum voltage | 27.6 kHz |
| Cavity wall dissipation power at maximum voltage | 11.8 kW |
| Maximum IOT output power | 16 kW |
| Amplitude stability | $8 \times 10^{-3}$ rms |
| Phase stability | 0.1° rms |

## 4.5 Buncher System

To reduce emittance dilution due to space charge effects in the beamline between the gun and the first superconducting cavity, the electron bunches are created at the photocathode with the rms duration of 10-30 ps or 5-14° at 1.3 GHz. On the other hand, to minimize a nonlinear energy spread due to RF waveform in the main superconducting linac, a much shorter bunch duration of about 2 ps rms is desirable. Hence, the bunch length has to be compressed after the gun. The first stage of the bunch compression happens in the beamline between the gun and the injector superconducting linac. As the beam is still non-relativistic at this point, the simplest method of bunch compression is the velocity bunching, a well-known technique used, for example, in klystrons. Rather moderate requirements for the buncher cavity voltage (up to 200 kV) make it possible to use a normal conducting structure. Table 4.5.1 summarizes buncher cavity and RF system specifications.

In order to maximize the energy variation along the bunch at a given cavity accelerating voltage $V_{\rm acc}$, the beam passes the buncher cavity $-90°$ off crest, i.e. at its zero-crossing. The RF power required to maintain a constant field in the cavity is then given by

$$P_{\rm forw} = \frac{V_{\rm acc}^2}{R/Q \cdot Q_{\rm ext}} \frac{(1+\beta)^2}{4\beta^2} \left[1 + \frac{Q_0^2}{(1+\beta)^2}\left(2\frac{\Delta\omega}{\omega} - \frac{I_b\, R/Q}{V_{\rm acc}}\right)^2\right] \tag{4.5.1}$$

where $\beta = Q_0/Q_{\rm ext}$ is the coupling factor of the input coupler, $\omega_c$ is the cavity resonant frequency, $\Delta\omega = \omega_c - \omega$, and $\omega$ is the RF frequency. It is desirable to minimize the required RF power with and without beam passing through the cavity. The minimum power of 5.8 kW is required at nominal accelerating voltage, if the cavity frequency is tuned to 1300.000 + 0.023 MHz and if the coupling factor is $\beta = 1.7$. Amplitude fluctuations of the buncher cavity voltage will affect the resulting bunch length. If the bunch length fluctuation should not be more than 0.1 ps rms, the amplitude stability requirement is only $8 \times 10^{-3}$ rms. The phase stability is derived from the required energy error and is 0.1° rms.

The buncher cavity [7] is a copper single-cell cavity that has an optimized spherical reentrant shape. A 3D view is shown in Fig. 4.5.1. The cavity input coupler is of a water-cooled coaxial

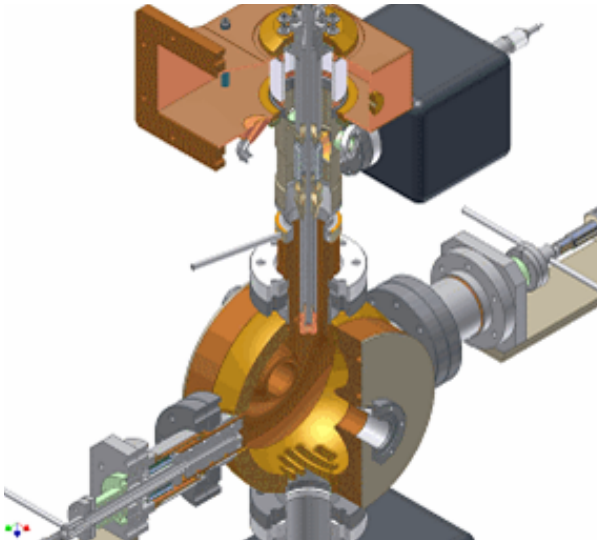

Figure 4.5.1: 3D view of the buncher cavity showing input coupler, plunger-type frequency tuner, pumping slots.

loop type. Its coaxial part is short and ends with a coax-to-waveguide transition, which incorporates a ceramic window. The coupling can be adjusted during installation by rotation of the coupling loop. The coupling loop, inner conductor and part of the outer conductor of coaxial line are water cooled. The cavity has two tuners with water-cooled 40 mm pistons. The pistons are moved by linear motion actuators with stepper motors. Two tuners provide a better field symmetry on the beam axis. Only one tuner is used for routine operation, the other one is used for preliminary frequency adjustment. During operation, the tuner has to compensate thermal effects (roughly 400 kHz from cold cavity to maximum voltage) and beam detuning. That corresponds to plunger travel of 2 mm. The full 15 mm stroke of one tuner gives a tuning range of 2.5 MHz.

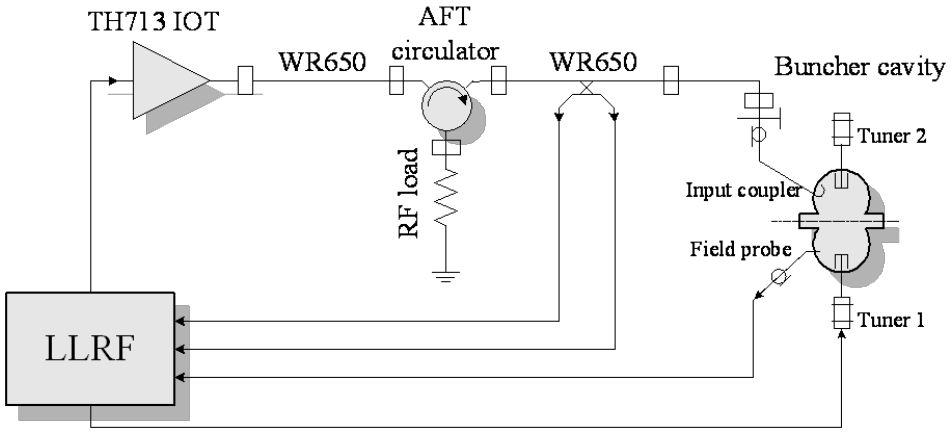


Figure 4.5.2: Block diagram of the buncher cavity RF system.

The buncher RF power station in the injector [8] comprises low level RF (LLRF) electronics, a high power amplifier (HPA), and waveguide transmission line components connecting the HPA to the cavity. The block diagram of the buncher RF is shown in Fig. 4.5.2. The HPA incorporates a 16 kW IOT tube in a commercial broadcast unit a photo of which is shown in Fig. 4.5.3. The HPA efficiency is 60% with a gain of 21 dB at maximum power output. The amplitude and phase ripple noise without the LLRF feedback are 0.13% and 0.5° respectively.


Figure 4.5.3: IOT inside the transmitter.

## 4.6 Injector Linac

### 4.6.1 Introduction

The ERL injector linac contains 5 2-cell superconducting RF cavities, each providing an energy gain of up to 1.2 MeV at maximum 100 mA beam current. RF power is transferred to each cavity via two input couplers, 'twin couplers', up to 120 kW per cavity. Efficient absorption of the HOM power is achieved by placing broadband HOM absorbers in the beam tube sections between the cavities. The cryomodule design is based on the TTF-III technology with modifications for CW operation.

A five-cavity injector cryomodule was designed and fabricated as part of the Cornell ERL Phase 1A effort with the goal of de In the following sections, the designs of the 2-cell SRF cavity, input coupler, HOM absorbers, LLRF system, and cryomodule are discussed in detail. The original injector was designed to support 100 mA beam currents, so this text reflects designs for 100 mA, even though we do not plan to operate at such a high level for the multi-pass ERL machine.

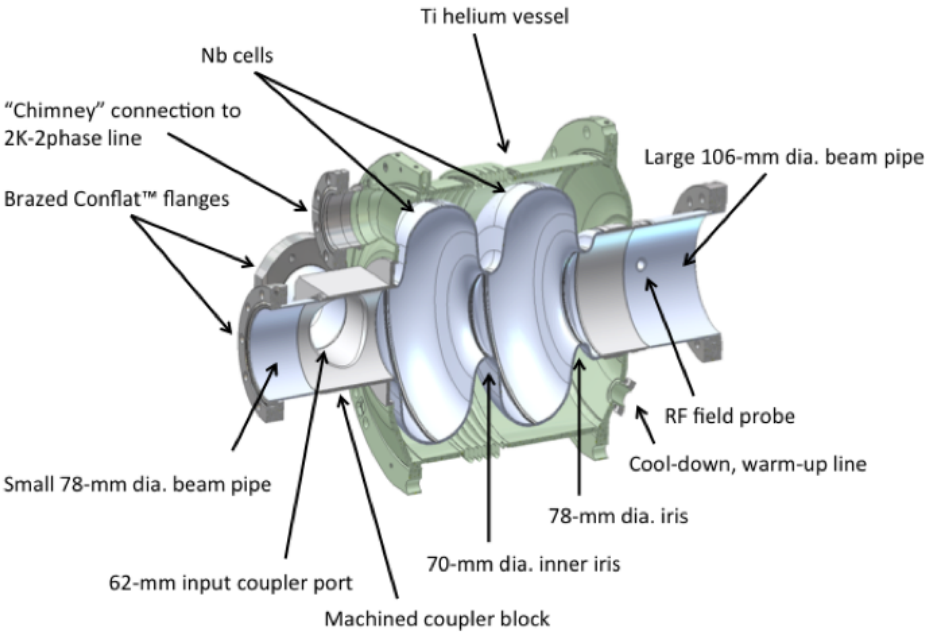


Figure 4.6.1: ERL injector cavity.

### 4.6.2 Injector cavities

Two-cell, 1.3 GHz superconducting cavities were developed for the ERL injector . The cavity design (Fig. 4.6.1) was optimized for handling high-current, low-emittance CW beams [9]. The cavity parameters are listed in Tab. 4.6.1. Efficient damping of the HOMs is essential to reduce resonant heating due to monopole HOMs and to avoid beam breakup instabilities due to dipole HOMs. Since the TTF-III technology was chosen as the baseline for the injector design, the inner iris diameter (70 mm) and the beam pipe diameter (78 mm) are identical to those of the TESLA cavity [10]. However, in this geometry the lowest dipole HOM (TE11-like) is trapped. To facilitate propagation of this mode toward a beamline HOM absorber, the diameter of one of the cavity beam pipes was increased to 106 mm. A 78 mm diameter iris at this end of the cavity keeps the electromagnetic fields of fundamental mode from leaking out of the cell. The cell shapes were optimized for a maximum value of $G \cdot R/Q$ to minimize the cryogenic load while ensuring that the frequency of the lowest TE11-like mode stays at least 10 MHz above the large beam pipe cut-off frequency.

To support a 100 mA CW beam, the input coupler has to be strongly coupled to the cavity and this induces a strong, non-symmetric local perturbation of the otherwise axially symmetric cavity fields. This produces a transverse kick to the beam even if it traverses the cavity on axis. To compensate for this kick, the injector cavity uses two identical symmetrically placed antenna type couplers (twin couplers) that are described below. An additional benefit of using twin couplers is a 50% reduction in the RF power per coupler. Optimization of the coupler antenna tip was part of the cavity design process. The result is a bent elliptic disc, which conforms to the radius of the beam pipe [11] and is shown in Fig. 4.6.2. Bending of the disc increased the coupling by 20%. Since one of the goals for the ERL injector was to explore a

Table 4.6.1: Parameters of the injector cavity

| | |
|---|---|
| Resonant frequency ($\pi$ mode) | 1.3 GHz |
| Accelerating voltage | 1.2 MV |
| Accelerating gradient, $E_{\mathrm{acc}}$ | 5.5 MV/m |
| Cells per cavity | 2 |
| $R/Q$ | 222 Ω |
| Geometry factor, $G$ | 261 Ω |
| Cavity quality factor, $Q_0$ | $> 1 \times 10^{10}$ |
| Nominal external quality factor, $Q_{\mathrm{ext}}$ | $5.4 \times 10^4$ |
| Cell-to-cell coupling | 0.7% |
| $E_{\mathrm{pk}}/E_{\mathrm{acc}}$ | 1.94 |
| $H_{\mathrm{pk}}/E_{\mathrm{acc}}$ | 42.8 Oe/(MV/m) |
| Small beam pipe diameter | 78 mm |
| Large beam pipe diameter | 106 mm |
| Inner iris diameter | 70 mm |
| Active cavity length | 0.218 m |
| Cavity length flange to flange | 0.536 m |

range of beam energies from 5 to 15 MeV, the input coupler was designed to be adjustable.

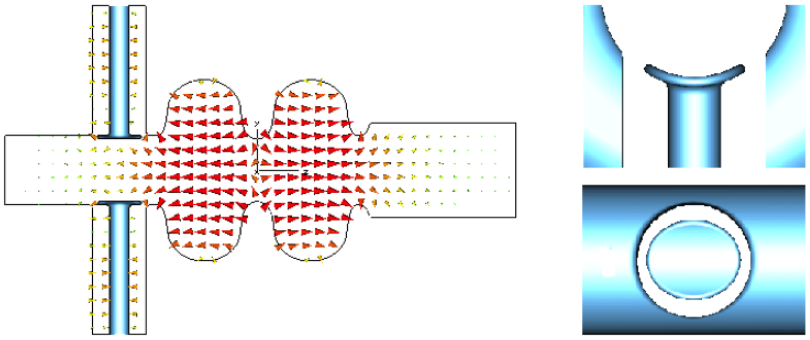

Figure 4.6.2: Geometry of the cavity and details of the coupler antenna with the electric field lines of the fundamental mode indicated

The TE11-like mode can have two polarizations resulting in two degenerate modes with identical resonant frequencies. The geometric perturbation introduced by the input couplers resolves the degeneracy and splits the modes into an 'in-plane' mode and a 'perpendicular' mode with respect to input couplers as shown in Fig. 4.6.3. The frequencies of the modes are different from the original one but stay high enough above the cut-off frequency. The in-plane mode is strongly coupled not only to the beam pipe but also to the input couplers resulting in an external $Q$ of 250, compared to the $Q_{\mathrm{ext}}$ of 1000 for the perpendicular mode.

Six cavities, one and five production cavities, were fabricated for the ERL injector . The inner surface of each completed cavity was etched to remove 120 $\mu$m with BCP 1:1:2 at a temperature below 15° C maintained by water-cooling the exterior of the cavity. Because of

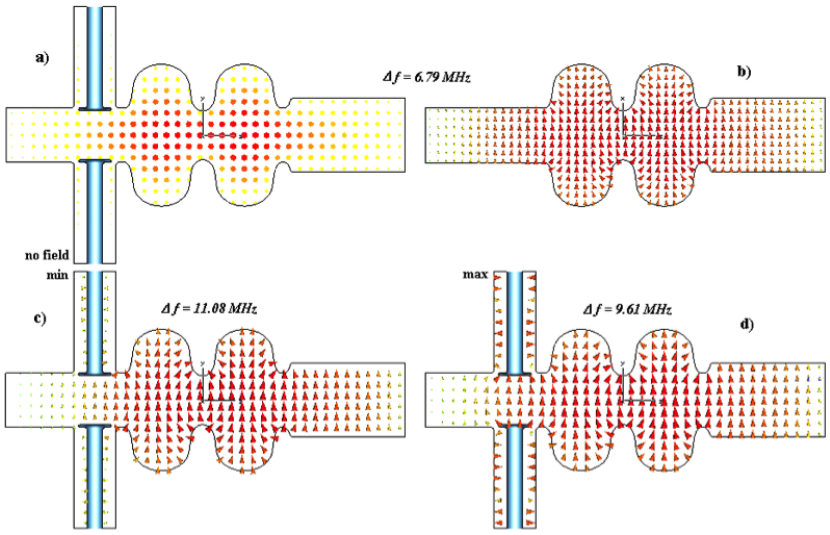


Figure 4.6.3: Electric field of the two dipole modes: a) and b) the 'perpendicular' mode; c) and d) the 'in-plane' mode with electric and magnetic walls at the ends of coaxial lines, respectively

the vertical orientation during etching, the cavity needed to be flipped to eliminate asymmetric removal across the cells. Brazed joints and knife edges at the ConFlat® flanges were protected with Teflon plugs to shield them from being attacked by the acid. After chemical etching, the cavity was rinsed with a closed-loop DI water system overnight followed by a four-hour session of high-pressure water rinsing in a clean room. All cavities reached the performance goal during vertical RF tests [12].

### 4.6.3 Injector input coupler

The input coupler is one of the key components of the injector linac due to strict requirements such as a high CW power transferred to the beam (up to 120 kW per cavity), strong coupling, wide range of coupling adjustment, and small distortion of transverse beam motion. Each injector cavity is equipped with two identical antenna type couplers symmetrically attached to a beam pipe of the cavity. This is a remedy to reduce RF power per single coupler, coupling to the cavity, and the transverse kick to the beam.

The design of the ERL injector couplers is based on the design of TTF III input coupler [13], consisting of a cold section mounted on the cavity in the clean-room and sealed by a 'cold' ceramic window, and a warm section incorporating a transition from the evacuated coaxial line to the air-filled waveguide. The warm coaxial line is sealed by a 'warm' ceramic window. Both windows are made of alumina ceramics and have anti-multipacting titanium nitride coating. Bellows in the inner and outer conductors of the coaxial line of the coupler allow a few mm of motion between the cryomodule cold mass and the vacuum vessel when the cavities are cooled from room temperature to 2 K. A low thermal conductivity is achieved by using stainless steel pipes and bellows with a 10–30 $\mu$m copper plating at the radio frequency conducting surfaces. Also, the bellows allow 16 mm of center conductor movement for coupling adjustment.

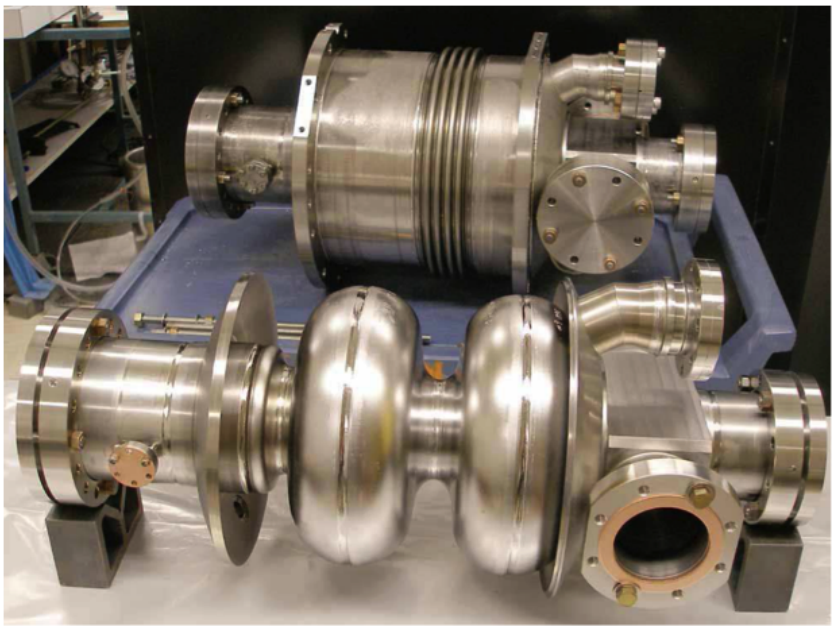

Figure 4.6.4: 2-cell cavity before and after welding the helium vessel

The ERL injector coupler design has, however, significant modifications necessary to handle much higher average RF power [14]:

- The cold part was completely redesigned using a 62 mm, 60 Ω coaxial line (instead of a 40 mm, 70 Ω) for stronger coupling, better power handling, and alleviating multipacting.
- The antenna tip was enlarged and shaped for stronger coupling.
- The 'cold' window was enlarged to the size of the 'warm' window.
- The outer conductor bellows design (both in warm and cold coaxial lines) was improved for better cooling (heat intercepts were added).
- Forced air cooling of the warm inner conductor bellows and warm ceramic window was added.

The parameters of couplers for the injector cavities are summarized in Tab. 4.6.2. The general design of the coupler is shown in Fig. 4.6.5.

Installed in a cryomodule, high power input couplers require conditioning at high RF power, especially if they were not pre-conditioned before installation. However, *in situ* conditioning is not as flexible as that in a dedicated set up: it is limited to only standing wave (full reflection) mode of operation. All input couplers were processed in pulsed mode up to 25 kW per coupler (50 kW klystron power) at full reflection. All couplers conditioned well, reaching these power levels within 25 to 75 hours (RF on time) of processing multipacting. If the conventional RF processing of multipacting is a limiting factor, two additional built-in measures of alleviate this phenomenon can be employed. First, the warm couplers can be baked *in situ* using special heating elements install on them. Second, a special capacitor assembly

Table 4.6.2: Parameters if the injector input power couplers

| | |
|---|---|
| Central frequency | 1.3 GHz |
| Bandwidth | ±10 MHz |
| Maximum RF power transferred to matched load | 60 kW |
| Number of ceramic windows | 2 |
| Qext range | $9.2 \times 10^4$ to $8.2 \times 10^5$ |
| Cold coaxial line impedance | 60 Ω |
| Warm coaxial line impedance | 46 Ω |
| Coaxial line OD | 62 mm |
| Antenna stroke | 16 mm |
| Heat leak to 2 K | $< 0.2$ W |
| Heat leak to 5 K | $< 3$ W |
| Heat leak to 80 K | $< 75$ W |

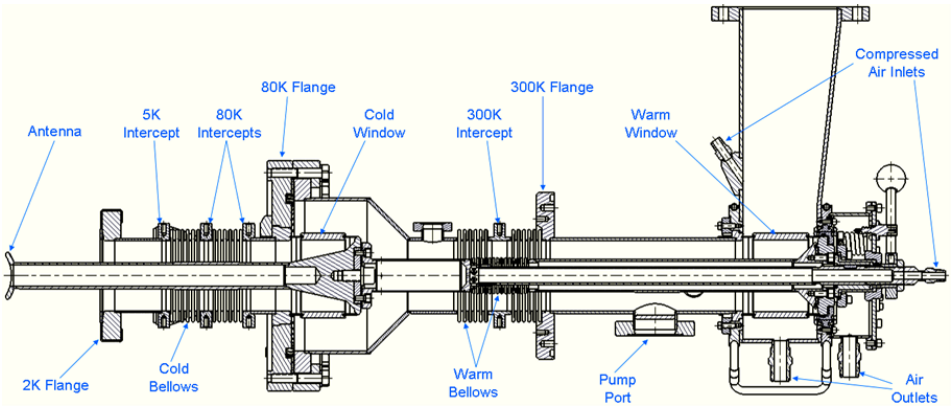


Figure 4.6.5: 2D section view of the injector input coupler.

can be installed, isolating the center conductor from ground and allowing use of DC bias for multipactor suppression.

### 4.6.4 Wakefield and HOM calculations

When the 100 mA beam current passes though the beamline in the injector cryomodule, the electron bunches will leave behind significant electromagnetic fields. The power transferred to these wakefields needs to be intercepted in the HOM absorbers located in the beam pipe sections between the individual cavities. In addition, these HOM absorbers need to damp monopole and dipole modes sufficiently to avoid excessive HOM power in case of resonant excitation of a monopole mode and to guarantee beam stability.

The longitudinal loss factor $k_{||}$ of a beamline section can be used to estimate the average power transferred from the beam to electromagnetic fields excited by the beam:

$$P_{\text{average}} = k_{||} \cdot q \cdot I \,, \tag{4.6.1}$$

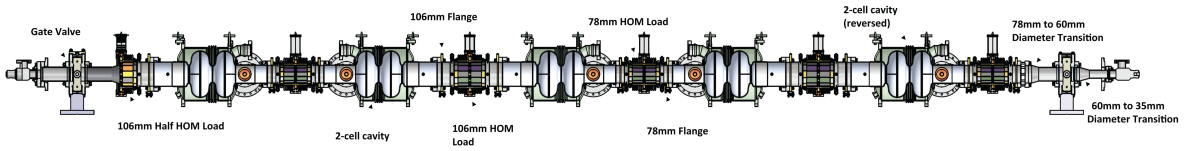


Figure 4.6.6: CAD model view of the Cornell ERL injector cryomodule beamline with five 2-cell cavities. Note that the full ERL injector will have 12 2-cell cavities. Beamline components from left (beam entrance) to right (beam exit): gate valve; 106 mm half HOM load; first SRF cavity; 78 mm HOM load; second SRF cavity; 106 mm HOM load; third SRF cavity; 78 mm HOM load; fourth SRF cavity; 106 mm HOM load; fifth SRF cavity; 78 mm HOM load; 78 mm to 60 mm diameter transition; gate valve; 60 mm to 35 mm diameter transition.

where $q$ is the bunch charge and $I$ is the average beam current. The total longitudinal loss factor of the beamline section with five 2-cell injector cavities as shown in Fig. 4.6.6 was calculated [15]. The result is a longitudinal loss factor of 6.4 V/pC per one-cavity section (32 V/pC for 5 cavities) at the design bunch length of $\sigma = 0.6\,\mathrm{mm}$, see Fig. 4.6.7. Accordingly, the average monopole mode HOM power excited by the 100 mA, 77 pC beam is found to be $\approx 50\,\mathrm{W}$ per cavity section, i.e. per HOM absorber.

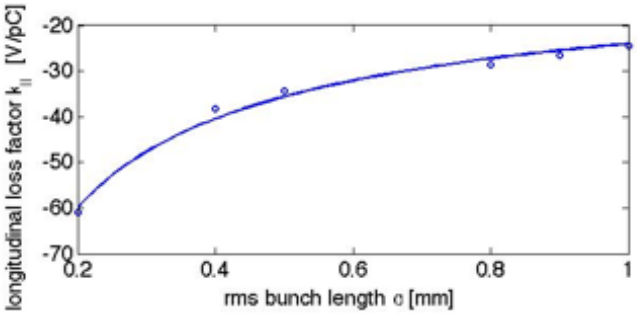


Figure 4.6.7: Total loss factor in the injector cryomodule beamline with 5 2-cell cavities as a function of bunch length.

To verify the effectiveness of the HOM damping scheme with HOM beam pipe absorbers located between the cavities as shown in Fig. 4.6.6, the resulting HOM damping was studied both numerically and experimentally. Figure 4.6.8 shows simulation results for the quality factors of monopole modes between 1.5 GHz and 5.5 GHz, as well as the product of $(R/Q)Q$, which is the figure of merit in case of resonant excitation of an HOM by the beam. The quality factors of the modes are reduced strongly to very low values of typically 100 to a few 1000. Only the modes of the accelerating TM010 passband at 1.3 GHz remain unaffected by the HOM dampers because their frequencies are below the cut-off frequency of the beam pipes at the cavity ends. Even in the unlikely event of resonant mode excitation, the power transferred to any of these strongly damped modes would be modest and well below the maximum power handling specifications of the HOM dampers. HOM measurements at the Cornell ERL injector cryomodule have confirmed these simulation results [16].

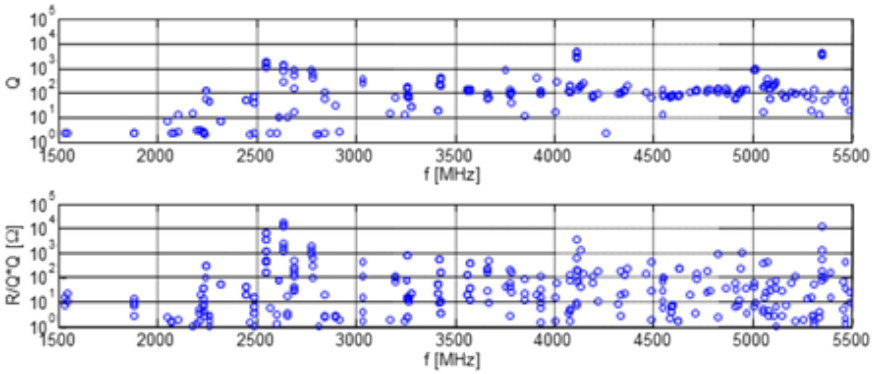


Figure 4.6.8: Simulated monopole mode damping in the full ERL injector (CLANS results). Top: Quality factor of all monopole modes between 1.5 GHz and 5.5 GHz. Bottom: $R/Q \cdot Q$ of these modes. Realistic complex dielectric properties where used in these simulations for the RF absorbing materials in the HOM dampers.

### 4.6.5 Injector HOM dampers

The requirements on the beam pipe HOM absorbers in the ERL injector are similar to the HOM damping requirements in the ERL main Linac. The only differences are (1) a factor of $\approx 4$ smaller average power to be intercepted per load and (2) slightly different beam pipe radii (39 mm and 53 mm instead of 55 mm in the main Linac). Therefore, the HOM dampers in the ERL injectors will be a modified version of the beam pipe HOM dampers developed for the ERL main Linac.

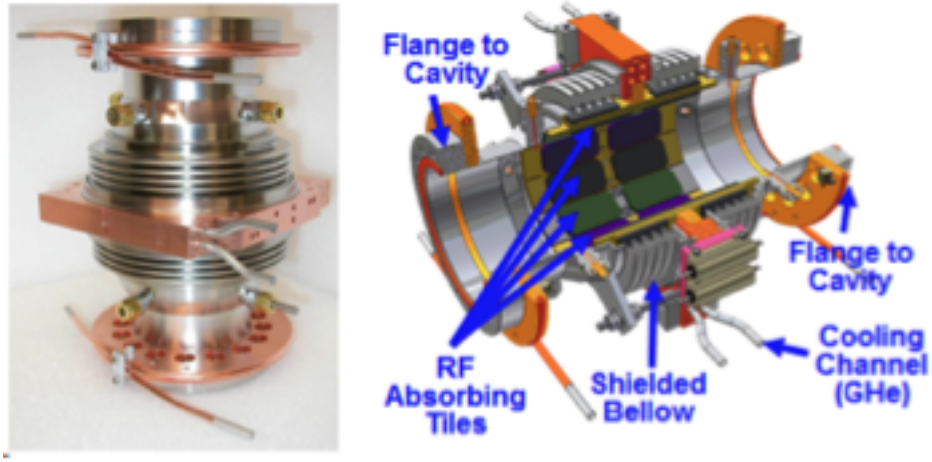


Figure 4.6.9: Cornell ERL injector HOM load. Left: Finished load. Right: Cut-open CAD model of the load showing the RF absorber tiles.

Cryogenic HOM beam pipe absorbers have been tested successfully in the Cornell ERL injector. Figure 4.6.9 shows one of the HOM loads prior to installation in the ERL injector beamline. The damping of HOMs in the injector cavities by these beamline absorbers was

investigated using a vector network analyzer to excite modes via pick-up antennas located at the cavity beam tubes and at the HOM loads (see Fig. 4.6.10). Preliminary results confirm very strong suppression of monopole and dipole modes with typical quality factors of only a few 1000 as predicted by simulations. Heater elements on the HOM absorber load bodies were used to verify the effective heat exchange to the high pressure cooling gas up to the maximum design heat load of 200 W; see Fig. 4.6.10. The measured temperature increase of the HOM load body was found to be in good agreement with simulation results.

The injector HOM designs suffered from several problems. The RF tile soldering was not robust, and several tiles detached and fell, generating dust and particles. In addition, two of the three tile types became insulating enough at 80 K that any charge accumulated on their surfaces would not bleed off. This charge could be from electrons scattered during beam tuneup, or from x-rays and UV light generated during cavity processing. The electrostatic fields generated from the charge buildup severely distorted the beam passing through the cryomodule, making the beam unusable. The tiles facing the beam were removed, and the solder joints improved on the others to eliminate these problems.

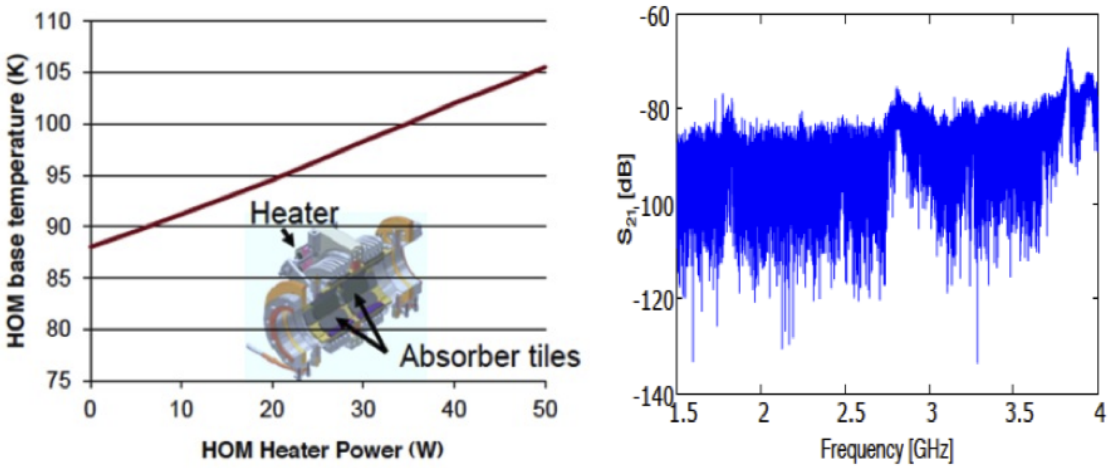


Figure 4.6.10: Left: Temperature of the HOM load temperature as function of power intercepted. The test was done at a relatively low cooling gas flow speed. Right: Vector network analyzer scan for HOMs between 1.5 GHz to 4 GHz. Shown is the transmission amplitude vs. scan frequency. Pick-up antennas on the cavities and HOM loads were used to couple to the HOMs.

### 4.6.6 Injector RF stability requirements and LLRF

The intra-bunch energy spread after the injector is about $\sigma_{\mathrm{inj}} = 15\,\mathrm{keV}$. It is desirable for the bunch-to-bunch energy fluctuation (bunch centroid energy) at the end of the injector to be below the intra-beam energy spread so that the total energy spread of the beam is dominated by the intra-bunch energy spread. The gun laser timing jitter, the buncher cavity as well as the five superconducting injector cavities each contribute to a bunch-to-bunch energy variation in the injector. We have to distinguish between uncorrelated and correlated (from

cavity to cavity) errors. For the ERL injector cavities, small fluctuations in the 100 mA beam loading will be the dominating source of field perturbation, which will cause correlated field errors. Accordingly, we shall assume here correlated field errors in the injector cavities. We will require that the bunch-to-bunch energy fluctuation caused by the injector SRF cavities increases the total energy spread at the end of injector by no more than 20%, i.e. to a total of 18 keV rms. Accordingly, the maximum allowable bunch-to-bunch centroid energy gain fluctuation is 10 keV, assuming no correlation between the intra-bunch energy spread and the bunch-to-bunch gain fluctuation. We will allow for 5 keV energy spread contribution from each phase errors and amplitude errors in the 12 injector cavities. This simple estimate results in a requirement for the relative amplitude stability of $\sigma_A/A = 5\,\mathrm{keV}/15\,\mathrm{MeV} = 3.3 \times 10^{-4}$. Assuming acceleration with a phase within 5 deg of on-crest then gives a requirement for the phase stability of $\sigma_p = 0.2^\circ$.

A digital LLRF control system will be used to stabilize the RF fields in the injector cavities in amplitude and phase to these stability levels. A combination of feedforward and feedback control will be used to stabilize the cavity fields in the presence of strong beam loading and other perturbations of the RF fields. Sensors will be used to monitor all relevant signals, including the cavity fields, the incident and reflected RF power, and the beam current. Any disturbances due to klystron noise and ripple can be handled using feedforward. Extremely reliable hardware, a high degree of automation, and sophisticated built-in diagnostics will ensure a high degree of operability, availability and maintainability of the LLRF system.

The LLRF control system has been tested extensively, showing excellent performance. This LLRF system is an improved generation of the LLRF system previously developed for CESR [17], with lower loop latency ($< 1\mu$s), reduced noise, and increased sample rates and ADC resolution (16 bits). The integral and proportional gains of the fast feedback loop used to stabilize the RF fields in the cavities were optimized. At optimal gains, exceptional field stabilities of $\sigma_A/A < 2 \times 10^{-5}$ in relative amplitude and $\sigma_p < 0.01^\circ$ in phase (in-loop measurements) have been achieved, far exceeding the ERL injector and ERL main linac requirements. In addition to the fast feedback loop, the system employs feedforward control to compensate beam loading and fluctuations in the high voltage of the klystrons, a state machine for automatic start-up and trip recovery, trip detection, and cavity frequency control.

### 4.6.7 RF Power System for the Injector Linac

The injector cryomodules house five 2-cell SC cavities, each delivering up to 120 kW to the beam. Because the cavities operate independently, the system consists of five identical channels. Each channel includes a set of LLRF electronics and RF interlocks, a klystron based HPA, and a waveguide distribution network. RF power is delivered to the cavities via twin input couplers [14] each carrying 60 kW. The main parameters of the system are given in Tab. 4.6.3 and a block diagram is presented in Fig. 4.6.11. A motorized, adjustable short-slot hybrid power splitter and a two stub phase shifter in one of the waveguide arms are used to are used to tune relative amplitude and phase between the two couplers [18]. A 170 kW ferrite circulator is used for klystron protection.

The klystrons were designed and manufactured by e2V cavity klystrons and have 165 kW saturated power output. Similar tubes are anticipated for the 12 cavity injector complement. To provide stable regulation of the cavity field the klystron must have finite gain and thus

Table 4.6.3: Main parameters of the injector cryomodule RF system and power source

| | |
|---|---|
| Number of RF channels | 5 |
| RF power per cavity | 120 kW |
| Maximum useful klystron output power with incremental gain of 0.5 dB/dB | $\geq$ 120 kW |
| Klystron efficiency at maximum useful power | $>$ 50% |
| Tube bandwidth at $-1$ dB | $\pm$2 MHz |
| Tube bandwidth at $-3$ dB | $\pm$3 MHz |
| Klystron gain at nominal operating conditions | $>$ 45 dB |
| Klystron beam high voltage | 45 kV |
| Typical klystron current | 5.87 A |
| Maximum klystron CW output power | 135 kW |
| Klystron saturated output power (pulsed) | 165 kW |
| Tube efficiency at saturated power | $>$ 60% |
| Cavity field amplitude stability | $9.5 \times 10^{-4}$ rms |
| Cavity field phase stability | 0.1° rms |

cannot run in saturation. The maximum power output for the tube was defined as 0.5 dB/dB of drive and specified to be no less than 120 kW. At this level the efficiency of the tubes is at least 50% and the bandwidth not less than $\pm$2.5 MHz at -1 dB level and not less than $\pm$3 MHz at -3 dB level.

### 4.6.8 Injector cryomodule

The ERL injector cryomodule design is based on TTF III technology with modifications for CW operation. This builds upon the considerable development work performed for this linac technology over the past 15 years. TTF III technology is at the forefront of SRF linac performance in regard to cavity gradient, $Q$, power coupled to the beam, cavity tuning, minimal cryogenic heat load, industrial fabrication, and operational reliability.

The modifications to TTF III technology for CW operation of an injector cryomodule are structurally subtle, but have significant operational differences. Among the modifications to the TTF III cryomodule are the following:

- Use 2 coax RF input couplers per cavity, where one 120 kW CW klystron feeds a cavity coupler pair, each coupler rated at 60 kW CW.
- The coax RF input couplers have outer conductors with 62 mm diameter and increased cooling for high average power.
- The SRF cavities have only 2 cells per cavity with a 0.2 m active length, operated at a nominal gradient of 6 MV/m (1.2 MeV) to deliver the 120 kW klystron power to the beam.
- 5 SRF cavities in the injector cryomodule.
- One side of the SRF cavity has a larger beam tube diameter, 106 mm, to allow better propagation and damping of HOMs.

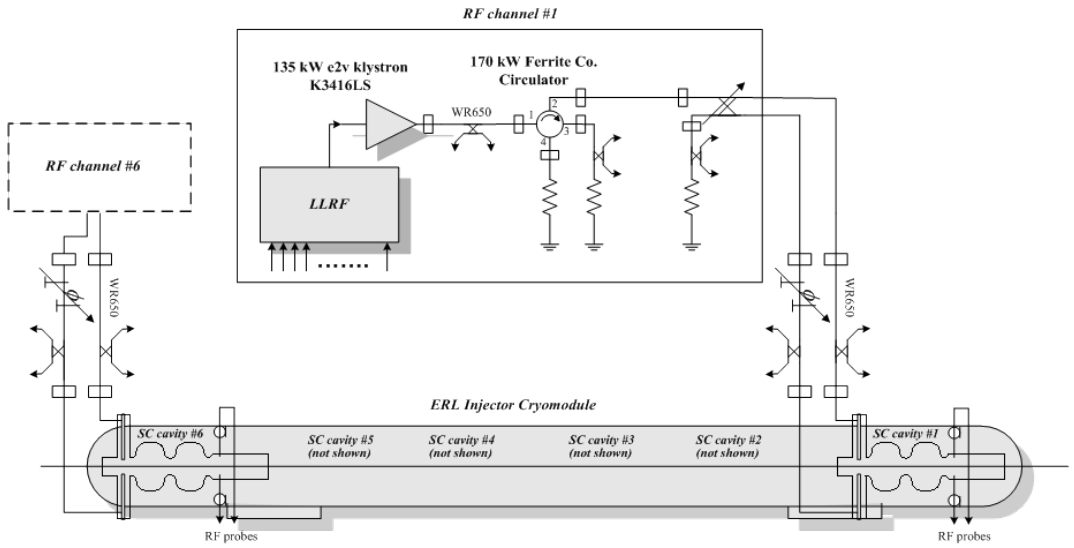


Figure 4.6.11: Block diagram of the ERL injector RF system (one cryomodule is shown).

- Implement beamline HOM Loads for strong broadband damping of HOMs generated by the high current and short bunches.
- Cooling of thermal intercepts is provided by small 'jumper' tubes with flowing He gas, such as to the HOM loads and the RF couplers, as opposed to copper straps.
- Use the INFN blade tuner with the addition of piezos for fast tuning.
- Locate access ports in the vacuum vessel to allow the tuner stepper motor to be accessible for replacement while the string is in cryomodule.
- Use precision fixed surfaces between the beamline components and the Gas Return Pipe(GRP) for easy 'self' alignment of the beamline.
- Use rails mounted on the inside of the vacuum vessel and rollers on the composite support posts to insert the cold mass into the vacuum vessel, as opposed to Big Bertha.
- Increase the magnetic shielding so that the cavity $Q$ is limited only by the BCS resistance.
- Do not include a 5 K shield.
- Increase the diameter of the cavity helium vessel port to 10 cm for the high CW heat load.
- Increase the diameter of the 2-phase 2 K He pipe to 10 cm for the high CW gas load.
- Use a module end-cap and cryogenic feed-cap with reduced length.

The ERL injector cryomodule is based on the TTF III module structure. All of the cavity helium vessels are pumped to 1.8 K (12 Torr) through a common 25 cm inside diameter

GRP which also serves as the mechanical support from which the beamline components are suspended. To minimize the heat load to the refrigeration plant, all of the 1.8 K cryomodule components are surrounded by 5 K intercepts to minimize the heat leak to 1.8 K, and the 5 K intercepts are likewise surrounded by 100 K intercepts, which absorb the heat load from the 293 K vacuum vessel. The GRP is suspended from composite support posts that are constructed from low-thermal conductivity G-10 fiberglass. The composite posts have integral metal stiffening disks and rings that also serve as thermal intercepts at 5 K and 100 K between the 1.8 K face that attaches to the GRP and the 293 K face that attaches to the vacuum vessel bosses that support the cold mass. There are stainless steel manifolds of smaller diameter than the GRP running the length of the module that transport the supply of liquid helium and the supply and return of 5 K and 100 K helium gas for the thermal intercepts. Jumper tubes with 5 mm inner diameter are connected between the 5 K and 100 K supply and return manifolds to the various thermal intercepts within a module. A shell of 6 mm thick, grade 1100 aluminum sheet surrounds the beamline and the GRP and is linked to the 100 K manifold to serve as a thermal radiation shield between the 293 K vacuum vessel and the cold mass. The aluminum 100 K shield has apertures through which the RF couplers pass and also has panels with instrumentation feedthroughs. The 100 K shield is mechanically suspended from one of the integral metal stiffeners in the composite support posts. Multi-layer insulation is wrapped around the exterior of the 100 K shield as well as all of the 1.8 K and 5 K cold mass components.

The magnetic shielding in the cryomodule must keep the field in the region of the SRF cavity to $< 2$ mG to have negligible residual SRF wall loss and provide a good safety margin for the goal of cavity $Q_0 = 2 \times 10^{10}$. Such a low field is accomplished by degaussing the carbon-steel vacuum vessel, lining it with Co-NETIC ® mu-metal shielding that will be at 293 K, and then wrapping each cavity's 1.8 K helium vessel with a magnetic shield that is formulated to have maximal shielding at the low temperatures around 4 K [19].

The injector cryomodule delivers high average power to the injected beam. Even with a modest cavity gradient of 6 MV/m and only 2 cells per cavity, the input RF power of 120 kW CW per cavity to the 100 mA beam is pushing the limits of input couplers, as described in §4.6.3. Having two RF couplers per cavity requires the vacuum vessel RF ports to be symmetrically located on each side of the cryomodule, as opposed to one coupler per cavity with ports along only one side of the module. Having only two cells per cavity makes the cavity much shorter than 7-cell or 9-cell cavities, and the cryomodule structure in the vicinity of the cavities more congested. The blade tuner is then slightly longer than the cavity helium vessel and the helium pumping port must be located on the end cone rather than on the OD of the helium vessel.

The beamline consisting of the cavities, HOM loads, cold couplers, tapers, and gate valves is assembled in a class 100 or better clean room. All components are flushed with filtered water or alcohol and individually receive a mild vacuum bake at 120° C for 24 hours. The components are mounted on an assembly fixture one by one in the clean room. Each added component is aligned to the other components with the only critical alignment being the azimuthal position about the beam axis. The azimuthal alignment is needed so that the flat precision mounting surface at their tops will mate to the planar precision surfaces on the GRP. This alignment can be accomplished with a simple accurate spirit level. Any longitudinal spacing or planar shift errors of the mounting surfaces are accommodated by the flex in the HOM load bellows. The

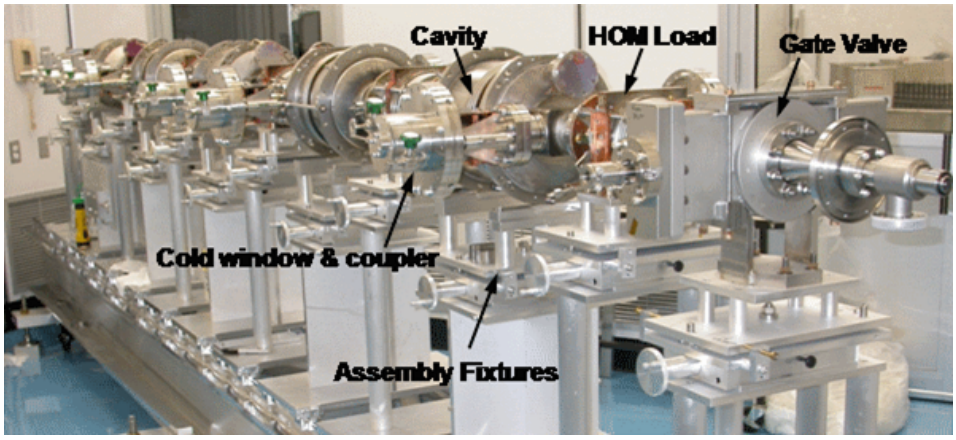


Figure 4.6.12: Assembled ERL injector beamline string in the clean room.

component mating vacuum flanges are then bolted together. A photograph of the assembled ERL injector beamline string in the clean room is shown in Fig. 4.6.12. After all components are assembled, the beamline string is vacuum leak tested while still in the clean room so that only filtered particulate-free air will pass through any potential leak. The pumping and purging during the leak test is performed at a slow rate of 1–2 Torr/minute through the viscous flow range of 760 Torr–1 Torr to minimize propagation of any particulate contamination throughout the beamline.

As a parallel operation to the beamline string assembly in a clean room, the cold mass assembly fixture can be set up in a high-bay area with overhead crane access. The composite support posts are attached to the GRP and the GRP is hung from the assembly fixture by the composite posts. The 2-phase pipe is then mounted to one side of the GRP and its exhaust is welded into the GRP.

After the beamline string passes the vacuum leak test, it is removed from the clean room and positioned underneath the cold mass assembly fixture. The string is raised and the precision mounting surfaces on the string and the GRP are brought together with integral alignment pins being engaged. The mating surfaces are then bolted together. A photograph of the injector beamline hung from the GRP is shown in Fig. 4.6.13. String attachment to the GRP in this manner proved to be quick and easy for the ERL injector, the entire procedure taking about 1 hour.

After the beamline is hung from the GRP, magnetic shielding layer I is attached to the helium tanks of the cavities. This shielding will reside at 1.8 K. Traditional Co-NETIC ® 'mu-metal' shielding derates at cryogenic temperatures to about 15% of its 300 K shielding capacity, so the magnetic shield I material is formulated to have maximal shielding at low temperatures [19].

The cavity blade tuners are attached after the magnetic shielding. The stepping motors of the tuners have to be wrapped in a copper sleeve that is tied to 5 K to prevent the motor heat from propagating to the helium vessel. The stepping motors are also wrapped with low temperature magnetic shielding since they can have stray fields of a few hundred mG, which would otherwise be present in close proximity to apertures in magnetic shield I.

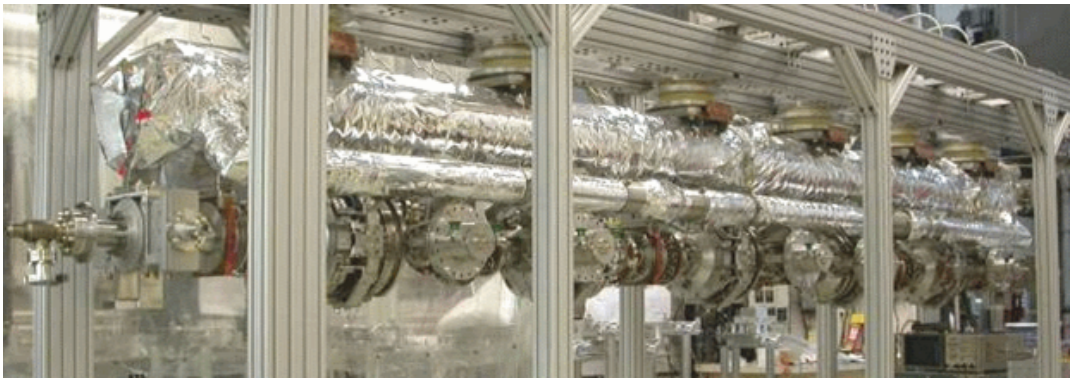

Figure 4.6.13: Beamline string hung from the GRP for the ERL injector .

Several cryogen manifolds run the length of the cryomodule. These manifolds include a 1.8 K liquid helium supply to the 'fill' ports located at the bottom of each of the cavity helium vessels, the supply and return of 5 K helium gas, and the supply and return of 100 K helium gas.

The liquid helium and 5 K gas manifolds are mounted close to the GRP using G-10 standoffs, thus keeping similar temperatures in close proximity to each other with low thermal conductivity connections between them. These manifolds are the next components mounted on the cold mass. Jumper tubes with 6 mm ID are then routed from the liquid helium manifold to the helium vessel fill ports. Jumper tubes from the 5 K gas manifolds are then connected to thermal intercepts on the HOM loads and RF couplers. This final joining of the stainless steel jumper tubes from the manifold to the thermal intercepts is performed by orbital welding. In standard TTF technology, the connections between the manifolds and the thermal intercepts are accomplished by copper straps. For the ERL injector with CW operation, both the 5 K and 100 K heat loads are large enough to require gas flow from the manifolds to the intercepts through jumper tubes.

The 100 K manifolds are mounted outboard of the 5 K manifolds and are attached to the 100 K thermal radiation shield. One of the 100 K supply lines cools the shield, and the return lines are hung from low thermal conductivity hangars. The material of the 100 K shield is grade 1100 aluminum, chosen for its high thermal conductivity and light weight. The shield is fabricated from standard flat panels that are cut and formed to shape. The top portion of the shield is attached to the 100 K ring of the composite support post and is 6 mm thick to support the weight of the cryogen manifolds and the lower portion of the shield.

After the cryogen manifolds and intercept jumpers are attached to the cold mass, low thermal conductivity coax cable is routed from the cavity RF field probes with thermal anchoring to the 5 K manifold, along with cabling from temperature sensors, helium level sticks, and other instrumentation. The lower half of the 100 K shield is attached and the instrumentation cabling is thermally anchored at this point to a 100 K instrumentation feed-through panel on the shield. The 100 K shield is then wrapped with 30 layers of Multi Layer Insulation (MLI) and the cold mass is ready for insertion into the vacuum vessel. A photograph of the completed 100 K shield being wrapped with MLI is shown in Fig. 4.6.14.

The cold mass that is wrapped with MLI is pushed into the vacuum vessel and then leveled

Figure 4.6.14: Photograph of the completed ERL injector 100 K shield being wrapped with MLI.

and aligned inside of the vacuum vessel using jack screws connected to the composite support posts at the top ports. The warm portions of the RF couplers are attached to the cold portions through side ports on the vacuum vessel while under small portable clean rooms. The vessel end plates are attached to the vacuum vessel and it is pumped out and vacuum leak tested.

## 4.7 Beam Stop

The primary beam stop (dump) must intercept the full beam current at the end of the energy recovery process, and safely dissipate the beam power as waste heat. The dump was originally designed to handle 600 kW of average power at a maximum energy of 15 MeV. For this project, the maximum current is 40 mA with an recovered energy of 6 MeV, so the existing hardware will be more than adequate.

The range of 15 MeV electrons is less than $8\,g/cm^2$ in practical beam dump materials, and thus the beam power is deposited over a very small depth. The natural beam spot size is quite small, even after energy recovery. The effective area of the beam then needs to be expanded to more than $1\,m^2$ where it intercepts the surface of the dump, to reduce the power density in the dump material to a level that can be safely handled. This expansion can be accomplished by several techniques, such as strongly defocusing the beam, rastering the beam over a larger area, or intercepting the dump surface at a shallow angle. All of these methods will be employed for the primary dump. Clearly the dump material must have a reasonably high-thermal conductivity, to limit the maximum temperature at the uncooled entrance face of the dump. As there is no significant shower multiplication from 15 MeV electrons, the surface of the dump, which is furthest from the cooling water, will have the highest temperature.

The only practical choice for the primary dump material is aluminum. Aluminum offers the very significant advantages of a high photoneutron threshold (13.3 MeV) and relatively low-residual radioactivity comprised primarily of short-lived isotopes. The relatively low-residual radioactivity of aluminum is a significant consideration for the ultimate disposal of a decommissioned beam dump. The aluminum used will be an alloy, and the various alloying elements

have lower photo-neutron thresholds. These elements will be responsible for a fraction of the residual radioactivity of a 15 MeV aluminum dump. Copper has a significantly lower photo-neutron threshold, and much higher residual radioactivity of longer-lived isotopes. Beryllium would be exceptionally expensive, and has a very low photoneutron threshold. Carbon, as pyrolytic graphite, is mechanically difficult, and has an extremely anisotropic thermal conductivity.

The dump must remain fully functional during several decades of operation at very high average power. With an aluminum dump, it is especially critical to control the water chemistry to avoid corrosion. Therefore, heat will be removed from the primary beam dump with a closed circuit de-ionized (DI) water circulation system, which will be continuously powered. The only acceptable metals in this system are aluminum and stainless steel. The water chemistry will be carefully monitored at all times to assure proper pH, resistivity, and the absence of harmful ions.

It is very desirable to minimize the deposition of beam power directly in the cooling water, to minimize hydrogen production through radiolysis [20]. At the same time, it is desirable to locate the cooling water as close as practical to the interior surface of the dump to minimize thermal effects. These realities led directly to the use of a dump shaped like an ogive (pointed arch) of revolution, similar to a high-power klystron collector. Even with an optimum thickness dump wall, there will be enough radiolysis in the cooling water to require monitoring the hydrogen level in the closed cooling circuit. It is anticipated that the modest quantities of hydrogen generated can be vented to the atmosphere, with no need for hydrogen recombination systems. Were hydrogen recombination to prove necessary, reliable hydrogen recombination systems were developed for the high-power beam dumps at SLAC, and were duplicated, with improved instrumentation, for the high-power dumps at Jefferson Lab [20, 21]. The 15 MeV beam energy is far too low to produce either tritium or $^{7}$Be through spallation of oxygen, so there will be no direct long-lived radioactivity in the DI water circuit. Heat will be removed from the closed DI water circuit with a water-to-water heat exchanger. The pumps, deionization and filtration equipment, surge tank, hydrogen-venting scheme, and water-to-water heat exchanger will be located remote from the dump itself, to allow servicing and to eliminate any potential for radiation damage. All plumbing and piping in the closed-circuit system will be of either aluminum or stainless steel.

The primary dump will be a powerful source of prompt, low-energy gamma radiation as well as a modest flux of low-energy neutrons. The primary radiation shielding for the dump will consist of steel and concrete blocks that completely surround it. Detailed calculations of the total radiation from the dump have been made with the code MCNPX.

If the dump were to be operated in normal air, significant quantities of nitric acid could be produced by radiolysis of nitrogen, leading to the production of nitric oxide, which oxidizes to form nitrogen dioxide, which, with water, forms nitric acid. As a consequence, dump area may need to be purge with an inert gas to eliminate the possibility of nitric acid formation. This solution has proven very effective with the two high-average power (1 MW) beam dumps routinely operated at Jefferson Laboratory.

Although it is very desirable to isolate the dump from the accelerator vacuum system, this is simply not possible. For example, even in a beryllium window, the power deposition from the $dE/dx$ losses of a 100 mA average current beam is 30 kW per mm of window thickness (the window thickness is irrelevant for cooling considerations). It is certainly not practical,

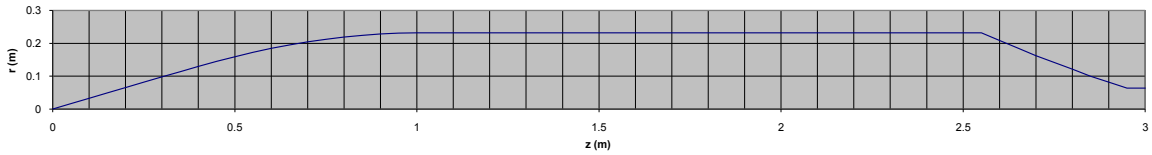


Figure 4.7.1: The inner surface profile of the beam dump

and likely not possible, to remove such a large amount of heat from a thin window in vacuum. Thus, the beam dump will of necessity be within the accelerator vacuum system. A differential vacuum pumping system will be used to isolate the high-gas load from the dump when operating at high average beam power from the much lower pressure in the beamline from the accelerator. Finally, a reasonably fast-acting, RF shielded gate valve will be located well upstream of the beam dump, to provide protection to the accelerator in the event of a dump failure. This is very important as the superconducting Linac is relatively close to the primary beam dump.

Figure 4.7.2: The completed beam dump before installation of the shielding blocks.

The profile of the inner surface is shown in Fig. 4.7.1. The 3-meter-long dump was assembled from three shorter segments by electron beam welding. A photograph of the completed dump is shown in Fig. 4.7.2. Water cooling channels are machined in the outer surface of the dump body, which is mounted inside an aluminum jacket. To reduce thermal stresses, the dump body is free to move longitudinally within the jacket. GEANT was used to calculate the power deposition in the dump body, and ANSYS calculations then determined the temperatures throughout the dump, the thermal stresses, etc. The results of some of these calculations are given in Fig. 4.7.3. Beam on-off cycles are sudden, and result in rapid temperature changes, which in turn may lead to eventual fatigue failure. The water flow was chosen to limit the maximum temperature differentials in the dump, leading to a very large number of temperature

cycles before the onset of fatigue failure. For the design of a 60 gpm water flow, the flow velocity is only 1.71 m/sec. Erosion of water channels will therefore not be a problem.

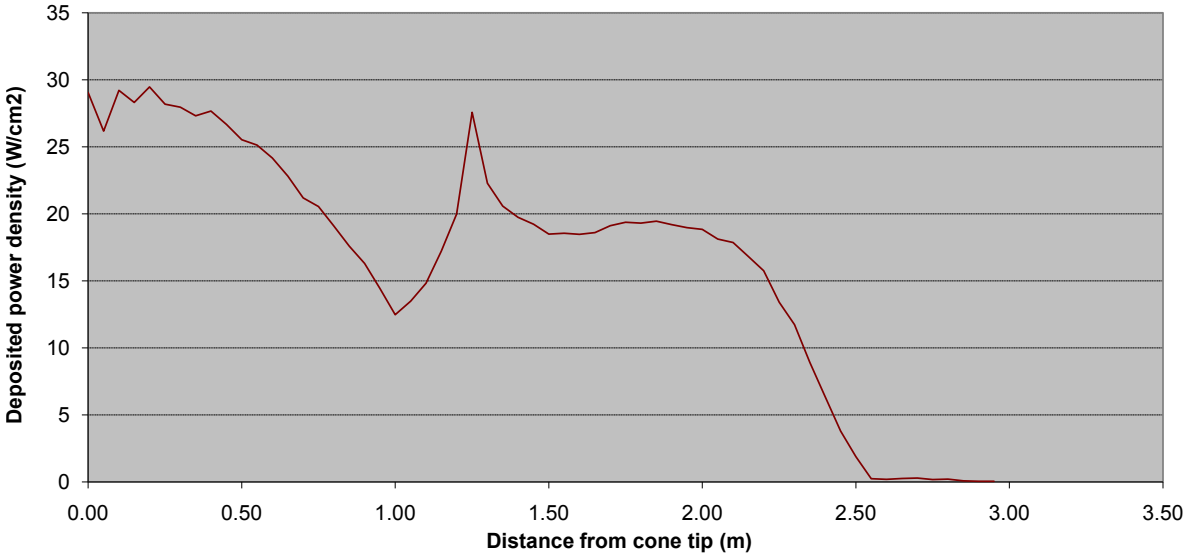


Figure 4.7.3: Energy deposition for 600 kW beam power at optimized condition

Two active devices are used to enlarge the beam area at the dump surface – a quadrupole that strongly over-focus the beam, and a sextupole with the coils powered such that one can make an arbitrary ellipse shape. The final result of the quadrupole field and sextupole kick is a raster pattern that move the beam spot in a circular path at 60 Hz. If either of these devices failed, the dump would rapidly overheat, quite possibly to the point of damaging, or even melting the dump surface, particularly if there were a transition from nucleate to film boiling at the water-metal interface. Redundant hardwired interlocks will assure that each of the beam focusing and rastering magnets is properly powered. On any interlock failure, the beam will be aborted. Similar interlocks will be provided on the cooling water flow, pressure differential, and temperature. Field strengths, cooling requirements, and sweep amplitudes of the said system for this design are based on previous operational experience.

It is important that the beam is not only properly enlarged, but that it is also correctly positioned in the dump. A quadrant detector at the entrance to the dump will assure the correct beam size and position at the dump entrance, while upstream BPMs will assure the correct entrance angle. Each element of the quadrant detector will cover close to 90 degrees of azimuthal angle, and will intercept a very small fraction of the beam. The elements must be water-cooled, protected from RF heating, and the ceramics providing electrical isolation shielded from the possibility of charging from stray scattered electrons. Basically, each element is a low-efficiency Faraday cup, and thus must be thick enough to assure beam electrons are dumped. Interlocks on the amplitude of the DC and 60 Hz left-right and up-down difference signals assure that the quadrupole over-focusing and raster amplitude are correctly set, and that the beam centroid is properly centered on the dump.

The existing beam dump has been tested up to power levels of 350 kW, so no problems are expected with the maximum beam parameters of 6 MeV and 40 mA for the CBETA project.

## References

[1] Haimson, J. *Recent Advances in High Voltage Electron Beam Injectors.* Nuclear Science, IEEE Transactions on, **22** (3), pages 1354 –1357 (june 1975).

[2] Fremerey, J. K. *Residual gas: Traditional understanding and new experimental results.* In *Proceedings of the 14th International Vacuum Congress (IVC-14)*, page 197. Birmingham, UK (1999).

[3] Temnykh, I. A. and C. K. Sinclair (2009). Unpublished.

[4] Akre, R., *et al. Commissioning the Linac Coherent Light Source injector.* Phys. Rev. ST Accel. Beams, **11** (3), page 030703 (Mar 2008).

[5] PriTel, Inc., Naperville, IL 60567.

[6] Bazarov, I. V., *et al. Efficient temporal shaping of electron distribution for high-brightness photoemission electron guns.* Phys. Rev. ST Accel. Beams, **11** (4), page 040702 (Apr 2008).

[7] Veshcherevich, V. and S. Belomestnykh. *Buncher Cavity for ERL.* In *Proceedings of the 2003 Particle Accelerator Conference*, pages 1198–1200. Portland, USA (2003).

[8] Belomestnykh, S., *et al. CW RF systems of the Cornell ERL Injector.* In *Proceedings of the XXIV Linear Accelerator Conference*, pages 857–859. Victoria, BC, Canada (2008).

[9] Shemelin, V., *et al. Dipole-mode-free and kick-free 2-cell cavity for the SC ERL injector.* In *Proceedings of the 2003 Particle Accelerator Conference*, pages 2059–2061. Portland, USA (2003).

[10] Aune, B., *et al. Superconducting TESLA cavities.* Phys. Rev. ST Accel. Beams, **3** (9), page 092001 (Sep 2000).

[11] Liepe, M., *et al. Design of the CW Cornell ERL injector cryomodule.* In *21st Particle Accelerator Conference (PAC 05)*, page 4290 (2005).

[12] Geng, R. L., *et al. Fabrication and performance of superconducting RF cavities for the Cornell ERL injector.* In *Proceedings of the 2007 Particle Accelerator Conference*, pages 2340–2342. Albuquerque, NM (2007).

[13] Dwersteg, B., *et al. TESLA RF Power Couplers Development at DESY.* In *Proceedings of the 10th Workshop on RF Superconductivity*, pages 443–447. Tsukuba, Japan (2001).

[14] Veshcherevich, V., *et al. Design of High Power Input Coupler for Cornell ERL Injector Cavities.* In *Proceedings of the 12th International Workshop on RF Superconductivity*, pages 590–592. Ithaca, NY (2005).

[15] Liepe, M. and R. Wolf. *Wake Fields in the Cornell ERL Injector.* In *the 2009 International Workshop of RF Superconductivity.* Berlin, Germany (2009).

[16] Liepe, M., *et al. High-current ERL Injector*. In *Proceedings of the 2009 International Workshop of RF Superconductivity*. Berlin, Germany (2009).

[17] Liepe, M. *et al. A new Digital Control System for CESR-c and the Cornell ERL*. In *SRF03* (2003).

[18] Belomestnykh, S., *et al. Development of High Power RF Power Delivery System for 1300 MHz Superconducting Cavities of Cornell ERL Injector*. In *Proceedings of XXII International Linear Accelerator Conference*, pages 694–696. Luebeck, Germany (2004).

[19] Amuneal Manufacturing Corp. Technical report, Philadelphia, PA, USA, Amumetal 4k (A4K) (2010). http://www.amuneal.com/magnetic-shielding/idea-share/whats-new-cryogenic-shielding.

[20] Walz, D. R., *et al. Beam Dumps, Energy Slits and Collimators at SLAC–Their Final Versions and First Performance Data*. IEEE Transactions on Nuclear Science, **14** (3), pages 923–927 (1967).

[21] Wiseman, M., *et al. High power electron beam dumps at CEBAF*. In *Proceedings of the 1997 Particle Accelerator Conference 3*, pages 3761–3763. Vancouver, B.C., Canada (1997).

# 5 Linac and RF systems

## 5.1 Introduction

For CBETA, the accelerator module in the ERL loop will be the MLC, which has been built as a prototype for the Cornell ERL project. This cryomodule houses six SRF 1.3 GHz, 7-cell cavities, powered via individual 5 kW CW RF solid state amplifiers, providing a total single-pass energy gain of up to 75 MeV. HOM beam line absorbers are placed in-between the SRF cavities to ensure strong suppression of HOMs, and thus enable high current ERL operation. The module, shown in Fig. 5.1.1, was finished by the Cornell group in November 2014 and was successfully cooled-down and operated starting in September 2015. Detailed design considerations and parameters for this cryomodule can be found in Cornell ERL PDDR [1]. In the following sections we will summarize the main features of the MLC as relevant for CBETA and describe the performance that has been measured so far.

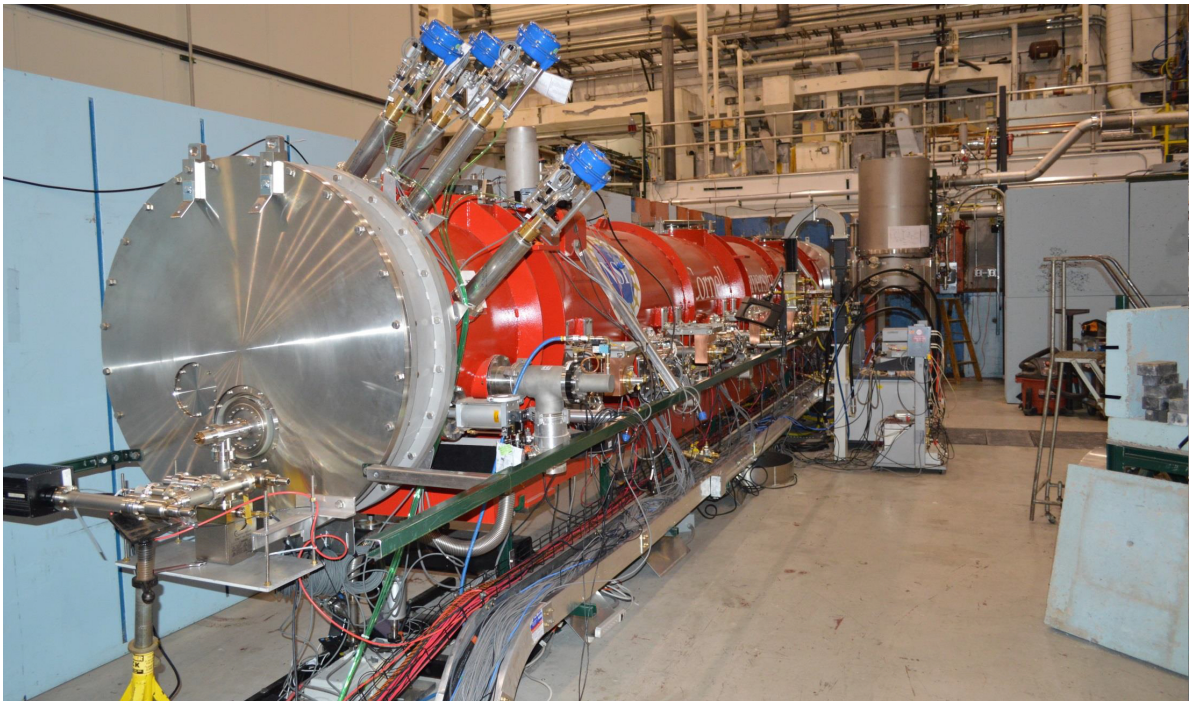

Figure 5.1.1: The Cornell Main Linac Cryomodule (MLC) installed for RF testing at Cornell.

## 5.2 MCL Overview

The layout of the linac cryomodule is shown in Fig. 5.2.1. The 10 m long module houses six superconducting cavities, operated in CW mode at 1.8 K. These 7-cell, 1.3 GHz cavities with a design $Q_0$ of $2 \times 10^{10}$ at 1.8 K can provide an average accelerating field of up to 16 MV/m (corresponding to 12.8 MeV energy gain per cavity). Each cavity is driven by a separate 5 kW solid state RF amplifier to ensure maximal flexibility and excellent RF field stability in high loaded Q operation. The RF power is coupled into the cavities via RF input couplers with fixed coupling ($Q_{ext} \approx 6 \times 10^7$). The shape of the cavities has been optimized to achieve a high BBU limit in ERL operation. Due to the high beam current combined with the short bunch operation, a careful control and efficient damping of the HOMs is essential, leading to the installation of beam line RF absorbers in-between the cavities for strong suppression of HOMs.
The cryomodule design has been guided by the ILC cryomodule [2–4], while modifications have been made to enable CW operation (instead of pulsed ILC operation with $\approx 1\%$ duty cycle) with correspondingly higher dynamic cryogenic loads. All beam line components within the cryomodule are suspended from the Helium Gas Return Pipe (HGRP), a 280 mm titanium pipe. This large diameter pipe returns the gaseous helium boiled off by the cavities to the liquefier and also acts as a central support girder. All beam line components inside the module are aligned within $\pm 1$ mm via fixed reference surfaces on the HGRP.

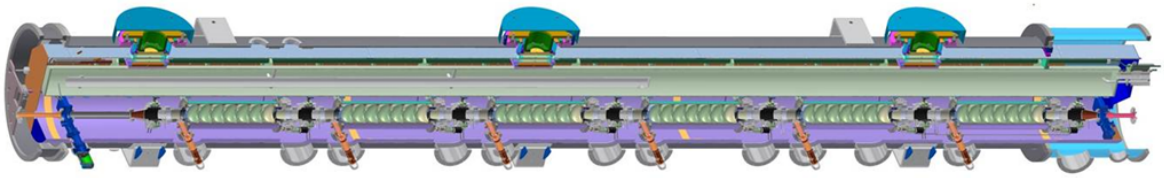

Figure 5.2.1: 3-D CAD model of the MLC prototype. It houses 6 superconducting 7-cell cavities with HOM loads located between them. The vacant space on the left could house a magnet/ BPM section. The overall length will be 9.8 m.

## 5.3 Beam Line Components

This section gives an overview of the key beam line components of the MLC: its accelerating SRF cavities, the RF power input couplers used to couple RF power into the cavities, the cavity frequency tuners used to adjust the RF frequency of the fundamental (accelerating) mode, and the HOM beam line absorbers used for HOM suppression and HOM power extraction.

### 5.3.1 SRF Cavities

The design and surface preparation of the 1.3 GHz, 7-cell SRF cavities for the MLC have been optimized for (1) supporting high beam currents in ERL operation, and (2) efficient cavity operation in CW mode. Table 5.3.1 lists key parameters of the optimized cavity. An operation temperature of 1.8 K has been chosen based on an optimization process aiming to minimize

AC cooling power demands. Design specifications were set at an accelerating gradient of 16 MV/m and a quality factor of $2 \times 10^{10}$ at 1.8 K, which, at the time of the decision, was an ambitious goal. An extensive R&D program was started ten years ago to ensure that these parameters can be achieved reliably. In addition, to verify strong HOM suppression and thus a high BBU-limit, HOM damping and high-current beam operation were studied in detail.
A prototype 1.3 GHz, 7-cell main-linac cavity was fabricated first and tested extensively. The cavity received a simple, high $Q_0$ surface preparation (bulk buffer-chemical polish (BCP) of 150 $\mu$m, outgassing at 650 C for 12 hours, tuning to 1297.425 MHz, final 10 $\mu$m BCP, 120 C heat treatment for 48 hours). After meeting quality factor and gradient specifications in the vertical test, the cavity was removed from the vertical test stand, and a helium jacket was welded to the cavity. The prototype cavity was then tested in a short single-cavity horizontal cryomodule (Horizontal Test Cryostat - HTC) in a three tier approach: With HTC-1, the cavity was only equipped with a low power probe coupler; the HTC-2 rebuilt added the RF power coupler to the cavity; and the final HTC-3 step added the HOM absorbers to the cavity package. The prototype cavity performance of the fully assembled prototype cavity in the test cryomodule (HTC-3) is shown in Fig. 5.3.1. The cavity performance again exceeded specifications, qualifying our cavity preparation recipe.
All six production cavities for the MLC have been produced in-house starting from flat metal

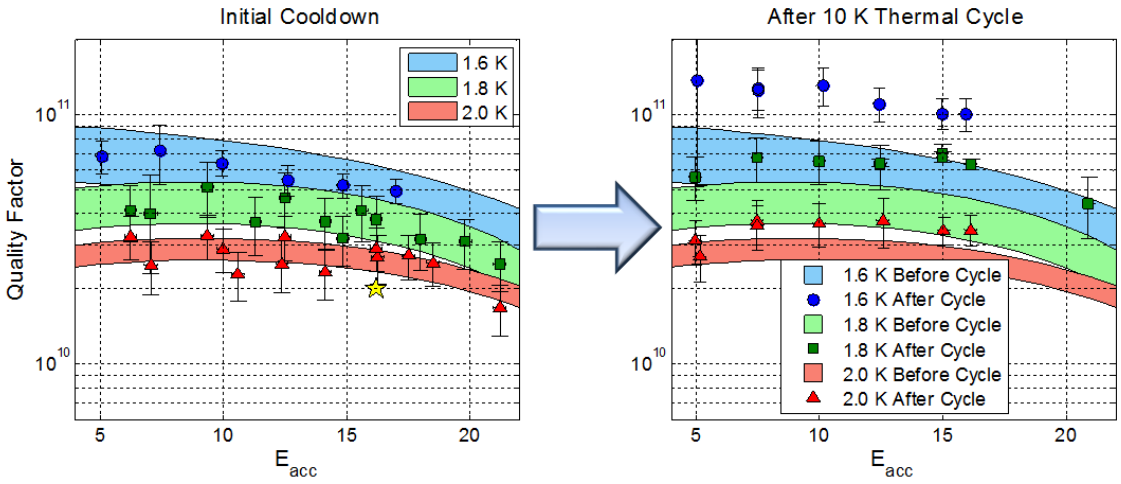


Figure 5.3.1: Performance of the 7-cell, superconducting cavity. The quality factor (which is inversely proportional to the cryogenic losses) was measured for different temperatures as a function of the accelerating field. The initial findings are shown on the left, the performance reported on the right diagram were yielded after a 10 K thermal cycle which increased the quality factor further. At 16 MV/m accelerating field and 1.8 K, a Q of $6{\times}10^{10}$ was achieved, surpassing the design goal by a factor of 3.

3 mm, RRR 300 niobium sheets. To investigate microphonics, we decided to build 3 unstiffened cavities as well as 3 cavities with stiffening rings between the cells. The process began with half cells formed by a deep drawing process in which sheet metal of RRR niobium is radially drawn into a forming die by a first press at 3 tons, then a second forming press (100 tons).

Table 5.3.1: MLC cavity design parameters. Note that $R/Q$ is always in the circuit definition.

| Parameter | Value |
|---|---|
| Type of accelerating structure | Standing wave |
| Accelerating mode | $TM_{0,1,0}$ $\pi$ |
| Fundamental frequency | 1.3 GHz |
| Design gradient | 16 MV/m |
| Intrinsic quality factor | $2 \times 10^{10}$ |
| Loaded quality factor | $6 \times 10^{7}$ |
| Cavity half bandwidth at $Q_{\mathrm{L}} = 6 \times 10^{7}$ | 11 Hz |
| Operating temperature | 1.8 K |
| Number of cells | 7 |
| Active length | 0.81 m |
| Cell-to-cell coupling (fundamental mode) | 2.2% |
| Iris diameter center cell / end cells | 36 mm / 36 mm |
| Beam tube diameter | 110 mm |
| Geometry factor (fundamental mode) | 270.7 Ω |
| $R/Q$ (fundamental mode) | 387 Ω |
| $E_{\mathrm{peak}}/E_{\mathrm{acc}}$ (fundamental mode) | 2.06 |
| $H_{\mathrm{peak}}/E_{\mathrm{acc}}$ (fundamental mode) | 41.96 Oe/(MV/m) |
| $\Delta f/\Delta L$ | 350 Hz/ $\mu$m |
| Lorentz-force detuning constant | 1 Hz / $(\mathrm{MeV/m})^2$ |
| Cavity total longitudinal loss factor for $\sigma = 0.6\,\mathrm{mm}$ | 14.7 V/pc |
| Cavity longitudinal loss factor for $\sigma = 0.6\,\mathrm{mm}$, non-fundamental | 13.1 V/pC |
| Cavity transverse loss factor for $\sigma = 0.6\,\mathrm{mm}$ | 13.7 V/pC/m |

The dies for the center cells were carefully designed to deal with the spring back effect. The equators of each cup have an additional straight length on them (1.5 mm). The purpose of this extra length is to allow for trimming later on to meet the target frequency and length. Those dumbbells are built in an intermediate step by welding two cups together on their irises. Ultimately six dumbbells were be welded together by electron beam welding to form the center-cells of the seven cell cavity and end-cells with end-groups are added. During the cavity production, we improved the mechanical tolerances in the cavity forming and welding, leading to a mean length deviation of the last 3 cavities by only 0.2 mm [5].
For the preparation of the production cavities, a simple recipe based on BCP similar to the preparation of the prototype cavity was chosen. Starting after fabrication, the damage layer was removed by bulk BCP (140 $\mu m$). A hydrogen degassing was then done at 650 C for 4 days, followed by final 10 $\mu$m BCP, a 120 C heat treatment for 48 hours to reduce BCS surface resistance, and a HF rinse removing and regrowing the oxide layer to reduce residual surface resistance. All cavities were performance tested vertically. The summary of these test is given in Figure 5.3.2. All six cavities exceeded the design quality factor, averaging to $2.9 \times 10^{10}$ at 1.8K. The reproducibility of the Q versus E curves for all cavities was very good. None of the

cavities needed additional processing - giving a 100% yield.

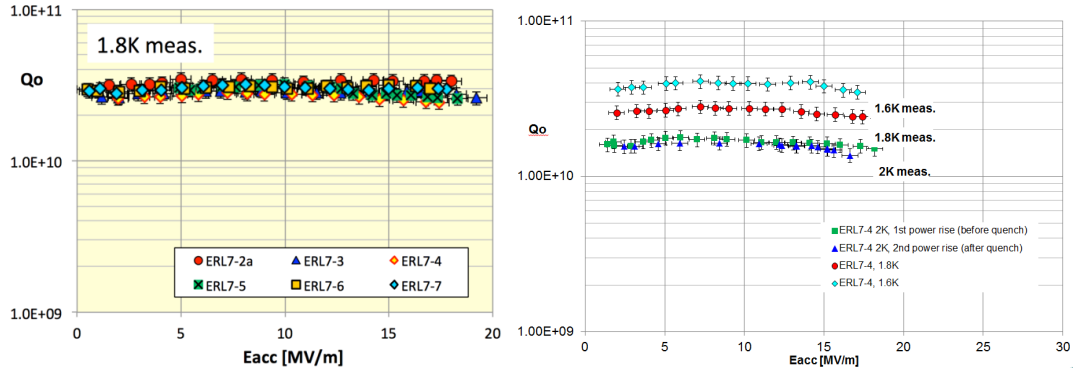


(a) (b)

Figure 5.3.2: Left: Vertical test results for all 6 MLC production cavities. All cavities exceeded the design specifications for the ERL ($Q_0 = 2 \times 10^{10}$ at 1.8 K). The right figure shows the Q vs E curves at different temperatures of a single cavity. The reproducibility of the results, gained without any reprocessing of a cavity, is very good.

### 5.3.2 Fundamental Power Couplers

Even though the ERL main linac input couplers only have to deliver up to 5 kW CW RF power to the cavities, the design is rather sophisticated: The design approach chosen for the whole module requires compensating the lateral movement between the straight mounting situation and the dog-leg geometry gained after cool-down (with an off-set of up to 1 cm). In addition, the mounting procedure is such that the cold part is fully mounted inside the cleanroom, hermitically closing the cavity. This approach has been found to be very successful as we have seen no cavity Q degradation after the coupler mounting procedure. The warm portion of the coupler is mounted outside the cleanroom with no special precaution on extreme cleanliness. Figure 5.3.3 shows a CAD model of the coupler, and Tab. 5.3.2 lists key parameters.

The external Q of the coupler is $6 \times 10^7$ (with the option to adjust it using a three-stub waveguide tuner) in order to minimize the RF power requirements taking into account the microphonics inside the module. A first prototype of the coupler was successfully tested to 5 kW CW RF power under full reflection. This was done without any conditioning required to reach this power level using a commercial 5 kW solid state RF amplifier. All six production couplers have been procured at CPI and were tested upon receiving on a test stand, applying 5 kW CW RF power under full refection without seeing any vacuum action. Essentially, no conditioning was required to reach this power level; see Fig. 5.3.4.

### 5.3.3 Cavity Frequency Tuners

The MLC cavity frequency tuner is based on the Saclay I tuner with a stepping motor drive for slow frequency adjustment ($> 500$ kHz tuning range) and a piezo-electric actuators for fast

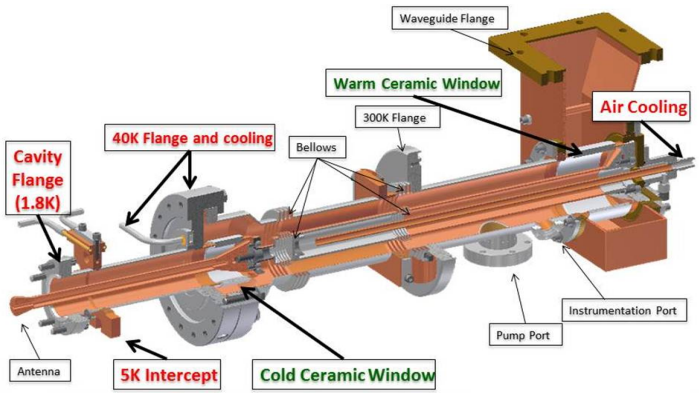


Figure 5.3.3: RF Power coupler. The coaxial transmission line has two bellows which allow for lateral movement during cool-down being up to 10 mm.

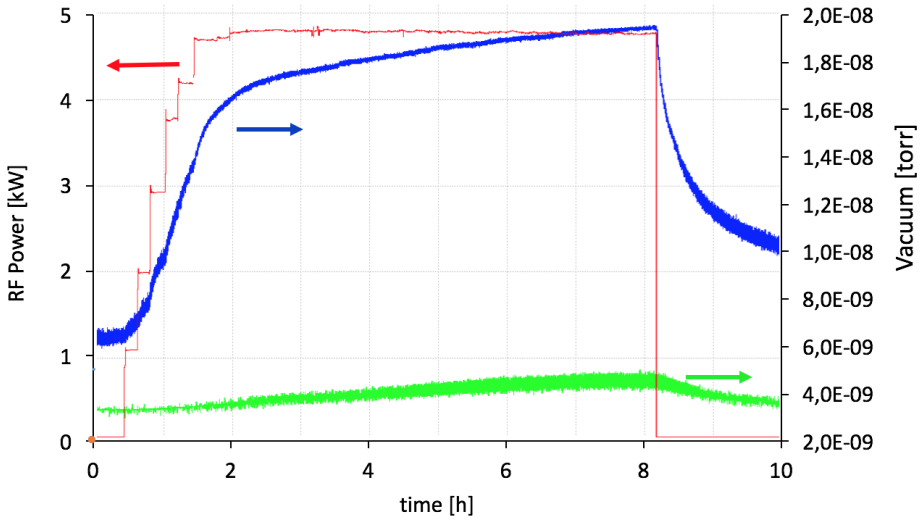


Figure 5.3.4: Typical testing results of the couplers, measured on a test-stand before the coupler was mounted to the string. Top curve shows the RF power as being ramped up, the curve below is the coupler vacuum, rising to $2 \times 10^{-8}$ Torr while the cavity vacuum (bottom curve) is only slightly affected.

Table 5.3.2: MLC cavity RF power input coupler parameters.

| Parameter | Value |
|---|---|
| Operating frequency | 1300 MHz |
| Maximum power (CW) | 5 kW |
| $Q_{ext}$ (fixed) | $6 \times 10^7$ |
| Static heat load to 2K | 0.05 W |
| Dynamic heat load to 2K | 0.06 W |
| Static heat load to 5K | 0.64 W |
| Dynamic heat load to 5K | 0.32 W |
| Static heat load to 40K | 3.78 W |
| Dynamic heat load to 40K | 5.94 W |

frequency control (> 1 kHz tuning range) for Lorentz-force compensation and microphonics compensation. The tuner frame and the piezo stacks were modified for increase stiffness to support high tuner forces of up to 26 kN for the main linac cavity version with stiffening rings. An illustration of the modified tuner is shown in Fig. 5.3.5.

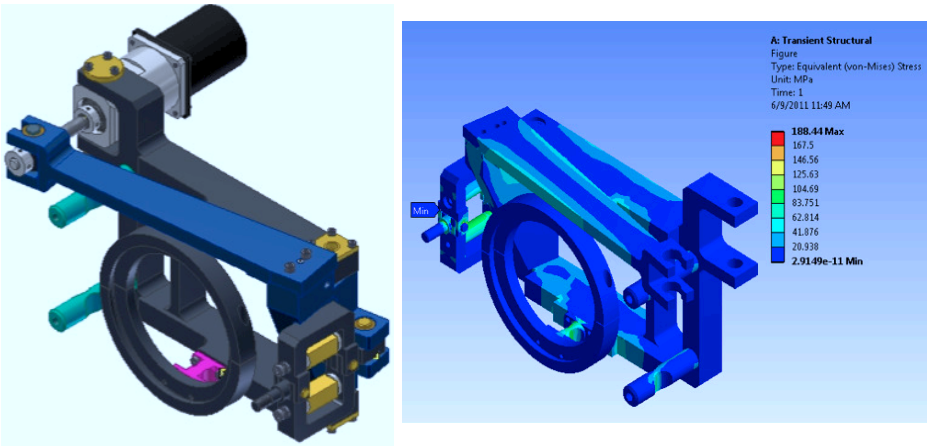


Figure 5.3.5: MLC cavity frequency tuner with fast piezoelectric actuators and increased stiffness for the main linac cavities. Left: CAD model. Right: ANSYS simulation of the von Mises stress for a tuning force of 26 kN applied to the cavity. The maximum stress is well below the yield strength of stainless steel at cryogenic temperatures.

### 5.3.4 HOM Absorbers

The guiding concept for the beam line HOM absorbers in the MLC is to have a broad band absorbing material covering the whole range from 1 to >40 GHz in the shape of a cylinder, located in the beam tube sections between the cavities, with the beam passing through the center. After several iterations, a final design was developed and tested, as depicted in Fig. 5.3.6.

The center assembly consists of a SiC cylinder from CoorsTek (SC_35) which is shrink fit

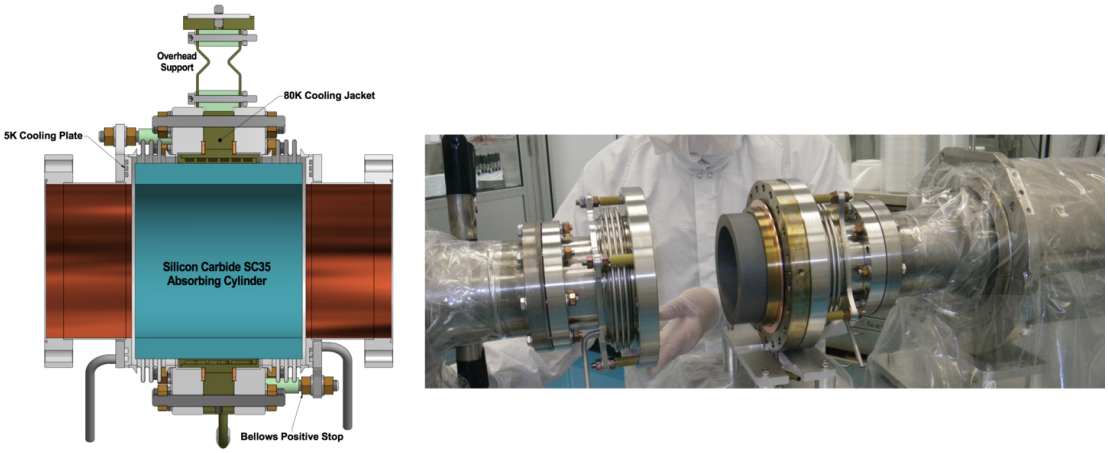


Figure 5.3.6: Cornell's HOM absorber used in the MLC. The absorbing material is SC_35 from CoorsTek, shrink-fitted into a Ti cylinder.

into a titanium cooling jacket and flange. The cooling jacket and flange locate, support, and provide cooling at 80 K to the absorbing cylinder using a cooling channel inside the titanium to ensure 400 W of HOM power can be extracted. The end pieces of the assemblies contain a 3 convolution bellows, a 5 K cooling plate, and taper seal flange to mate with the cavities. The bellows allows for small length variations in the string, small angular misalignments of cavity flanges, as well as adds a long thermal path from 80 K to 5 K. There are positive stops that prevent the bellows from compressing and closing the gap between the 5 K cooling jacket and the absorbing cylinder to less than 1 mm. This prevents any rubbing of metal to ceramic that could create particles. The beam tubes have a copper plating about 10 micron thick to prevent beam induced heating. More details on the design can be found in [6, 7].
Two prototype HOM absorbers where build with a slightly mechanically different design: the absorbing ceramic was identically, but it but brazed into a tungsten cylinder. As part of designing and verifying parameters for the MLC, these prototypes were tested in a HTC together with the prototype 7-cell cavity. Excellent higher order mode damping was found with no observed dipole mode having an external Q higher than $10^4$ while the Q of the fundamental mode was unaffected ($6 \times 10^{10}$ at 1.8 K). Figure 5.3.7 shows the quality factors of the cavity with and without the absorber. More details are published in [8].
To quantify the HOM power extracted and measure the heating effects, tests with beam were conducted on the prototype absorbers. For that, the HTC was moved to the Cornell ERL photo-injector and located directly behind the injector cryomodule. The layout of the beam line is show in Fig. 5.3.8. For the beam test, we ran different beams with currents up to 40 mA through the HTC and measured the heating in various locations. As expected, the heating scaled with beam current, shorter bunches lead to higher heating. The total HOM power absorbed was about 6 W at 40 mA. One must consider however that a portion of the HOM spectrum is not bound to the region of the cavity and its adjacent HOM loads due to it being above the cut-off frequency of the beam pipe. A high-frequency HOM wakefield can therefore

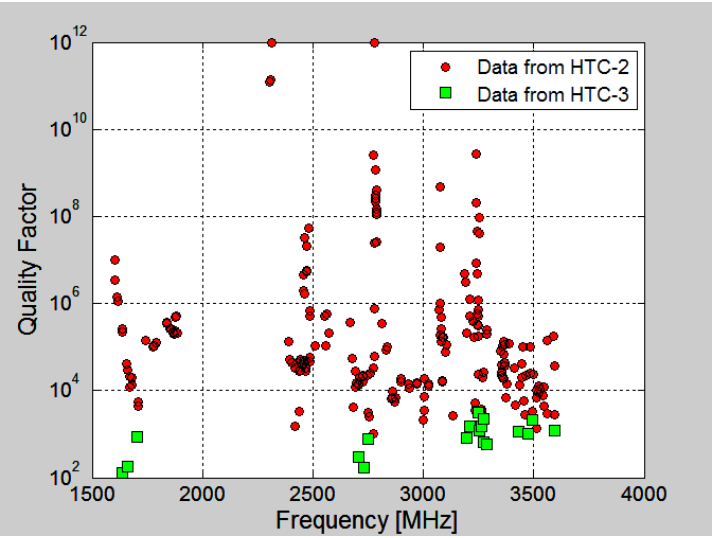


Figure 5.3.7: External Quality factor of the Cornell 7-cell ERL cavity without (red) and with (green) HOM absorbers installed.

propagate beyond the HOM load without losing all its energy. Simulations show that this underestimation is no greater than a factor of 2, and that therefore no more than 12 W of HOM power were excited by the 40 mA beam. This then results in an estimate of the longitudinal loss factor of the cavity of $\approx 10$ V/pC, slightly lower than the simulated value. In addition to the high current operation, the beam was used to excite and probe individual HOMs in the cavity, with the purpose of measuring their loaded quality factor $Q_L$. This beam-based HOM search revealed the presence of only 8 modes with a $Q_L > 10^5$, all of which are highly likely quadrupole or sextupole modes, and thus due not to pose any danger of causing BBU in the ERL.

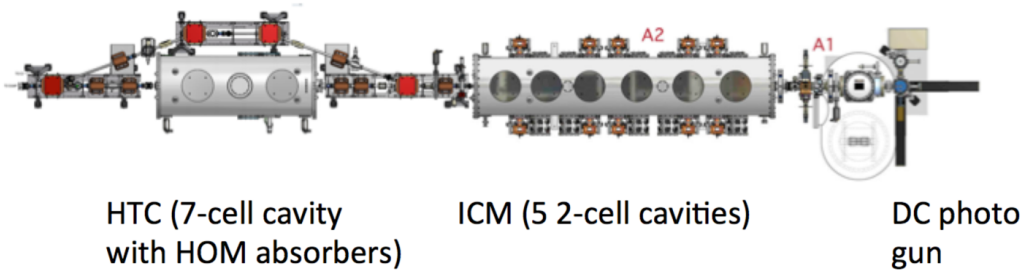


Figure 5.3.8: The horizontal test cryostat (HTC) placed behind the photo injector for testing of the 7-cell cavity equipped with HOM absorbers with beam. A beam current of up to 40 mA was run through the set-up.

## 5.4 MLC Design

### 5.4.1 Mechanical Design

All components within the cryomodule are suspended from the HGRP. This large diameter titanium pipe has a combined function: it returns the gaseous helium boiled off the cavity vessels to the liquefier and acts as a central support girder. The HGRP is Grade 2 Titanium, 280 mm in diameter with a wall thickness of 9.5 mm which is supported by 3 support post, the middle one being fixed while the outer two slide by 7 and 9 mm during cool-down, respectively. With a 1 ton weight force of the beam line string, the maximum vertical displacement of the HGRP is 0.1 mm and the natural frequency is 88 Hz. Simulations show that a 3-posts support system is well suited to ensure an acceptable vertical displacement and vibration characteristics. A series of ANSYS modal finite element analyses were performed to evaluate the cryomodule design mechanical stability in more detail, including individual piping lines inside the module. The location and stiffness of piping supports were considered in the design to make sure the natural frequencies are higher than 60 Hz. A 2-Phase 2 K pipe feeds helium to the helium vessels of the individual cavities through 6 chimneys. The diameter of this pipe is strongly increased (compared to the ILC cryomodule design) to accommodate CW operation.

### 5.4.2 Cryogenic Cooling Scheme

The cryogenic cooling of the module consists of 3 different temperature loops. The cavities are cooled by liquid helium obtained by a JT-Valve located at the module entrance. Sub-cooled to 1.8 K by pumping the He-atmosphere down to 20 mbar ensures an optimum operation regime for the superconducting cavities. The second loop consisting of supercritical 5 K helium is used to cool the intercept all transitions to warmer temperatures in order to assure a minimal heat transfer to the 1.8 K system. Finally, a 80 K loop provides cooling for the coupler intercepts, cools the thermal radiation shield of the module and removes the heat generated in the HOM absorbers. As shown in Fig. 5.4.1, the loads are partially in parallel, partially in series. As the expected heat load especially at the HOM absorbers are expected to vary individually on a scale of 0 to 400 W, a careful investigation of the stability of parallel flows was performed [6]. Figure 5.4.2 gives the cross-section of the module showing the spatial arrangement of the cooling loops.

### 5.4.3 80 K Thermal Shield

The thermal shield (Al1100-14) of the module is cooled by the 80 K delivery line which is connected to the shield on one side. As a result, the cool-down process is asymmetric. To avoid damage to the shield due to thermal stress during cool-down, thermal and thermo-structural finite element analyses (FEA) were performed to study the temperature gradient, deformation and thermo-mechanical stresses of the 80 K thermal shield with a helium gas cool-down rate of 4 K per hour - being an adequate assumption. The simulated results indicated that with a cooling rate of 4K/hour, the temperature gradient reaches a maximum of 13 K on the entire shield, occurring 15 hours after the start of the cool down. This situation is shown in Fig. 5.4.3. Once fully cooled down, the steady state maximum temperature gradient is only

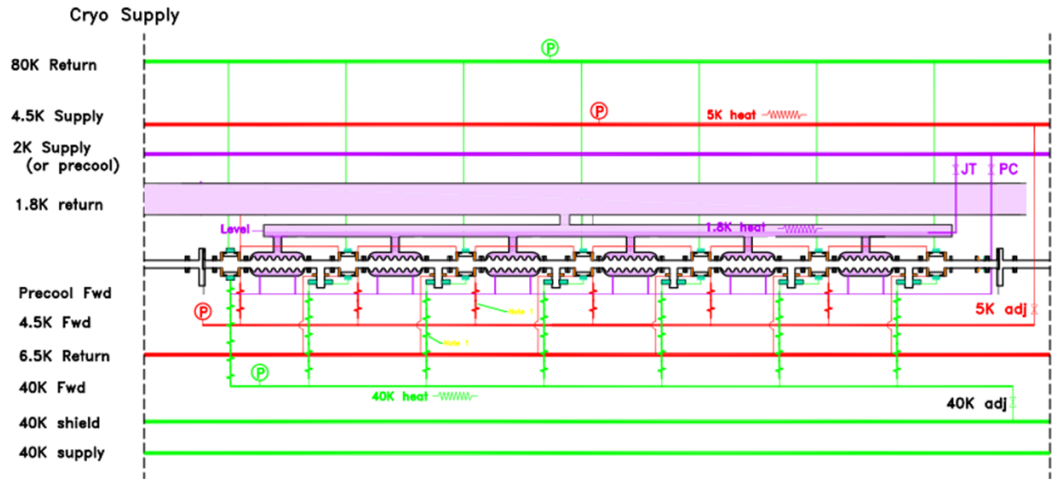


Figure 5.4.1: Diagram of the different cooling loops within the MLC: The 1.8 K loop feeds the cavities, the 5 K loop intercepts the cavity, coupler and HOM flanges and the 80 K loop cools the radiation shield, the HOM Absorbers and intercepts the power coupler.

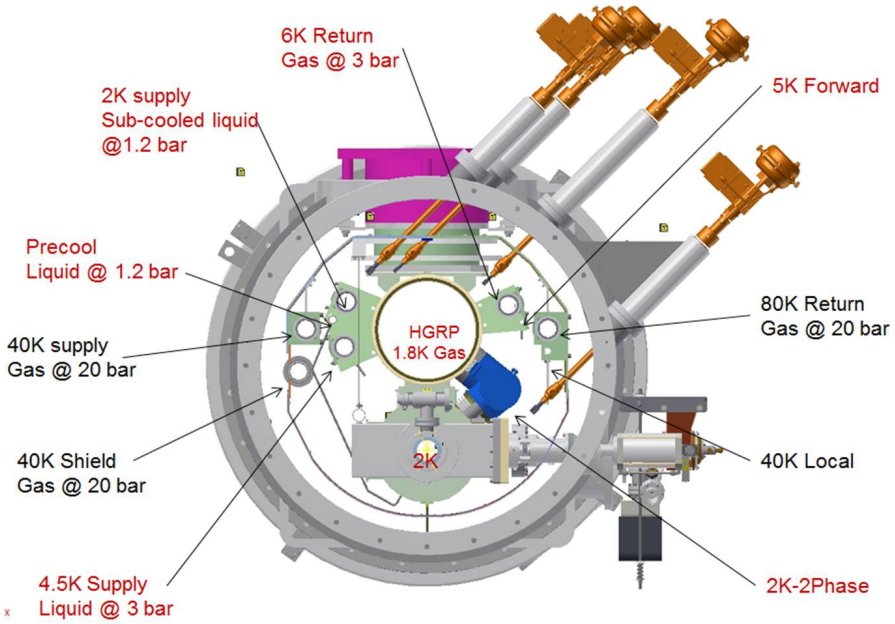


Figure 5.4.2: Cross-section of the MLC, giving more details on the piping and positioning of the components.

2.2 K. It should be mentioned that the thermal shield will be bent during cool-down estimated to be 6 mm at max.

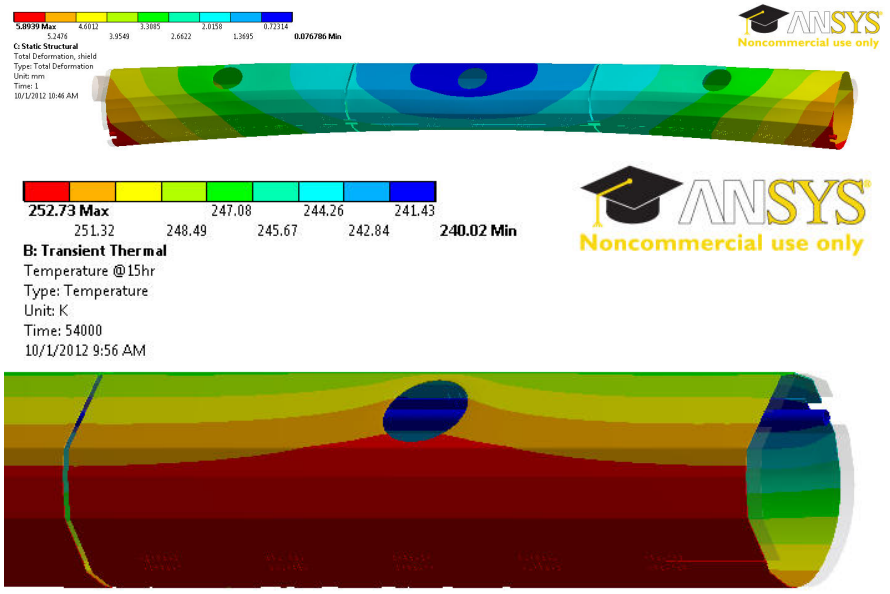


Figure 5.4.3: Cool-down analysis of the thermal shield (Aluminum). As it is cooled only on one side, the cool-down will not be uniform, resulting in an up to 13K temperature difference (a) and a lateral bending of up to 6 mm (b).

### 5.4.4 Magnetic Shielding

High $Q_0$ cavity operation requires excellent shielding of the Earth's magnetic field, so that the residual ambient magnetic field at the cavity locations is reduced to $< 2$ mG. A 80 K Mu-metal magnetic shield is attached to the outside of the 80 K thermal shield. In addition, every cavity is enclosed by a second, individual magnetic shield, made from cryoperm.

### 5.4.5 Vacuum Vessel

The cylinder of the vacuum vessel is 965.2 mm in diameter, rolled longitudinally welded carbon steel (A516 GR70) pipe. All precision required surfaces were machined in a single spool piece setup. Figure 5.4.4 shows a photograph of the vacuum vessel.

### 5.4.6 Alignment

The alignment concept of the cryomodule relies on the helium gas return pipe, acting as a strong-back of the module. Suspended by 3 composite post assemblies from the outer vessel, it provides precision surfaces for all cavity mounts and beam line components. The position of these surfaces where surveyed upon receiving the pipe, initially displaying larger than the specified $\pm 1$ mm accuracy. However, when preloaded with the approximate weight of the cold-mass, alignment was within specifications. This data is given in Fig. 5.4.5.

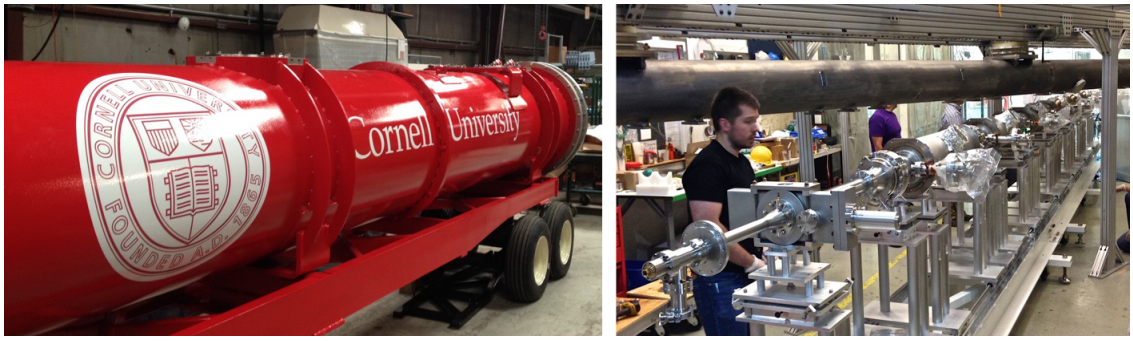


Figure 5.4.4: Left: Vacuum Vessel as received by Cornell University. Right: Marriage step: the cavity string coming from the clean room assembly is rolled under the HGRP providing precision alignment.

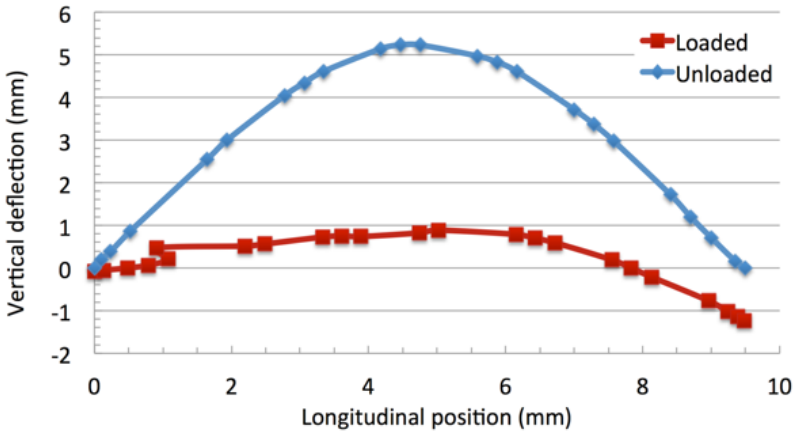


Figure 5.4.5: Vertical position of the reference surfaces on the helium gas return pipe defining the positions of all beam line components. In a module string, the right end will receive more support resulting in a better vertical positioning.

## 5.5 Assembly Process, Cool-down, and Performance Testing

### 5.5.1 MLC Assembly

While production of components started earlier, the actual assembly began in March 2014, when the first cavities where connected to a string inside the cleanroom. For space reasons, two half strings, consisting of three cavities with attached cold section of the coupler and 4 HOM absorbers as well as a gate valve were assembled. Each substring was leak checked and connected to the other later on. In May, cold mass assembly continued outside the cleanroom. Mating the pre-aligned cavity string with the precision surfaces on the HGRP strong-back turned out to be not an issue at all. All bellows located at the HOM absorber package were able to compensate for deviations and only the longitudinal position of one HOM absorber had to be adjusted.
Installation of the cavity magnetic shield, the tuner, the thermal and magnetic shield, all cryogenic piping and jumpers, instrumentation and cabling as well as a wire position monitor to track alignment during cool-down took 3 months. The cold-mass was moved it into the vacuum vessel in September 2015. As final assembly steps, the warm portion of the couplers, feed-throughs and cryogenic valves were installed. All circuits were leak checked and pressure tested.

### 5.5.2 Preparation for Testing

In preparation for the testing of the MLC, the module was transported across the Cornell campus. No special damping frame was used. However, all movements were done with extreme care and transportation speed was set to 5 km/h max. In addition, we measured mechanical shocks using accelerometers. The data, given in Fig. 5.5.1, revealed a maximum g force of 2.3 (lasting less than 10 ms), which occurred while pulling the module (siting on its own wheels) in place after lifting it from the truck. During the road trip, max g-factors were below 1.5.

### 5.5.3 Initial Cool-down

In order to facilitate a smooth and controlled cool-down, a new heat exchanger can was built – the piping diagram is given in Fig. 5.5.2. It allows to add a warm stream of gas forwarded to the cold-mass, resulting in a very controlled cool-down, as shown in Fig. 5.5.2. This was mandatory as the thermal shield is cooled by conduction only with an extruded pipe running just along one side. As a result, the cool-down of the shield is asymmetric and we calculated stress limits on the aluminum transitions which required us to keep the temperature spread across the shield below 20 K. In the initial cool-down we maintained 10 K, becoming 15 K below 200 K with an average cool-down rate of 1.25 K/h.
During cool-down, we also monitored the movement of the two outer, sliding support posts. The cavities in the MLC are aligned via the helium gas return pipe, made out of titanium, being suspended from the vacuum vessel by three support posts. As a result of the cold-mass shrinking as a whole with the central post fixed, the two outer posts are sliding. Figure 5.5.3 gives the movement of these posts as the temperatures on the cool-mass go down. The movement was as expected.

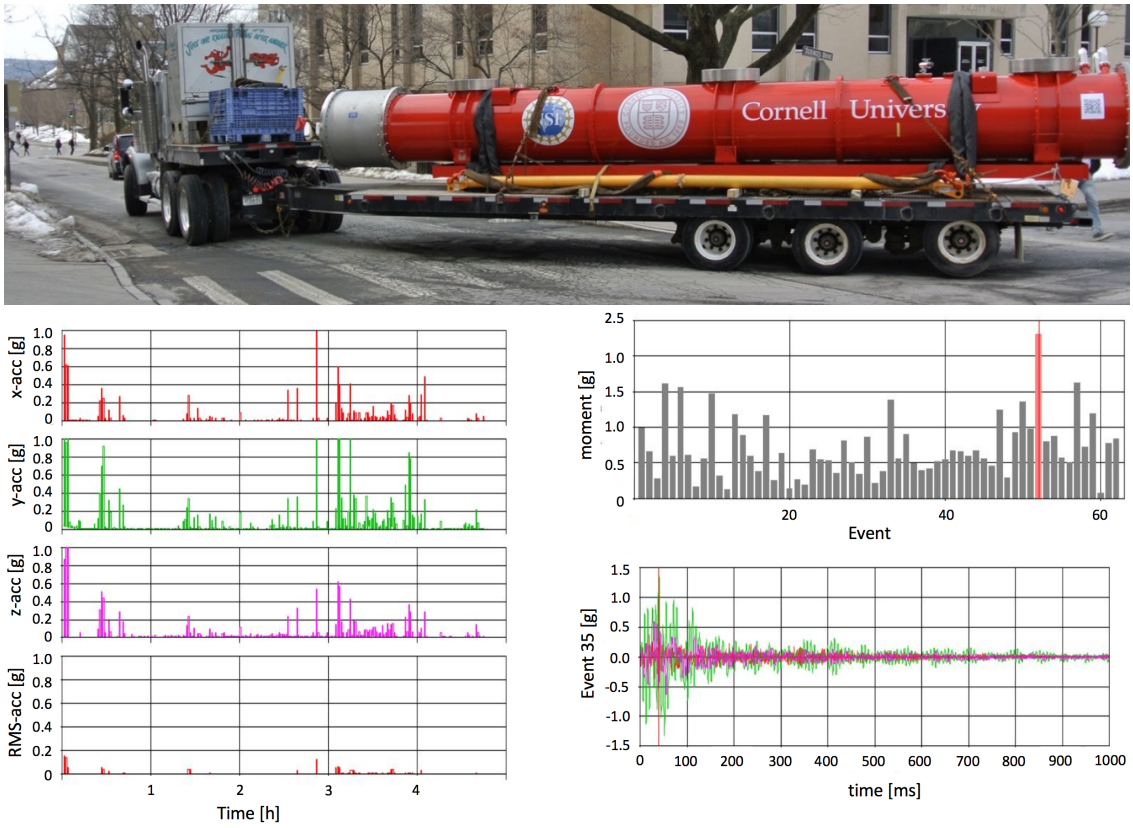


Figure 5.5.1: Accelerometer data taken during the transportation of the cryomodule across the campus.

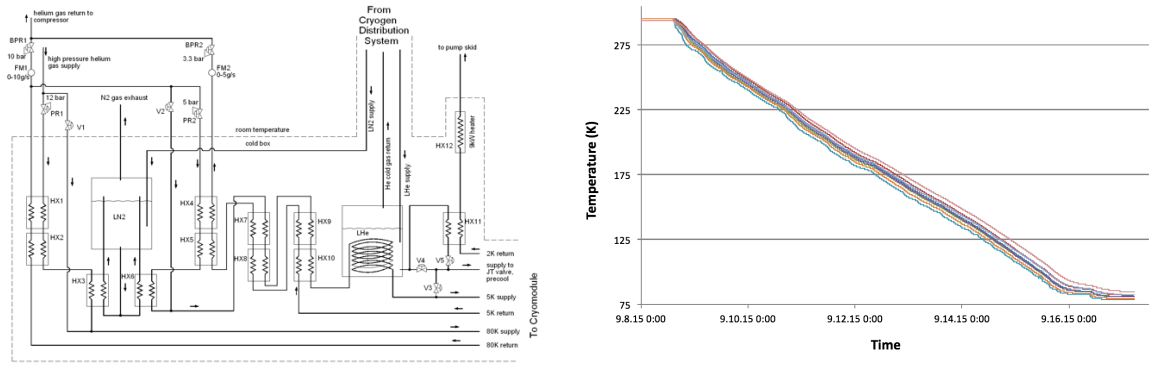


(a) (b)

Figure 5.5.2: Left: Heat exchanger can build to cool-down and operate the main linac cryomodule. Special emphasis was given towards achieving a smooth and controlled cool-down to 77 K. Right: Temperatures on the thermal shield during the cool-down. Due to the design of the thermal shield the temperature spread across the shield had to stay below 20 K, leading to a cool-down rate of approximately 1.25 K/h.

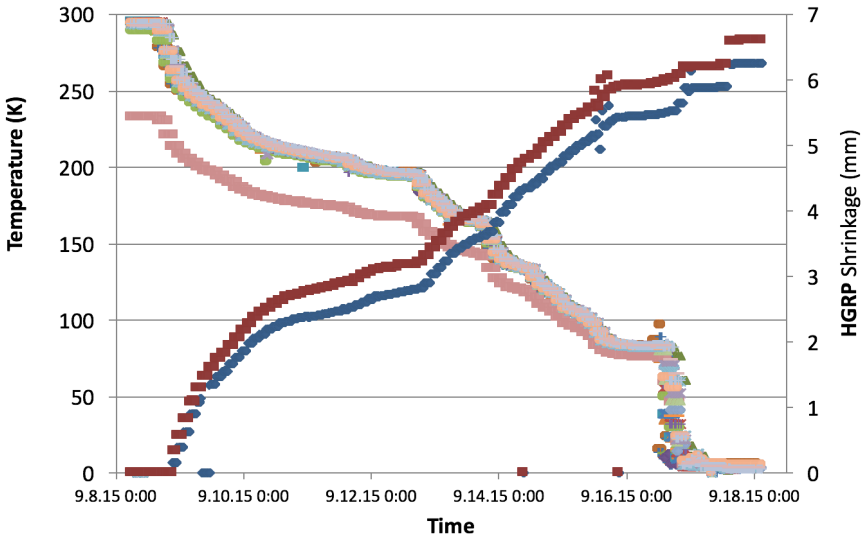


Figure 5.5.3: Movement of the outer (sliding) support posts: as the temperature of the HGRP goes down the posts move inwards. The movement was as expected.

### 5.5.4 Cool-down Cycles

Recent findings have indicated that the performance of an SRF system also depends on details of the cool-down process. Findings at Cornell indicate that for conventionally treated cavities a slow cool-down leads to a higher quality factor of the cavity. We were able to explain this finding by describing the role of thermo-currents that are excited at the material transitions between the niobium (cavity) and the titanium (enclosing helium vessel), driven by temperature gradients [9, 10]. So-called nitrogen-doped cavities, however, seem to require a fast cool-down and it was found that this helps expelling residual magnetic field more efficiently than a slow cool-down. It should be noted that N-doped cavities are stronger effected by trapped magnetic flux compared to conventional treated cavities. To study the impact of slow and fast cool-down speeds on the MLC cavities' performances as well as to verify the reproducibility of these cycles, a total of 5 thermal cycles were completed on the MLC, trying very slow and extremely fast cool-downs. Results are given in Fig. 5.5.4. We found that for a slow cool-down some cavities went through transition several times with some unwanted warm-up in between. We also learned that on the fast procedure the final cool-down speed depended on the cavity position, especially how close the cavity was in relation to the Joule-Thompson valve.

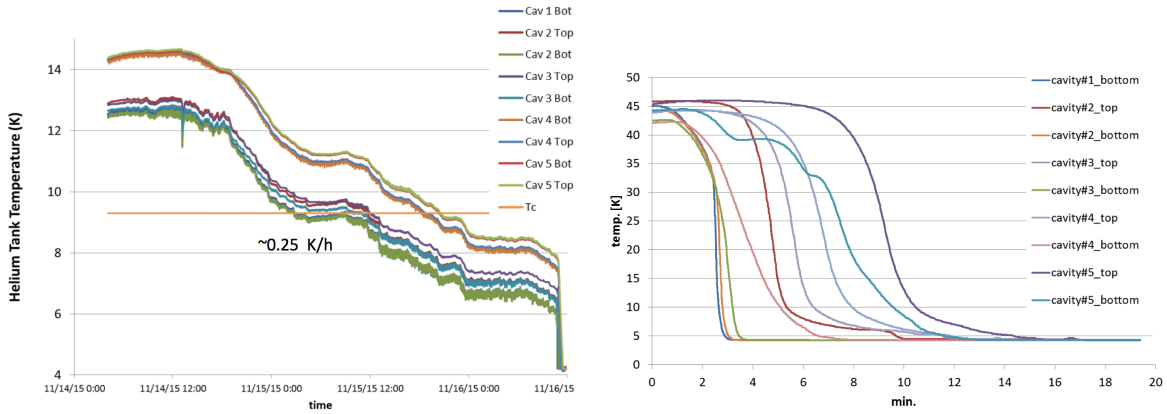


(a) (b)

Figure 5.5.4: Slow (left) and fast (right) cool-down cycle performed in order to measure cycle dependent impacts on the cavity performance. For the slow cool-down we were able to get 0.25 K/h while the fast cool-down resulted in 0.5 K/min – 2 K/min, depending on how close the cavity was to the JT valve.

### 5.5.5 RF Test Results

Test results from all 6 cavities are summarized in Fig. 5.5.5 and Tab. 5.5.1. After some initial processing 5 of the 6 cavities perform close to their design specifications. One cavity is currently limited by a premature quench which we hope to overcome by a thermal cycle and pulse processing. Even so the quality factors are slightly lower than the design, the cavities (except #4) easily reach the design gradient. From Fig. 5.5.5 one could also conclude that in our case the cool-down speed did not strongly affect the cavity performance. The data shows

slightly higher Qs for the slow cool-down. This might indicate that we have a slightly higher residual magnetic field inside the MLC (as compared to our short test module HTC).

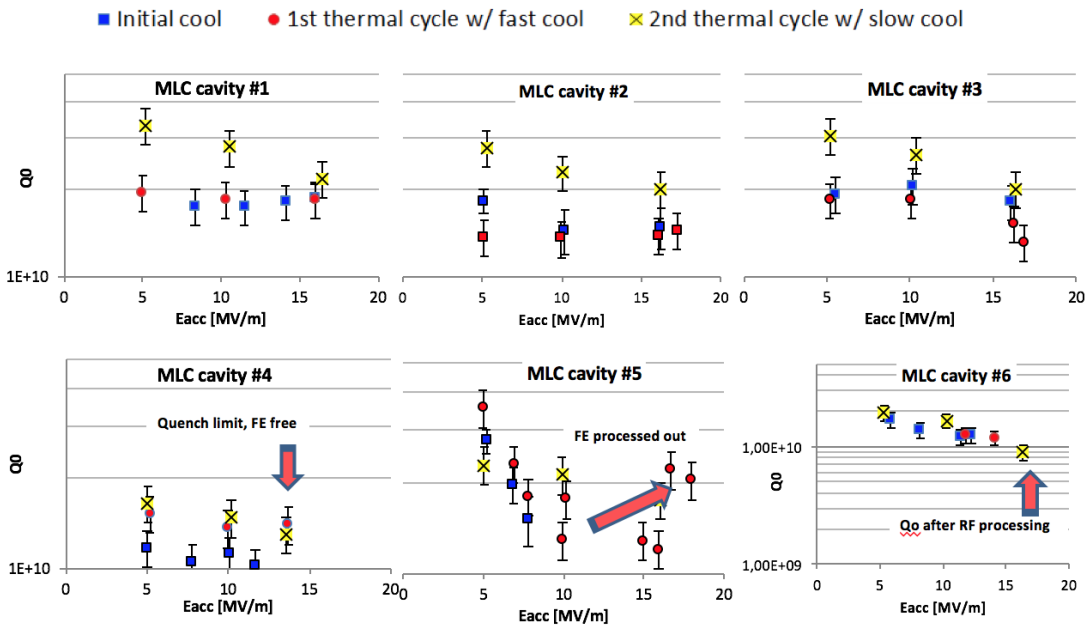


Figure 5.5.5: Summary of the MLC cavity performance. All data were taken at 1.8 K. Two cavities had to be RF processed to increase the field and to remove field emission. Cavity #4 is still limited by an early quench, but administrative procedures (for now) prevented us from processing this cavity further.

### 5.5.6 HOM Damping Studies

Higher order mode scans on multiple cavities in the MLC were completed, showing no unexpected results, i.e. no high Q dipole modes. Figure 5.5.6 shows a comparison of the MLC HOM loaded quality factor ($Q_L$) measurements and simulation. This comparison indicates that (1) the measured HOM frequencies agree well with simulation results, and (2) that the $Q_L$ of dipole HOMs of the MLC cavities are strongly damped below the target value of $\approx 10^4$ for high $R/Q$ dipole modes. The MLC results also agreed well with results from a previous HOM study on the prototype 7-cell cavity in the HTC. The measured $Q_L$ values $> 10^7$ shown in Fig. 5.5.6 belong to quadrupole and sextupole modes, which do not contribute to the BBU limit. Currently, HOM scans on the remaining cavities continue in order to confirm the results.

### 5.5.7 Tuning and Microphonics

To better understand the trade-offs in the mechanical behavior of the cavities, the MLC was built with two types of cavities: three had stiffening rings added in order to minimize the pressure responds ($df/dp$) and to minimize microphonics, while the remaining three cavities

Table 5.5.1: Cavity performance inside the MLC.

| | | $Q_0/10^{10}$ | $E_{acc}$ [MV/m] | $Q_{ext}/10^7$ |
|---|---|---|---|---|
| Cavity #1 | ERL 7-3 | 1.88 | 16.0 | 5.13 |
| Cavity #2 | ERL 7-5 | 1.98 | 16.2 | 5.38 |
| Cavity #3 | ERL 7-4 | 2.01 | 17.2 | 6.90 |
| Cavity #4 | ERL 7-7 | 1.45 | 13.7 | 5.67 |
| Cavity #5 | ERL 7-2a | 1.78 | 16.0 | 5.38 |
| Cavity #6 | ERL 7-6 | 1.91 | 16.0 | 6.14 |
| Design | | 2.0 | 16.2 | 6.5 |

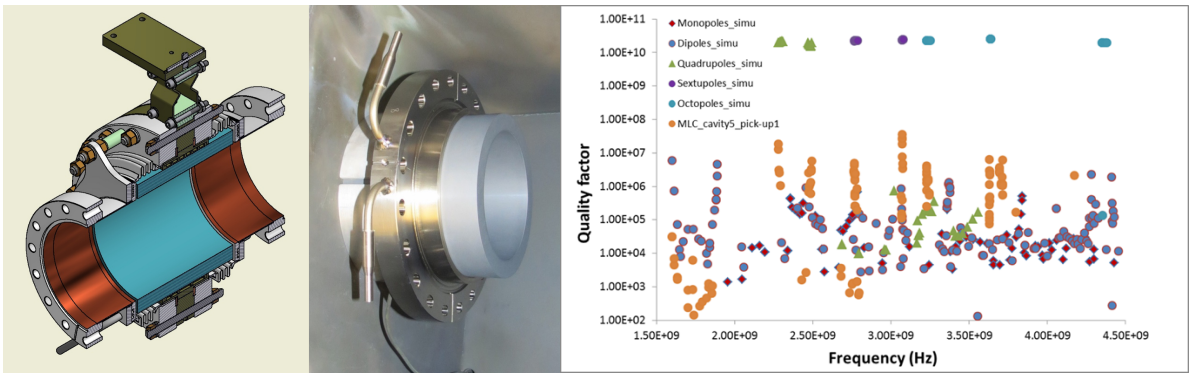


(a) (b)

Figure 5.5.6: Performance of the higher order mode absorber. On the left a schematic view of the absorber is given, where is absorbing material (a SiC composite) is shown in blue. The absorbing cylinder is pictured in the center. On the right, the measured quality factors of some higher order modes, compared to undamped resonances are given showing that the absorber operates as designed.

were built without stiffening. One concern was that the stiffened cavities might overload the tuner and can not be tuned to frequency. In addition, our initial testing indicated that and unstiffened cavity would meet our requirements and in addition would be easier to fabricate. Figure 5.5.7 shows the pressure response curve for a stiffened and an unstiffened cavity. As expected, the pressure sensitivity of the stiffened cavity is smaller by more than a factor of two. However, with the pressure stability in our system being 0.1 mbar both values are well acceptable. Table 5.5.2 gives measured values for all cavities, while also reporting on the tuning that was necessary after cool-down. As two cavities are close to their tuning range limits, we will slightly lower our operating frequency to 1299.9 MHz. A typical curve that we measured on the coarse tuner is given in Fig. 5.5.8, displaying a 150 Hz hysteresis which will be counteracted by the piezo actuators being used for fine tuning. First measurements of the cavity microphonics levels indicated a rather high level of mechanical motions, likely driven by vibration sources outside of the MLC. Especially the unstiffened cavities seem to have very

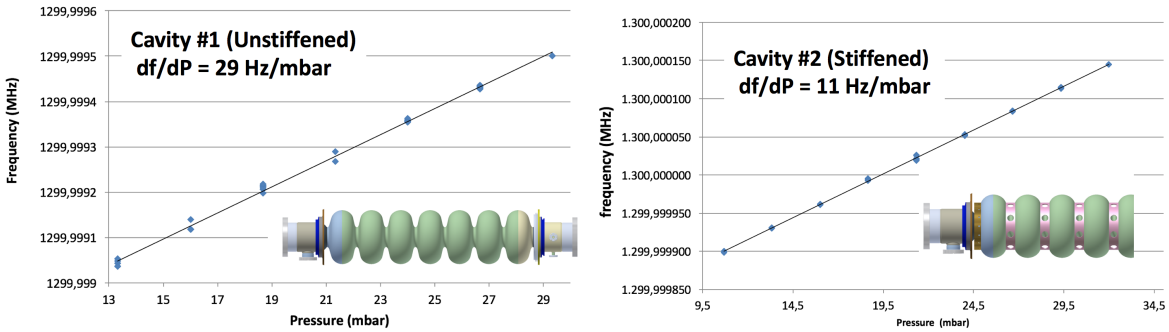


(a) (b)

Figure 5.5.7: Tuning sensitivities of the unstiffened and the stiffened cavities.

Table 5.5.2: Tuning and pressure sensitivity of the MLC cavities. unstiffened (U) and stiffened (S) cavities are denoted. Cavity #4 and #6 were close to the tuning range.

| | | Before tuning [MHz] | Post tuning [MHz] | Tuner range [kHz] | Pressure sensitivity [Hz/mbar] |
|---|---|---|---|---|---|
| Cavity #1 | ERL 7-3 (U) | 1299.525 | 1300.000 | +470 | 29 |
| Cavity #2 | ERL 7-5 (S) | 1299.724 | 1300.00 | +270 | 11 |
| Cavity #3 | ERL 7-4 (U) | 1299.650 | 1300.00 | +340 | 35 |
| Cavity #4 | ERL 7-7 (S) | 1299.615 | 1299.996 | +381 | 13 |
| Cavity #5 | ERL 7-2a (U) | 1299.677 | 1300.00 | +323 | 25 |
| Cavity #6 | ERL 7-6 (S) | 1299.554 | 1299.939 | +385 | 13 |
| Design | | 1299.700 | 1300.000 | +400 | |

strong mechanical vibrations. We are currently in the process of taking accelerometer data as well as fast He-pressure sensor data to understand the source of the microphonics and the path under which the couple into the module. First results indicate that vibrations by the MLC insulation vacuum pump strongly were coupled into the MLC, which can be resolved easily by adding vibration isolation between the pump and the MLC.

## References

[1] G. Hoffstaetter, M. T. e., S. Gruner. *The Cornell Energy Recovery Linac: Project Definition Design Report.* Technical report (2013).

[2] Horlitz, G., D. Trines, and T. Peterson. *The TESLA 500 cryogenic system layout.* Adv. Cryog. Eng., **41**, pages 911–920 (1996).

[3] Pagani, C., *et al. Further improvements of the TESLA Test Facility (TTF) cryostat in view of the TESLA collider.* Adv. Cryog. Eng., **45A**, pages 939–946 (2000).

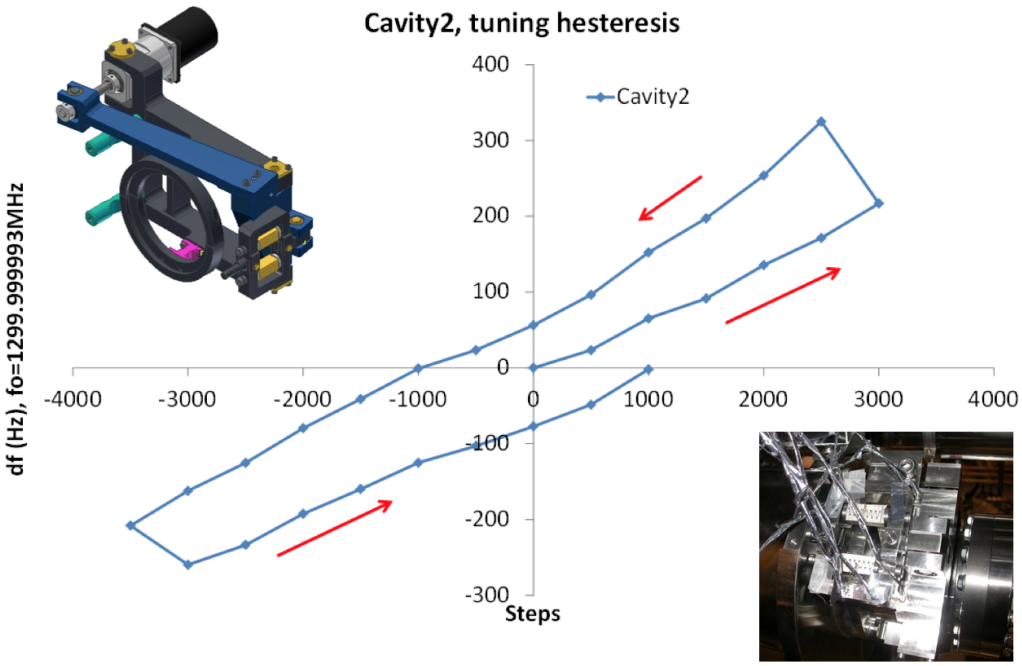


Figure 5.5.8: Result of testing of the course tuner driven by a stepper motor. The observed hysteresis of 150 Hz is as expected and will be compensated by the action of the fine tuner driven by piezo actuators.

[4] Peterson, T., *et al. ILC cryogenic systems reference design.* In *AIP Conf. Proc.*, volume 985, pages 1565–1572 (2008).

[5] Eichhorn, R., *et al. Achieving High Accuracy in Cornell's ERL Cavity Production.* Proc. of the 2013 North American Part. Acc. Conf, Pasadena, CA, USA (2013).

[6] Eichhorn, R., *et al. Cornell's HOM Beamline Absorbers.* In *Proceedings, 4th International Particle Accelerator Conference (IPAC 2013)*, page WEPWO059 (2013).

[7] Eichhorn, R., *et al. Higher Order Mode Absorbers for High Current ERL Applications.* In *Proceedings, 5th International Particle Accelerator Conference (IPAC 2014)*, page TH-PRI111 (2014).

[8] Valles, N., *et al. HOM studies of the Cornell ERL Main Linac Cavity in the Horizontal Test Cryomodule.* In *Proc. of the 2013 Int. Conf. on RF Supercond., Paris, France*, volume 1090 (2013).

[9] Eichhorn, R., *et al. Thermocurrents and their role in high Q cavity performance.* Phys. Rev. Accel. Beams, **19**, page 012001 (Jan 2016).

[10] Eichhorn, R. and J. May-Mann. *Asymmetric Thermo-currents Diminishing SRF Cavity Performance.* In *Proceedings, 6th International Particle Accelerator Conference (IPAC 2015)*, page WEPTY068 (2015).

# 6 Cryogenics for the CBETA project

## 6.1 Overview

### 6.1.1 Thermal loads expected

There are two places in the CBETA experiment where cooling to cryogenic temperatures is required: the ICM, and the MLC. The ICM contains five 2-cell niobium superconducting cavities which will be operated at 2.0K to accelerate an electron beam from about 400KeV as it emerges from the gun to about 10MeV. The six 7-cell superconducting cavities in the MLC will be operated at 1.8K to achieve a maximal energy of 200MeV of the electron beam after four passes through this assembly. There are additional significant thermal loads from input couplers and higher-order-mode absorbers which will be taken out at temperatures near 80K and 5K, where it is more thermodynamically efficient to cool these loads. The primary source for the cooling near 80K is supplied from a central liquid nitrogen facility in the laboratory, which is a 30,000 liter tank refilled at regular intervals upon demand by an external vendor. The primary cooling source for both the 5K and 2K cooling is provided by a 4.2K helium liquefaction/refrigeration system whose main function is cooling for the main Wilson Lab synchrotron ring, but which has additional capacity that will be used for the CBETA project. The approximate heat loads that must be extracted from each of these cryomodules at the operating temperature points are shown below in Tab. 6.1.1.

Because of very substantial heat loads expected at intermediate temperatures in the cryomodules, it was considered necessary to provide cooling from cryogen streams in close proximity to the heat loads (too much temperature drop between coolant and heat source if conductive cooling through copper braid were attempted), the decision was made to provide cooling to the localized heat sources by a series of parallel flow channels in each cryomodule, and to assure uniform cooling power between the different channels, it was important to have single phase fluid rather than two-phase flow for the coolant. So pressurized helium gas is the most desirable coolant for the 5K and 80K thermal anchor points. The coolant flows for each cryomodule were provided in separate heat exchanger cans (HXC's) which cooled high pressure helium gas flow from compressors in the central helium liquefaction facility by heat exchange with the primary $LN_2$ and LHe coolant sources. A separate HXC was used for each cryomodule, partly because the cryomodules were built and tested at different times and the HXC's already existed, partly because the ideal characteristics for the coolant streams are somewhat different for the two cryomodules. The temperature of the pumped helium for the MLC has been chosen as 1.8K to achieve a very high intrinsic Q for the superconducting cavities not simply to reduce the heat load into the liquid helium but to reduce the power requirements for the RF amplifiers being used to accelerate the beam. Since almost all of the RF power absorbed by the beam being accelerated is compensated by the returning beam being decelerated, it is primarily the losses in the cavities which load the amplifiers. It would be even better

Table 6.1.1: An indication of the expected heat loads from the two cryomodules under various operating conditions. Many of these values have been directly measured, some involve extrapolations (the MLC has not been tested with a beam current passing through it).

**MLC Thermal Loads**

| Coolant temperature | 1.8 K | | 5 K | | 80 K | |
|---|---|---|---|---|---|---|
| | Watt | g/sec He | Watt | g/sec He | Watt | g/sec He |
| Static Heat Load, No RF, No Beam | 16 | 0.8 | 40 | 1.6 | 150 | 0.75 |
| Heat Load with 48 MeV, 1 mA (× 4) | 43 | 2.15 | 45 | 1.5 | 200 | 1 |
| Heat Load with 48 MeV, 40 mA (× 4) | 50 | 2.5 | 50 | 1.67 | 900 | 4.5 |

**ICM Thermal Loads**

| Coolant temperature | 1.8 K | | 5 K | | 80 K | |
|---|---|---|---|---|---|---|
| | Watt | g/sec He | Watt | g/sec He | Watt | g/sec He |
| Static Heat Load, No RF, No Beam | 15 | 0.75 | 40 | 1.6 | 150 | 0.75 |
| Heat Load with 48 MeV, 1 mA (× 4) | 40 | 2 | 50 | 1.67 | 200 | 1 |
| Heat Load with 48 MeV, 40 mA (× 4) | 45 | 2.25 | 90 | 3.00 | 1200 | 6 |

from the point of view of the RF amplifiers to run at the even lower temperature of 1.6K, but the increases in RF efficiency at the lower temperature come at a large additional cryogenic cost to provide cooling at the lower temperature. Operation at 2K is a better compromise for the ICM, since the energy going to the beam is not recovered in any case, and the demands on the pumping system are much lower when operating at twice the helium vapor pressure. The cavities in the ICM have lower intrinsic Q in any case (for reasons that are not completely understood), and so there is in any case not much gain in operating at reduced temperature. Extensive testing of the ICM at both 1.8K and 2K was carried out over a period of some years, while developing higher current low emittance operation, and the 2K operation was found to be much more economical. A temperature below the helium superfluid transition (2.17K) is however highly desirable, since the thermal conductivity of the liquid helium is much higher in this condition, and the uniformity of the cooling on the cavity walls is greatly improved.To achieve the low pressures and moderately high mass throughput of helium required for the 1.8K/2K heat loads in these cryomodules, we have used a parallel combination of multiple pump skids, each consisting of a Tuthill MB2000 Roots blower backed by a Tuthill KT-500 Rotary Piston pump. The ICM testing in the past has used two of these skids in parallel, as has the MLC testing. At the present time we have a total of three of these pump skids, two of which are intended to be used for the ICM (which is intended to continue development operations during much of the time period for the installation of the new beamline and magnet systems), and one of which will be used to finalize testing of the MLC over the next several months, on a basis of testing one cavity operation at a time. The purpose of this initial testing is to better understand and improve microphonics in the RF cavities, and to experiment with stabilization of cavity tuning using piezoelectric feedback, which was not yet completed in the MLC testing before reorganizing the LOE site to accommodate the new test ring. We will

need an additional 3 pump skids (as soon as money becomes available for their purchase) to provide the full cooling power required for simultaneous operation at full field of the six SRF cavities in the MLC.

### 6.1.2 Use of existing Wilson Lab cryoplant

The liquid helium refrigeration plant in Wilson Lab consists of 3 independent liquefier/refrigerator systems each capable of producing 600W of refrigeration at 4.2K, each with its own compressor system. In its primary role, this system provides cooling for the CESR RF system and several superconducting wigglers that are used in the operation of the CHESS facility. During the testing phases of the cryomodules to be used in the CBETA project, it has also provided the refrigeration for these systems. Normally, the available refrigeration power has been in a range which can be handled by two of the three systems in operation, while the third system has been available as a near-immediate backup in case of performance degradation or failure of one of the operating refrigerators. Simultaneous operation of the CESR/CHESS operations along with the CBETA project will bring the total refrigeration demand to a level where it will in general be necessary to use all three of the systems simultaneously, with only modest additional capacity available. This should not present excessive risk to the operation of CESR/CHESS under the assumption that if maintenance or repairs to one of the systems should become necessary between scheduled down periods, the CBETA operations would be put into a standby mode for several days while the unscheduled maintenance was performed. Prior system performance for many months of continuous operation would indicate that very few, if any, shutdowns of CBETA would occur because of main cryoplant failures during the test period, and that they would typically represent periods on the order of a few days if a significant repair were in fact necessary.The compressors used for the helium refrigeration have additional capacity beyond what is minimally needed to run the 3 expansion-engine refrigeration systems, and this extra capacity is what has been used in the past to provide the compressed helium gas flow for operating the 80K and 5K cooling systems. The available capacity appears to be adequate to meet the needs for both the 1mA benchmark operation and the eventual 40mA conditions, but the figures for the load that must be absorbed from higher-order modes generated in the MLC involve extrapolation from the single 7-cell cavity that has already been tested with beam in it, and at a lower average beam current. As there is expected to be some variation from cavity to cavity, and as the HOM power goes as the beam current squared, there is some level of uncertainty as to whether there will be adequate compressor power at the higher current operation. If not, there might be a need to add an additional smaller compressor to make up for the shortage in capacity. Should there be a problem, it should be possible to determine at intermediate beam currents between 1mA and 40mA what level of shortage there might be, and how much additional compressor capacity might be needed (or whether it would alternatively be acceptable to deal with slightly greater temperature rise in the HOM loads).

### 6.1.3 Subsystem Components

The majority of the changes to the building infrastructure needed to deliver cryogenic fluids to the cryomodules in the LOE location have already been completed. This has included a re-

routing of the $LN_2$/LHe transfer line and a local valve box from the earlier Phase 1a test area in LO to the new location in LOE, moving the ICM from its former test location to the final location for the CBETA testing, connection of the HEX can for the ICM into its new location (after rebuilding it for more convenient/efficient operation), re-installing the control wiring for the ICM in the new location, moving the pumping skids for the ICM into a temporary location for testing of the ICM during the installation of the new beam tube and the magnet ring, installation of the temporary 6" pumping line to the HXC, and connection of the cooling water and electrical power for the pumping skids. For the MLC and its HXC, for the next several months there will be continuation of testing without beam, to further characterize microphonics and to test compensation by tuning adjustments with piezos. This has involved moving the related pump skid into a new location and constructing a new pumping line, but this is ready for operation. The exact final location of all pumping skids has not yet been decided upon, but the rearrangement of this part of the plumbing and utilities connection should be a straightforward task once the MLC has been moved into its final configuration for the ring.From the perspective of the cryogenics group, the relocation of the cryogenic transfer lines between the valve box and the HXC for the MLC is the primary specialized task remaining to be completed when the MLC gets moved to the final location for the CBETA ring. The position of these components has already been decided, however, and the path for routing the cryogen transfer line from the valve box has also been allowed for. The addition of 3 additional pump skids and the position change for the helium pumping lines will require some time to accomplish, but are much simpler to install than the vacuum insulated transfer lines.

## 6.2 Heat Exchanger Cans in greater detail

### 6.2.1 Construction and Interfacing

The HXC's for the ICM and MLC currently use a near-identical design, the original HXC for the ICM having been modified prior to the current installation to take advantage of some performance improvements introduced subsequent to the initial manufacture, during the course of many test experiments done in a smaller test cryostat, and then the production of the HXC for the MLC. Each of the cans is about 1m in external diameter and 1.2m high, but situated on legs somewhat over a meter above floor level to provide a convenient connection into the cryomodules relative to the height of the beamline. Each of these cans accepts through a vacuum insulated transfer line an inlet flow of $LN_2$ (at around 30psig and 77K) and LHe (at about 3psig and 4.5K), and returns a stream of cold He vapor from the can through another tube in this same transfer line to a low-pressure input to the Wilson Laboratory helium refrigeration system. It also accepts a stream of high-pressure helium gas (up to 20 bar at 300K), which is passed through a series of heat exchangers to provide coolant streams at various lower temperatures that are circulated through the associated cryomodule before being returned through the heat exchangers in the HXC and finally returned to the low-pressure input of the building helium compressors. And finally, a portion of the 4.5K LHe that enters the HXC is fed through an additional heat exchanger at slightly above atmospheric pressure, subcooled to around 3K by returning low-pressure gas coming back from the cryomodule, and dropped to around 2K by a Joule-Thompson expansion valve on delivery to the cryomodule at

a pressure of around 20 mbar (MLC) or 40 mbar (ICM) maintained by a room- temperature pumping system fed by the return flow through the low temperature heat exchanger, the gas being returned to near room temperature by electric heating before leaving the HXC, in order to avoid condensation on the length of room-temperature pumping line.

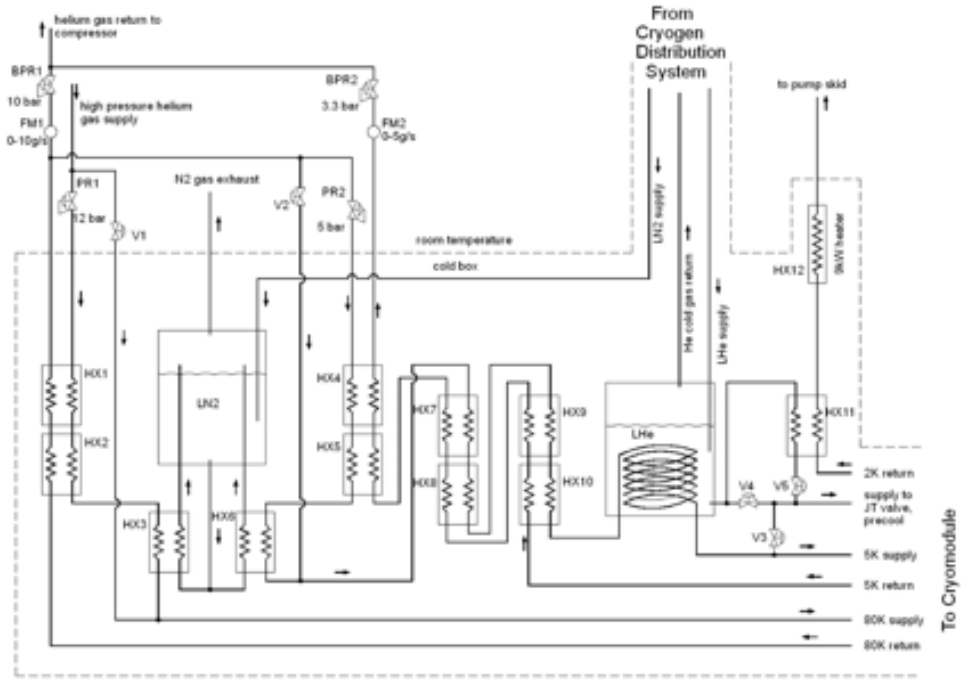


Figure 6.2.1: Schematic view of the helium flow through the HXC for the MLC.

High-pressure pure helium gas from the laboratory compressors enters the HXC through a pressure regulator PR1, typically set to about 12 bar, into the 80K system, whose output is maintained at typically 10 bar by BPR1. The gas is pre-cooled by returning gas flow from the cryomodule through brazed-plate exchangers HX1 and HX2 before being finally cooled to 77K by heat exchange with $LN_2$ in HX3. The flow of $LN_2$ is maintained by a thermosiphon from a $LN_2$ pot maintained at a constant fill level through a pressure-activated valve controlled from a level meter in the pot. The flow rate of the gas through this part of the system is monitored by the mass-flow meter FM1, and may be remotely adjusted by a pressure-actuated valve situated in the cryomodule. In practice we have chosen the set point of this valve manually rather than through a feedback system, although the latter plan would have been possible. Part of the returning gas stream is then sent through pressure regulator PR2 at a pressure of around 5 bar back into the 5K cooling system of the HXC, while the remainder is returned to the low pressure inlet to the compressor system. Similarly to the 80K cooling stream, this 5K coolant stream is first passed through a series of heat exchangers to pre-cool to 80K, then counter-cooled with returning cold gas through another series of 4 brazed-plate heat exchangers to near 5K, then finally to about 4.5K by passage through a spiral of copper tubing immersed in a 4.3K helium bath, before finally being sent on to the cryomodule. As in the case of the 80K system, the flow rate is set by a pressure-actuated valve mounted on the cryomodule. The

outlet pressure from the HXC is maintained at about 3.3 bar by BPR2, and the exiting gas returned to the compressor system input.

Finally, cooling for the cavities is provided by a pumped liquid helium system. Helium from the previously mentioned 4.3K helium bath is passed through a Hampson-style heat exchanger to a temperature around 3K, but still at near-atmospheric pressure, and fed through an actuated throttle valve in the cryomodule which performs a Joule-Thomson expansion to drop the pressure to about 20 mbar, with the throughput of the valve controlled by feedback to maintain a constant liquid helium level in the cryomodule. The temperature of the helium is controlled by adjusting the speed of the Roots blowers which are the first stage of the pumping system with a properly tuned PID feedback system, using the pressure of the helium as a measure of the temperature. It is desired to control the temperature of the pumped helium bath to the fraction of a mK level, not so much because the properties of the superconducting cavities depend that strongly on the temperature, but because variations of the pressure on the outer walls of the cavities, which are immersed in the helium bath, slightly affects the geometry of the cavities and hence the natural frequency, and the efficiency of coupling to the RF system. The discussion of the HXC's up to this point has been discussing is steady-state operation. During the process of cool-down from room temperature to the normal operating point, it is important to have very uniform cooling to avoid distortions and excessive stresses because of differential thermal contraction. In practice, this means quite slow cool-down rates (on the order of 10K/hr, combined with a very uniform ramping of the temperature of the input fluids. This is achieved by mixing the high-pressure gas flows after the cooling to 80K with a variable amount of room-temperature gas flow, starting with almost 100% 300K gas initially, reducing finally to 100% 80K gas. This is done by manual control of valves V1 and V2. Also, during the pre-cool operations, a considerable proportion of the gas which would normally all pass through the 5K system is diverted through V3 through the cavity helium system to pre-cool the cavities and the helium gas return pipe in the cryomodules. This works out rather conveniently, because there is rather little thermal mass in the thermal anchors which are cooled by the 5K system, so cooling those takes very little of the mass flow. Once the system in the cryomodules is down below 100K, there is very little further thermal expansion to be concerned with, so below this point the cooling may be done more rapidly, and with less concern about any thermal gradients which may temporarily occur. The primary difference between this scheme for the MLC HXC and the one for the ICM is that in the latter case the flow control valves for all systems are located in the HXC rather than in the cryomodule. Also, the temperature of the pumped helium in the ICM is 2.0K rather than 1.8K, since without energy recovery for this module, there are fewer gains for the RF system by operating the system at lower temperature, so the reduced cryogenic costs by operating as slightly higher temperature outweigh any added RF costs.

### 6.2.2 Prior performance

The testing which has already been carried out in testing both the ICM and the MLC has indicated that we should be in good shape as far as producing adequate high pressure flow for both the 5K and 80K systems. The situation with the heat exchanger for the 2K system in the ICM has also been thoroughly tested. The heat exchanger for the 1.8K system has only been checked at half capacity because of limits on availability of more pump skids. Extrapolation

from the half-flow performance leaves us confident that it will work fine when we get the additional pump skids.

## 6.3 Cryomodules in greater detail

### 6.3.1 Construction and Interfacing

The cartoon view of the MLC shown below in Fig. 6.3.1 illustrates the main features of the cryogenic distribution within the cryomodule. A more complete description may be found in the following reference [1]. The outer vacuum jacket of the cryomodule is a steel cylinder approximately 1m in diameter and 10m long. The series of six seven-cell niobium SRF cavities, each in its own surrounding helium chamber is supported from a 250mm titanium tube, the Helium Gas Return Pipe (HGRP) which doubles as a stable mechanical mount and part of the pumping system for maintaining the superfluid helium at 1.8K (approximately 20 mbar pressure). At one end of each cavity is an input coupler (IC) for introducing the 1.3GHz power into the cavity, and between each cavity and the next (and at each end of the string of cavities) is a higher-order mode absorber (HOM) to remove energy from unwanted higher-frequency RF fields which are generated by interaction between the fields in the cavities and the very short bunched structure of the electrons in the beam. All the cryogenic components are enclosed in a cooled 80K aluminum shield to intercept the room-temperature thermal radiation load, and specific thermal intercepts are placed on all the support structures to remove most of incoming heat loads at the higher temperatures of 80K and 5K, rather than at the operational temperature of 1.8K. All the cold structures are additionally wrapped in 10-30 layers of "superinsulation" in order to further reduce the heat transport by thermal radiation. Because the cavity performance is adversely affected by the presence of static magnetic fields above the milligauss level, there are also magnetic shielding layers at low temperatures around each cavity, and at room temperature outside the 80K shield. The HGRP is supported from the vacuum vessel by 3 cylindrical G10 posts, equipped with mechanisms for external positioning adjustment to allow fine control of the beamline location. The central support post is fixed in location, while the end posts allow for longitudinal motion of the HGRP relative to the vacuum vessel caused by thermal contraction of about 20mm in the length of the HGRP upon cooling to operational temperature from room temperature. Bellows sections incorporated into the HOM absorbers allow for the smaller changes in position relative to the HGRP experienced by the cavities. Because of the magnitude of the heat loads being absorbed at both 5K and 80K under normal operating conditions, it was necessary to get the coolant fluids very near to the source of heat generation. Cooling through copper braids as is commonly done in low duty cycle machines would in this machine have produced excessive temperature gradients. Thus convective flow of helium through an array of parallel tubing flow channels was used to get the heat exchange area very near to the sources of heat production. With multiple parallel flow paths, thermal runaway problems must always be considered, as if there is a greater heat load in one flow channel, the density of the coolant will decrease, and the viscosity decrease, thus diminishing the flow, in turn increasing the temperature rise. The key to avoiding this is to insert a flow-limiting impedance in the supply side of the lines prior to the point where the heat load is introduced, establishing effectively a current source. This has been implemented and tested in our MLC. Also, the 80K heating in the HOM's is much greater than that in the IC's,

so to simplify the plumbing the 80K cooling loop on each IC is placed in series and in front of the 80K cooling on the adjacent HOM, This gives then a very small temperature rise in the IC, which is desirable in part because there is necessarily a stronger thermal connection between the 80K and 5K anchors in the IC's than in the HOM's.The input flows into the 5K and 80K manifolds is adjusted by remotely controlled electro-pneumatic valves, and may be adjusted to provide an adequate cooling for the current operating conditions of the machine, which may vary significantly with beam current.The cooling for the cavities to be maintained at 1.8K is supplied by an input stream from the associated HXC at roughly 3K and slightly above 1 bar absolute pressure, and restricted by a JT valve, remotely controlled, usually by automated PID feedback to maintain a constant level in the 100 mm diameter so-called "2K-2phase line" (2K2$\phi$) which is physically slightly above the string of helium vessels for each cavity, each connected to the line by a short connecting line of the same diameter. The top of this 2K2$\phi$ line is attached to the HGRP again by a short connecting line, and the pressure of the gas is regulated by adjusting the blower speed of the room-temperature pumping system connected to the line. Because the superfluid helium is an excellent thermal conductor, temperatures gradients between the evaporating surface and the cavities is no more than the mK range under normal operating conditions.From a cryogenic perspective, the ICM differs only in minor ways from the MLC. It is about half the length, has five two-cell cavities rather than six seven-cell ones, has a different model of HOM from what is used in the MLC, and more significantly has much higher power dissipation in the IC's, because there is no energy recovery so vastly more power must be supplied from the RF system. There are also two IC's per cavity, both to symmetrize the RF fields in this lower energy regime, and to cut in half the amount of power required to be handled by each IC. Also, the four valves to regulate the flow of the cryogen streams into the cryomodule are in this case located in the associated HXC, rather than in the cryomodule itself. The cryogenic loads for the two types of cryomodule are actually remarkably similar at the nominal 40mA operating conditions as may be seen from Table 1, the main difference being in more 5K cooling required for the input coupler operation (and less expensively, somewhat more 80K cooling also for the IC's). Because the Q of the cavities used in the ICM is about a factor of 4 lower than those in the ICM (for reasons still not completely understood), the performance depends much less critically on the cavity temperature – there is essentially no performance improvement from operating at 1.8K instead of 2K. Thus, it will be run at 2K, since this puts much less demands on the pumping system (the vapor pressure of the helium is twice as high). We therefore have a lower capital cost (fewer pump skids), and somewhat lower operational costs. If we were operating in an energy-recovery mode, the lower cavity Q would be disastrous, because there would be much higher loading placed on the RF system, but in this case, almost all the power delivered by the rf system goes directly into the electron beam rather than internal losses in the cavities anyway.

### 6.3.2 Prior performance

At this point the ICM has seen several years of testing (the performance of the cryomodules from other than the cryogenic aspects may be seen in more detail in other sections of the design review document), and the cryogenic system has been demonstrated to be adequate for essentially all aspects of operation which will be required for the CBETA project. In particular, it has been at the full 10MeV level which will be utilized, and at or above the same average

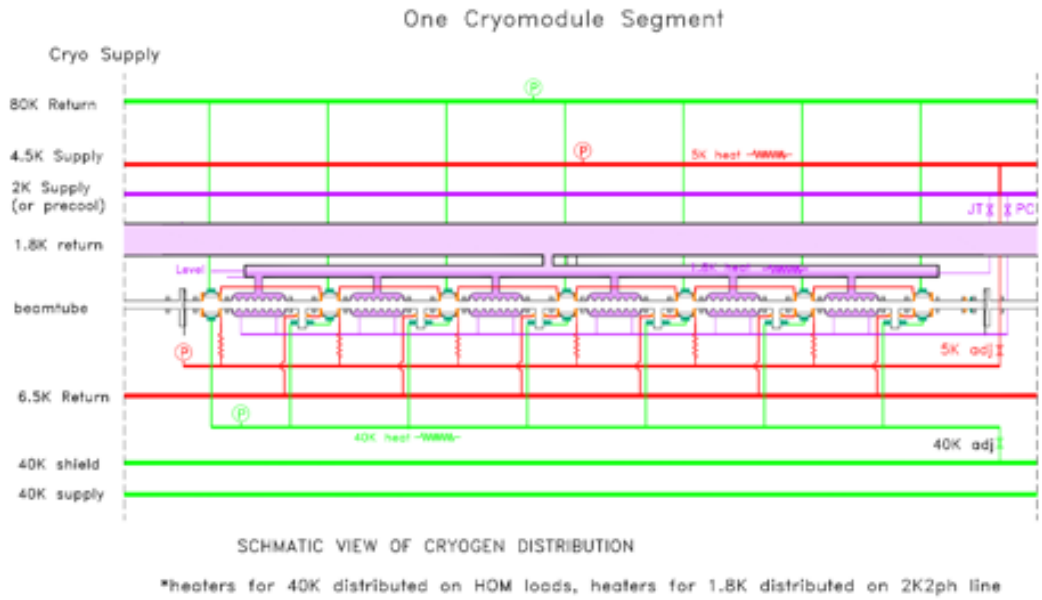


Figure 6.3.1: Schematic view of the MLC as it would be placed in a string of many cryomodules. In the case of the CBETA testing, there is just one cryomodule, with end caps on each of the main supply and return lines.

beam current. This means that the capabilities of the 2K pumping system and heat exchanger have already been fully tested, as have the cooling of the 5K and 80K intercepts for the input couplers. The 80K cooling power of the HOM loads has been less well investigated, however, because the HOM power is expected to vary as the square of the bunch charge and only linearly in duty cycle. So in the CBETA operation where only one bunch in four is populated, but at four times the average charge, the average HOM power will be 4 times what has actually been tested under beam loading. However, if this power goes according to theoretical expectations, we have tested with direct electrical heaters that it will also has the capacity to handle this heat load.Much of the required performance of the MLC cryogenic system has also been demonstrated, but budgetary limitations have prevented us from testing some of the performance parameters. We do not yet have enough High Power Amplifiers (HPA's) to simultaneously test all cavities at full RF power, nor enough pump skids to provide the level of 1.8K helium throughput if we did. However, all cavities have been individually tested at the needed RF power levels, and power demand levels and pumping characteristics have met design expectations. We are quite confident that when the new HPA's and pump skids are purchased and installed, there should be no difficulties with the 1.8K pumping system. We have not yet put a beam through the entire system, but have been able to test with electrical heating of resistive loads that we will be able to handle the requisite demands on the 5K and 80K cooling loops.

## 6.4 Sensors and Controls for the cryogenics system

Both cryomodules and both HXC's have a large number of installed thermal sensors installed (probably more than might be needed in a production model, but very useful for diagnostics in a prototyping phase). In general, thermometers for 80K and above have been platinum resistance thermometers, and for thermometers which also need to cover the range below 80K, we have used Cernox thermometers. These have been read out with CryoCon modules which can each handle 8 sensors with quite adequate readout speed (1 sec or less). We have measured helium pressures on the pumped helium with capacitance manometers operated at room temperature, and we have used the output from these to regulate pumping speed, and hence control temperature. Level measurement of $LN_2$ baths in the HXC's has been done with commercial capacitive level sensors. Level measurement of the helium has been with commercial superconducting wire level monitors (because of the crucial nature of this output, and the great difficulty of making replacements, each cryomodule has 4 sensors installed, though we have not yet had failures – there have been occasional failures in similar level sticks installed in many other cryostats in the overall facility over a period of many years). For the high-pressure helium system we are using room-temperature mass-flow meters based on a thermal transport principle. For measurement of mass flow on the 1.8K/2K pumping systems, we have been using a combination of similar mass-flow meters, or for higher precision on testing of cavity Q's by thermal means, mechanical gas-flow meters on the output of the pumping skids. There are some somewhat more specialized systems, built in-house for measuring transverse movements of the beamline/cavities upon cool-down with capacitive measurement of spacing from a stretched wire, piezoelectric systems for fine-tuning of cavity frequencies, low-temperature stepping motors for doing coarser control of cavity frequencies. Vacuum measurements are made, depending on system and pressure range with cold cathode gauges, pirani or convection gauges, ion-pump currents.Generally, the outputs from all the sensors are fed locally to a PLC, which also controls many local control loops, and then are further integrated to a general EPICS control system which allows full remote control, readout, and archiving of signals.

## 6.5 Safety Issues (that have already been considered for our prior test operations)

As is general with cryogenic systems, the primary considerations for personnel protection are issues of direct contact with cold surfaces, avoidance of any possibility of asphyxiation from reduced oxygen because of displaced air by release of cryogenic gases, and assurance of pressure relief on all systems which might either be closed off, or have sudden pressure buildup because of sudden heat load. Because both the ICM system and the MLC system have been the object of extended testing in Wilson Lab, extensive prior consideration has been given to these questions, and have been incorporated into Wilson Lab safety plans. In general, it has been more straightforward than many of the laboratory cryogenic safety situations, because neither system has a very large volume of cryogenic fluids contained in it, and it is enclosed in a room with a very large volume (much easier to ensure safety against sudden cryogen release than some of the systems in the tunnel). Only mild adjustments in the existing safety plans

have been necessitated by moving cryostats into a new location. One less major consideration, condensation from cryogenic transport lines, typically only occurring start-up operations, have also been addressed by catching basins and drain tubes in strategic areas to avoid risk of water dripping on electrical circuits, or providing slippery spots on floors where workers might be walking.

## 6.6 Aspects still under development

There are two potential areas that might impact readiness of the cryogenic system for CBETA operation. One is that there was a small leak between the helium space and the insulation vacuum in the ICM during the last several years of operation. This was small enough so that operation could be maintained (though with a somewhat higher static heat load) by continually pumping on the insulation vacuum space with a turbo pump. Unfortunately the size of this leak was never documented at room temperature. Between the last run of the ICM and the present time, the system was partially disassembled to improve the uniformity of the high-pressure flow distribution for 5K and 80K cooling. A small leak was localized at this time, but in a place very hard to repair in situ, and it was decided that this was probably the same leak that has been there all along, so was not repaired. We have added considerably greater pumping capacity, but until we cool the system back down, we will not be 100% sure this is indeed the same, unchanged leak we saw before. This will be verified in the first half June, but if the leak rate turns out to be too high, it may be necessary to again remove the ICM to another location and perform repairs, which would result in a minimum of a month's work for several people, or potentially several times that if the repair should require more extensive disassembly.The second aspect of things is that the tuning sensitivity of several of the cavities in the MLC to microphonics has been marginal. There has not yet been time to thoroughly examine this issue. While not enough to make the immediate 1 mA beam current impossible, it is probably necessary to either eliminate some of the sources of the microphonic noise, or else to use active piezoelectric control to compensate if we are to achieve the full 40 mA goal. This should be done as soon as there is an opportunity (depends somewhat on both budget and personnel availability).

## References

[1] Eichhorn, R., *et al. First results from the Cornell high Q cw full linac cryo- module.* IOP Conference Series: Materials Science and Engineering, **101** (1), page 012020 (2015).

# 7 Vacuum System

## 7.1 Vacuum system layout and sections

The vacuum system layout will conform to the accelerator lattice layout. Accordingly, the vacuum system will consist of the following sections, as shown in Fig. 7.1.1.

- Injector and merger
- Main linac cryomodule
- Demerger and beam dump
- Splitters and combiners
- FFAG arcs and straight

beam pipe The injector includes the electron gun and the ICM. This section is already exist from the Cornell Prototype ERL Injector project, and is to be relocated and reused for the CBETA project. The detail of this section is described in the Injection section of this report. The short merger beam line that connects the injector to the main LINAC is also described in the injector section.

The MLC is a self-containing accelerator section from vacuum system point of view, and is described in a separated section in this report. The interface between the MLC and the rest of the CBETA vacuum system will be described in §7.3.7 below.

The electron beams of 4 different energies (exiting and entering the MLC) will be split into four separated beam pipes and then recombined into a single beam pipe for optics and timing reasons. One of important features of this section is to provide beam path length adjustments for each of four energy electron beams.

The FFAG arcs and long straight sections consist of more or less repetitive structures of magnets. Thus units of repetitive simple beam pipes will be designed for the FFAG sections.

The energy recovered electron beam (with lowest energy) is demerged into a high power beam dump. The beam dump transport beamline is also exist from the Cornell Prototype ERL Injector project, and is to be relocated and re-used for the CBETA project.

## 7.2 Vacuum system requirements and design considerations

Vacuum beam pipes are part of beam transport system. A list of vacuum requirements and design considerations is given below.

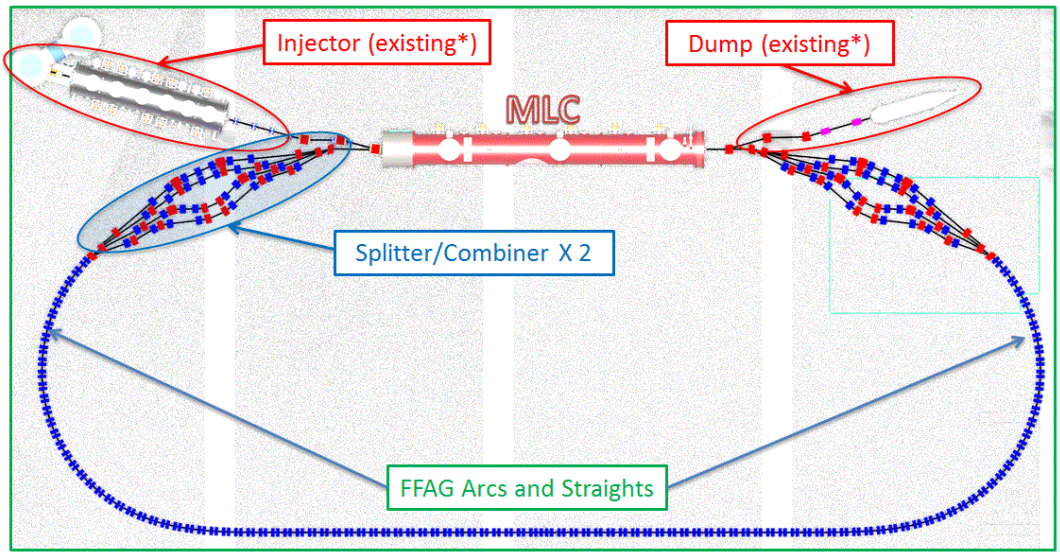


Figure 7.1.1: CBETA Layout and vacuum sections.

- Produce adequate level of vacuum, through proper beam pipe material selection and preparation, and vacuum pumping. The required level of vacuum will be determined by acceptable beam losses due to residual gas scattering, among other factors.
- Aluminum (6061-T6 or -T4) is preferred material for the beam pipes for its good electric conductivity (resistive-wall), no residual radioactivity (from beam losses) and low magnetization (from cold work and welding etc.)
- Provide sufficient large beam apertures, while allowing magnets position adjustment.
- With high beam current and closely spaced electron bunches, design efforts will be made to keep low beam impedance, including smooth beam pipe inner profiles, RF shielded bellows and gate valves, gentle transitions between different beam pipe cross sections, etc.
- Beam pipes will host various beam instrumentation and diagnostics, such as BPMs and instrumentation ports (for beam viewers, etc.)

## 7.3 Vacuum system construction, installation, and operation

### 7.3.1 FFAG Arcs and Straight

In the FFAG arcs and straight, permanent magnets are arranged in more or less periodic double-magnet cells. The relatively short drifts between magnets are reserved as much as possible for vacuum pumping, beam instrumentation. Therefore, it is efficient use of these drifts by constructing beam pipe assembly through multiple FFAG magnet cells, reducing number of beam pipe flanges. A typical 4-cell FFAG arc beam pipe assembly is depicted in Fig. 7.3.1. The FFAG beam pipes may be made of extruded 6061-T6 (or -T4) aluminum with

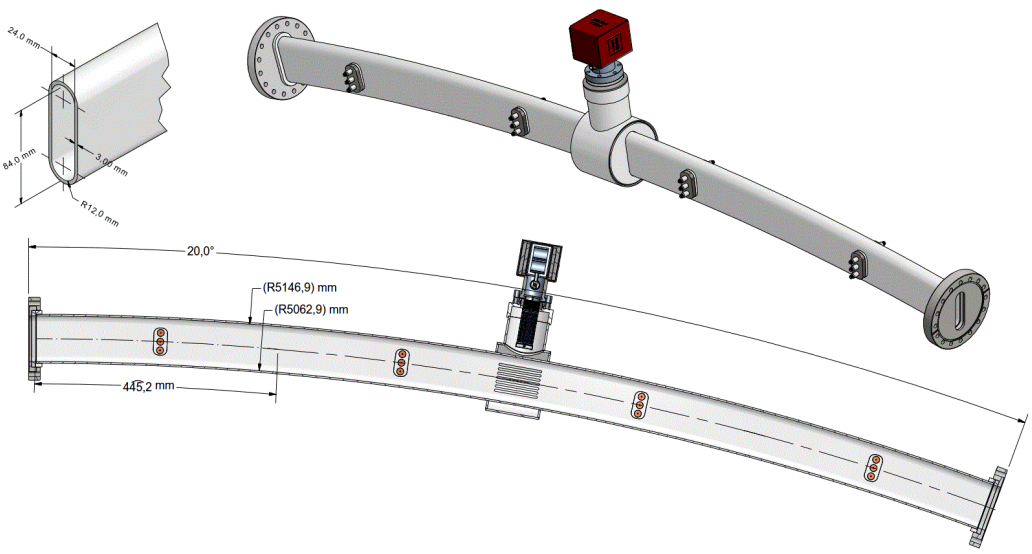


Figure 7.3.1: A conceptual FFAG arc 4-cell beam pipe design. The 1.8-m long beam pipe assembly houses 4 sets of BPMs on the 7-cm drifts between QF and QD magnets, and one pump port on the 12-cm middle drift between FFAG cells. Beam instrumentation ports may be added at two additional 12-cm long drifts.

cross section designed to meet both required beam apertures and magnet clearances, as shown in Fig. 7.3.2.

### 7.3.2 Splitter and Combiner

To keep low beam impedance, the beam splitting and combining vacuum chambers may be made of aluminum alloy (6061-T6) with smooth beam path transitions, as illustrated by an example vacuum chamber used for the Cornell Prototype Injector project, in Fig. 7.3.3.

The separated beam pipes will be designed to allow independent beam path length adjustment by using sets of 4 RF-shielded bellows in CBETA's final configuration. However, during staged beam operations starting from single beam to multiple beams, simple beam pipes with low cost non-RF-shielded bellows may be used for various initial beam path configurations.

Beam collimators (or/and scrappers) may also installed in these single beam chambers, together with BPMs and other beam instruments.

### 7.3.3 RF-shielded bellows

Bellows with RF shields are needed to provide adequate flexibility of the vacuum system in vacuum component installation and operations. Two examples of RF shielded bellows have been successfully constructed and operated in the Cornell photoinjector and in the Cornell Electron storage Ring (CESR), as shown in Fig. 7.3.4.

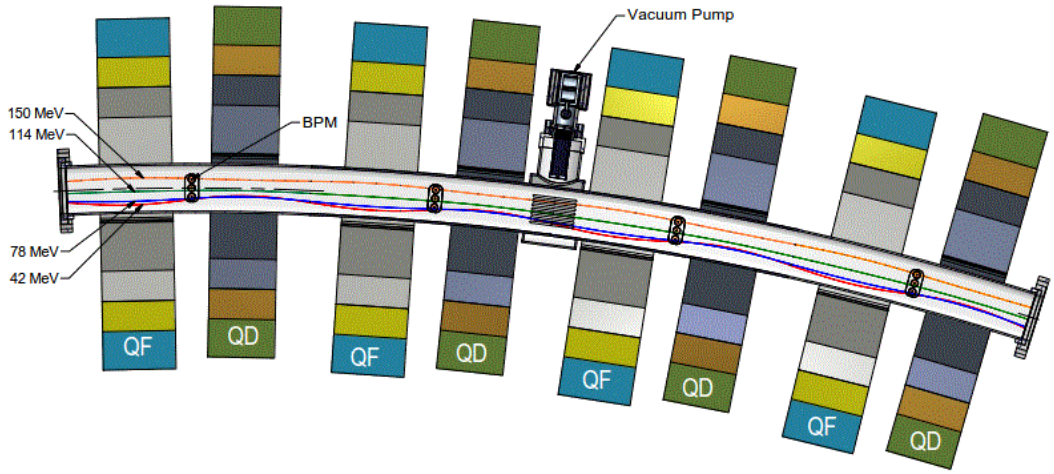


Figure 7.3.2: The conceptual beam pipe with 4 sets of magnet cells. Beam trajectories for 4 beams also shown. The beam pipe provides adequate beam aperture (with 12-mm closest approach between 42-MeV beam to inner wall). The minimum clearance of the beam pipe to the magnet pole tips is roughly 2-mm.

### 7.3.4 Ion clearing electrodes

Ion trapping may not be avoidable without active clearing method, due to the nature of in the final CBETA CW beam operations. Low impedance clearing electrodes may be deployed at various locations to reduce ill-effect from the ion trapping. Thin electrodes directly deposited onto the interior walls of beam pipes have been successfully implemented in CesrTA and Super KEKB. A clearing electrode beam pipe of this style was made and tested in the Cornell prototype ERL injector (see Fig. 7.3.5).

### 7.3.5 Vacuum system construction and installation

All vacuum beam pipes will be fabricated following stringent ultra-high vacuum (UHV) procedure and practice. All beam pipe assemblies will be certified to be leak-free, and will be baked in vacuum up to 150 C. Most of the beam pipes will be delivered to BNL to be assembled onto the girder units. The baked beam pipes will be back-filled with chemically filtered nitrogen (with moisture and THC at ppb level) for transportation and girder assembling. The same nitrogen system must be used to purge the beam pipes whenever any flange is to be opened for connection, etc. Operational experiences of Cornell prototype ERL injector, as well as CESR vacuum systems have demonstrated that in situ bake-out is not necessary with above beam pipe preparation and installation procedures.

The injector, the ICM and the beam dump are to be installed and surveyed into locations. These sections are equipped with RF-shielded gate valves.

The splitter/combiner and the FFAG sections will be installed in corresponding girder units. The detail installation sequence will be developed during the engineering design process to minimize air exposure of the vacuum beam pipes. Further system and cost optimization will

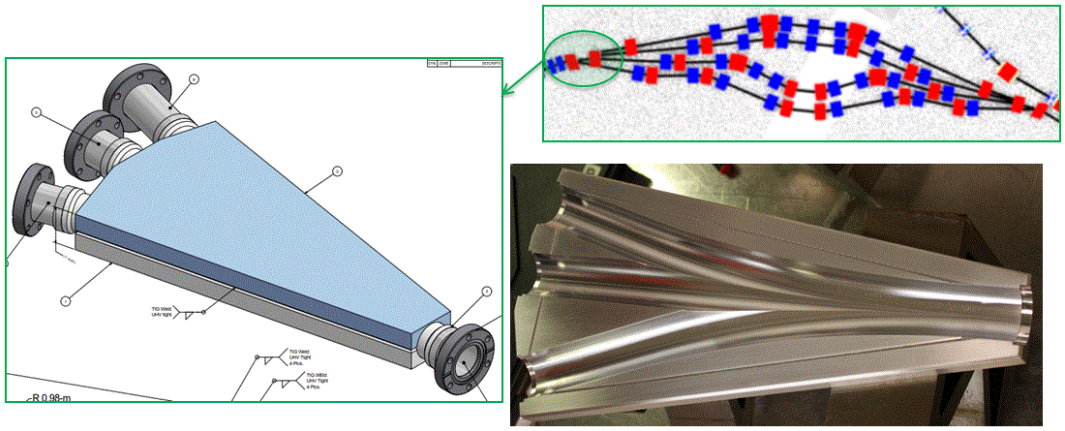

Figure 7.3.3: Example design for beam splitting and combing chamber, by welding two machined aluminum halves with smooth beam path transitions.

be carried out to decide if any additional RF-shielded gate valves are needed in these sections. During the initial operations low cost UHV gate valves without RF-shield may also be used at locations where staged reconfigurations is expected, such as the splitter section.

### 7.3.6 Vacuum pumping

With very limited spaces between magnets, compact and high capacity non-evaporable getter (NEG) pumps will be used, such as CapaciTorr (sintered NEG modular pump) and NexTorr (combination NEG and ion pump), see Fig. 7.3.6 for example pumps. The locations of pumps will optimized during CBETA engineering designs, with aid of vacuum simulations (see Section 4).

### 7.3.7 Vacuum instrumentation and operation

Ionization vacuum gauges and ion pumps will be used as primary vacuum signals for monitoring of the vacuum system performance. Residual gas analyzers (RGAs) will also installed in strategic location for vacuum system diagnostics and in-situ trouble-shooting. Vacuum system inter-lock based on combinations of ion gauges, ion pumps and low vacuum gauges (such as Pirani gauges) will be implemented to protect critical accelerator components, such as the DC photo-cathode electron gun, ICM and MLC, etc.

## 7.4 Vacuum pumping and performance simulations

With highest beam energy of 200 MeV, synchrotron radiation induced gas desorption from the beam pipe wall is negligible. Therefore thermal outgassing is the only source of gas in the beam pipes. With pre-installation bake-out of all beam pipes, and venting/purging with chemically filtered nitrogen, low thermal outgassing rate ($< 1 \times 10^{-9}$ torr-l/s-cm$^2$) can be achieved within 24-hour of pump-down, and continuing decrease with time as $\dot{q} = q_i t^{-\alpha_i}$ (with $\alpha_i \approx 1$).

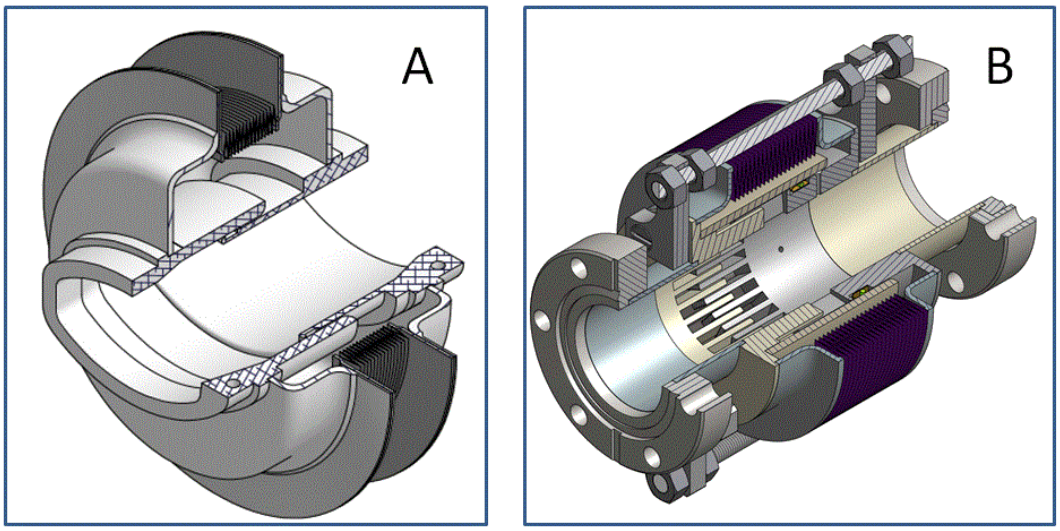


Figure 7.3.4: RF shielded bellows used in CESR (A) and in Cornell Prototype photoinjector (B).

Vacuum system performance design will be aided by 3D vacuum simulations, using a 3D tracking program, MolFlow+ [1]. As examples, Fig. 7.4.1 compares simulated pressure profiles with two different pumping configurations in a 4-cell FFAG beam pipe, and the results showed one pump per 4-cell beam pipe is sufficient. Figure 7.4.2 demonstrates the continuing improvement over time for a 4-cell FFAG beam pipe with one pump per cell. Vacuum simulations will be carried out for all the CBETA sections as more engineering details of the beam pipes becoming available.

## References

[1] http://test-molflow.web.cern.ch/ (2013).

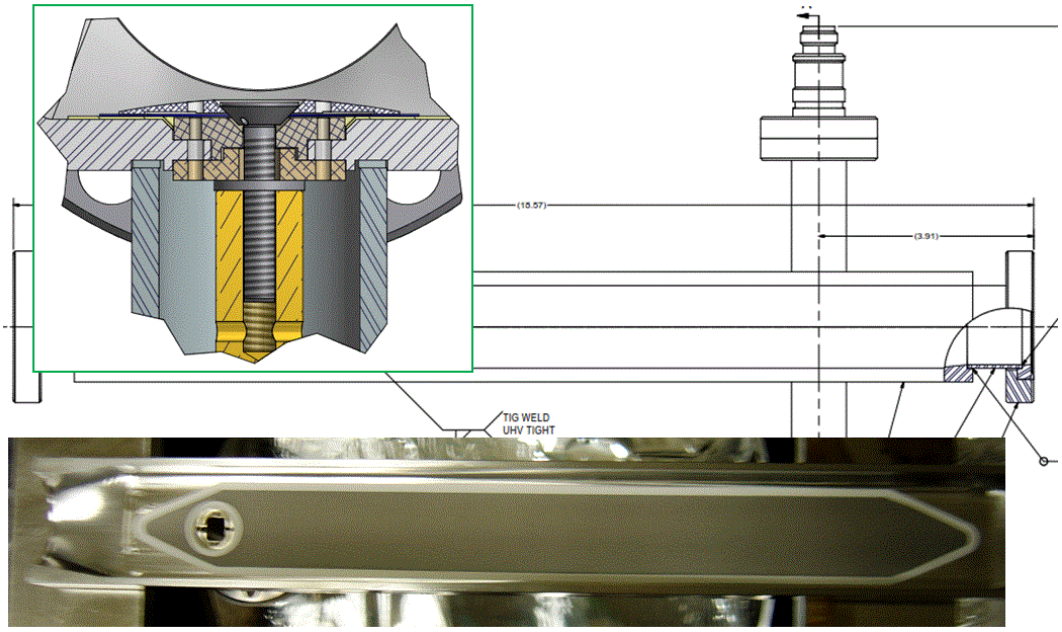


Figure 7.3.5: Low impedance ion clearing electrode chamber tested in the Cornell prototype ERL injector. The electrodes are made of a tungsten thin film (0.1-mm in thickness) on top of a thin ( 0.2-mm) alumina substrate. Both alumina and tungsten thin films are deposited via thermal-spray technique. A low profile electric connection is shown in the insert.

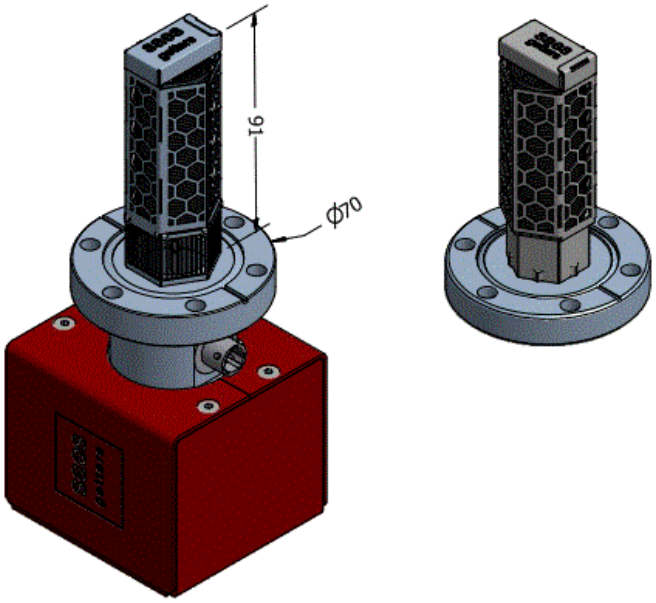


Figure 7.3.6: Typical vacuum pumps for CBETA vacuum system, with a 200-l/s NexTorr (left) and a 200-l/s CapaciTorr (right).

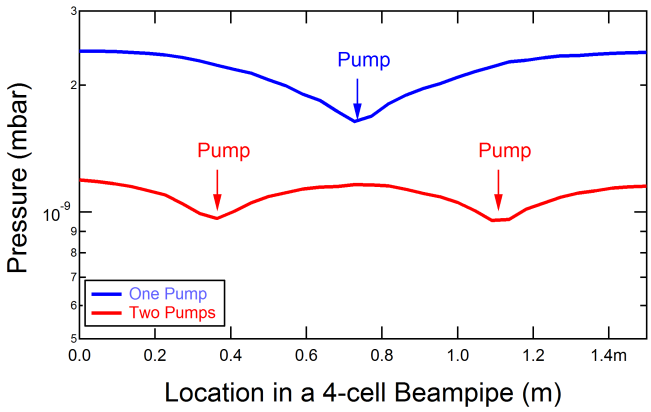


Figure 7.4.1: Simulated pressure profiles in a 4-cell FFAG beam pipe, comparing one-pump and two-pump per beam pipe configurations.

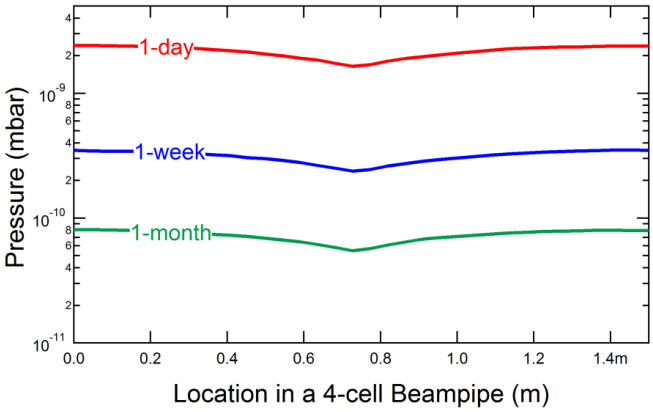


Figure 7.4.2: Simulated vacuum improvement with time for a 4-cell FFAG beam pipe in one-pump configuration.

# 8 Diagnostics and Control

## 8.1 Introduction

The salient feature of CBETA for diagnostics is the presence of multiple beams which need to be individually diagnosed and controlled. The following sections describe the components of the beam diagnostics and control system with particular attention given to how these components will handle multiple beams.

### 8.1.1 Beam position measurement system

The transverse beam size in the CBETA FFAG arcs is measured in tens of microns. Lattice errors in the arcs that are a fraction of the beam size can lead to orbit oscillations which will degrade the beam quality. Somewhat larger lattice errors can lead to beam loss. Commissioning and operation of CBETA will require the ability to measure and correct orbits at the micron level. While these tolerances are tight, they are within the state of the art in presently operating accelerators. CBETA presents the additional requirement of measuring the orbit of multiple beams simultaneously. It will also support multiple operating modes, as described in section 2.8.

The proposed CBETA bunch patterns have in common the presence of a probe bunch separated in time from other bunches. The position of the probe bunch is observed for each energy pass at each BPM. We will be relying on the probe bunch to be an accurate representative of the other bunches in the loop. The BPM signal processing will be a time-domain based system (as opposed to an RF system) in order to distinguish closely spaced bunches. The minimum useful separation in time of the probe bunch from other bunches is determined by the capabilities of the BPM electronics as discussed below. The planned separation in time is 8.5 RF cycles at 1300 MHz, approximately 6.7 nS.

In the FFAG arc the BPMs must provide accurate position information for multiple orbits over a large horizontal aperture, approximately +/- 25 mm from the nominal center. This will require more than four pick-ups per BPM as discussed below.

#### BPM Pick-ups

The CBETA BPM pick-ups will be buttons. They are more readily accommodated in the limited longitudinal space between elements of the FFAG arcs. Calculation of the response for the BPM pick-up indicates the need for more than four buttons per BPM in order to provide adequate sensitivity over the large required horizontal aperture.

BPM designs were evaluated in a manner similar to [1]. First, a simple 2D model of the beam pipe cross section, along with the desired layout of the BPM button detectors, was created using Poisson [2]. Field maps were generated with each button individually set to a potential

Table 8.1.1: Merit Function for BPM Designs

| Number of Buttons | Button Width (mm) | Merit ($\mu$m) |
|---|---|---|
| 4 | 1 | 69 |
| 4 | 2 | 22 |
| 4 | 3 | 12 |
| 6 | 1 | 9 |
| 6 | 2 | 4 |
| 8 | 1 | 5 |

of 1 Volt. From these field maps, the approximate integrated signal on each button can be determined, for a small beam of charge $q$ located at any $(x, y)$ position. These calculations can be used for two purposes: first, in a real machine, the measured button signals can be compared with these predictions, and a best fit $x, y, q$ can be determined; and second, the sensitivity of these best fit values to noise can be calculated, and used as a figure of merit for the BPM design.

To define the merit function, we assumed that each button would have an r.m.s. noise level $\delta q = 10^{-3}q$, uncorrelated with the other buttons. Then we calculated the r.m.s. errors $\delta x, \delta y$ that this noise level would produce in the best fit beam position as a function of the actual beam position $x, y$. These errors were averaged over a region within the pipe where the beam is likely to be, producing two numbers– the average $x$ and $y$ error within the beam region. Finally, the merit function was defined as the larger of these two numbers, which in almost all cases was the average $x$ error, due to the elongated shape of the pipe. Thus, in most cases, the merit functions we report can be interpreted as an average uncertainty in the horizontal beam position for a noise level of $10^{-3}$.

The beam pipe simulated here is a flat pipe with rounded ends. The full width of the flat part of the pipe is 64 mm, and the round ends have an inner radius of 12 mm. Thus, the height of the pipe is $2 \times 12 = 24$ mm, and the full width of the pipe is $64 + 2 \times 12 = 88$ mm. Button widths were 1, 2, or 3 cm, and were placed symmetrically along the top and bottom of the pipe at positions that minimized the merit function. We also tried centering the buttons over the centroid of the (offset) beam orbit, but the performance difference was negligible. The results for various numbers and sizes of buttons are summarized in Tab. 8.1.1.

From the results, it's clear that there is a big performance improvement moving from 4 to 6 buttons, but it becomes much more marginal above that. In addition, from the point of view of this model, larger buttons always give better performance.

### BPM Electronics

The preliminary electronic design concept is to use two BNL designed V301 modules (with four 400 MSPS analog to digital converters (ADC) per module) for each button set and pass data between the modules using point-to-point high speed serial data links. Although the latest revision of the V301 module includes a connector with direct connections to the Multi-

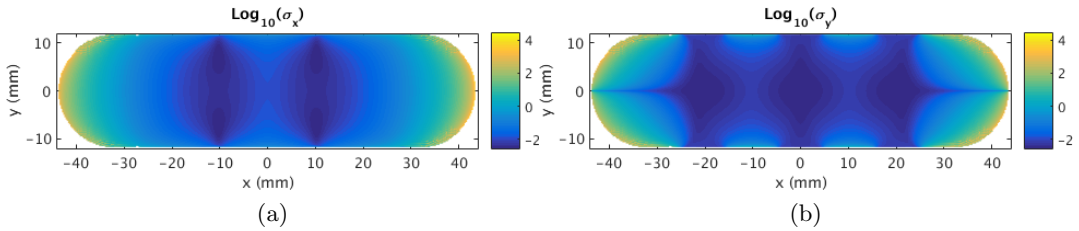


(a) (b)

Figure 8.1.1: The error in the best fit x and y beam position as a function of the actual beam position for the case of six buttons with a width of 1 cm. The figure color is on a logarithmic scale.

Gigabit Transceiver (MGT) pins on the Xilinx Zynq gate array, gate array code has not yet been developed to use these links. Therefore this part of the design will be developed. In addition, several challenges exist with this solution including determining if all required data can be sent between the two modules within the required time period. Other details that will be addressed include development of the algorithm for converting the 6 or 8 button signal measurements to beam position.

In order to distinctly measure each energy bunch, sufficient longitudinal separation between bunches is necessary. Separation of approximately 6.7 ns for probe bunches is expected to be provided. The following two potential solutions are being explored:

1. Use fast analog switches to select the bunch of interest, with a bandpass filter in the front end analog circuit to generate a ringing signal for under-sampled ADC measurements that will be used for the position calculation.

2. Synchronize the ADC clock to the beam and generate the ADC trigger on the peak of the bunch signal of interest. In this case a low pass filter would be used to broaden the pulse width, but any ringing of the signal must settle to zero before the next bunch arrives. A bandpass filter would not be used, and a fast analog switch would not be used.

The challenges associated with both options will be explored to determine which analog signal processing method is optimum. Regarding option 1, the fast analog switches will likely create transients in the filter response, and a glitch removal circuit will likely be needed. This has been done in other accelerators but will require substantial design effort. Regarding option 2, configuring the ADC timing to the peak of the selected bunch is not trivial. A low jitter beam synchronous clock will be required, and continuous tracking of the peak will be needed. Challenges related to both options include hardware, firmware and software design and development to select the bunch of interest. Timing for each accelerating/decelerating energy bunch will be different and it may be possible to measure only a single accelerating or decelerating energy bunch at any given time. Selection of the specific bunch for measurement and coordination of timing changes will be required. Automatic sequencing of bunch selection may be possible.

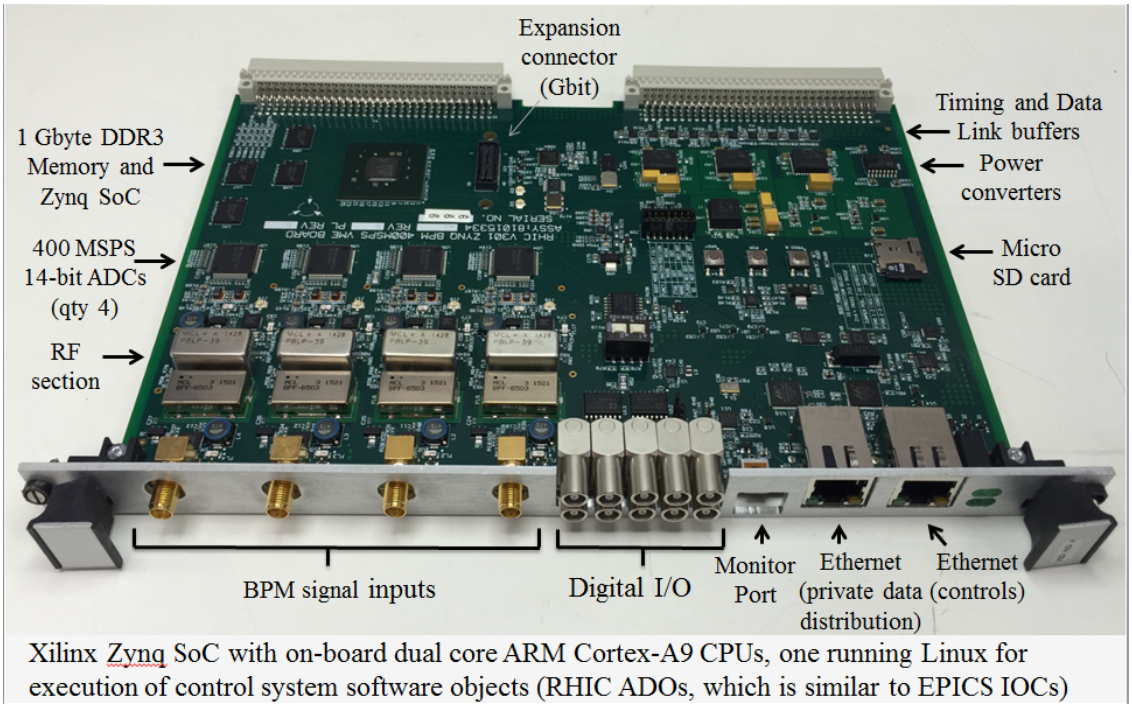


Figure 8.1.2: BNL V301 BPM electronics module

### 8.1.2 Bunch Arrival Monitors

Operation of CBETA requires measurement and control of phase of the beam arrival at the linac relative to the RF.

In previous work frequency domain beam monitors have been developed for the injector which provide beam phase information. These monitors achieved a phase accuracy of 0.1° under typical operation conditions. The monitors compare the 1.3 GHz frequency component of the beam signal to the RF master oscillator signal. Similar monitors can function in the presence of two beams by measuring both the 1.3 GHz and 2.6 GHz frequency components of the beam signal. Placing these monitors near the end of end of the spreaders (where there are only two beams) just before the linac will provide the required bunch arrival time information.

The bunch arrival time is controlled through adjustment of the path length through the spreaders.

### 8.1.3 Beam Size

View screens with resolution of about 30 um will be used to obtain the beam profile for low beam currents. While the beam size in the FFAG arcs is comparable to this the screens may still be useful for detecting conditions which cause the beam size to grow. In the spreaders the horizontal beam size will be larger due to dispersions and view screens will then provide useful quantitative measurements.

Two different screen materials will be used to cover several orders of magnitude in beam current: BeO that is sensitive to sub-nano-Ampere average currents, and less sensitive CVD

diamond screens that can take up to 1 $\mu$A of beam current. RF shielded assemblies will be employed throughout when the screens are retracted to minimize perturbations due to wakefields on the beam and heating effects.

View screens are a destructive monitor, observation of the beam results in elimination of all subsequent passes. For this reason one may not observe decelerating beams in CBETA on view screens, i.e. a screen inserted to intercept a decelerating beam will first intercept the accelerating beam. In the FFAG arcs one can insert a view screen from the outer radius so as to intercept only the highest energy beam, or by inserting further intercept the next lower energy beam. The two lowest energy beams have insufficient horizontal separation to allow viewing the second energy beam while still allowing the lowest energy beam to pass.

### 8.1.4 Beam Loss Monitors

Beam losses in accelerator with continuous injection can contain high power. A high energy 20 um size electron beam of 40 mA is capable of drilling through a 3 mm thick aluminum beam pipe in as little as 10 uS [3]. The radiation associated with partial beam losses can make operation of the accelerator problematic. Thus beam loss monitoring is required for both machine protection and facilitation of operation.

BPM based current measurements or wall current measurements comparing the current out of the injector to the current delivered to the dump can provide a measure of the total beam loss around the ring. At current levels high enough to present a prompt machine hazard this total loss measurement will be one input to the machine protection system.

Beam loss will additionally be monitored by gamma and neutron radiation detectors to provide localized measurements of losses around the ring.

## References

[1] Helms, R. W. and G. H. Hoffstaetter. *Orbit and optics improvement by evaluating the nonlinear beam position monitor response in the Cornell Electron Storage Ring.* Phys. Rev. ST Accel. Beams, **8**, page 062802 (Jun 2005).

[2] http://laacg.lanl.gov/laacg/services/download_sf.phtml (2012).

[3] Wesch, S., *et al. Machine Protection Considerations for BERLinPro.* In *Proceedings, 5th International Particle Accelerator Conference (IPAC 2014)*, page THPRI091 (2014).

# 9 Personnel Safety

## 9.1 General considerations

All CBETA-related activities will be organized and operated within CLASSE and its safety protocols. CLASSE holds no higher priorities than ensuring the health and safety of all. These values have been woven into the fabric of laboratory administration and operation. Synergistic relationships with CLASSE and Cornell University provide important policy guidance, institutional support, and oversight. The CLASSE approach to workplace safety is built around three overlapping commitments: to continuously provide a *safe laboratory environment*, to engender an abiding *culture of safety* in all personnel, and to address and anticipate safety challenges with *proactive management*.

The first line of defense against potential hazards is a *safe laboratory environment*. Exterior doors are locked outside of business hours; entry at off-hours is by keycard access or explicit permission of a staff member. Fire alarms are tied into the University centralized systems. State fire officials conduct inspections of the entire laboratory on an annual basis. Designated staff members are trained for specific roles in emergency situations. Only trained and/or licensed personnel operate industrial equipment, such as cranes, forklifts, and large vehicles. Machine tools are periodically inspected for correct operation and presence of appropriate guards. A spill control plan is in place for oil-filled transformers. An arc-flash hazard study of laboratory high-voltage AC distribution panels is nearly complete and recommended changes will be implemented soon. A lock-out/tag-out program is in place to cover work near equipment with remote power control, as is a policy governing hot work and welding. Personal protective equipment and safety training specific to their tasks is made available to workers who need it. Fume hoods for handling chemical samples are used, and detailed written safety procedures exist for hazardous tasks. MSDS are stored in notebooks near where the hazardous substances are used. Cryogenic installations and transfer lines are protected with sufficient insulation, redundant overpressure protections, oxygen-deficiency measurements where useful, and a multitude of instrumentation monitoring details of operation.

Radiation safety at CLASSE is regulated by Cornell's Environmental Health and Safety policies and authorized via a permit system, which are, in turn, governed by the New York State Department of Health (NY is an NRC-agreement state, and the regulations are embodied in 10 NYCRR Part 16 [1]). Cornell University is licensed by New York State to internally regulate radioactive material (RAM) and RPE, and has its own Radiation Safety Manual [2], Radiation Safety Officer (RSO), and Radiation Safety Committee (RSC).

Mitigation of radiation hazards from radiation-producing equipment (RPE) is dealt with via redundant engineering controls and administrative controls as well. Permanent shielding, generally consisting of concrete, lead, and/or iron, surrounds all RPE so as to restrict potential exposure to personnel outside its shielding to below 2 mrem in one hour or 100 mrem in one year. Locations just outside the shielding where radiation dose rates are expected to

be below those listed above but which are considered potentially vulnerable to higher levels, are designated as *controlled areas*, in accordance with Cornell University policy. Access to controlled areas is restricted to authorized personnel wearing radiation badges or those accompanying a CLASSE host with a real-time-readout dosimeter. Entrances to controlled areas are clearly signed. Exclusion areas, inside which personnel should not be present during RPE operation, are protected by more sophisticated access controls: all entryways are equipped with interlocked gates and/or light beams that, if tripped during RPE operation, cut power to the RPE and cause audible and visible alarms. Radiation detectors monitor the radiation in controlled areas, and trip off the RPE if conservative thresholds are exceeded. Exclusion area interlocks cannot be set until a full in-person search has been conducted; the integrity of interlock operation is verified by periodic operational tests of interlock components

CLASSE seeks to establish and maintain a *culture of safety*, which entails much more than simply compliance with a set of rules. A culture of safety is embodied by: each of us taking responsibility for our own safety and that of people we work with, supervise, or host; safety being valued on par with scientific achievement and/or task completion; safety concerns always being taken seriously and promptly addressed; safety challenges being approached with intellectual rigor; new activities being planned from the start with safety in mind; new participants receiving relevant safety training immediately. Such practices are self-reinforcing, but can be undermined by even occasional lapses, so considerable vigilance on the part of supervisory personnel is required.

*Proactive management* ensures that: specific safety responsibilities of each staff member, student, user, or visitor are clearly delineated and communicated; appropriate training and resources are provided to those who need it; mechanisms are in place to maintain accountability and establish and publicize appropriate safety-related policies; compliance with relevant University and governmental safety and environmental regulations and ordinances is attained; and intra-university resources are leveraged when helpful.

CLASSE has an extensive online Safety Handbook [3]. A central safety document database has been implemented (using the CERN EDMS system) and is home to procedures, radiation permit applications, meeting minutes, internal incident reports, and more. An in-house training database has tracked safety training history for each worker for nearly ten years. Conversion to a University-wide Learning Management System (LMS) will occur in June 2016. The new LMS uses a Saba cloud-hosted and browser-based solution, and manages courses, classes, learner transcripts, and web-based content and assessments, allowing learners and administrators alike access to what they need to achieve safety objectives.

Clear lines of accountability for performance related to safety have been shown to be crucial to superior safety achievement, especially in academic research settings. The CLASSE Safety Committee and CLASSE Safety Director, which set, communicate, and implement laboratory safety policy, speak and act with the imprimatur of the CLASSE Laboratory Director, who appoints both. Each staff member is accountable to a supervisor, and each student to an advisor.

## 9.2 More on Radiation Safety

The ERL linac, including its gun, accelerating components (ICM), and beam dump(s), as well as the CBETA SRF MLC have already been operating safely and compliantly in the L0E high-bay area at Wilson Laboratory for several months; aside from the MLC, those components operated similarly in the adjacent L0 high-bay area for a decade prior. A Cornell University RPE permit is in force, and will be amended as upgrades toward CBETA progress. The current layout of shielding blocks, actively interlocked radiation monitors, area dosimeters, and entry interlocks will all be modified, in stages, as the project progresses.

## 9.3 Accident Rate and Training Compliance

Cornell University tracks all accidents, injuries and exposures for the campus as a whole, and CLASSE tracks its approximately 300 workers separately. One metric that allows for comparison with other institutions is that of OSHA's *Total Recordable Cases* (TRC), defined as the number of accidents, injuries, or exposures that results in treatment beyond first aid or lost work time, per 100 workers per year. Campus-wide the TRC rate has hovered just above 2 for many years, in line with other colleges and Universities. CLASSE has maintained a TRC rate below 2.0 for 15 years (as long as it has been tracked), and below 1.0 since 2013, comparable to the DOE-lab average trend over 15 years, as seen in Fig. 9.3.1.

CLASSE administers more than two-dozen internal safety trainings, each specific to a particular hazard at the Laboratory. Cornell University Environmental Health and Safety also provides a large assortment of general safety trainings, of which about two dozen are taken by Laboratory personnel. Most such trainings are recurring (meaning the training must be retaken periodically), with recurrence times ranging from one to five years (comporting with state and/or federal regulations when applicable). Many trainings are in-person instructor-led trainings (ILT) and many are web-based trainings (WBT). The new LMS will ease access to these trainings while minimizing the administrative burden. The learning plan of each worker is populated with courses appropriate to her duties: the average CLASSE worker has about eight such courses on their learning plan, with large variations from one person to the next, depending on duties. In recent years we have tracked compliance on a person-trainings basis (treating each course assigned to any worker as the countable item), and on a people basis (treating each worker as 100% compliant with all required trainings or not as the countable item). Since tracking these metrics began, compliance has improved up to 98% and 88%, respectively, as shown in Fig. 9.3.2. (Due to recurring courses, individuals can cycle out of compliance when a course expires but regain it by refreshing the training, so the individuals out of compliance are a constantly churning group of different people temporarily in that state.) New workers are not permitted to engage in hazardous activities until relevant training is completed.

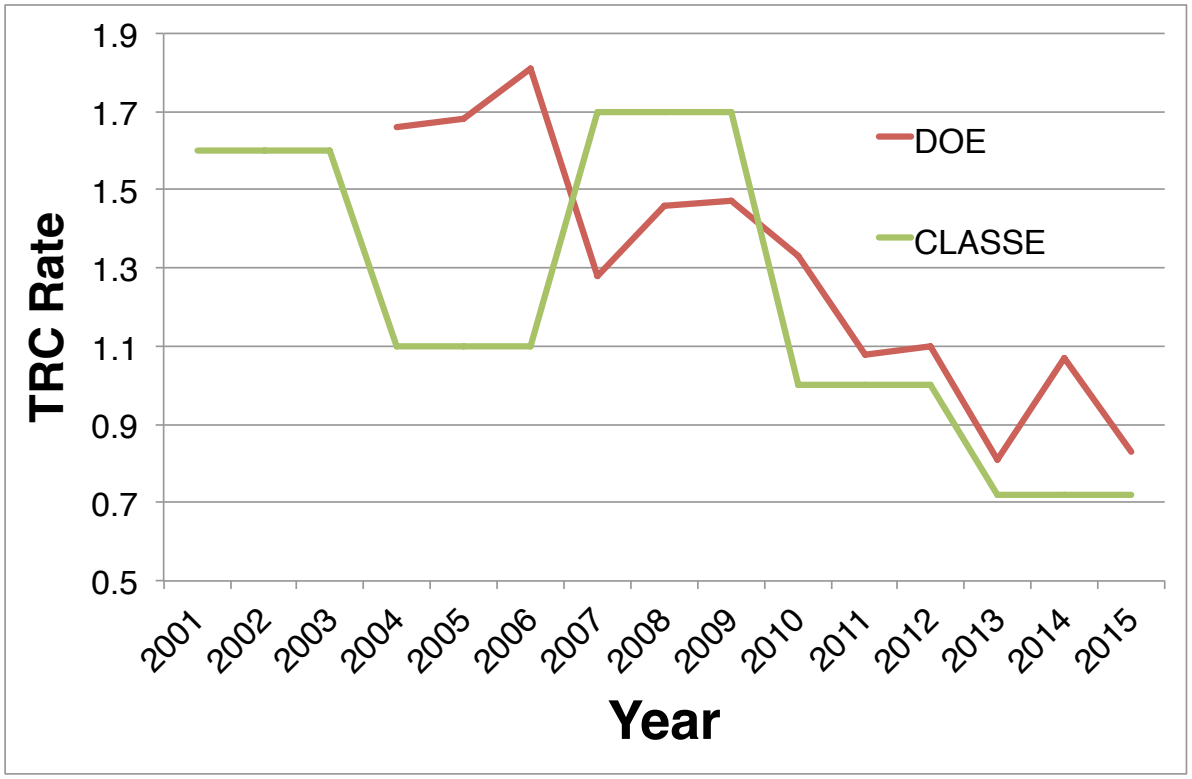


Figure 9.3.1: Accident rate at CLASSE and DOE-Lab-average vs. time. The TRC rate counts accidents that result in either lost time or treatment beyond first aid, or both, per 100 workers per year.

## 9.4 CBETA-specific safety challenges

### 9.4.1 New collaborators

CLASSE already has a large variety of personnel using its facilities: technical staff, faculty, postdocs, undergraduate and graduate students, Cornell and (mostly) non-Cornell CHESS users, and visiting scientists. New onsite CBETA collaborators will be subject to the same requirements as everyone else with regard to training and compliance.

### 9.4.2 Radiation safety

Personnel safety systems will be designed using similar criteria and equipment as other systems at CLASSE, meeting University and NY State standards. CLASSE has experience shielding electron beams at CESR, which have higher energy (5.3 GeV) and lower currents (∼100 mA). Shielding will be designed with the largest credible beam loss scenario, and likely require iron-loaded concrete walls to a tunnel enclosing the ring on sides and top. The simulation tool MCNP will be employed for this task.

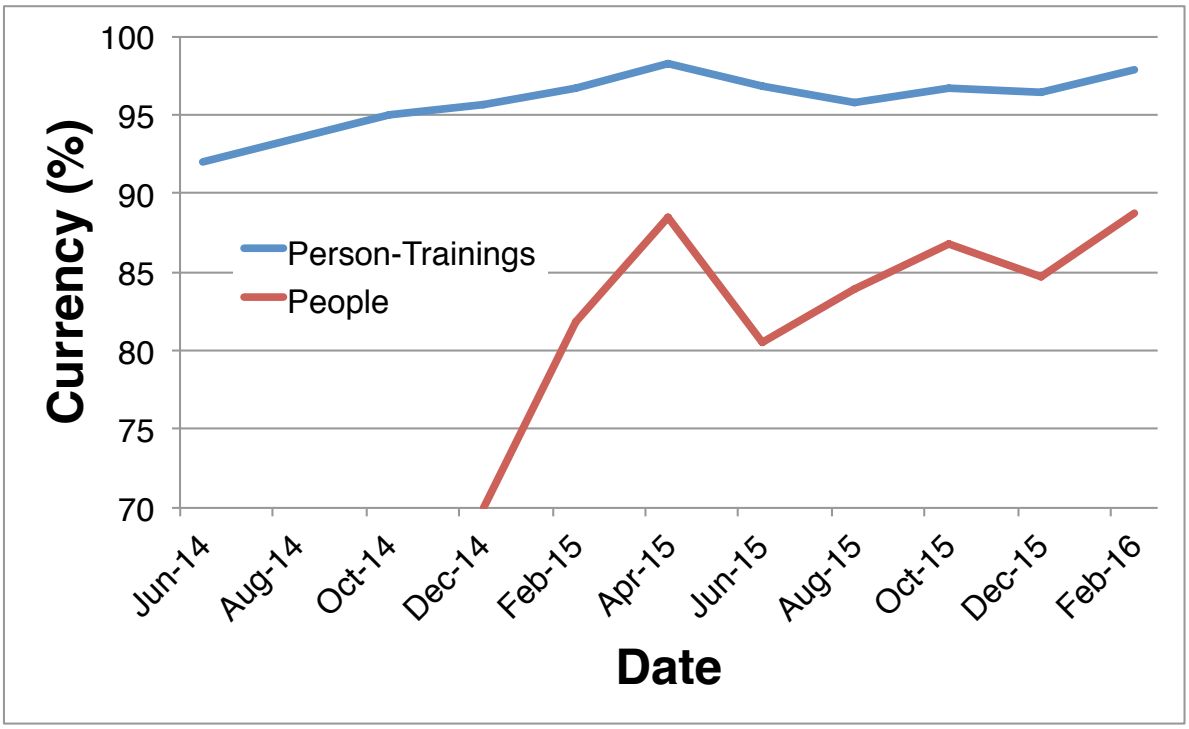


Figure 9.3.2: Compliance percentage for all CLASSE staff vs. time, where person-trainings counts each individual required training for each person as the countable unit, and people counts those with 100% compliance on all their required trainings relative to all CLASSE personnel.

### 9.4.3 Cryogenic safety

The CBETA cryogenic plant will be part of the larger CLASSE central facilities, which already satisfy CESR and existing ERL/MLC operations. Liquid helium and liquid nitrogen lines and volumes are designed to avoid trapped volumes and equipped with overpressure relief and backup burst disks, as elsewhere in the Laboratory. Particular attention will have to be paid to worst-credible-case accidents inside the shielding tunnel.

### 9.4.4 Electrical safety

All electrical lines are designed and built with best-practice criteria, including separation of high-voltage and low-voltage cable/conduit runs. Remotely powered equipment will be serviced with OSHA-compliant lock/tag/verify capabilities and procedures.

## References

[1] https://www.health.ny.gov/environmental/radiological/radon/radioactive_material_licensing/docs/part16.pdf.

[2] https://sp.ehs.cornell.edu/lab-research-safety/radiation/radiation-safety-manual/Pages/default.aspx.

[3] https://wiki.lepp.cornell.edu/lepp/bin/view/Safety/Handbook/WebHome.

# 10 Commissioning

## 10.1 Concepts and Philosophy

An ERL is a non-equilibrium system that lacks a closed orbit and may not possess global transverse or longitudinal stability. Dynamically it is more closely related to time-of-flight spectrometers and injector systems than the conventional linear and circular accelerators that it superficially resembles. ERLs therefore encounter numerous unique operational challenges [1, 2]. Firstly, longitudinal motion dominates the dynamics: timing and energy control set the system architecture, and thus RF phase and gradient control must be assured, as must the lattice momentum compaction, the correlation of time of flight with energy. Secondly, the non-equilibrium nature of an ERL means that stability is a significant challenge. Thirdly, halo effects dominate high power operation (much as they do in injector chains); losses can be performance limiting: activation, damage (burn-through), and background for users are all issues. Finally, as inherently multi-pass systems, ERLs must control multiple beams with different properties (energy, emittance, position, phase) during transport through and handling in common beamline channels. Successful machine operation thus requires a comprehensive strategy for machine commissioning, monitoring machine health, system stabilization, and machine protection.

ERL operation comprises a series of phases: commissioning, beam operation, and machine tuning/recovery. During each phase, system behavior falls into various classes that can be differentiated by the time scales on which they are manifest: "DC" conditions, those associated with the machine set point, "drift" effects, slow wandering of the set-point (due to, for example, thermal effects) degrading system output, and "fast" effects (at acoustical to RF time scales), resulting in beam instabilities. A fourth class, that of transient effects (for example, RF loading during beam on/off transitions and fast shut-down in the event of sudden beam loss for machine protection purposes), can occur throughout all operational cycles.

Machine commissioning has combined goals of validating system design architecture and defining a recoverable system operating point. For an ERL, this requires demonstration of the control of phenomena of concern such as BBU and the micro-bunching instability ($\mu$BI), while generating settings for hardware components.

Following pre-commissioning "hot" checkout of accelerator components and testing of hardware subsystems, beam operations commence with threading of low power beam so as to establish a beam orbit and correct it to specified tolerances. At this stage, system performance is error dominated. Some errors (such as RF phases or magnet installation errors) can be readily detected and corrected; others are subliminal, below the resolution of diagnostics or individual measurements, and will accumulate. Thus, some corrections are local (eliminating the error) and others must be global (such as the compensation of cumulative errors).

This requires orbit correction systems based on beam position monitors and steerers (typically every quarter-betatron wavelength); unique to a multi-pass ERL with common transport

of multiple beams in a single beam line is the requirement that the system correct perturbations locally so that the multiple passes respond identically and the orbits not diverge unacceptably from turn to turn. Similarly, a baseline for longitudinal beam control must be established, by synchronizing the beam to the RF using recirculator arcs as spectrometers for precision measurements of energy gain. Any path length adjustments needed to set RF phases and insure energy recovery per the design longitudinal match are thus determined.

With a 6-D phase space reference orbit thus defined, the beam and lattice behavior is tuned and validated. Lattice performance is measured, tuned, and certified using differential orbit/lattice transfer function measurements; these, too, will require pass-to-pass discrimination for beams in common transport. Both transverse and longitudinal measurements (using phase transfer function diagnostics [3]) are necessary for a full analysis of lattice behavior. Corrections must be applied to 'rematch the beam to the lattice acceptance' and bring both transverse (betatron motion/focusing) and longitudinal (timing/momentum compaction) motion into compliance with design (or to establish an alternative working point).

Certification of lattice performance allows analysis, tuning, and validation of beam parameters, and matching of the beam to the lattice. This requires measurements of both betatron (emittance, beam envelope functions) and longitudinal (bunch length/energy spread/emittance, phase/energy correlation) properties. Disentangling the properties of multiple beams in common transport may prove challenging and require use of beyond-state-of-the-art techniques. If beam properties differ excessively from specification, matching of the beam to the lattice is performed using appropriate correction algorithms. As with orbit correction, perturbations will likely require local correction so as to avoid excessive pass-to-pass divergence of beam properties.

Given a validated working point, beam power scaling is performed, with currents increased from tune-up levels to full power CW. Transient control and beam stabilization (see below) must be investigated and demonstrated during commissioning; they remain a persistent activity through the operational lifetime of the machine, and are therefore discussed below.

## 10.2 Goals and Overview

The basic goal of commissioning is to demonstrate reproducible/recoverable machine operation with specific performance parameters, as presented at the end of this document. Given the precedence of longitudinal dynamics in an ERL, this requires, at the highest level, the proper adjustment of linac phases and gradients and transport system momentum compactions to confirm that they are in compliance with the design longitudinal match. Provision must therefore be made for measurement of time of flight and/or energy as a function of phase, with adequate resolution to set phases and calibrate RF gradients to the tolerances required for successful FFAG operation. This must be done on a pass-by-pass basis, initially setting RF parameters, and meeting subsequent phasing requirements by adjusting turn-to-turn path lengths in the recirculator. This is an iterative process, in which an initial orbit is established (the beam is "threaded"), and the RF is phased to the available resolution. Performance assessments (for both machine and beam) are then used to evaluate if iteration is required (to improve steering, phasing, and beam quality, correct machine errors, or improve address beam physics effects) or if the commissioning process moves forward. At the next level, the

system "spectrometer" characteristics are validated. Commissioning activities move forward until beam quality is sufficiently degraded that progress slows or stops, or losses exceed tolerances for safe system operation. Characterization and analysis procedures are then applied to determine if performance limitations are due to the linac, the transport system, or are rooted in beam dynamical effects. This will involve measurements of beam energy, timing (phase) and time of flight, beam properties, and lattice characterization (typically using differential orbit measurement).

## 10.3 Commissioning Flow

The first goal is to commission the injector and merger, matching the target emittance and Twiss parameters for a variety of bunch charges, booster and linac settings. Additionally, high current operation through the merger will be investigated to see what limitations are present. After that the linac will be installed, which will preclude any further high current operation until full energy recovery is achieved (due to power limitations). After linac operation is verified and the FFAG ring and spreaders are completed, the FFAG will be commissioned one pass at a time, first at zero average current, and then by slowly raising the current to see what problems arise and when they arise.

- Commission injector
- Bring linac on line (power limited)
- Single Turn ERL operation
  - Low power operation
  - Ramp power
- Multi-turn ERL operation
  - Low power operation
  - Ramp power

## 10.4 Outline of Process

1. Hot check out of all systems
   a) Power individual subsystems
      i. Gun
      ii. Vacuum
      iii. RF
      iv. Diagnostics
   b) Certify PPS, MPS, interlocks
   c) Exercise controls and high level applications

2. Commission injector
    a) Beam properties/performance after ICM
    b) High current operation, without merger
    c) Beam properties/performance through merger
    d) High current operation through merger
3. Bring linac online
    a) Thread beam at low gradient
    b) Phase using RF transient
    c) Raise gradient/energy
    d) Center beam in linac
    e) Phase using spectrometer
        i. Thread into 1st spreader line (configured as spectrometer; insertable dump)
    f) Validate lattice
        i. Fine tune steering
        ii. Difference orbits
    g) check/validate/refine beam properties
4. First turn
    a) Configure both spreaders for 1 turn operation
    b) Thread 1st spreader
    c) Validate spreader lattice (difference orbits)
    d) Validate beam properties through spreader; match to arc
    e) Thread arc: steer, looking for beam on BPMs, minimizing Beam Loss Monitors (BLMs), watching viewers
    f) Thread 2nd spreader to insertable dump
    g) With beam parked on insertable dump
        i. Refine arc and spreader orbit
        ii. Validate arc and spreader lattice (difference orbits)
        iii. Validate beam properties through arc, properties into spreader
    h) Set reinjection match
    i) Remove insertable dump; thread linac 2nd pass
    j) Set path length to recover beam energy
    k) Fine-tune recovery steering
    l) Validate linac 2nd pass lattice; validated recovered beam properties
    m) Set up MPS/BLMs

Table 10.5.1: Injector Parameters

| | | |
|---|---|---|
| Bunch Charge | 0-1000 | pC |
| Emittance $\epsilon_{x,y}$ (rms, norm.) | $\lesssim 1$ | $\mu$m |
| Bunch Length $\sigma_t$ (rms) | $< 4$ | ps |
| Matching Twiss: $\alpha_{x,y}$ | -1 | |
| $\beta_{x,y}$ | 12.5 | m |
| Energy Spread (at 6 MeV) | $\lesssim 2 \times 10^{-3}$ | |

n) Set up high-power pulsed

o) Optimize orbit and focusing to limit losses

p) Go CW and ramp current

i. Loss management: iterate high power pulse (may be RF drive limited)

5. Next turn(s)

a) Repeat process for 2nd turn

b) Repeat process for 3rd turn

c) Repeat process for final turn

## 10.5 Injector and Merger

These tests will be performed before the FFAG is completed, as preliminary tests of the injector components. During this phase, a complete 6D phase space diagnostic section will be installed in place of the linac in order to completely characterize the low energy beam. This also presents the best opportunity to test our ability to correct various beam properties using our online simulation, and, in the process, validate and improve that model, since we will have full knowledge of our bunches. Of primary interest is determining a set of optics as a function of bunch charge that can deliver a beam that is matched to the FFAG lattice. Specific matching parameters are shown in Tab. 10.5.1. Later, if we discover that we need to ramp the current by ramping up the bunch charge, we will need a way to move smoothly between these optimal settings. Finally, the high power beam dump will also be installed during this phase, and any initial current limitations from halo or other sources can be studied through the merger.

The procedure for commissioning the injector and merger is already established and tested, and has been successfully used in the past [4] The same procedure will be used here, with slight modifications to also test our ability to match the FFAG lattice parameters.

### 10.5.1 Linac

When threading the beam through the linac, we assume that all cavities must be on in order to get the beam fully through the linac. As a result, we cannot phase each cavity independently as with the ICM cavities. Instead, we will first use a monitor of the transient RF forward

power in a low duty cycle mode. By maximizing the forward power used, we will roughly maximize the energy gained by the beam. This should be sufficient to get the beam into the 1st spreader and onto the insertable dump. Then, using the spreader as a spectrometer, we can fine tune the phasing of each cavity individually.

## 10.6 First Turn

### 10.6.1 FFAG, First Turn

On the first pass, it's likely that the beam can be threaded through the FFAG using typical orbit correction procedures: minimizing beam loss, using viewscreens, etc. After the beam is roughly threaded through the FFAG and onto the insertable dump in the 2nd spreader, the charge can be increased enough for a detailed measurement of its orbit and automated correction. On subsequent passes, it is likely that the system will be too complicated for non-automated correction, so it is very important that we verify this correction procedure as well as possible during the first pass. In addition, if there are any overall correlations in the corrections put on the beam, this may indicate that either the magnets need to be shifted, or the BPM centers are systematically off. The first pass is the best opportunity to address this– perhaps by physically shifting magnets until there is no correlation in the correction optics.

### 10.6.2 Linac, Second Pass

Rough phasing for the second pass through the linac can be accomplished by examining the arrival time at the last BPM in the spreader. The arrival phase at that BPM can first be calibrated by connecting it to the same measurement hardware as the last BPM in the injector. Since the linac is already phased to be on-crest with respect to the arrival at that BPM, the only missing information is the difference in path length from both BPMs to the first cavity. This path length can be estimated well enough to allow the beam to be roughly phased for energy recovery. After that, spectrometer phasing into the beam dump will fine-tune the phasing.

### 10.6.3 High Current, First Turn

Initially, the linac will be phased to recover energy after the first pass through the FFAG. After the beam is successfully threaded into the dump after a single pass, the next challenge is to raise the current. There are two strategies to do this: increase the number of bunches at a fixed charge, or increase the bunch charge. The first option requires a large rejection ratio of laser pulses, so that the rejected part of the beam does not add up to a significant current. Otherwise, it is likely that rejected beam will be badly matched to the FFAG lattice and be lost. The second option will require us to find a path in optics settings from zero to full bunch charge that preserves the lattice matching. Both methods may or may not be practical, and will require testing during commissioning.

As we turn up the current, re-steering to minimize beam loss, the primary limitation is likely to be beam halo. Halo management will be difficult in the FFAG, since there is very little

room for tweaking optics there. The focusing in the spreaders might be the nearest knobs to turn, and we may even be required to adjust the focusing in the injector.

## 10.7 Multiple Turns

Subsequent turns will proceed similarly to the first turn, though orbit correction will have to be automated to some extent, as the correctors will impact all passes simultaneously. BPM arrival time in the second spreader will again be used to roughly phase the linac, and either spectrometer phasing into the first spreader or dump will again be used to fine tune the phasing. Each turn will be added individually, initially phased for energy recovery, so that high-current operation can be tested for 1, 3, 5 and 7 passes through the ring.

## References

[1] Douglas, D. *Operational' Beam Dynamics Issues.* In *ERL2009 Proceedings, Cornell University, Ithaca, NY, USA* (2009).

[2] Douglas, D. *Beam Physics Issues Encountered During the Operation of CW SRF ERLs.* In *EIC 2014, Jefferson Lab, Newport News, VA, USA,* (2014).

[3] Benson, S. V., *et al. Electron Beam Diagnostics of the JLab UV FEL.* Conf. Proc., **C110328**, pages 1446–1448 (2011).

[4] Gulliford, C., *et al. Demonstration of low emittance in the Cornell energy recovery linac injector prototype.* Phys. Rev. ST Accel. Beams, **16**, page 073401 (Jul 2013).